

**A PRACTICAL MODEL FOR LOAD-UNLOAD-RELOAD CYCLES ON SAND**

**by**

**ANTONE E. DABEET**

**B.Sc., The American University in Cairo, 2005**

**A THESIS SUBMITTED IN PARTIAL FULFILLMENT OF  
THE REQUIRMENTS FOR THE DEGREE OF  
MASTERS OF APPLIED SCIENCE**

**in**

**THE FACULTY OF GRADUATE STUDIES  
(CIVIL ENGINEERING)**

**THE UNIVERSITY OF BRITISH COLUMBIA  
(VANCOUVER)**

**October 2008**

**© Antone Dabeet, 2008**

## ABSTRACT

The behaviour of sands during loading has been studied in great detail. However, little work has been devoted to understanding the response of sands in unloading. Drained triaxial tests indicate that, contrary to the expected elastic behaviour, sand often exhibit contractive behaviour when unloaded. Undrained cyclic simple shear tests show that the increase in pore water pressure generated during the unloading cycle often exceeds that generated during loading. The tendency to contract upon unloading is important in engineering practice as an increase in pore water pressure during earthquake loading could result in liquefaction.

This research contributes to filling the gap in our understanding of soil behaviour in unloading and subsequent reloading. The approach followed includes both theoretical investigation and numerical implementation of experimental observations of stress-dilatancy in unload-reload loops. The theoretical investigation is done at the micro-mechanical level. The numerical approach is developed from observations from drained triaxial compression tests. The numerical implementation of yield in unloading uses NorSand – a hardening plasticity model based on the critical state theory, and extends upon previous understanding. The proposed model is calibrated to Erksak sand and then used to predict the load-unload-reload behaviour of Fraser River sand. The trends predicted from the theoretical and numerical approaches match the experimental observations closely. Shear strength is not highly affected by unload-reload loops. Conversely, volumetric changes as a result of unloading-reloading are dramatic. Volumetric strains in unloading depend on the last value of stress ratio ( $q/p$ ) in the previous loading. It appears that major changes in particles arrangement occur once peak stress ratio is exceeded. The developed unload-reload model requires three additional input parameters, which were correlated to the monotonic parameters, to represent hardening in unloading and reloading and the effect of induced fabric changes on stress-dilatancy. The calibrated model gave accurate predictions for the results of triaxial tests with load-unload-reload cycles on Fraser River sand.

# TABLE OF CONTENTS

<b>ABSTRACT.....</b>	<b>ii</b>
<b>TABLE OF CONTENTS.....</b>	<b>iii</b>
<b>LIST OF TABLES .....</b>	<b>vii</b>
<b>LIST OF FIGURES.....</b>	<b>ix</b>
<b>LIST OF SYMBOLS .....</b>	<b>xvi</b>
<b>ACKNOWLEDGEMENTS .....</b>	<b>xix</b>
<b>1. INTRODUCTION.....</b>	<b>1</b>
1.1. Research Objectives.....	4
1.2. Thesis Organization.....	5
<b>2. LITERATURE REVIEW .....</b>	<b>6</b>
2.1. Experimental soil behaviour.....	6
2.1.1. Typical stress-strain behaviour of sand .....	7
2.1.2. The Critical State.....	11
2.1.3. The state parameter.....	17
2.1.4. Yielding of sands.....	20
2.2. Triaxial testing .....	22
2.3. Soil constitutive models .....	25
2.3.1. Elasto-plastic soil modelling .....	25
2.3.2. Simple soil models .....	29
2.3.3. Cam-Clay soil model.....	32
2.4. Stress-Dilatancy.....	37
2.5. The NorSand soil model .....	45
2.5.1. Yield surface and flow rule .....	47
2.5.2. Hardening of the yield surface.....	50
2.5.3. Typical evolution of the yield surface .....	52
2.5.4. Elastic properties of NorSand.....	53

2.5.5. Summary of the NorSand model .....	53
<b>2.6. Soil behaviour in unloading .....</b>	<b>55</b>
2.6.1. A Simple physical model.....	55
2.6.2. Thermo-mechanical approach .....	56
2.6.3. Unloading in NorSand.....	62
2.6.4. Summary .....	65
<b>3. DILATANCY IN UNLOAD-RELOAD LOOPS: A THEORETICAL INVESTIGATION.....</b>	<b>66</b>
3.1. Micro-Mechanical perspective for dilatancy in unloading.....	66
3.2. Micro-Mechanical perspective for dilatancy in reloading.....	71
3.3. Summary.....	74
<b>4. DILATANCY IN UNLOAD-RELOAD LOOPS: AN EXPERIMENTAL INVESTIGATION.....</b>	<b>75</b>
4.1. Sands Tested .....	75
4.1.1. Erksak Sand.....	75
4.1.2. Fraser River Sand .....	76
4.2. Testing program.....	77
4.2.1. Erksak Sand Testing Program .....	77
4.2.2. Fraser River Sand .....	79
4.3. Experimental observations.....	80
4.4. Implications of experimental observations .....	93
<b>5. A MODEL TO ACCOMMODATE UNLOAD-RELOAD LOOPS USING NORSAND .....</b>	<b>96</b>
5.1. Yield surface and internal cap .....	98
5.2. Flow rule.....	100
5.2.1. Flow rule in unloading.....	100
5.2.2. Flow rule in reloading.....	102
5.2.3. Potential surface in unloading .....	106
5.3. Hardening in loading, unloading and reloading.....	109
5.4. Comparison with other models.....	114
5.5. Summary.....	120
<b>6. MODEL CALIBRATION.....</b>	<b>121</b>
6.1. Monotonic calibration for Erksak sand .....	121
6.1.1. Critical state parameters .....	122

6.1.2. Elasticity parameters.....	128
6.1.3. Plasticity parameters.....	130
6.1.4. Summary of Erksak monotonic calibration .....	132
<b>6.2. Monotonic calibration for Fraser River sand.....</b>	<b>135</b>
6.2.1. Critical State parameters.....	135
6.2.2. Elasticity parameters.....	139
6.2.3. Plasticity parameters.....	139
6.2.4. Summary of Fraser River Sand monotonic calibration.....	142
<b>6.3. Unload-reload calibration to Erksak sand.....</b>	<b>142</b>
6.3.1. Overview of Erksak Unload-Reload Calibration.....	146
<b>6.4. Summary.....</b>	<b>150</b>
<b>7. PREDICTIONS OF FRASER RIVER SAND UNLOAD-RELOAD BEHAVIOUR.....</b>	<b>151</b>
7.1. Model parameters .....	151
7.2. Model predictions.....	152
7.3. Discussion of model predictions.....	154
7.4. Summary.....	156
<b>8. SUMMARY AND CONCLUSIONS.....</b>	<b>160</b>
8.1. Context of Research.....	160
8.2. Research Objectives.....	161
8.3. Methodology .....	161
8.4. Conclusions.....	161
8.5. Suggestions for Future Work.....	163
<b>REFERENCES .....</b>	<b>165</b>
<b>APPENDIX A: PREDICTION OF STRESS DILATANCY IN UNLOADING .....</b>	<b>170</b>
<b>APPENDIX B: RESULTS OF THE UNLOAD-RELOAD CALIBRATION FOR ERKSAK SAND .....</b>	<b>176</b>
<b>APPENDIX C: FRASER RIVER SAND MONOTONIC CALIBRATION RESULTS .....</b>	<b>183</b>

<b>APPENDIX D: STEPS TO IMPLEMENT THE LOAD-UNLOAD-RELOAD MODEL IN A CODE .....</b>	<b>189</b>
<b>APPENDIX E: TRIAXIAL TESTING PROCEDURE.....</b>	<b>192</b>

## LIST OF TABLES

Table 2.1. Summary of NorSand equations (modified after Jefferies and Shuttle, 2005).	54
Table 2.2. Summary of NorSand parameters (after Jefferies and Shuttle, 2005).	55
Table 4.1: Index properties of Fraser River and Erksak sands	76
Table 4.2: Drained triaxial compression tests on Erksak Sand with load-unload-reload cycles (data from <a href="http://www.golder.com/liq">www.golder.com/liq</a> )	78
Table 4.3: Undrained monotonic triaxial compression tests on Erksak sand (data from Been et. al., 1991)	78
Table 4.4: Drained triaxial compression tests with load-unload-reload cycles on Fraser River sand (data provided by Golder Associates)	79
Table 4.5. Monotonic triaxial compression tests on Fraser River sand (data provided by Golder Associates)	80
Table 4.6. Direction of volumetric changes in unloading for the load-unload-reload tests on ES	81
Table 5.1. Equations used in the triaxial compression version of NorSand and their step by step implementation in an Euler integration code	96
Table 5.2. Summary of the unloading part of the model.	115
Table 5.3. Comparison between hardening in the proposed model and Drucker and Seereeram (1987).	119
Table 6.1. Typical ranges for monotonic parameters (same as Table 2.2, modified after Jefferies and Shuttle, 2005).	122
Table 6.2. $M_{tc}$ using stress-dilatancy method for the unload-reload tests on Erksak sand.	126
Table 6.3. Summary of $M_{tc}$ values for Erksak sand	127
Table 6.4. Summary of monotonic calibration for Erksak sand	134
Table 6.5. Summary of NorSand monotonic calibration to Fraser River sand	141
Table 6.6. Summary of the unload-reload calibration for Erksak sand.	146

<b>Table 7.1. Parameters used for Fraser River sand unload-reload predictions. ....</b>	<b>152</b>
---	------------



## LIST OF FIGURES

Figure 1.1. The behaviour of an elastic material in loading and unloading.....	2
Figure 1.2. Results of a triaxial test on Erksak sand in volumetric strain vs. axial strain (reproduced after Golder, 1987). ....	2
Figure 1.3. Drained simple shear tests on Fraser River sand (modified after Sriskandakumar, 2004). ....	3
Figure 1.4. Cyclic direct simple shear test on Fraser River Sand (modified after Wijewickreme et al. , 2005). ....	4
Figure 2.1. Schematic of typical results of a drained triaxial test on loose and dense sand samples (a) deviator stress vs. axial or deviator strain (b) volumetric strain vs. axial or deviator strain. ....	9
Figure 2.2. Schematic of typical results of an undrained triaxial test on loose and dense sand samples (a) deviator stress vs. axial or deviator strain (b) pore pressure vs. axial or deviator strain. ....	10
Figure 2.3. Schematic of stress strain curves for different mean effective stress values at constant initial void ratio. ....	11
Figure 2.4. Effect of sample preparation method (a) deviator stress vs. axial strain (b) volumetric strain vs. axial strain. (modified after Mitchell and Soga, 2005). ....	12
Figure 2.5. Results of simple shear tests on 1-mm diameter steel balls at constant normal effective stress of 138 kPa (reproduced from Roscoe et. al., 1958). ....	13
Figure 2.6. Drained triaxial compression tests on Chattahoochee River sand (reproduced after Vesic and Clough, 1968) ....	14
Figure 2.7. Critical State Line for Erksak 330/0.7 sand (reproduced from Been et al., 1991). ....	15
Figure 2.8. The projection of the critical state line (a) $p' - q$ (b) $e - \log p'$ .....	18

Figure 2.9. Stress paths for three undrained triaxial tests on Kogyuk 350/2 Sand (reproduced from Been & Jefferies, 1985). .....	19
Figure 2.10. Peak friction angle as a function of state parameter for several sands (modified from Been & Jefferies, 1985). .....	19
Figure 2.11. Projection of the yield surface in $p'$ - $q$ plane for Aoi Sand (reproduced from Yasufuku et al., 1991). .....	21
Figure 2.12. Family of yield envelopes for Fuji River sand (reproduced from Ishihara and Okada, 1978). .....	21
Figure 2.13. Schematic of the triaxial apparatus. ....	24
Figure 2.14. An example of a yield surface. ....	27
Figure 2.15. Definition of dilatancy (modified after Jefferies & Been, 2006). ....	27
Figure 2.16. Definition of normality. ....	28
Figure 2.17. Example of the yield surface hardening. ....	29
Figure 2.18. Tresca yield criteria in 3-D stress space. ....	30
Figure 2.19. Normality to Tresca and Mohr-Coulomb surface. ....	30
Figure 2.20. Mohr-Coulomb yield criteria in 3-D stress space. ....	32
Figure 2.21. Parallel CSL and NCL in $e$ - $\log p'$ plot. ....	36
Figure 2.22. Original Cam-Clay yield surface. ....	36
Figure 2.23. Typical assembly of rigid rods (a) stress conditions (b) deformation characteristics (reproduced from Rowe, 1962). .....	39
Figure 2.24. Forces acting on a rigid block sliding on an inclined surface (reproduced from Rowe, 1962). .....	40
Figure 2.25. Comparison between Rowe's stress-dilatancy, Cam-Clay flow rule, and Nova's rule. ....	42
Figure 2.26. Dilatancy component of strength as a function of mean effective stress at failure and relative density (reproduced from Bolton, 1986). ....	45
Figure 2.27. Infinite number of NCL's (reproduced from Jefferies and Shuttle, 2002)... ..	47
Figure 2.28. NorSand yield surface (modified after Jefferies and Shuttle, 2005). ....	51
Figure 2.29. Minimum dilatancy as a function of state parameter at image for 13 sands (modified after Jefferies and Been, 2006). .....	52
Figure 2.30. The Saw Tooth Model a) loading phase b) unloading phase. ....	56

Figure 2.31. Energy balance as introduced by palmer (1967). .....	58
Figure 2.32. Stress-dilatancy for Cam-Clay loading, Nova loading, and Jefferies (1997) unloading.....	60
Figure 2.33. Schematic representation of work storage and dissipation according to Collins (2005). .....	61
Figure 2.34. Movement of yield surface in NorSand: Case of unloading from a point on the internal cap.....	64
Figure 2.35 Movement of yield surface in NorSand: Case of unloading from a point before reaching the internal cap.....	65
Figure 3.1 Micro-mechanical representation of dilatancy for a uniform packing of rigid rods during both loading and unloading a) Minimum void ratio for $\beta = 60^\circ$ b) Maximum void ratio for $\beta = 45^\circ$ c) Minimum void ratio for $\beta = 30^\circ$ .....	68
Figure 3.2. Two different uniform assemblies of rigid rods; the dashed rectangle represents the basic unit volume (reproduced after Li and Dafalias, 2000). .....	71
Figure 3.3 Theoretical expression based on grain to grain friction ( $\phi_\mu=25^\circ$ ) for the uniform packing in Figure 3.1 a) compared with a drained triaxial test on Erksak 330/0.7 ( $p' = 100$ kPa and $e_o = 0.653$ ) in stress ratio vs. dilatancy space, b) Angle between the vertical direction and the tangent at the interface between grains.....	73
Figure 3.4. Rowe's stress-dilatancy relation based on grain to grain friction for the two packings in Figure 3.2.....	74
Figure 4.1. Data from ES_CID_867 (a) stress ratio vs. axial strain (b) volumetric vs. axial strain (c) stress ratio vs. dilatancy.....	85
Figure 4.2. Data from ES_CID_867 in shear stress vs. axial strain.....	86
Figure 4.3. Results of FR_CID_02 in shear stress vs. axial strain.....	86
Figure 4.4. Zoom on loops 1 and 2 for test ES_CID_867. ....	87
Figure 4.5. Zoom on the elastic zone in Figure 4.1c.....	88
Figure 4.6. Data from ES_CID_868 (a) stress ratio vs. axial strain (b) volumetric vs. axial strain (c) stress ratio vs. dilatancy.....	89
Figure 4.7. Comparison of ES_CID_870 and ES_CID_872 with similar $e_o$ and initial $p'$ but different number of U-R loops (a) axial strain vs. stress ratio (b) axial strain vs. volumetric strain. ....	90

Figure 4.8. Comparison of ES_CID_861 and ES_CID_862 with similar $e_o$ and initial $p'$ but different number of U-R loops (a) axial strain vs. stress ratio (b) axial strain vs. volumetric strain. ....	91
Figure 4.9. Stress ratio vs. dilatancy for pre-peak and post-peak reloading loops (ES_CID_862). ....	92
Figure 4.10. Stress ratio vs. dilatancy for different reload loops (ES_CID_867).....	92
Figure 4.11. $D_{min}$ vs. $\psi$ at $D_{min}$ for first and second loading of Erksak sand.....	93
Figure 4.12. The saw tooth model (a) loading (b) unloading (Same as Figure 2.35). ....	94
Figure 5.1. Yield surface and internal cap in NorSand, same as Figure 2.28 (modified after Jefferies and Shuttle 2005). ....	99
Figure 5.2. Demonstration of interpreted elastic and elasto-plastic zones on the results of ES_CID_682 in stress ratio vs. dilatancy plot. ....	100
Figure 5.3. Drained triaxial tests on Erksak sand with unload-reload loops plotted in the dilatancy vs. $\eta$ space. ....	102
Figure 5.4. $\eta_L$ and $M_u$ for L3 and U3, respectively, for ES_CID_862. ....	103
Figure 5.5. Correlation between $M_u$ and $\eta_L$ from previous loading (drained triaxial tests on Erksak sand).....	103
Figure 5.6. Predicted and measured stress-dilatancy for ES_CID_866.....	104
Figure 5.7. Change of $M_i$ for different reloading loops (ES_CID_862). ....	106
Figure 5.8. The shape of the potential surface in unloading.....	109
Figure 5.9. Expanded scale view of U2/L3 for ES_CID_868 in Figure 4.6a. ....	111
Figure 5.10. The direction of plastic strain increment ratios in unloading with the corresponding yield surfaces and internal caps. ....	113
Figure 5.11. The direction of plastic strain increments ratios in unloading normal to the potential surfaces. ....	114
Figure 5.12. Predicted and measured stress-dilatancy for ES_CID_866.....	117
Figure 5.13. Drucker and Seereeram model (reproduced from Drucker and Seereeram, 1987). ....	118
Figure 5.14. Hardening according to Jefferies (1997) (same as Figure 2.35). ....	119
Figure 6.1. $M_{tc}$ using Bishops method for Erksak sand. ....	124
Figure 6.2. $M_{tc}$ using stress-dilatancy method (ES_CID_871). ....	125

Figure 6.3. Range of $M_{tc}$ using the stress-dilatancy method from the last reloading loops for the 9 tests in Table 4.2.....	126
Figure 6.4. CSL determination for Erksak sand from loose undrained tests. ....	127
Figure 6.5. Enlarged view of the elastic part in L3 for ES_CID_866. ....	129
Figure 6.6. The elastic bulk modulus from Equations 6.1 and 6.3 against $p'$ for the elastic zone in L3 for ES_CID_866. ....	130
Figure 6.7. Trend lines through $D_{min}$ vs. $\psi$ at $D_{min}$ for first and second peaks for Erksak sand .....	131
Figure 6.8. Best fit to $H$ vs. $\psi_o$ for Erksak sand.....	132
Figure 6.9. Example fit to test ES_CID_867. ....	133
Figure 6.10. Recommended procedure for obtaining NorSand parameters.....	135
Figure 6.11. $M_{tc}$ using Bishop method for Fraser River sand.....	137
Figure 6.12. Enlarged view of the dilatant zone for FR_CID_03.....	137
Figure 6.13. $M_{tc}$ using stress-dilatancy method for FR_CID_04.....	138
Figure 6.14. CSL for Fraser River sand.....	138
Figure 6.15. Peak dilatancy vs. $\psi$ at peak for Fraser River sand. ....	140
Figure 6.16. Best fit for $H$ for monotonic triaxial tests on Fraser River sand. ....	140
Figure 6.17. Example fit to test FR_CID_03.....	141
Figure 6.18. Model fits using different $H_u$ values compared to laboratory data (a) U2 for ES_CID_867 (b) U3 for ES_CID_867. ....	144
Figure 6.19. Model fits for different $H_r$ values compared to L4 for ES_CID_867. ....	145
Figure 6.20. Model simulation for a changing and constant $H_r$ values.....	145
Figure 6.21. Model fits for constant and changing $\chi$ values compared to ES_CID_867. ....	146
Figure 6.22. Comparison between calibrated NorSand model and ES_CID_867.....	148
Figure 6.23. Zoom on the second loop of comparison between calibrated NorSand model with elasto-plastic unloading and ES_CID_867.....	149
Figure 6.24. Zoom on the second loop of comparison between calibrated NorSand model and ES_CID_867 with plastic unloading.....	149
Figure 6.25. Zoom on the first loop for ES_CID_867.....	150
Figure 7.1. Predictions for Test FR_CID_01 (a) $q-\epsilon_I$ (b) $\eta-\epsilon_I$ (c) $\epsilon_v-\epsilon_I$ . ....	157

Figure 7.2. Predictions for Test FR_CID_02 (a) $q-\varepsilon_I$ (b) $\eta-\varepsilon_I$ (c) $\varepsilon_v-\varepsilon_I$ .....	158
Figure 7.3. Model simulation for Test FR_CID_02 in $\varepsilon_v-\varepsilon_I$ with constant $\chi$ of 4.34. ....	159
Figure A.1. Predicted and measured stress-dilatancy for ES_CID_860.....	171
Figure A.2. Predicted and measured stress-dilatancy for ES_CID_861.....	171
Figure A.3. Predicted and measured stress-dilatancy for ES_CID_862.....	172
Figure A.4. Predicted and measured stress-dilatancy for ES_CID_866.....	172
Figure A.5. Predicted and measured stress-dilatancy for ES_CID_867.....	173
Figure A.6. Predicted and measured stress-dilatancy for ES_CID_868.....	173
Figure A.7. Predicted and measured stress-dilatancy for ES_CID_870.....	174
Figure A.8. Predicted and measured stress-dilatancy for ES_CID_871.....	174
Figure A.9. Predicted and measured stress-dilatancy for ES_CID_872.....	175
Figure A.10. Predicted and measured stress-dilatancy for ES_CID_873.....	175
Figure B.1. Load-unload-reload calibration results compared to laboratory data for ES_CID_860. ....	176
Figure B.2. Load-unload-reload calibration results compared to laboratory data for ES_CID_861. ....	177
Figure B.3. Load-unload-reload calibration results compared to laboratory data for ES_CID_862. ....	178
Figure B.4. Load-unload-reload calibration results compared to laboratory data for ES_CID_866. ....	179
Figure B.5. Load-unload-reload calibration results compared to laboratory data for ES_CID_867. ....	180
Figure B.6. Load-unload-reload calibration results compared to laboratory data for ES_CID_868. ....	181
Figure B.7. Load-unload-reload calibration results compared to laboratory data for ES_CID_873. ....	182
Figure C.1. Monotonic calibration results compared to tests data for FR_CID_03 .....	183
Figure C.2. Monotonic calibration results compared to tests data for FR_CID_04. ....	184
Figure C.3. Monotonic calibration results compared to tests data for FR_CID_05. ....	185
Figure C.4. Monotonic calibration results compared to tests data for FR_CID_06. ....	186
Figure C.5. Monotonic calibration results compared to tests data for FR_CU_01.....	187

Figure C.6. Monotonic calibration results compared to tests data for FR_CU_02.....	188
Figure D.1. A diagram illustrating loading in NorSand.....	189
Figure D.2. Description of unloading in the model. ....	190
Figure D.3. Description of reloading in the model. ....	191

## LIST OF SYMBOLS

$c$	Mohr-Coulomb stress parameters representing cohesion
CSL	critical state line
$D$	dilatancy ( $\dot{\varepsilon}_v / \dot{\varepsilon}_q$ )
$D_r$	relative density
$e$	void ratio
$E$	elastic young's modulus
$G$	elastic shear modulus
$H$	hardening/softening modulus in loading, a NorSand model input parameter
$H_r$	hardening/softening modulus in reloading, a NorSand model input parameter
$H_u$	softening modulus in unloading, a NorSand model input parameter
$I_r$	dimensionless shear rigidity parameter ( $G/p'$ ), a NorSand model input parameter
$K$	elastic bulk modulus
$M$	critical state stress ratio ( $q/p'$ at critical state), a NorSand model input parameter
$M_i$	stress ratio at image state (image is the boundary between contraction and dilation)
$M_u$	stress ratio at $D^p = 0$ for the case of unloading
$N$	volumetric coupling coefficient, a NorSand model input parameter
NC	normally consolidated
OCR	over-consolidation ratio
$p$	mean stress, for triaxial conditions $p = (\sigma_1 + 2\sigma_3)/3$
$p_o$	mean effective stress under initial conditions
$p_{cap}$	mean effective stress on the internal cap
$p_{fy}$	mean effective stress at first yield in unloading
$p_{ref}$	reference pressure equal to 100 kPa (often assumed equivalent to atmospheric pressure)



$q$	shear stress invariant, for triaxial conditions $q = (\sigma_1 - \sigma_3)$
$v$	specific volume, $1 + e$
$W$	total work done
$\Gamma$	Altitude of CSL in $e$ - $\log p'$ space at 1 kPa, a NorSand model input parameter
$\varepsilon_1$	major principal strain (axial strain in a triaxial test)
$\varepsilon_3$	minor principal strain (radial strain in a triaxial test)
$\varepsilon_v$	volumetric strain, for triaxial conditions $\varepsilon_v = (\varepsilon_1 + 2\varepsilon_3)$
$\varepsilon_q$	shear strain invariant, for triaxial compression $\varepsilon_q = 2(\varepsilon_1 - \varepsilon_3)/3$
$\chi_1$	slope of the line relating $D_{min}$ to $\psi$ at $D_{min}$ defined for the first peaks; is equivalent to usual usage of $\chi$
$\chi_2$	slope of the line relating $D_{min}$ to $\psi$ at $D_{min}$ defined for the second peaks
$\eta$	stress ratio, $\eta = (q/p')$
$\eta_L$	the last value of stress ratio in a loading/reloading phase
$\kappa$	slope of the elastic swelling lines
$\lambda_{10}$	slope of CSL in $e$ - $\log_{10} p'$ space
$\lambda_e$	slope of CSL in $e$ - $\log_e p'$ space, a NorSand model input parameter
$\psi$	state parameter, $\psi = (e - e_c)$
$\theta$	angle of dilatation
$\phi_{cv}$	constant volume friction angle
$\phi_f$	Rowe's mobilised friction angle
$\phi_{max}$	peak friction angle
$\phi_\mu$	grain to grain friction angle
$\nu$	Poisson's ratio
$\rho$	soil density
$\sigma_1$	major principal stress (axial stress for triaxial conditions)
$\sigma_3$	minor principal stress (radial stress for triaxial conditions)
$\sigma_n$	normal stress on the plane of failure
$\tau$	shear stress on the plane of failure

### **Subscripts**

- dot over a symbol denotes increment
- c critical state
- i denotes image conditions
- q shear invariant
- o initial,
- tc triaxial compression
- u unloading
- v volumetric

### **Superscripts**

- ' effective stress
- e elastic
- p plastic

## **ACKNOWLEDGEMENTS**

I would like to express my deepest gratitude to my supervisor Dr. Dawn Shuttle for her guidance, support and encouragement. Without her advice this work would not have been accomplished.

I would like to thank my reviewer Dr. John Howie for his useful comments and my official supervisor Dr. Jim Atwater. The author would also like to acknowledge the help of Mike Jefferies, Roberto Bonilla, and Golder Associates for providing access to the laboratory testing on which this research is based. Thanks to my professors and colleagues at the Geotechnical group at UBC for their encouragement and useful discussions. The financial support provided by the University of British Columbia Graduate Fellowship and the Vancouver Geotechnical Society is highly appreciated.

Finally, I owe an enormous debt to my family for their constant support during the pursuit of my Masters degree at UBC. This work is dedicated to my mother.

## 1. INTRODUCTION

The behaviour of sands during loading has been studied in great detail. However, little work has been devoted to understanding the response of sands in unloading. This is surprising as the behaviour of sands in unloading is of great practical importance, particularly for earthquake engineering.

An elastic material is expected to expand upon unloading in a conventional triaxial test as illustrated in Figure 1.1. The figure on the left hand side is a schematic illustrating the expected elastic trend of decreasing volume associated with increasing confining stress in a conventional triaxial test. The solid square represents the original element size before loading and the dashed square is the deformed element. According to elasticity, the element is expected to recover its original size upon removing the confinement, as shown in the figure on the right hand side.

Drained triaxial tests indicate that, contrary to the expected elastic behaviour of increase in volume in unloading, sand may exhibit contractive behaviour when unloaded. Figure 1.2 is a plot of the results of a triaxial test on Erksak sand with a single load-unload-reload cycle. Positive volumetric strains denote contraction, i.e. decrease in volume, while negative volumetric strains denote dilations, i.e. increase in volume. During loading, phase a-b, the sample initially contracts. This trend is reversed at  $\varepsilon_1 = 2.2\%$ . Upon unloading, phase b-c, significant amount of contraction is observed. Finally, the trend in reloading, phase c-d, is similar to that of first loading.

Drained cyclic simple shear tests show similar behaviour in unloading (Sriskandakumar, 2004). The results of two identical drained simple shear tests on Fraser River sand are plotted in Figure 1.3. A cyclic shear stress of 50 kPa is applied. It can be

noticed that unloading is associated with contraction, in some cycles more than that in loading. In drained simple shear tests, because the vertical effective stress remains constant, the expected elastic volumetric strains are zero. This is contrary to the observed behaviour.

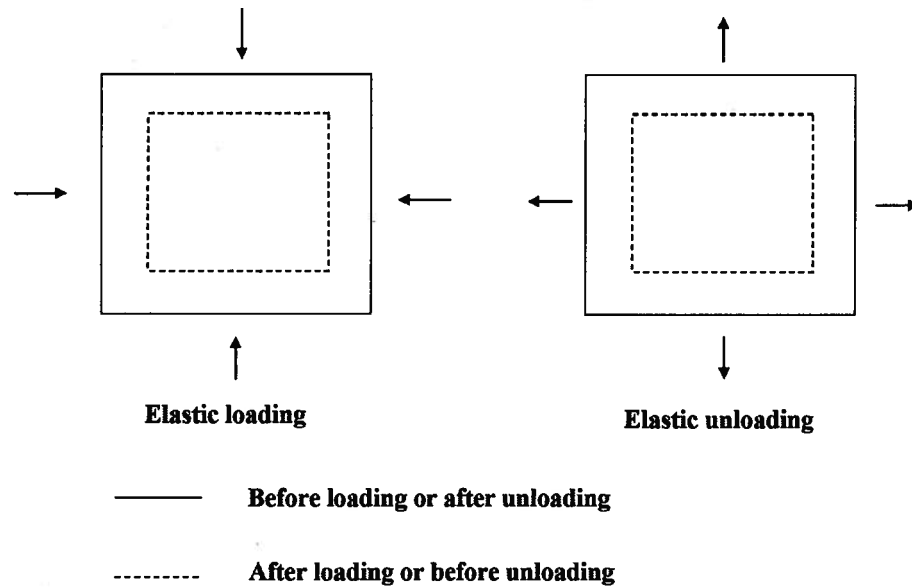


Figure 1.1. The behaviour of an elastic material in loading and unloading.

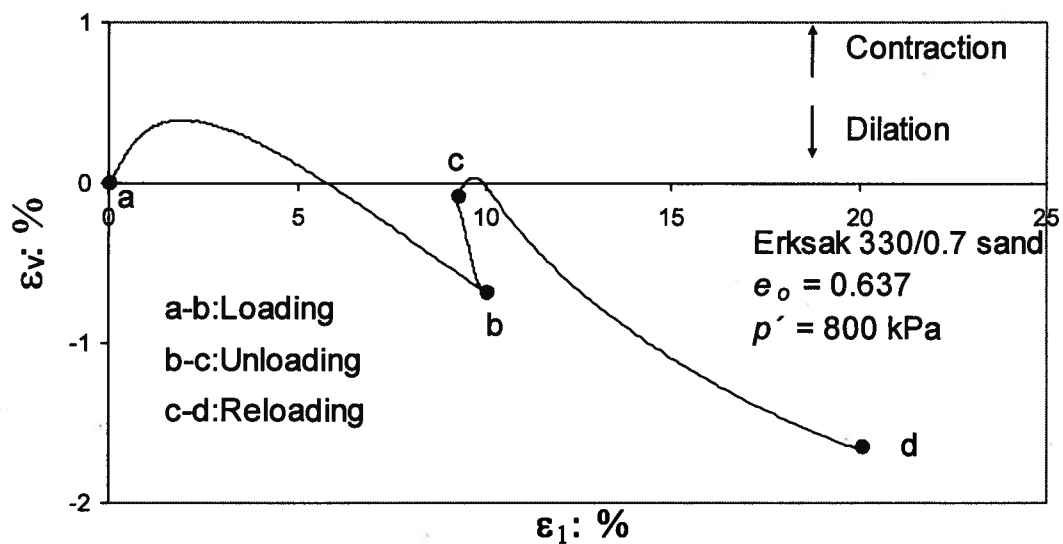


Figure 1.2. Results of a triaxial test on Erksak sand in volumetric strain vs. axial strain (reproduced after Golder, 1987).

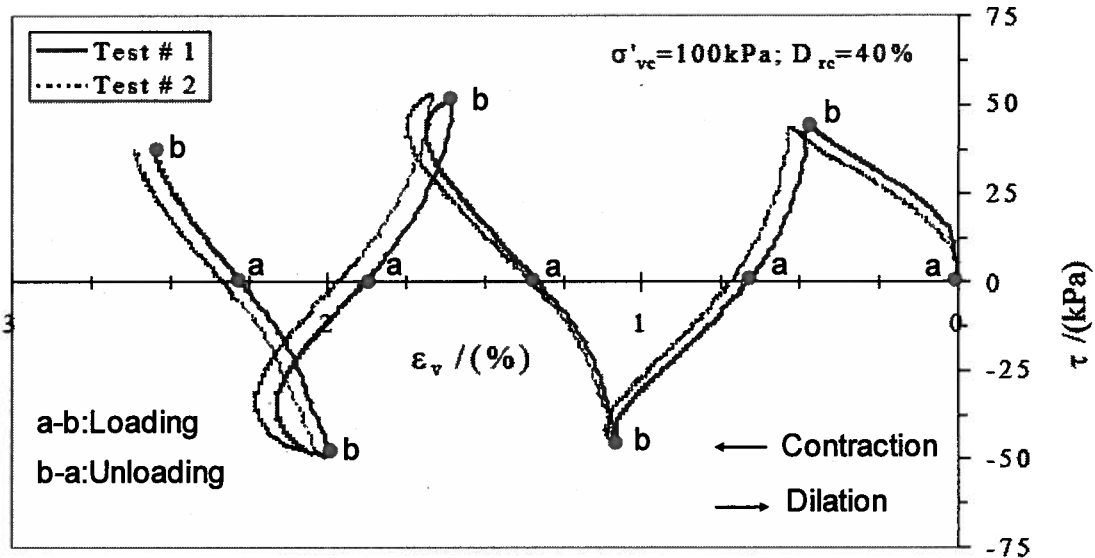


Figure 1.3. Drained simple shear tests on Fraser River sand (modified after Sriskandakumar, 2004).

The tendency to contract upon unloading during an earthquake is one contributory factor in soil liquefaction. The importance of contraction during unloading may be observed in undrained cyclic simple shear tests. Figure 1.4 shows a cyclic simple shear test on Fraser River Sand reported in Wijewickreme et al. (2005). Vertical effective stress is plotted on the x-axis and the applied shear stress is plotted on the y-axis. A decrease in the vertical effective stress is associated with an increase in pore water pressure. It can be observed that, apart from the first two cycles, the increase in pore water pressure generated during the unloading cycle often exceeds that generated during loading.

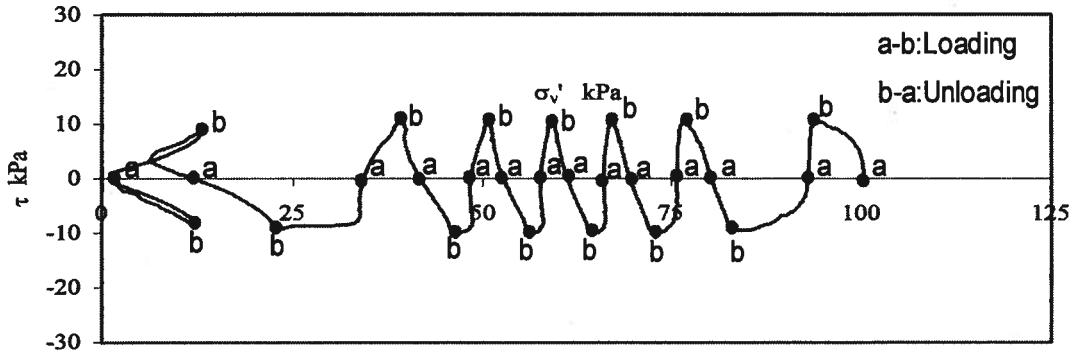


Figure 1.4. Cyclic direct simple shear test on Fraser River Sand (modified after Wijewickreme et al. , 2005).

Observed soil behaviour from both drained and undrained testing clearly indicates that soil behaviour in unloading is not wholly elastic. A constitutive model that yields in unloading is needed to predict this soil behaviour, and is the topic of this thesis. A basic requirement of such a model is stress-dilatancy, i.e. the inter-relationship between stress ratio ' $\eta$ ' and dilatancy ' $D$ ', where  $\eta = q/p$  and  $D = \dot{\epsilon}_v / \dot{\epsilon}_q$ . ( $\dot{\epsilon}_v$  and  $\dot{\epsilon}_q$  are the increments of volumetric strain and shear strain invariant respectively).

## 1.1. Research Objectives

The main objectives of this work are:

1. Develop theoretical understanding of stress-dilatancy in unloading. This investigation includes the interaction between soil fabric and stress-dilatancy.
2. Utilize the theoretical understanding to guide development of unload-reload behaviour, including yielding during unloading, into a constitutive model.

This work will include developing an expression for stress-dilatancy in unloading based on a discrete element approach, including the effect of fabric changes on dilatancy in

reloading, fabric represents “the arrangement of particles, particle groups and pore spaces in a soil” (Mitchell and Soga, 2005). Soil fabric is expected to change due to cyclic loading, consequently changing stress-dilatancy in reloading as compared to that for first loading.

A continuum model that yields in unloading is developed. The model uses the ideas from the theoretical investigation of stress-dilatancy in unloading and reloading. The work will involve calibration of the model to experimental data and using the calibrated model to predict the results of drained load-unload-reload tests. The introduced model utilizes the NorSand soil model, a critical state hardening plasticity model, as its starting point.

## **1.2. Thesis Organization**

The thesis is organized into 8 chapters. Chapter 2 provides an overview of literature relating to constitutive modelling for soils, with particular emphasis on soil behaviour in unloading. The theoretical investigation into stress-dilatancy in both unloading and reloading phases is investigated from a micro-mechanical point of view in Chapter 3. Chapters 4 through 7 review experimental data to develop an improved constitutive model for yielding in unloading and reloading. Chapter 4 presents drained triaxial data on Erksak sand and Fraser River sand which includes load-unload-reload cycles. Chapter 5 uses the findings of Chapters 3 and 4 to develop an extension to the continuum constitutive model, NorSand. Chapter 6 presents calibrations of the model. Monotonic calibration of NorSand is done for both Erksak sand and Fraser River sand. Load-unload-reload calibration of the model is then undertaken on Erksak sand. The calibrated model predictions for load-unload-reload tests on Fraser River sand are presented in Chapter 7. The conclusions from this work are summarized in Chapter 8.



## **2. LITERATURE REVIEW**

The behaviour of sands depends on many factors, including density and mean effective stress. Constitutive models are necessary to capture the effect of these and other factors on soil behaviour, and to predict this behaviour for real engineering problems. This chapter focuses on soil constitutive modelling with particular emphasis on soil behaviour in unloading. First, a brief description of the typical behaviour of sands as observed from laboratory data and the basics of triaxial testing is introduced. This is followed by a description of the fundamentals of elasto-plastic constitutive models and some of the commonly-used soil models are introduced, with emphasis on the critical state model, Cam-Clay. The interrelationship between stresses and dilatancy is then discussed. Then the NorSand soil model, used as the basis for the unloading/reloading development later in this thesis, is introduced. Finally, a review of conceptual models for soils in unloading is introduced.

### **2.1. Experimental soil behaviour**

Much of our understanding of soil behaviour comes from laboratory testing. The main advantage of laboratory testing is that the initial conditions and stress path can usually be controlled. Typical soil behaviour is explained in this section by a review of laboratory testing in the literature. The discussion includes selected factors which are observed from laboratory testing to affect stress-strain behaviour. The critical state theory is also introduced, together with a description of yield characteristics of sands.

### 2.1.1. Typical stress-strain behaviour of sand

Typical schematics of stress-strain curves for dense and loose sand in drained tests and with the same applied stress conditions, starting from uniform all-around pressure, are shown in Figure 2.1a. In Figure 2.1a the deviator stress,  $q$ , is  $\sigma_1 - \sigma_3$  for triaxial conditions. The axial strain is  $\varepsilon_1$  and the deviator strain,  $\varepsilon_q$ , is  $2(\varepsilon_1 - \varepsilon_3)/3$  for triaxial compression. Both  $\varepsilon_1$  and  $\varepsilon_q$  are commonly used to plot stress-strain curves in the literature. They give similar trends. Typical behaviour for dense sand shows a peak value of deviator stress before dropping to constant stress at larger strains. Conversely, loose sand does not show a peak but instead directly reaches the same constant value of stress as the dense sand at large strains for identical mean effective stress conditions.

Figure 2.1b plots data in volumetric strain vs. axial or deviator strain. Volumetric strain,  $\varepsilon_v$ , is defined as  $\varepsilon_1 + 2\varepsilon_3$  for triaxial conditions. In this thesis, positive strains are compressive. Therefore positive volumetric strains denote contraction while negative volumetric strains denote dilation. It can be seen that dense sand contracts initially during shear and then dilates until a state is reached where volumetric strain remains constant. Loose sand contracts during shear until it reaches constant volume conditions at large strains. Reynolds (1885) was first to show that dense sand dilates when sheared towards failure while loose sand contracts.

Typical undrained behaviour of sand is shown in Figure 2.2. As the undrained condition prevents volume change, the tendency to change in volume results in a pore water pressure change of opposite sign, which changes the effective stress conditions. Dense sand shows an increased strength with axial or deviator strain. This is associated with the development of negative (or decreasing) pore pressure.

The strength of loose sand increases to a peak value. This is followed by a decrease in strength until reaching a constant value of strength which is independent of the strain level. The corresponding pore pressure increases with increasing strain level. The rate of increase decreases with strain, eventually reaching a constant pore pressure.

Soil strength is directly related to mean effective stress. For higher mean effective stresses soil has a stiffer response and higher strength. Figure 2.3 is a schematic demonstrating the effect of mean effective stress on stress-strain curve. The three plots have identical initial void ratios.

Although the behaviours described in Figure 2.1, Figure 2.2 and Figure 2.3 are generally applicable, differences in soil behaviour are observed for different soils, and also for the same soil using different preparation methods. This occurs because different sample preparation methods result in different initial fabric. Fabric refers to “the arrangement of particles, particle groups, and pore spaces in a soil” (Mitchell and Soga, 2005). Oda (1972) performed triaxial tests on a uniform sand composed of rounded to sub-rounded grains with sizes between 0.84 to 1.19mm (Figure 2.4). The two samples have a similar initial void ratio and mean effective stress. The only major difference between the two samples is the preparation method. One of the samples was prepared by tapping the sides of the mould. The other sample was prepared by tamping. The sample prepared by tapping demonstrates a stiffer response, associated with a more dilative behaviour, compared to that prepared by tamping.

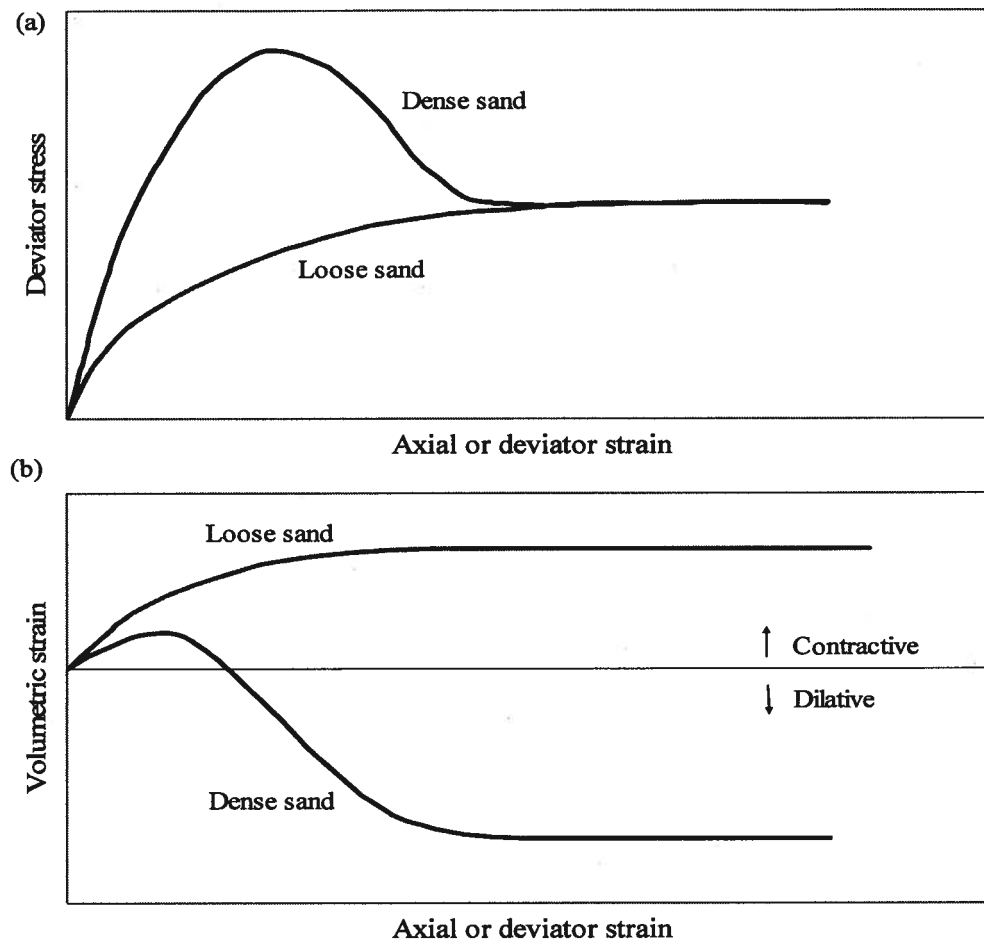


Figure 2.1. Schematic of typical results of a drained triaxial test on loose and dense sand samples (a) deviator stress vs. axial or deviator strain (b) volumetric strain vs. axial or deviator strain.

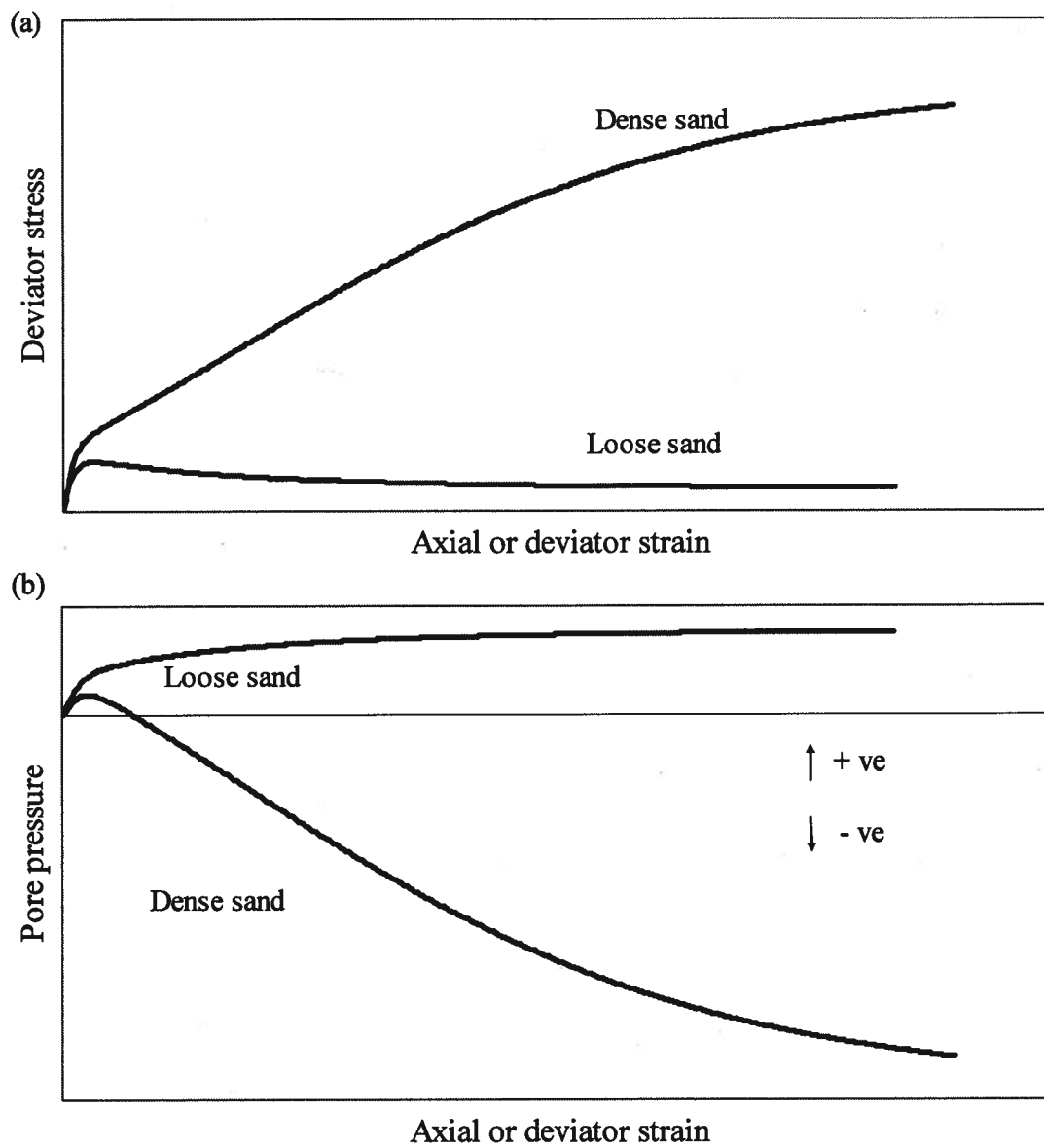


Figure 2.2. Schematic of typical results of an undrained triaxial test on loose and dense sand samples (a) deviator stress vs. axial or deviator strain (b) pore pressure vs. axial or deviator strain.

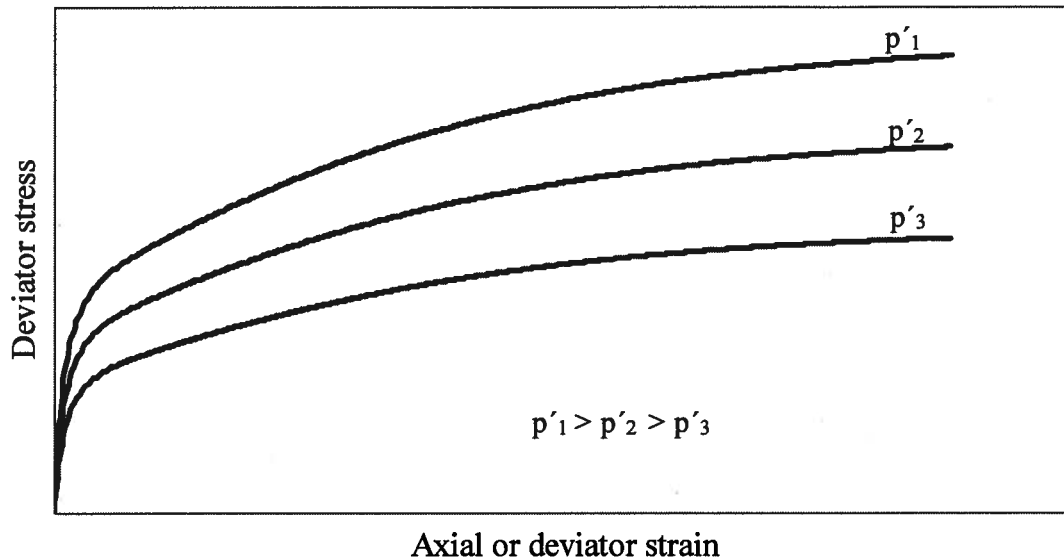


Figure 2.3. Schematic of stress strain curves for different mean effective stress values at constant initial void ratio.

### 2.1.2. The Critical State

The concept that soil will eventually reach a constant stress and void ratio state was first introduced by Casagrande in 1936. He observed from shear box tests that both dense and loose sand, under same vertical effective stress, eventually reach a constant void ratio at which shear deformation continues at constant shear stress. These observations were independently confirmed over twenty years later by Roscoe et. al. (1958) who performed simple shear tests on 1-mm diameter steel balls. All Roscoe et al.'s tests were done under constant normal effective stress of 138 kPa. Regardless of the initial density, for the same applied load of 138 kPa all samples reach similar specific volume at large shear displacements (see Figure 2.5). The specific volume is the volume occupied by a unit mass and is equal to  $(1 + e)$ .

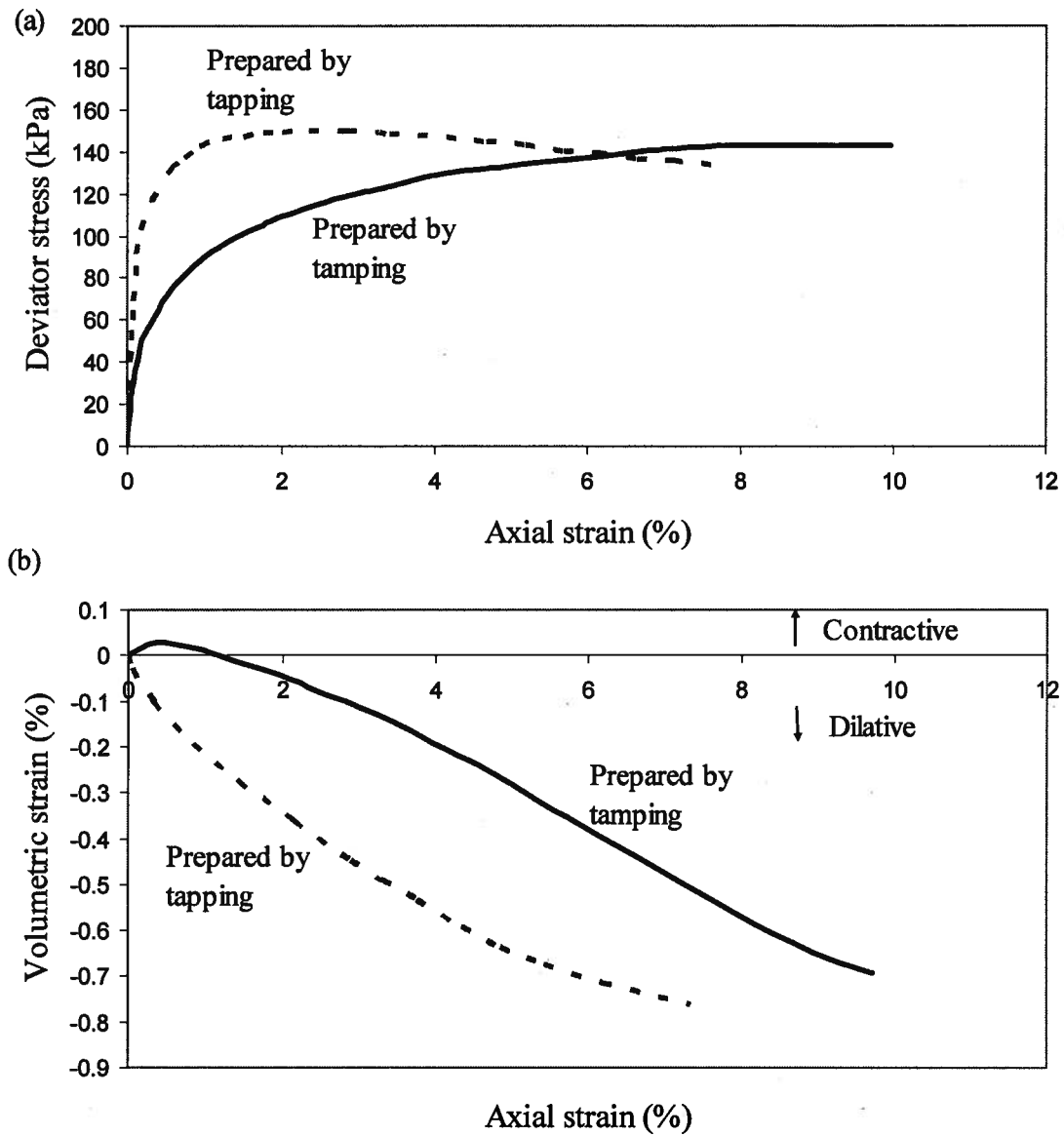


Figure 2.4. Effect of sample preparation method (a) deviator stress vs. axial strain (b) volumetric strain vs. axial strain. (modified after Mitchell and Soga, 2005).

This idea of a unique relation existing between stress level and void ratio led to the development of what has become known as Critical State Soil Mechanics (CSSM). The critical state is defined as ‘the state at which a soil continues to deform at constant stress and constant void ratio’ (Roscoe et. al., 1958).

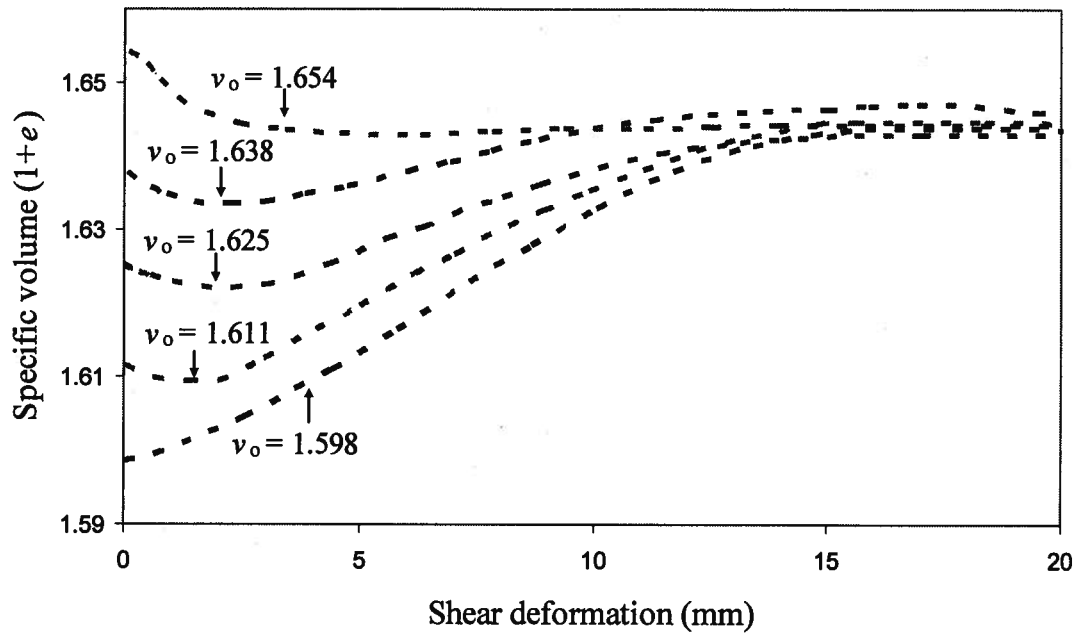


Figure 2.5. Results of simple shear tests on 1-mm diameter steel balls at constant normal effective stress of 138 kPa (reproduced from Roscoe et. al., 1958).

However, this constant void ratio, usually known as the critical void ratio, has been experimentally shown to vary with stress level. The results of drained triaxial tests on Chattahoochee River Sand are presented in Figure 2.6 (Vesic and Clough, 1968). These drained triaxial tests investigate the dependence of the critical void ratio on stress level. The two tests have identical void ratios but different values of mean effective stress. Figure 2.6 shows that although all of the samples are dense, the sample with the higher mean effective stress contracts matching the behaviour of loose sand. Higher mean effective stresses cause the particles to move around each other, rather than over, and crush, rather than simply override when sheared. This results in contractive behaviour. Therefore, the critical void ratio is a function of stress level.



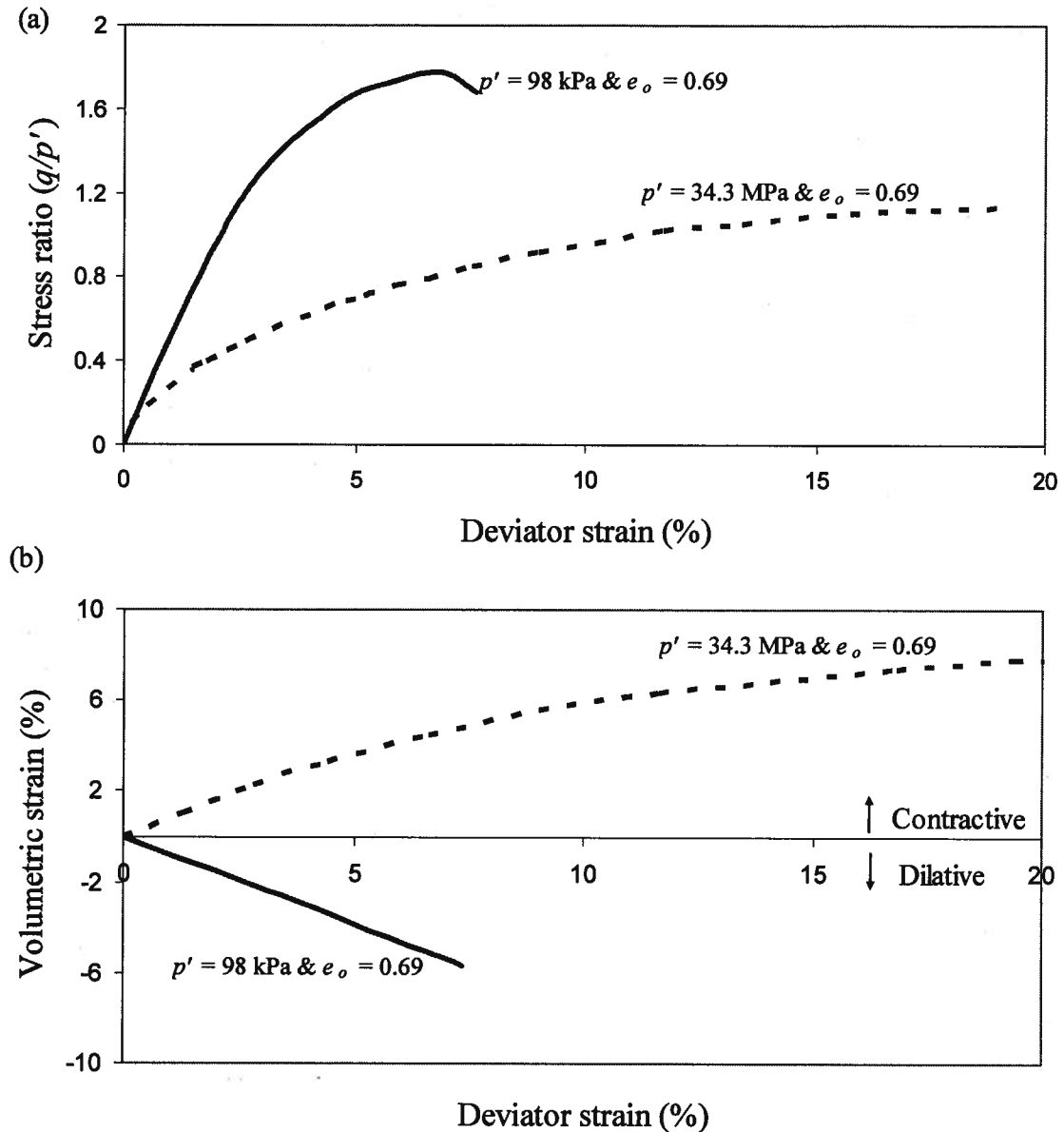


Figure 2.6. Drained triaxial compression tests on Chattahoochee River sand (reproduced after Vesic and Clough, 1968)

The experimental observations described above led to the development of a theoretical framework for soil behaviour, known as Critical State Soil Mechanics (CSSM). CSSM is based on two axioms:

1. A unique critical state exists.
2. The critical state is the final state to which all soils converge with increasing shear strain.

CSSM presents a fundamental framework for all soils. Because all soils eventually reach critical state irrespective of the current void ratio and stress conditions, having a unique critical state is very useful. A unique critical state is an ideal framework around which to construct soil models around.

The question of the uniqueness of the critical state was investigated by Been et al. (1991) who provided evidence to indicate that the critical state is likely unique, being both independent of fabric, loading rate, stress path, and initial density. Figure 2.7 shows that both moist compacted and pluviated samples in undrained tests finish at the same critical state line. Drained tests were also observed to follow the same trend. The change in the slope of the critical state line at about 1000 kPa is thought to be due to grains crushing at high mean effective stress levels.

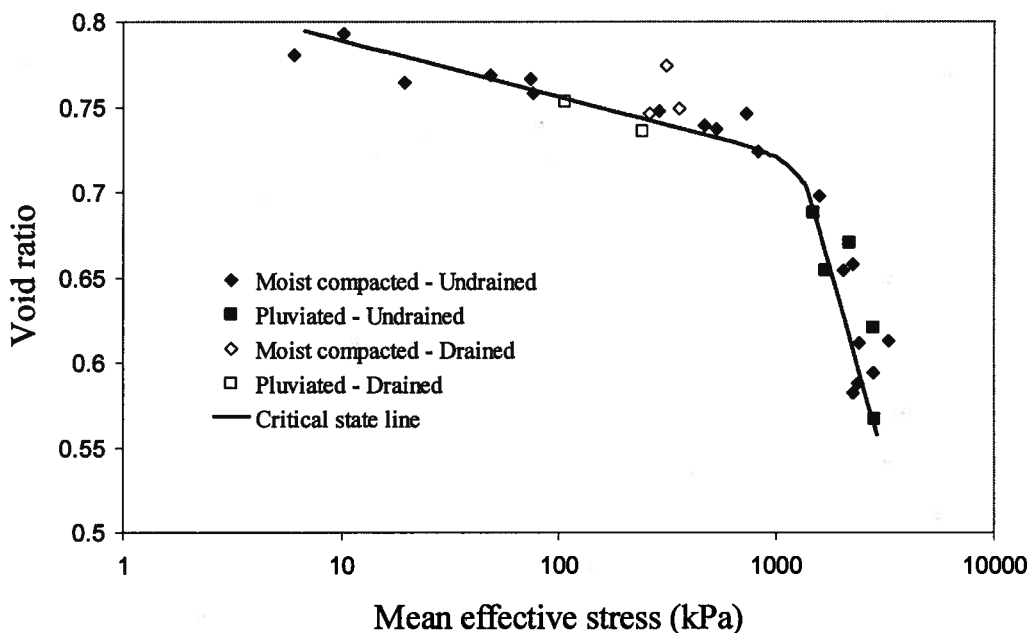


Figure 2.7. Critical State Line for Erksak 330/0.7 sand (reproduced from Been et al., 1991).

The critical state is also unique in the  $p'$ - $q$  space. Both loose sand and dense sand, under identical mean effective stress conditions, finished at the same value of deviator stress, see Figure 2.1a. Irrespective of the sample preparation method, the two samples in Figure 2.4a reached similar deviator stress values in the higher axial strain range (i.e. > 6%).

Hence soil behaviour can be understood within the framework of the critical state in the three dimensional space of  $p'$ ,  $q$  and  $e$ . The slope of the projection of the critical state line in  $p'$ - $q$  is known as the critical friction ratio,  $M$  (Figure 2.8a). The projection of the critical state line in  $e - \log_{10} p'$  is given by:

$$e_c = \Gamma - \lambda \log_{10} p' \quad (2.1)$$

Where  $e_c$  is the void ratio at the critical state,  $\Gamma$  is  $e_c$  at  $p' = 1$  kPa in  $e - \log p'$  plot, and  $\lambda_{10}$  is the slope of the critical state line (see Figure 2.8b). Note that  $\lambda$  is defined in terms of  $\log_{10}$  and  $\log_e$  (and in this thesis are termed  $\lambda_{10}$  and  $\lambda_e$  respectively). Both are perfectly acceptable. However care should be taken as  $\lambda$  is often used in the literature without clarifying the base of the log used.

The critical state is a very useful tool as both dense and loose sand are considered to end up at the critical state. At a particular mean effective stress level, soil with  $e < e_c$  is termed dense while soil with  $e > e_c$  is termed loose. Drained dense tests dilate to reach the critical state while drained loose tests contract to reach the critical state (Figure 2.8b). As the critical state line is defined to be unique, undrained tests reach the same line as for drained tests. This makes the critical state an extremely useful reference property for accurate prediction of soil behaviour.

### 2.1.3. The state parameter

Been & Jefferies (1985), using the results of seventy triaxial tests on Kogyuk sand, show that the “bulk characteristics of sands are not sufficient to characterize mechanical behaviour of granular materials”. Relative density or void ratio alone does not govern soil behaviour. Dense sand can behave similarly to loose sand at high confining pressures as was previously shown for Chattahoochee River sand (Figure 2.6). The state of soil was described by Been & Jefferies as “a description of the physical conditions” which includes the influence of confinement and void ratio. In this sense, the behaviour of sand is controlled by the state parameter,  $\psi$ . In order for the state parameter concept to be useful, it needs to be defined relative to a reference condition that is unique and is independent of initial conditions. The critical state is a proper framework as it satisfies both conditions. Equation 2.2 defines the state parameter.

$$\psi = e - e_c \quad (2.2)$$

The state parameter is dependent on mean effective stress as the critical void ratio is dependent on mean effective stress. It therefore represents soil behaviour better than relative density. This is for two reasons: First, relative density does not specify the current state relative to critical state. Accordingly, relative density cannot be used to predict whether soil contracts or dilates before it reaches the critical state. Second, soil strength depends on dilatancy, defined as the ratio between an increment of volumetric strain and an increment of shear strain, and not void ratio, and dilatancy is inversely proportional to mean effective stress. Figure 2.9 shows that tests with similar initial state parameters have similar behaviour regardless of the difference in their relative densities, while tests with similar relative densities behaved very differently. The results of the three tests are normalized to mean effective stress at the critical state,  $p'_{cs}$ . Tests 103 and 108 have similar initial state parameter. They demonstrate similar behaviour regardless of the difference in relative density (33% for test 103 and 50% for test 108). However, tests 103 and 37 with identical  $D_r$  of 33%, and very different state parameters, show different behaviour.

The state parameter also influences some soil design parameters. A unique relation between the peak friction angle and the state parameter has been observed for a range of different sands (see Figure 2.10). Although there is scatter in the data, the trend of decreasing peak friction angle as state parameter increases is clear.

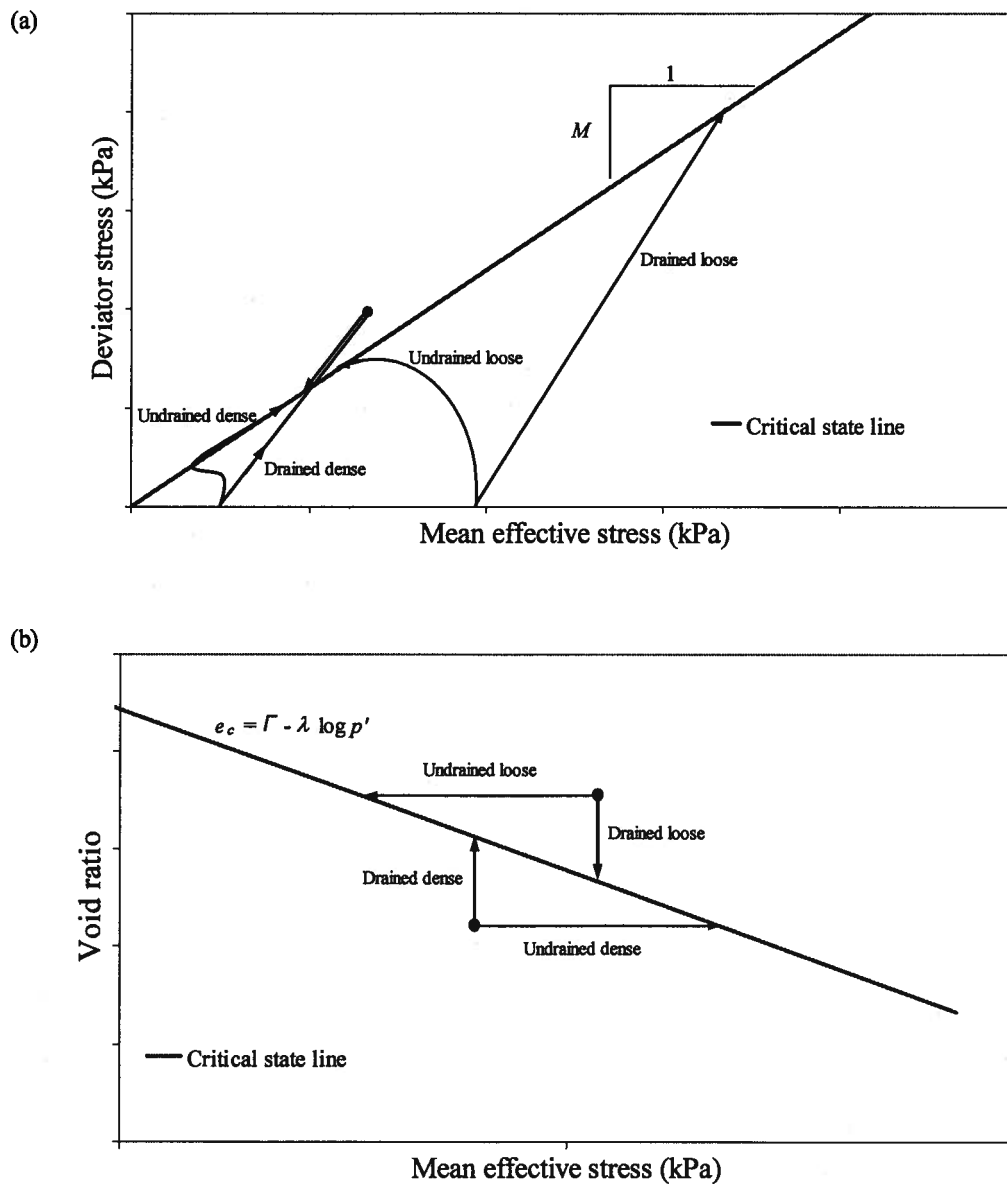


Figure 2.8. The projection of the critical state line (a)  $p' - q$  (b)  $e - \log p'$ .

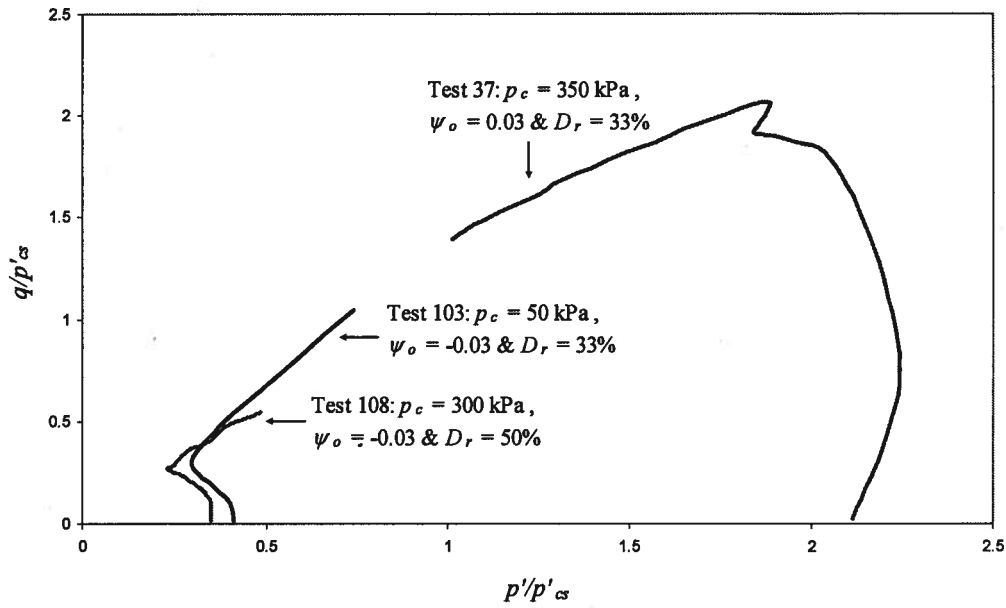


Figure 2.9. Stress paths for three undrained triaxial tests on Kogyuk 350/2 Sand (reproduced from Been & Jefferies, 1985).

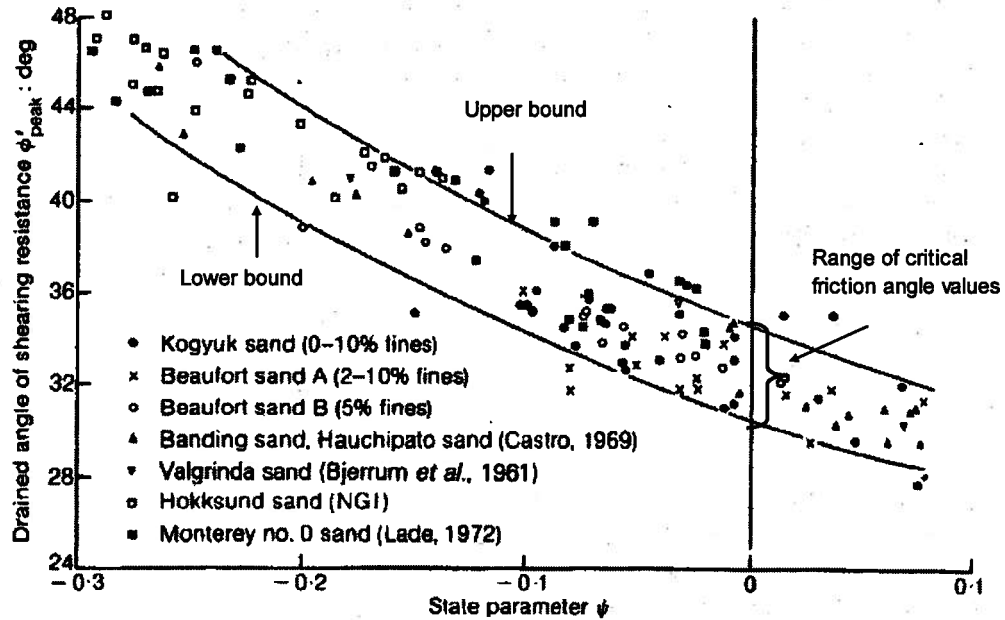


Figure 2.10. Peak friction angle as a function of state parameter for several sands (modified from Been & Jefferies, 1985).

#### 2.1.4. Yielding of sands

The yielding point has been classically used to signify the end of recoverable deformation, usually observed experimentally as a significant decrease in stiffness. The yield surface may be intersected along any stress path and is composed of an infinite number of yielding points in the  $(e-p'-q)$  space. One of the earliest studies on yielding of soils is reported in Roscoe et al. (1958). Roscoe et al. derived an isometric yield curve from 39 drained simple shear tests done on 1 mm diameter steel balls. From a theoretical viewpoint, it is more useful to plot the projection of the yield surface in the  $p'-q$  space, as shown for Aoi Sand in Figure 2.11 (Yasufuku et al., 1991). The data for all eight drained triaxial tests in Figure 2.11 started from the same stress state with  $OCR=2$ . The hollow circles indicate yielding as evident from a sharp change in stress strain curves. The yield surface was drawn through these yield points. Note that the curve is not symmetric around the  $p'$  axis due to sand anisotropy. By repeating the same procedure for different consolidation stresses, a family of yield curves can be defined as shown in Figure 2.12 for Fuji River sand (Ishihara and Okada, 1978). Experimental studies suggest that the yield surfaces typically have a similar shape, as can be seen for Aoi sand and Fuji River sand.

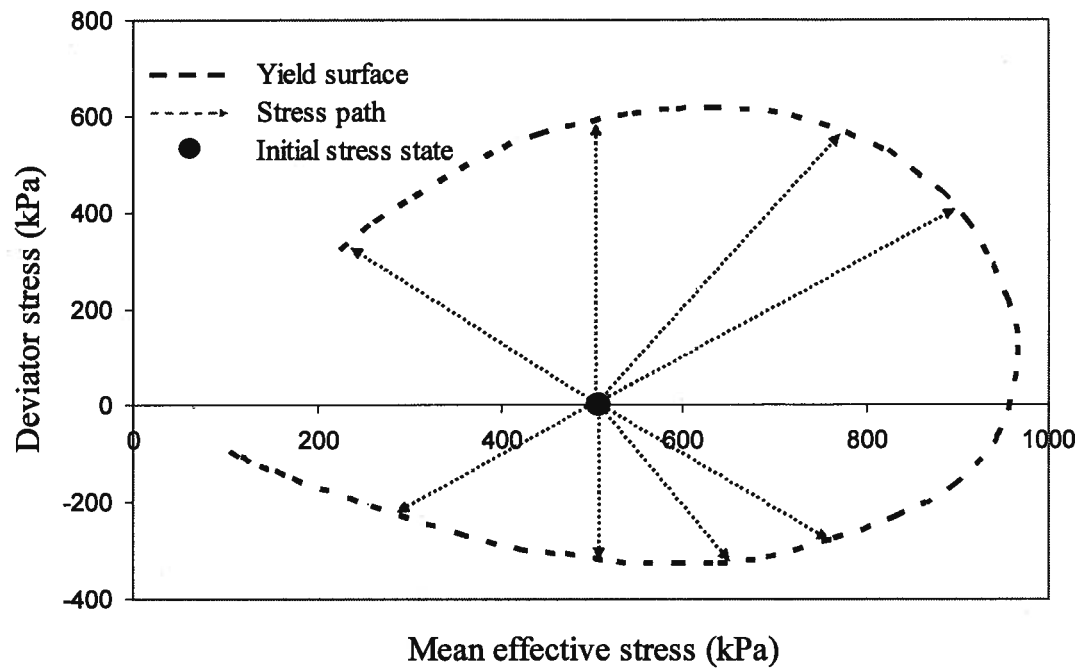


Figure 2.11. Projection of the yield surface in  $p'$ - $q$  plane for Aoi Sand (reproduced from Yasufuku et al., 1991).

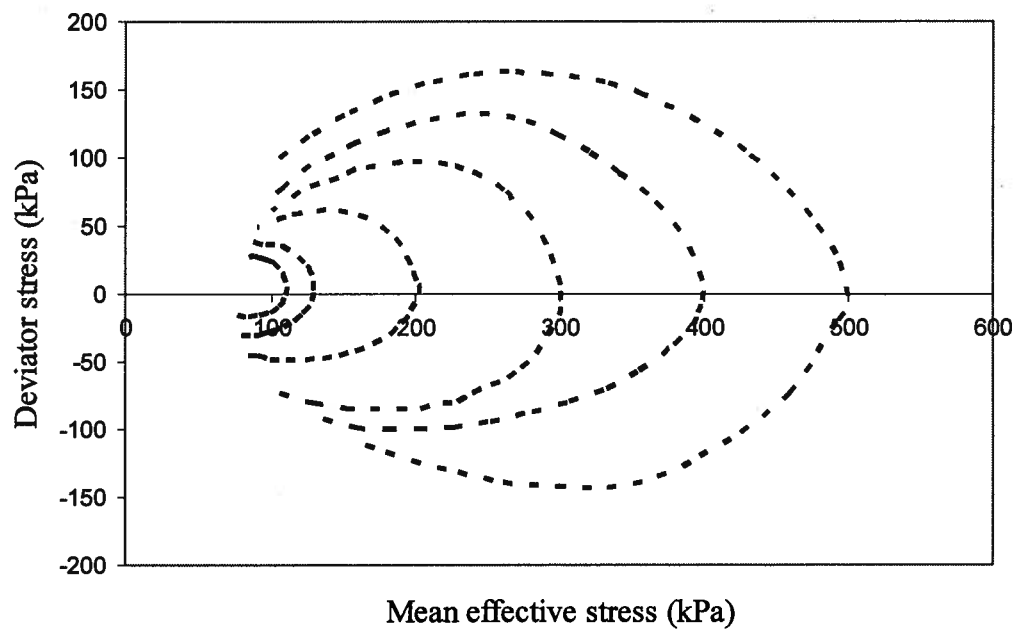


Figure 2.12. Family of yield envelopes for Fuji River sand (reproduced from Ishihara and Okada, 1978).



## 2.2. Triaxial testing

Although no laboratory testing was undertaken as part of this work, existing triaxial tests form the basis for the constitutive model development.

Triaxial testing is commonly used in both industry and research. This section describes conventional triaxial compression testing. The test involves consolidating a cylindrical specimen under confining pressure,  $\sigma_3$  (for convenience it is assumed that the consolidation is hydrostatic). A deviator stress of  $\Delta\sigma$  is then applied in the vertical direction. The total stress in the vertical direction is  $\sigma_1 = \sigma_3 + \Delta\sigma$ .

A typical arrangement of a conventional triaxial equipment is shown in Figure 2.13. A multi-speed drive unit is used to apply the axial load. The triaxial cell is filled with de-aired water. The soil sample has two porous discs (at the sample bottom and top) and is surrounded laterally by a rubber membrane. The top and bottom porous discs are attached to the upper and lower platens, respectively. The applied load is measured by a load cell. The axial displacement is measured using a linear displacement transducer (LVDT). There are three pressure connections to the system that are used to measure the pore pressure or volume changes and apply back pressure and cell pressure. The typical size of the cylindrical soil specimen is 36mm in diameter and 76mm in length.

Typically, specimens are hydrostatically consolidated by increasing the cell pressure. Non-hydrostatic consolidation could be done as well, though less common, by applying deviator stress in the consolidation phase. Water is allowed to drain out of the back pressure line until the pore pressure is equal to the back pressure. During consolidation, the sample contracts and the effective stress increases to a value equal to the cell pressure less the back pressure. During the shearing stage the sample is loaded by increasing the axial load in increments for stress controlled testing or by applying displacement increments for strain controlled testing. For undrained tests, water is not allowed to drain

during this stage and pore pressure is measured. For drained tests, water is allowed to drain and volumetric strains are measured usually using a differential pressure transducer. The axial displacement is measured using the LVDT.

Triaxial data is presented in this thesis in terms of the mean effective stress,  $p'$ , and shear stress,  $q$ , invariants, where  $p' = (\sigma'_1 + 2\sigma'_3)/3$  and  $q = (\sigma_1 - \sigma_3)$ . Volumetric strain,  $\varepsilon_v$ , is defined as the sum of the principal strains (i.e.  $\varepsilon_v = \varepsilon_1 + 2\varepsilon_3$ ). For stresses and strains used to be work conjugate (meaning that the invariants, or the individual stresses and strains, can be used interchangeably), they must satisfy the following during a loading increment:

$$q\varepsilon_q + p'\varepsilon_v = \sigma'_1\varepsilon_1 + \sigma'_2\varepsilon_2 + \sigma'_3\varepsilon_3 \quad (2.3)$$

Substituting the values of  $p'$ ,  $q$ , and  $\varepsilon_v$  in Equation 2.3 and rearranging gives the following expression for the shear strain invariant,  $\varepsilon_q$ :

$$\varepsilon_q = \frac{2}{3}(\varepsilon_1 - \varepsilon_3) \quad (2.4)$$

The primary advantage of triaxial testing is that all of the principal stresses are known and can be directly controlled. Hence, when used as part of constitutive model development, no stresses or strains are left to be inferred. Having to assume stress conditions, introduces uncertainty into the appropriateness of any model. However, the test is limited to applying only two independent principal stresses. This is a stress path that rarely, if ever, corresponds to the nature of loading conditions in the field.

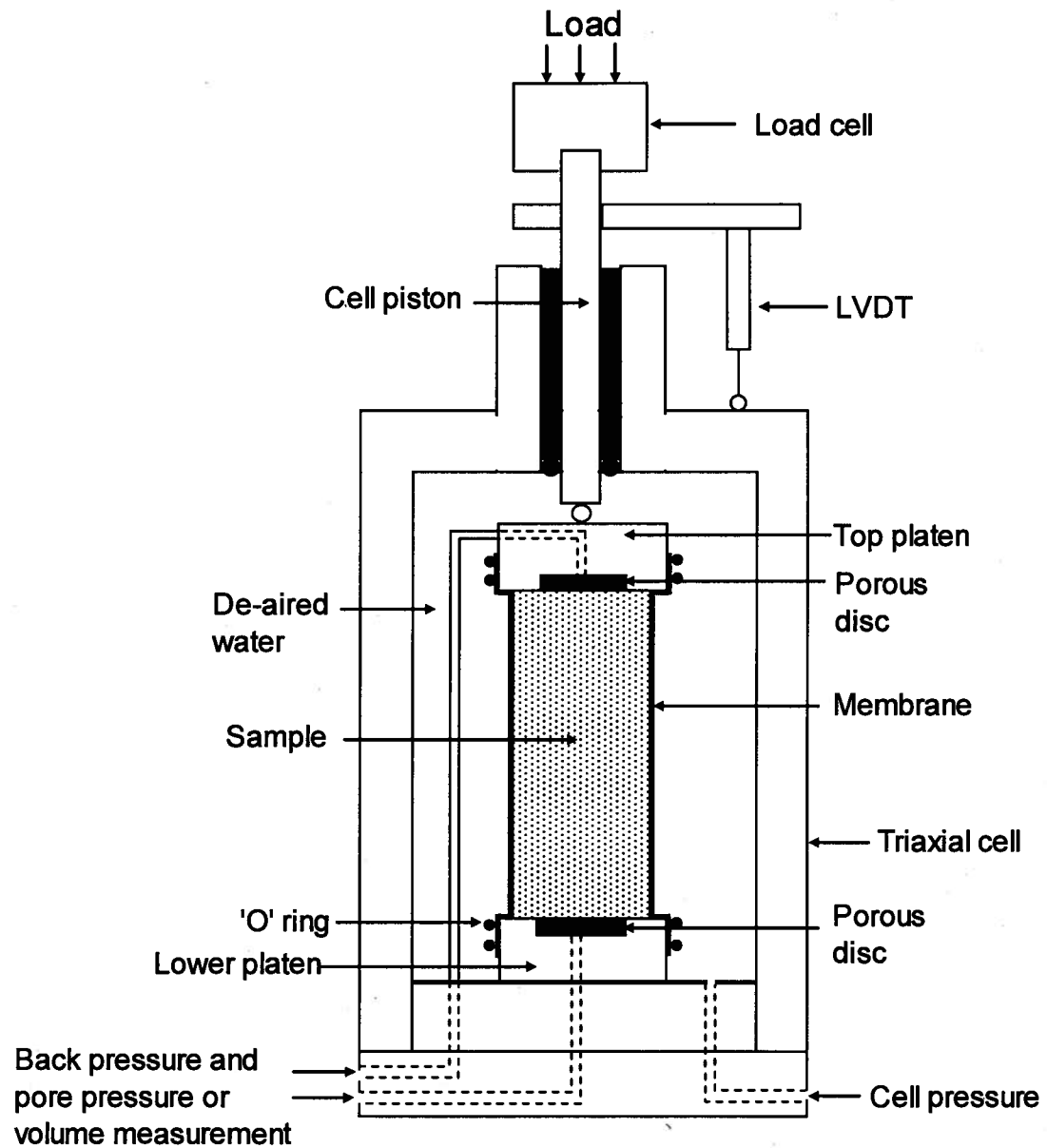


Figure 2.13. Schematic of the triaxial apparatus.

## **2.3. Soil constitutive models**

Soil constitutive modelling provides qualitative and quantitative understanding of soil behaviour. 'Proper' models provide us with an understanding of soil constitutive behaviour based on an appropriate framework that is derived from mechanics. The need for 'good' constitutive models is ever increasing because, with the advance in computers, more complex numerical analyses are becoming a routine practice.

Soil behaviour depends on many factors including stress level and void ratio. Because it is impractical to perform tests at every possible combination of stress level and void ratio, a useful constitutive model should be able to accurately predict changes in strength and deformation characteristics for the full range of applicable combinations of stress level and void ratio.

A brief description of elasto-plastic soil modelling is presented in this section. This is followed by an overview of some commonly-used soil models.

### **2.3.1. Elasto-plastic soil modelling**

Soil is an elasto-plastic material (i.e. exhibits both elasticity and plasticity). Elasticity is associated with recoverable strains, and purely elastic behaviour is usually only observed in soil at very small strains. Plasticity is associated with irrecoverable deformations. A typical elasto-plastic continuum model comprises: elasticity, a yield surface, a flow rule, a hardening/softening rule.

**Elasticity:** Elastic strains are recoverable. The direction of an elastic strain increment follows that of the stresses.

**Yield surface:** The yield surface is the boundary between elastic and plastic strains. Figure 2.14 is an example of a typical yield surface. A stress probe inside the yield surface causes elastic strains while a probe outside the surface causes plastic strains.

**Flow rule:** A flow rule controls the direction and relative magnitude of the plastic strain increments. As soil changes in volume due to shearing a flow rule is needed (also known as a stress-dilatancy relation). There are two definitions in literature for dilatancy: the absolute and the rate definition illustrated in Figure 2.15. The rate definition is more widely used in constitutive model development, and in North American practice generally, and is used in this thesis. Accordingly, dilatancy is defined as the ratio between an increment of volumetric strain to an increment of shear strain (i.e.  $D = \dot{\epsilon}_v / \dot{\epsilon}_q$ ).

Associated flow was commonly used in the original soil constitutive models because these models do not violate Drucker's postulate (Drucker, 1951). This means that the plastic strain increment ratio,  $\dot{\epsilon}_v^p / \dot{\epsilon}_q^p$ , is normal to the yield surface (Figure 2.16). Once the yield surface is defined, the flow rule is then automatically defined. This results in simpler and more stable models compared to non-associated flow models (i.e. plastic strain increment ratio is not normal to the yield surface).

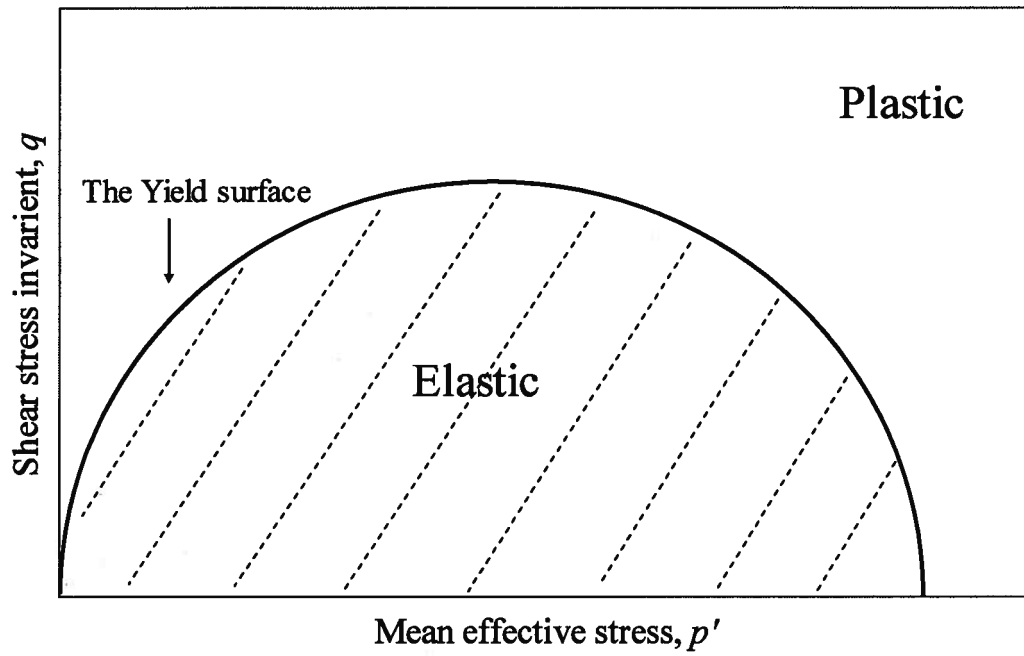


Figure 2.14. An example of a yield surface.

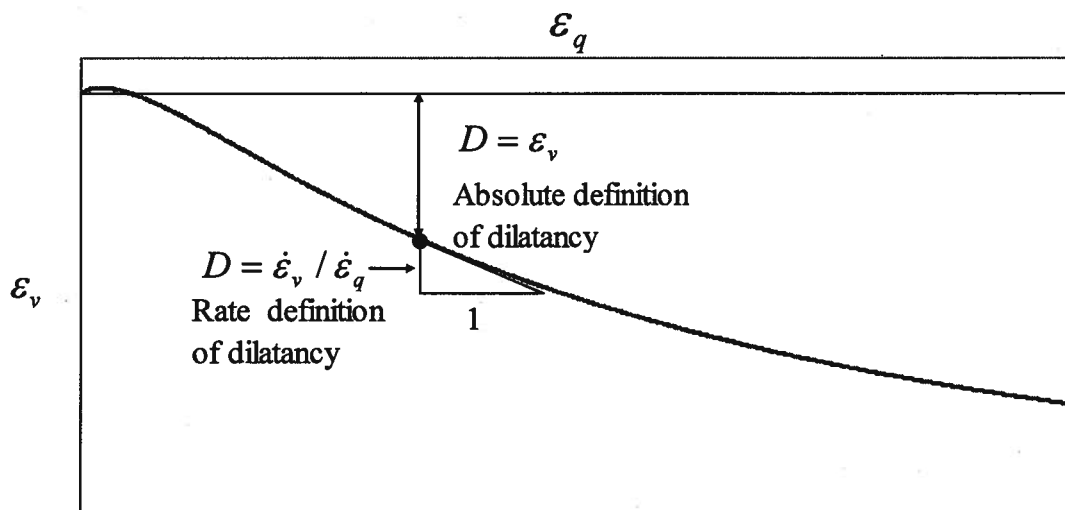


Figure 2.15. Definition of dilatancy (modified after Jefferies & Been, 2006).

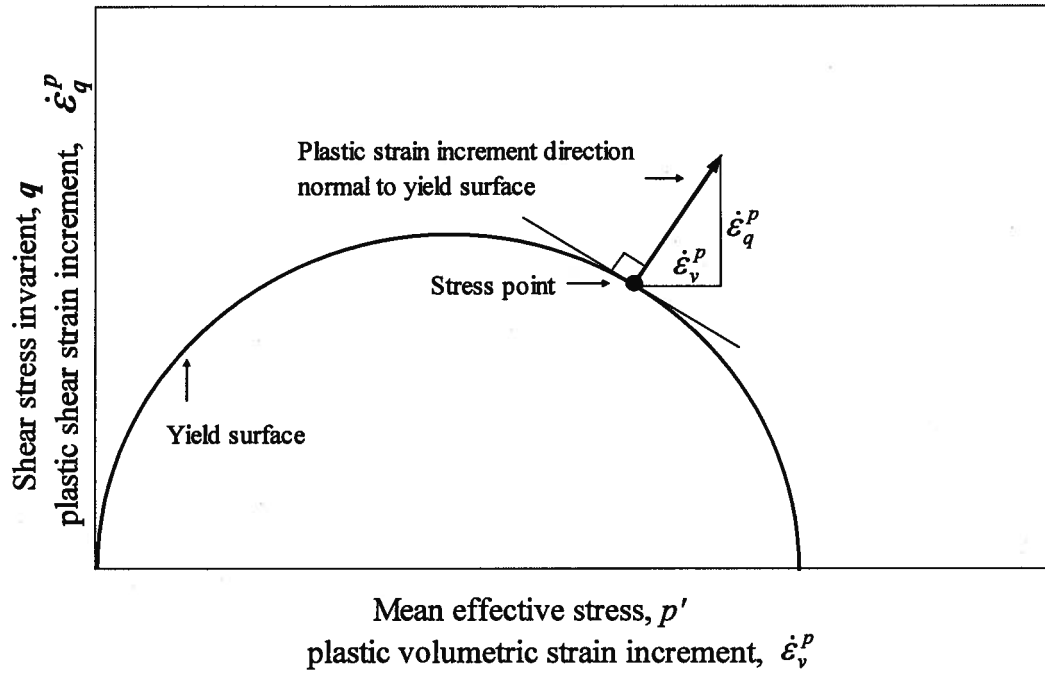


Figure 2.16. Definition of normality.

**Hardening/softening rule:** The hardening/softening rule specifies the movement of the yield surface due to an applied plastic strain increment. The yield surface size is increased for the case of hardening while it decreases for the case of softening. An example of a hardening yield surface is shown in Figure 2.17. The stress point follows the hardened yield surface according to the specified loading path. The requirement for a stress point during loading to start and finish on the current yield surface is called the consistency condition.

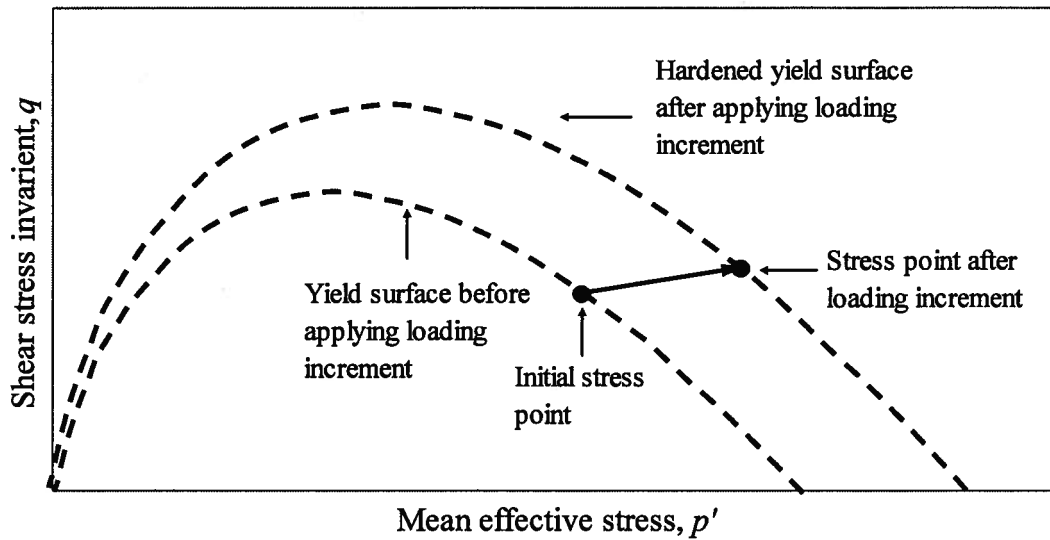


Figure 2.17. Example of the yield surface hardening.

### 2.3.2. Simple soil models

#### 1) The Tresca model

The Tresca soil model is widely used for representing the undrained behaviour of clay in a total stress analysis. In the Tresca model yielding occurs when the maximum shear stress reaches a critical value,  $c$  (see Figure 2.19). For undrained conditions, Poisson's ratio,  $\nu$ , is 0.49999, implying a condition of no volume change. The Tresca model requires two parameters: the critical shear stress value,  $c$ , and the elastic Young's modulus,  $E$ . This yield criterion results in the yield surface in 3-D stress space shown in Figure 2.18. Maximum shear stress is independent of mean stress. This makes the Tresca model ideal for modelling the unconsolidated undrained (UU) behaviour of soils where the shear strength is not affected by an increase in confinement. Normality to Tresca's surface results in vertical plastic strain increments, i.e. zero plastic volumetric strains with shearing (Figure 2.19).



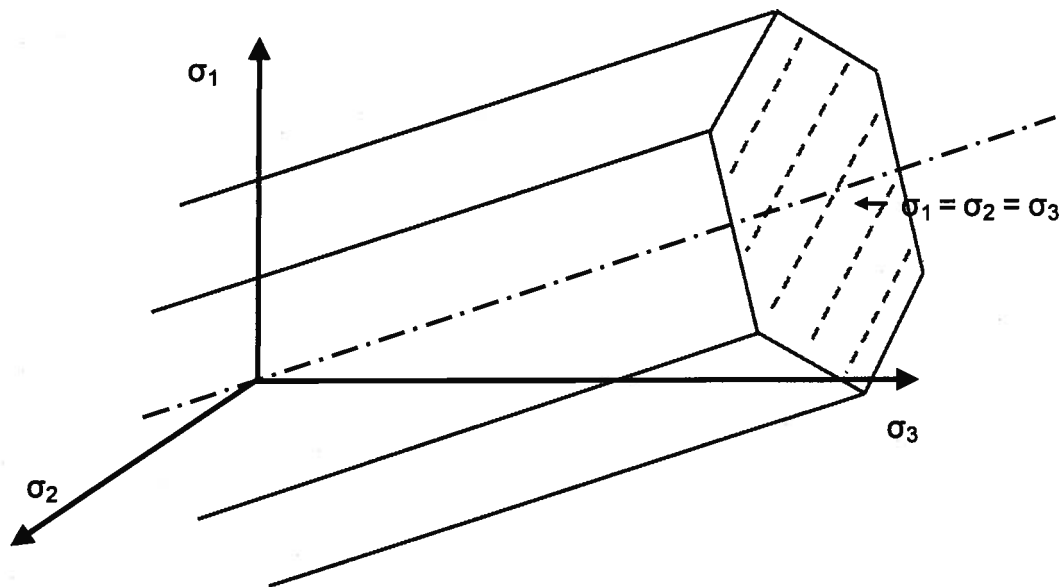


Figure 2.18. Tresca yield criteria in 3-D stress space.

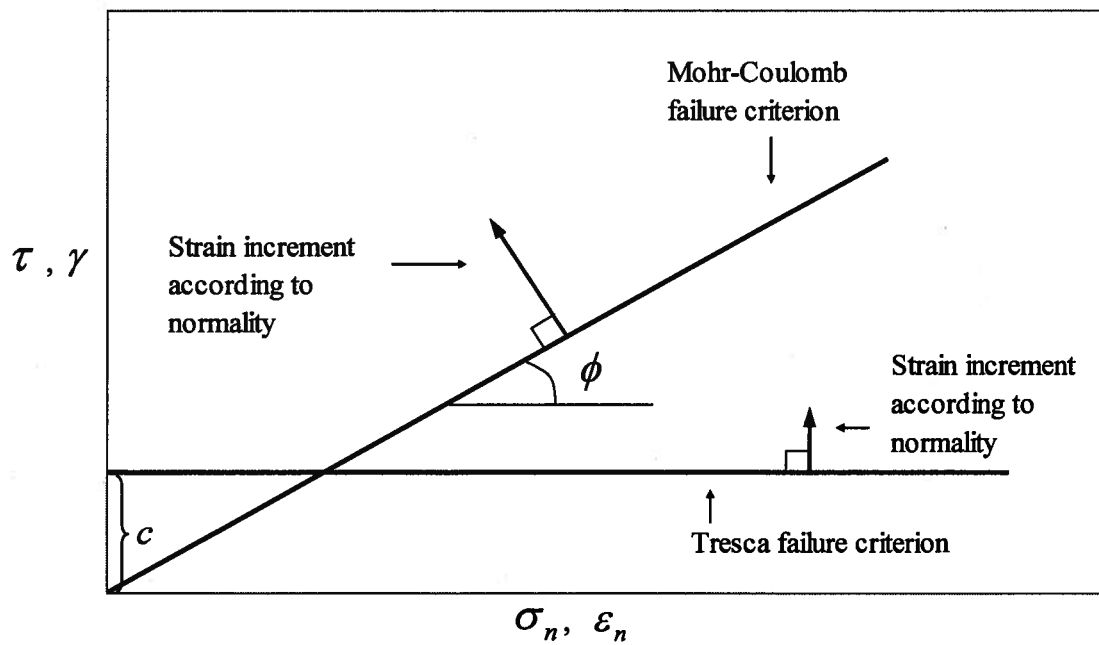


Figure 2.19. Normality to Tresca and Mohr-Coulomb surface.

## 2) The Mohr-Coulomb model

The Mohr-Coulomb (MC) model is a very simple elastic perfectly plastic soil model (i.e. the yield surface does not harden with increasing shear). Like the Tresca model, elasticity is assumed linear elastic, but now the shear strength is no longer constant, but is a function of the mean stress. MC failure surface in the 3-D stress space is shown in Figure 2.20. Unlike Tresca, MC is applied as an effective stress model. MC requires two strength parameters,  $c'$  and  $\phi'$ , where  $c'$  represents the part of strength that is independent of normal stress and  $\phi'$  is the effective friction angle. It represents the part of strength that is dependent on normal stress. Accordingly shear strength,  $\tau$ , that causes yield is given by:

$$\tau = c' + \sigma'_n \tan \phi' \quad (2.5)$$

Equation 2.5 is plotted in Figure 2.19 for  $c = 0$ . MC requires two additional elasticity parameters (Young's modulus,  $E$ , and Poisson's ratio,  $\nu$ ) and the dilation angle. Applying normality to MC surface, i.e. using associated flow, implies that the dilation angle is equal to the friction angle. This results in unreasonably high volumetric strains and hence MC is typically used as a non-associated flow model with a dilation angle close to zero. MC gives reasonable predictions for strength in unconfined problems but it models both volume changes and pre-yield stresses badly.

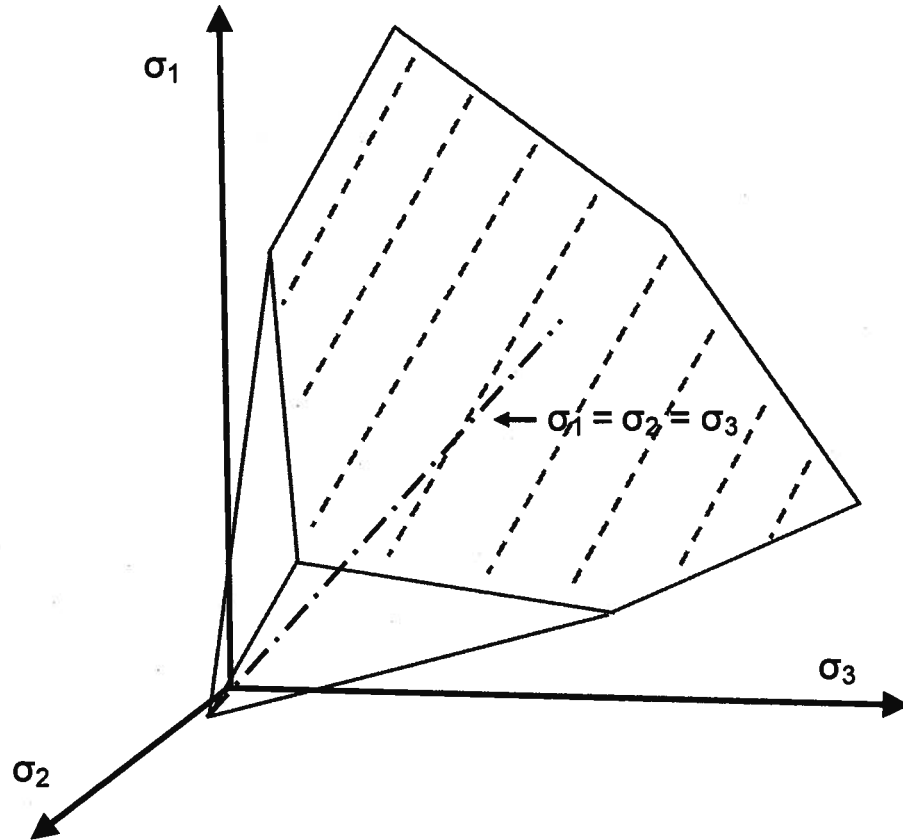


Figure 2.20. Mohr-Coulomb yield criteria in 3-D stress space.

### 2.3.3. Cam-Clay soil model

Cam-Clay is an associated flow constitutive model based on critical state soil mechanics, and one of the earliest advanced constitutive models for soil. There are two versions of Cam Clay widely referenced in engineering practice. The original version of Cam-Clay was developed in the 1960's by Schofield and Wroth (1968). Original Cam Clay (OCC) is not widely found in commercial software, although it is important to explain the development of ideas used in the model, and as the basis of some later critical state models, including the NorSand model used as the starting point for the current work. Conversely, Modified Cam Clay (MCC) is found as an inbuilt model in almost all commercial codes used for geotechnical analysis. MCC is an extension of OCC that sought to address some of the deficiencies of the original model.

The Original Cam-Clay model is a work dissipation model (Schofield and Wroth, 1968). As for any elasto-plastic model, it is composed of elasticity, yield surface, a flow rule and a hardening rule. OCC accounts for elastic volumetric strains only (i.e. it is rigid in elastic shear). The slope of the elastic swelling line in  $e$ - $\log p'$  space, shown in Figure 2.21, is  $\kappa$ .

The rate of total work done on a unit volume of soil is given by:

$$\dot{W} = q \dot{\varepsilon}_q + p' \dot{\varepsilon}_v \quad (2.6)$$

As only plastic strains are involved in the dissipated work (the elastic strains are recoverable), Equation 2.6 may be rewritten in terms of plastic strain as:

$$\dot{W}^p = \dot{W} - \dot{W}^e = q \dot{\varepsilon}_q^p + p' \dot{\varepsilon}_v^p \quad (2.7)$$

Dividing by  $p'$  and  $\dot{\varepsilon}_q^p$  gives:

$$\frac{\dot{W}^p}{p' \dot{\varepsilon}_q^p} = D^p + \eta \quad (2.8)$$

The term on the right hand side represents the dimensionless normalized plastic work dissipated. OCC is based on the assumption that the rate of dissipation is constant and is equal to, the friction ratio at the critical state,  $M$ . This results in the OCC flow rule as:

$$D^p = M - \eta \quad (2.9)$$

All OCC yield surfaces intersect the critical state line at the current critical state value of mean effective stress,  $p'_c$  (see Figure 2.22). The normal consolidation line, NCL, is

assumed to be parallel to the critical state line, CSL (see Figure 2.21). This assumption poorly represents observed sand behaviour. Jefferies and Been (2000) showed, for Erksak sand, that there are an infinite number of normal consolidation lines that are not parallel to CSL. The OCC yield surface may be derived as follows. By definition:

$$q = \eta p' \quad (2.10)$$

Taking the differential of 2.10 gives:

$$\dot{q} = p' \dot{\eta} + \eta \dot{p}' \quad (2.11)$$

As OCC uses associated flow, to satisfy normality (i.e. plastic strain increments normal to the yield surface as shown in Figure 2.22),

$$\frac{\dot{q}}{\dot{p}'} = -\frac{\dot{\epsilon}_v}{\dot{\epsilon}_q} = -D^p \quad (2.12)$$

From 2.11 and 2.12,

$$\frac{\dot{p}'}{p'} + \frac{\dot{\eta}}{D^p + \eta} = 0 \quad (2.13)$$

Substituting the value of  $D^p$  from Equation 2.9 in Equation 2.13. Integrating and substituting  $\ln(p'_c)+1$  for the integration constant at critical state conditions, i.e.  $p' = p'_c$ , gives the equation of the yield surface as:

$$\frac{\eta}{M} = 1 - \ln\left(\frac{p'}{p'_c}\right) \quad (2.14)$$

Under normally consolidated hydrostatic conditions,  $p' = p'_o$  and  $\eta = 0$ . Substituting in Equation 2.14, gives  $p'_c = p'_o / 2.718$ .

The OCC yield surface hardens for the case of  $\eta < M$  and is associated with intersecting it at mean pressures greater than  $p'_c$ . A hardening yield surface is associated with contractive volumetric strains (see Figure 2.22). Hardening continues until  $\eta = M$  where soil reaches the critical state and further shear strain increments do not cause any change in volume. If the stress point touches the yield surface at  $\eta > M$ , softening occurs. This is associated with dilation until the stress point reaches critical state. The OCC hardening rule, given in Equation 2.15, is written in terms of the increment of plastic volumetric strain. It is noteworthy that at critical state  $\dot{\epsilon}_v^p = 0$  and therefore movement of the yield surface stops. Hence all stress paths will end at the critical state.

$$\frac{\dot{p}_c}{p_c} = \frac{(1+e)\dot{\epsilon}_v^p}{\lambda - \kappa} \quad (2.15)$$

Roscoe and Burland (1968) modified Original Cam-Clay in what became the Modified Cam-Clay (MCC) model. The major difference between the two models is the shape of the yield surface. One of the problems with OCC is that it predicts shear strains for the case of hydrostatic loading. The elliptical yield surface of MCC predicts only volumetric strains for the hydrostatic loading condition. OCC overestimates the values of strain increments at small strains. MCC accounts for elastic shear while OCC is rigid in elastic shear.

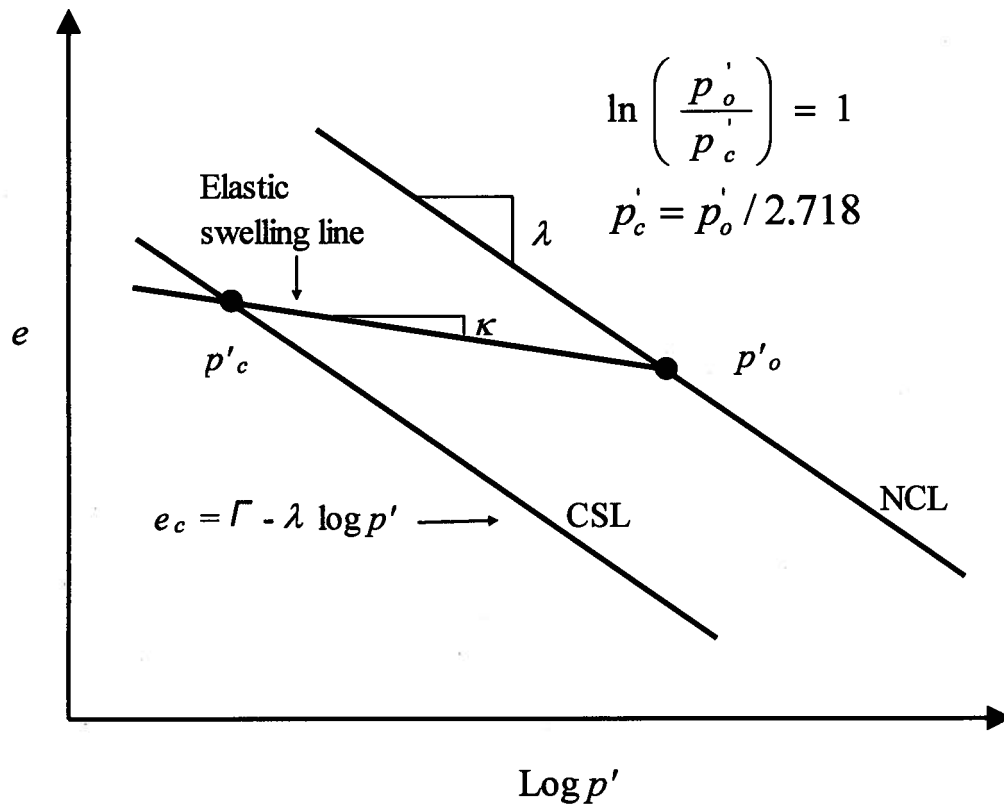


Figure 2.21. Parallel CSL and NCL in  $e$ - $\log p'$  plot.

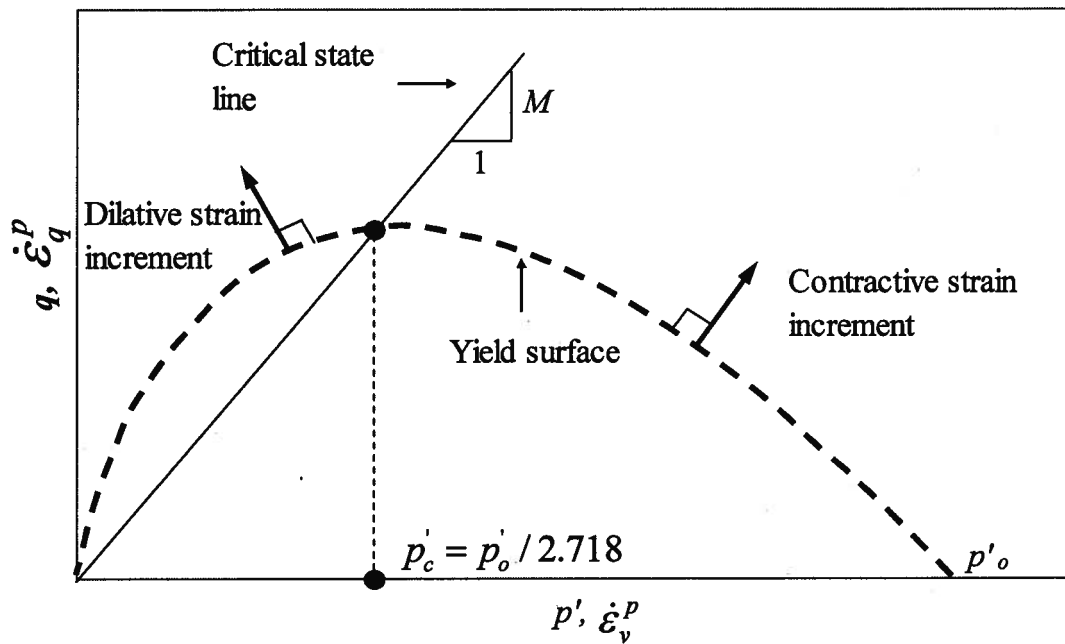


Figure 2.22. Original Cam-Clay yield surface.

## 2.4. Stress-Dilatancy

Dilatancy was defined in Section 2.3.1 as the ratio between an increment of volumetric strain and an increment of shear strain (i.e.  $D = \dot{\epsilon}_v / \dot{\epsilon}_q$ ). This section discusses stress-dilatancy (i.e. the inter-relationship between stress and dilatancy) in more detail. An objective of this thesis is to investigate stress-dilatancy in unloading and reloading.

Reynolds (1885) showed that dense sand dilates when sheared towards failure while loose sand contracts.

The work of Taylor showed that soil strength is due to both the frictional resistance between the particles and the tendency of dense soil particles to override each other. The difference between the critical friction angle and the peak friction angle is caused by dilatancy.

Rowe (1962) introduced a relation between stresses and dilatancy based on the study of particles in contact. Particles are assumed rigid, have circular cross-sections and are identical. The forces at the contacts are assumed purely frictional. The importance of Rowe's work is that it relates stresses to dilatancy throughout deformation to failure.

To explain Rowe's model a typical assembly of rods is shown in Figure 2.23a. The angle of deviation of the tangent at the contacts between particles from direction 1 is defined as  $\beta$ .  $L_1$  and  $L_2$  are the loads on each rod in directions 1 and 2 respectively. A typical unit volume is  $l_1 l_2$  (it is assumed that the rods have unit length in the third direction). The volume of the assembly can be expressed by an integer number times the number of typical units of volume.

The conditions at each contact between two particles in the assembly are similar to those shown in Figure 2.24. This figure shows a rigid block sliding on an inclined



surface making an angle  $\beta$  from the direction of  $L_1$ . The component of the reaction force normal to the surface is  $N$ . The component of the reaction force parallel to the surface is  $N \tan \phi_\mu$ , where  $\phi_\mu$  is the particle to particle friction angle. Resolving the forces in the  $L_1$  and  $L_2$  directions gives:

$$\frac{L_1}{L_2} = \tan(\phi_\mu + \beta) \quad (2.16)$$

From Figure 2.23a:

$$\tan \alpha = \frac{l_1}{l_2} \quad (2.17)$$

From Equations 2.16 and 2.17:

$$\frac{\sigma_1'}{\sigma_2'} = \frac{L_1 l_1}{L_2 l_2} = \tan \alpha \tan(\phi_\mu + \beta) \quad (2.18)$$

Where  $\sigma_1' = L_1/l_2$  and  $\sigma_2' = L_2/l_1$ .  $\delta_1$  and  $\delta_2$  are the deformations in directions 1 and 2 respectively at an angle  $\beta$  relative to those at an angle  $\beta_o$  (see Figure 2.23b). From the geometry, the following can be derived:

$$\frac{\dot{\varepsilon}_2}{\dot{\varepsilon}_1} = \frac{\dot{\delta}_2 l_1}{\dot{\delta}_1 l_2} = \tan \alpha \tan \beta \quad (2.19)$$

Where  $\dot{\varepsilon}_1 = \dot{\delta}_1/l_1$  and  $\dot{\varepsilon}_2 = \dot{\delta}_2/l_2$ . Assuming that vertical compression, lateral expansion and volume increase are all positive gives:

$$\frac{\dot{\varepsilon}_2}{\dot{\varepsilon}_1} = \left( 1 + \frac{\dot{\varepsilon}_v}{\dot{\varepsilon}_1} \right) \quad (2.20)$$

Where  $\dot{\varepsilon}_v = \dot{\varepsilon}_1 + \dot{\varepsilon}_2$ . From Equations 2.18, 2.19 and 2.20:

$$\frac{\sigma_1' \dot{\varepsilon}_1}{\sigma_2' \dot{\varepsilon}_2} = \frac{\sigma_1'}{\sigma_2' (1 + \dot{\varepsilon}_v / \dot{\varepsilon}_1)} = \frac{\tan(\phi_\mu + \beta)}{\tan \beta} \quad (2.21)$$

The term on the left hand side of Equation 2.21 represents the ratio between work done in the direction of the major principal stress on the assembly to that done by the assembly on the direction of the minor principal stress. This ratio is equal to one for the case where the particle to particle friction angle,  $\phi_\mu$ , is equal to zero, i.e. in the absence of inter-particle friction the dissipated work is equal to zero and therefore all work done on the major principal stress is transferred to the minor principal stress.

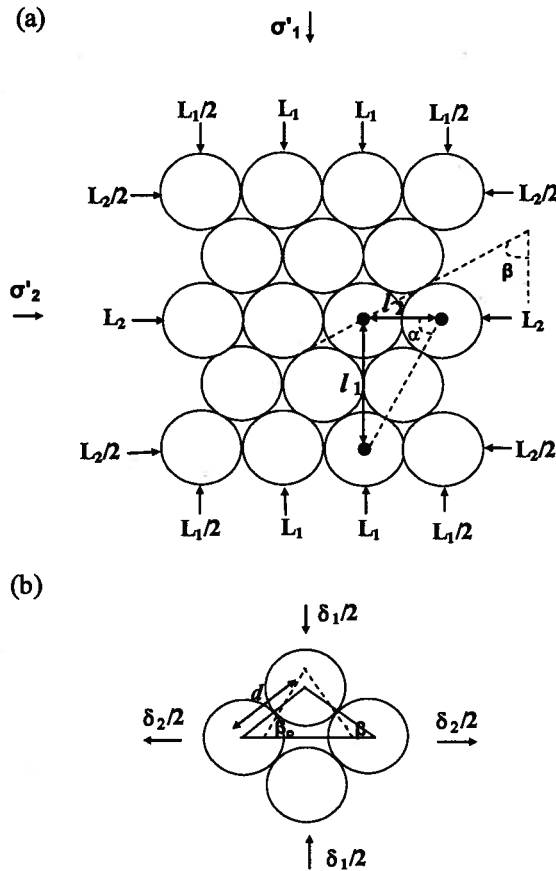


Figure 2.23. Typical assembly of rigid rods (a) stress conditions (b) deformation characteristics (reproduced from Rowe, 1962).

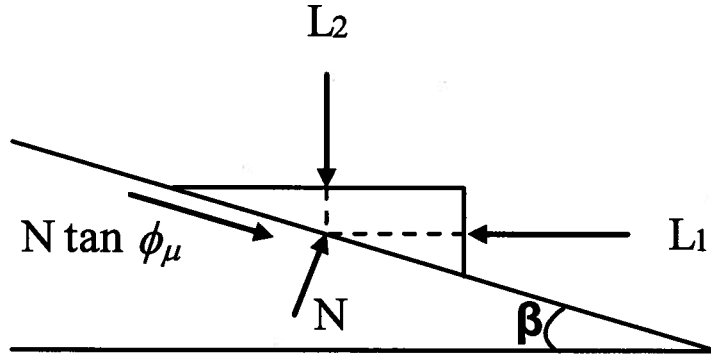


Figure 2.24. Forces acting on a rigid block sliding on an inclined surface (reproduced from Rowe, 1962).

For a random mass of irregular particles, the value of  $\beta$  changes with loading as the particles orientations changes. It is assumed that this relocation happens such that “the rate of internal work done is minimum” (Rowe, 1962). This assumption changes Equation 2.21 to:

$$\frac{\sigma_1'}{\sigma_2'(1 + \dot{\epsilon}_v / \dot{\epsilon}_1)} = \tan^2(45 + 0.5\phi_\mu) \quad (2.22)$$

From experimental observations Rowe found it necessary to use  $\phi_f$  (defined as the functional or mobilised friction angle) instead of  $\phi_\mu$ , where  $\phi_f$  varies depending on density and boundary conditions. The sign of the volumetric strain increment is changed so that volume decrease is positive following the sign convention used in soil mechanics. Rowe (1962) showed that Equation 2.22 is valid regardless of the boundary conditions. For triaxial conditions, the minor principal stress is  $\sigma_3'$ . This gives:

$$\frac{\sigma_1'}{\sigma_3'} = K \left( 1 - \frac{\dot{\epsilon}_v}{\dot{\epsilon}_1} \right) \quad (2.23)$$

Where,

$$K = \tan^2(45 + 0.5\phi_f) \quad (2.24)$$

For triaxial conditions, Rowe (1969) showed that  $\phi_f$  varies between the inter-particle friction angle and the critical state friction angle. Under plane strain,  $\phi_f$  is equal to the friction angle at the critical state for any packing up to peak stress ratio. In the  $p'$ - $q$  space, rearranging Equations 2.23 and 2.24 and assuming  $\phi_f = \phi_{cv}$  results in Equation 2.25 for triaxial compression.

$$\frac{\varepsilon_v}{\varepsilon_q} = \frac{9(M - \eta)}{9 + 3M - 2M\eta} \quad (2.25)$$

Where,

$$M = \frac{6 \sin \phi_{cv}}{3 - \sin \phi_{cv}} \quad (2.26)$$

Schofield and Wroth (1968) introduced the Cam-Clay dilatancy rule based on plastic work dissipation mechanism as in Equation 2.27 (Cam-Clay was described in detail in Section 2.3.2). Roscoe and Burland (1968) modified Original Cam-Clay in what became the Modified Cam-Clay (MCC) model. Equation 2.28 is the MCC flow rule.

$$D^p = M - \eta \quad (2.27)$$

$$D^p = \frac{M^2 - \eta^2}{2\eta} \quad (2.28)$$

Cam-Clay is widely used for soft clay, but the dilatancy rule does not match sand data well, particularly for dense sands. Nova addressed this issue in 1982 and developed an improved stress-dilatancy rule based on observations from laboratory data (Equation

2.29). Nova's equation contains an additional volumetric coupling parameter ( $N$ ) which usually falls in the range of 0.2-0.4.

$$D^p = \frac{(M - \eta)}{(1 - N)} \quad (2.29)$$

Figure 2.25 plots the Rowe, Cam-Clay and Nova flow rules for  $M=1.27$  and  $N=0.25$ . It is noteworthy that the trends are fairly similar in the dilatant range (i.e. for negative  $D^p$ ) for a typical critical friction ratio of 1.27 (i.e.  $\phi_{cv} = 31.6^\circ$ ).

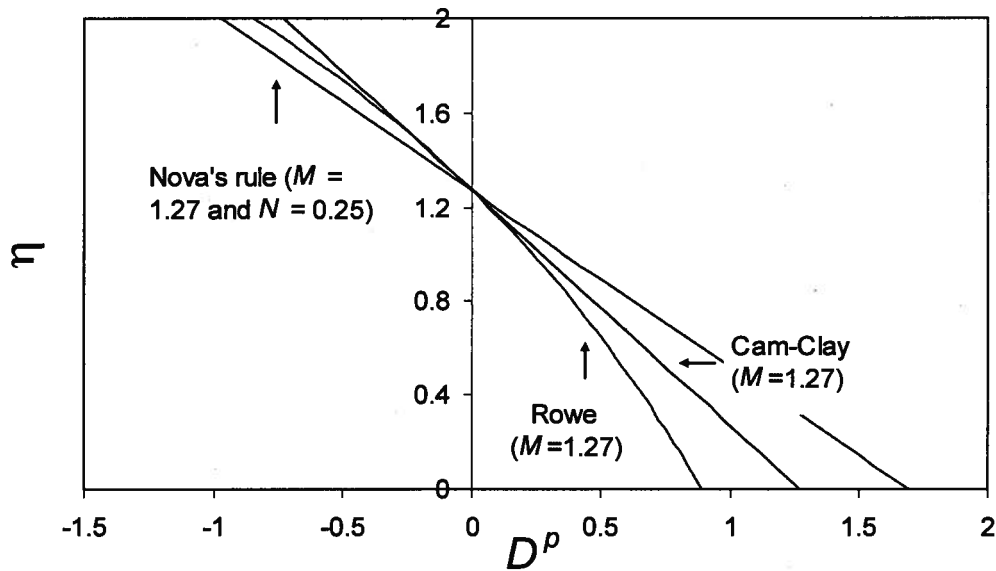


Figure 2.25. Comparison between Rowe's stress-dilatancy, Cam-Clay flow rule, and Nova's rule.

Bolton (1986) used a large database of both triaxial and plane strain tests to relate the component of strength that is caused by dilatancy to initial density and mean effective stress. The component of strength caused by dilatancy is represented by the difference between the peak friction angle,  $\phi'_{max}$ , and the friction angle at the critical state,  $\phi'_{cv}$ . Triaxial data show that  $\phi'_{max} - \phi'_{cv}$  is directly proportional to relative density and inversely

proportional to mean effective stress at failure (see Figure 2.26). Bolton presented Equation 2.30 from fits to triaxial laboratory data. Equation 2.30 is plotted in Figure 2.26 for different  $D_r$  values. This relation is very useful as knowing effective stress conditions, relative density and critical friction angle, peak friction angle could be computed.

$$\phi'_{\max} - \phi'_{cv} = 3[D_r(10 - \ln p') - 1] \quad (2.30)$$

From plane strain data, Bolton found that the relation between the fraction of strength caused by dilatancy, i.e.  $\phi' - \phi'_{cv}$ , and the angle of dilation,  $\theta$ , is as in Equation 2.31, where  $\theta$  is defined as in Equation 2.32. Bolton showed that his Equation, i.e. Equation 2.31, is very similar to Rowe's relation in Equation 2.23.

$$\phi' - \phi'_{cv} = 0.8\theta \quad (2.31)$$

$$\theta = \sin^{-1} \left( \frac{\dot{\epsilon}_v}{\dot{\epsilon}_q} \right) = \sin^{-1} \left( \frac{-\dot{\epsilon}_v}{\dot{\epsilon}_1 - \dot{\epsilon}_3} \right) \quad (2.32)$$

Equation 2.31 is valid for plane strain boundary condition for the whole stress path including at peak. Bolton's work implies that the fraction of strength at peak caused by dilatancy,  $\phi'_{\max} - \phi'_{cv}$ , for triaxial boundary conditions is:

$$\phi'_{\max} - \phi'_{cv} = 0.48\theta_{\max} \quad (2.33)$$

The problem now is that, unlike for plane strain, the dilation angle does not have a physical meaning for triaxial conditions. To derive Equation 2.33, it was assumed that the definition of the dilation angle in Equation 2.32 is valid for triaxial conditions.

Vaid and Sasitharan (1992) performed triaxial tests on Erksak sand with different stress paths and initial densities. Assuming that the definition for the dilation angle, Equation 2.32, is valid for triaxial conditions, they confirmed that at peak stress the friction angle is

uniquely related to  $\theta_{\max}$  regardless of the confining pressure and relative density. They also found this relation between peak friction angle and peak dilatancy to be independent of stress path. They used different triaxial stress paths in the  $p'-q$  space which included both compression and extension tests. Accordingly, Vaid and Sasitharan proposed a relation between  $\phi'_{\max} - \phi'_{cv}$  and maximum dilation angle for triaxial conditions. They measured  $\phi'_{cv}$  using the Bishop method that involves plotting the data in peak dilation vs. peak friction angle (Bishop, 1971). A best fit linear trend line is plotted through the data points and the friction angle corresponding to zero peak dilatancy is  $\phi'_{cv}$ . Their proposed relation is given by:

$$\phi'_{\max} - \phi'_{cv} = 0.33\theta_{\max} \quad (2.34)$$

The factor on the right hand side of Equation 2.34 is lower than that in Equation 2.33, i.e. 0.33 is lower than 0.48. Equations 2.33 and 2.34 were developed for triaxial conditions. It should be noted that Equation 2.33 was developed to fit the data for 11 sands on average. Therefore, it is not surprising that Equation 2.34, developed for Erksak sand, is different from Equation 2.33.

Overall, according to Bolton, from Equations 2.31 evaluated at peak and Equation 2.33, the fraction of strength caused by dilatancy,  $\phi'_{\max} - \phi'_{cv}$ , for triaxial conditions is around 60% of that for plane strain conditions.

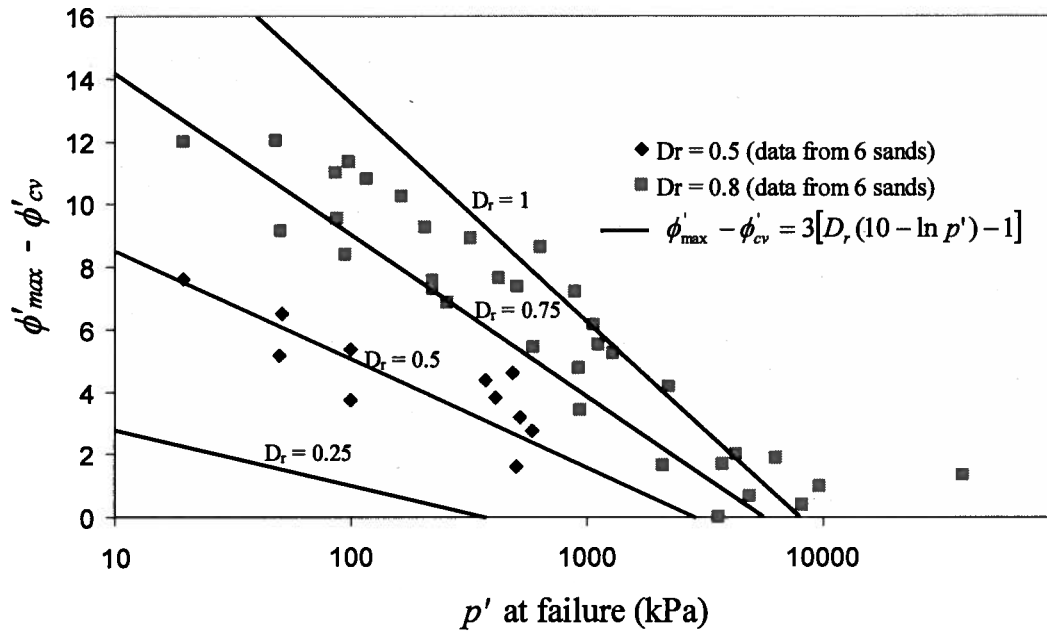


Figure 2.26. Dilatancy component of strength as a function of mean effective stress at failure and relative density (reproduced from Bolton, 1986).

## 2.5. The NorSand soil model

The constitutive model development in the following chapters is based on the general framework of the NorSand soil model. Therefore, NorSand is described in some detail in this section. The discussion is limited to triaxial compression boundary conditions. NorSand is an elasto-plastic critical state soil model developed by Jefferies (1993). Over the last 15 years the NorSand model has been updated, primarily to incorporate varying critical image stress ratio,  $M_i$ , and to provide improved predictions under plane strain. The version of Jefferies and Shuttle (2005) is described below. This section focuses on the monotonic version of NorSand. The cyclic version will be described in section 2.6.3.

NorSand was the first critical state model to realistically model sand in that, unlike Cam-Clay, it predicts realistic dilatancy for dense soils (Jefferies and Shuttle, 2005). Like Cam-Clay, NorSand assumes normality, but NorSand also imposes a limit on the



hardening of the yield surface which allows for more realistic prediction of dilatancy for dense soils. The model requires 8 input parameters that can be easily determined from laboratory data (three critical state parameters, three plasticity parameters, and two elasticity parameters).

NorSand, like other critical state models, is based on two basic axioms:

- A unique critical state exists
- The critical state is the final state to which all soils converge with increasing shear strain.

One of the main features of all versions of NorSand, which is a significant difference from Cam-Clay, is that NorSand has an infinity of normal consolidation lines (NCL) and not every yield surface is required to pass through the critical state. This behaviour was first reported by Tatsuoka and Ishihara (1974), from triaxial tests on Fuji River sand, who demonstrated that the normal consolidation line (NCL) for sands is not unique, instead being a function of density. They showed that looser samples yield at higher deviator stress for a given mean effective stress. Jefferies and Been provided additional data to confirm this finding in 2000 for Erksak sand (Jefferies and Been, 2000). The concept is illustrated in Figure 2.27. For every normal consolidation line there is a conjugate yield surface at each value of initial mean effective stress. The implications of having infinite NCL locations are:

- The yield surface could exist anywhere in the  $e-q-\log(p')$  space. It does not necessarily need to intersect the critical state line as in Cam-Clay. Therefore, the hardening of the yield surface cannot be uniquely controlled by void ratio, and the slopes of NCL and the swelling line as for the OCC/MCC model. Hardening in NorSand is controlled by the plastic hardening parameter,  $H$ , that is a function of the state parameter and soil fabric.
- To get representative predictions for dense sand in OCC/MCC, a high over-consolidation ratio must be used even if the sand was normally consolidated,

i.e. it did not experience higher mean effective stresses in its history. In NorSand, the “intrinsic state” of soil is separated from overconsolidation and there is no need to assign an over-consolidation ratio to properly model dense normally consolidated sand (Jefferies, 1993). Instead, the concept of the state parameter previously discussed is utilized to determine the current location in  $e$ - $\log p'$  space relative to the critical state.

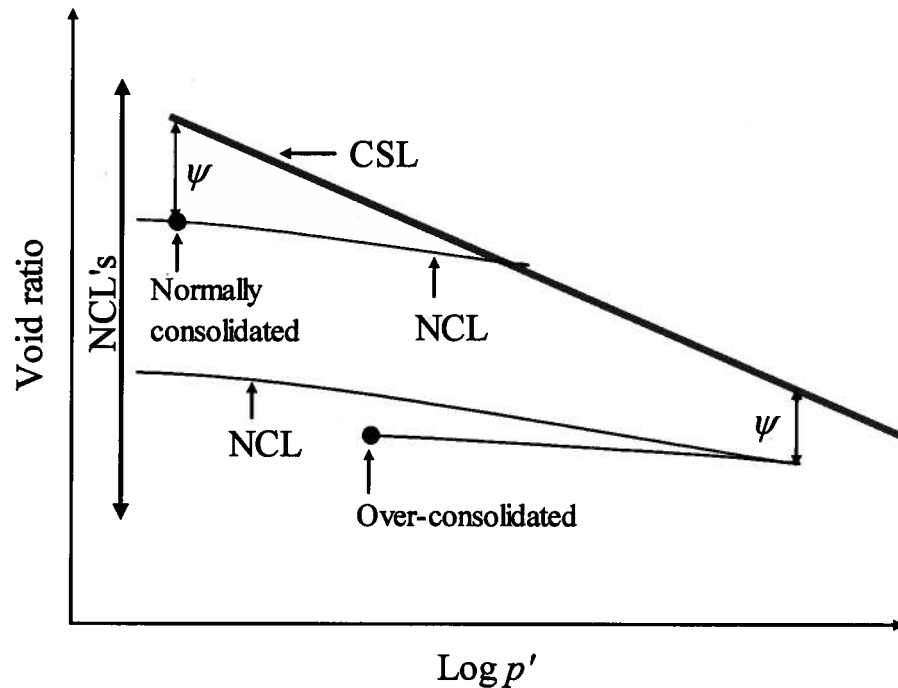


Figure 2.27. Infinite number of NCL's (reproduced from Jefferies and Shuttle, 2002).

### 2.5.1. Yield surface and flow rule

NorSand's outer yield surface has an identical shape to the Original Cam-Clay surface (see Figure 2.28). In addition NorSand's yield surface also has a straight vertical cap at a limiting dilatancy which occurs at a stress ratio coincident with peak stress conditions. In NorSand peak stress ratio,  $\eta_{limits}$ , is associated with peak dilatancy or  $D_{min}$  if the sign is taken in consideration (Figure 2.28). In the following discussion the curved portion of

the yield surface is called the outer yield surface and the vertical portion is called the inner cap or inner yield surface. A soil stress path may intersect the inner cap in unloading. This behaviour will be described in Section 2.6.3. Therefore the focus here is on the outer yield surface.

NorSand defines the image condition as the boundary between the contractive and dilative behaviour in dense sands (see Figure 2.28). The image condition is differentiated from the critical state in that it satisfies only one condition of the critical state. At the image condition,  $D^p = 0$  but  $\dot{D}^p \neq 0$ . The stress ratio  $(q/p')$  at image,  $M_i$ , is a function of  $M$  and  $\psi$ . As soil reaches the critical state with shearing, the value of  $M_i$  approaches  $M$  until they are eventually equal at the critical state. The idea of changing  $M_i$  is very similar to Rowe's mobilised stress ratio, or mobilised friction angle  $\phi_f$ , in Equation 2.24.

NorSand's flow rule is very similar to the Original Cam-Clay flow rule except the variable  $M_i$  is used instead of  $M$ , as in Equation 2.35. The model uses associated flow (i.e. plastic strain ratio increments are normal to the yield surface).

$$D^p = M_i - \eta \quad (2.35)$$

The derivation of NorSand yield surface follows the same steps as that for Cam-Clay (Equations 2.10-2.14). Substituting the value of  $D^p$ , i.e. Equation 2.35, in Equation 2.13 gives NorSand yield surface as:

$$\frac{\eta}{M_i} = 1 - \ln\left(\frac{p'}{p_i}\right) \quad (2.36)$$

An expression for  $M_i$  is needed and Nova's rule in Equation 2.29 is adopted here for peak conditions. Combining Nova's rule at peak with equation 2.35 gives:

$$M_i = M + ND_{\min}^p \quad (2.37)$$

Been and Jefferies (1985) showed by plotting experimental data that there is a relation between  $D_{min}$  and state parameter,  $\psi$ . There are three versions of this plot in the literature depending on  $p'$  and  $e$  at which  $\psi$  is evaluated:

1. Data is plotted in  $D_{min}$  vs. the state parameter at initial conditions,  $\psi_o$ .
2. Data is plotted in  $D_{min}$  vs. the state parameter evaluated at  $D_{min}$ .
3. Data is plotted in  $D_{min}$  vs. the state parameter for image conditions evaluated at  $D_{min}$ ,  $\psi_i$  where  $\psi_i = e - e_{ci}$  ( $e_{ci}$  is the critical void ratio evaluated at  $p'_i$ ). A plot is shown in Figure 2.29.

The three versions of the  $D_{min}$  vs.  $\psi$  plot show a trend of increasing dilation rate with increasing state parameter. The slope of the trend line through the data points is  $\chi$ , a NorSand model parameter that is used to impose a limit on the minimum allowable dilation rate and is a function of soil fabric. The second version of the  $D_{min}$  vs.  $\psi$  plot is the one adopted in this thesis. Accordingly,  $\chi = D_{min} / \psi$ . As elastic strains are negligible at peak conditions,  $\chi = D_{min} / \psi$  can alternatively be written as:

$$D_{min}^p = \chi \psi \quad (2.38)$$

Combining Equations 2.37 and 2.38 gives an expression for  $M_i$  as:

$$M_i = M + \chi N \psi \quad (2.39)$$

The derivation considered dense sand only. As loose sand is expected to dissipate plastic work similar to dense sand, Equation 2.39 is changed to Equation 2.40, i.e. made symmetric about the critical state (Jefferies and Been, 2006).

$$M_i = M - \chi N |\psi| \quad (2.40)$$

For a given outer yield surface, the location of the point at  $D_{min}$  needs to be defined (see Figure 2.28). Evaluating Equation 2.36 at peak conditions and rearranging gives,

$$\left( \frac{p'_i}{p'} \right)_{\max} = e^{(-D_{min}^p / M_i)} \quad (2.41)$$

Substituting the value of  $D_{min}^p$ , as in Equation 2.38, in Equation 2.41 gives,

$$\left( \frac{p'_i}{p'} \right)_{\max} = e^{(-\chi \psi / M_i)} \quad (2.42)$$

The relative position of the  $M_i$ ,  $M$  and  $\eta_{limit}$  lines in Figure 2.28 is not constant. According to Equation 2.40,  $M_i$  tends to  $M$  as the critical state is approached until they are eventually equal at the critical state where  $\psi = 0$ .  $\eta_{limit}$  also decreases until it is equal to  $M$  at critical state (see Equation 2.42).

### 2.5.2. Hardening of the yield surface

The NorSand outer yield surface hardens until the point corresponding to  $D_{min}$  is reached. This is followed by a softening response until the yield surface stops changing in size at the critical state. As the NorSand yield surface size is controlled by the dimensionless ratio of  $(p'_i / p')$ , the hardening rule, representing the change in the size of the yield surface, is expressed by  $(\dot{p}'_i / \dot{p}')$ . The NorSand hardening rule takes the form of:

$$\left( \frac{\dot{p}_i}{p} \right) = H \left[ \left( \frac{p_i}{p} \right)_{\max} - \left( \frac{p_i}{p} \right) \right] \dot{\varepsilon}_q^p \quad (2.43)$$

Where  $H$  is the plastic hardening modulus, a model parameter. The hardening rule is a function of  $\dot{\varepsilon}_q^p$  because using  $\dot{\varepsilon}_v^p$  instead would result in a model that never gets past image as when  $\eta = M_i$ ,  $\dot{\varepsilon}_v^p = 0$ . The hardening rule gives better fit to data if it is give a dependence on the shear stress level (Jefferies and Been, 2006). An exponential function is used to introduce this dependence. Hence, equation 2.43 is changed to:

$$\left( \frac{\dot{p}_i}{p} \right) = H e^{(1-\eta/M_i)} \left[ \left( \frac{p_i}{p} \right)_{\max} - \left( \frac{p_i}{p} \right) \right] \dot{\varepsilon}_q^p \quad (2.44)$$

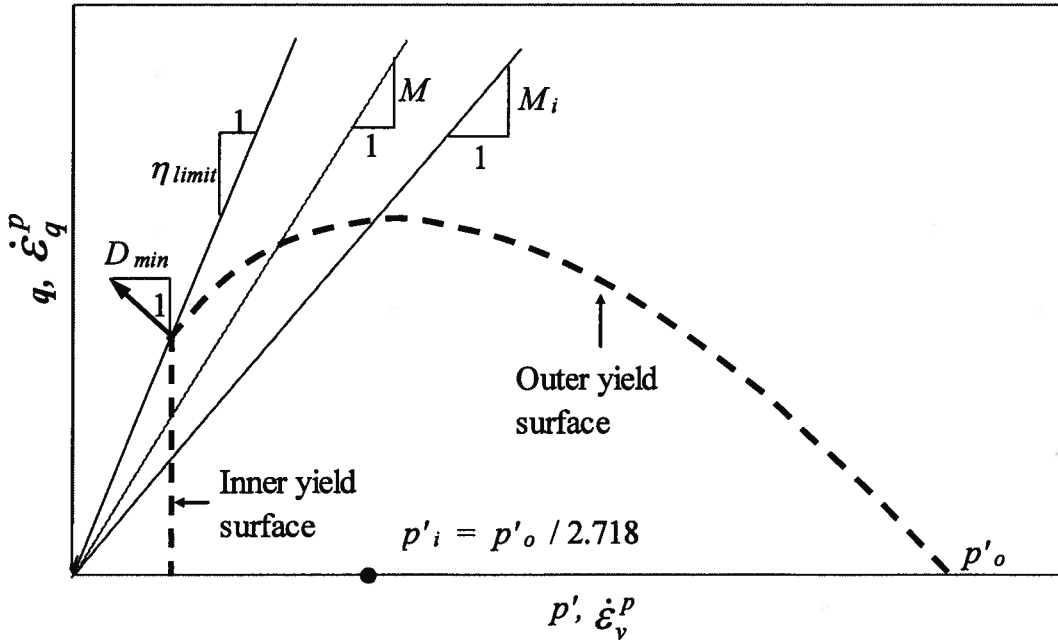


Figure 2.28. NorSand yield surface (modified after Jefferies and Shuttle, 2005).

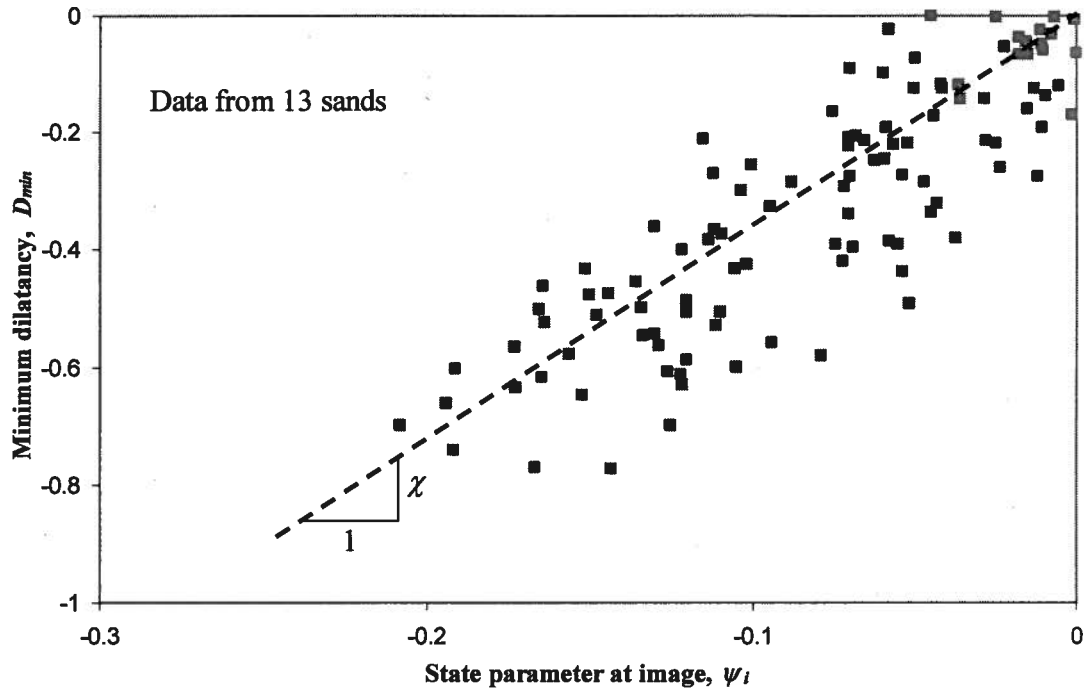


Figure 2.29. Minimum dilatancy as a function of state parameter at image for 13 sands (modified after Jefferies and Been, 2006).

### 2.5.3. Typical evolution of the yield surface

The hardening and softening of NorSand yield surface is described as follow (see Jefferies 1993):

- It is assumed that we are starting with a soil denser than the critical state.
- With increasing shear strain the yield surface hardens, with the size of the yield surface during hardening controlled by the mean effective stress at image,  $p'_i$ . Soil remains contractive until the current mean effective stress equals  $p'_i$ .
- Although the current stress ratio is equal to  $M_i$ , the movement of the yield surface does not stop because the image state only satisfies one condition of the critical state. The hardening continues with increasing shear strain in a

dilative manner until it reaches the surface corresponding to the limiting stress and maximum allowable dilation rate.

- At this point, softening starts with a decreasing rate as it approaches the critical state.
- At the critical state  $M_i = M$  and the yield surface does not move any further.

#### **2.5.4. Elastic properties of NorSand**

In Cam-Clay elasticity, the elastic shear strains are ignored. NorSand does not ignore the elastic part of shear strains and variations on elasticity including standard linear elasticity and a range of stress dependent models have been implemented.

#### **2.5.5. Summary of the NorSand model**

The full set of equations that specify the NorSand model presented in the preceding sections are given in Table 2.1. Table 2.2 lists the parameters used in the model and their typical ranges. The parameter ranges were primarily obtained from calibrations to sand, so care should be exercised when applying to other soil types.



Table 2.1. Summary of NorSand equations (modified after Jefferies and Shuttle, 2005).

Aspect of NorSand	Equation
Internal model parameters	$\psi = e - e_c,$ $e_c = \Gamma - \lambda_e \ln(p')$ and, $M_i = M - \chi N  \psi $
Yield surface	$\frac{\eta}{M_i} = 1 - \ln\left(\frac{p'_i}{p'_i}\right)$ with $\left(\frac{p'_i}{p'_i}\right)_{\max} = e^{(-\chi\psi / M_i)}$
Flow rule	$D^p = M_i - \eta$
Hardening of outer yield surface	$\left(\frac{\dot{p}'_i}{p'_i}\right) = H e^{(1-\eta / M_i)} \left[ \left(\frac{p'_i}{p'_i}\right)_{\max} - \left(\frac{p'_i}{p'_i}\right) \right] \dot{\varepsilon}_q^p$
Elasticity	$I_r = G / p'$

Table 2.2. Summary of NorSand parameters (after Jefferies and Shuttle, 2005).

Parameter	Typical range	Description
<b>Critical state</b>		
$\Gamma$	0.9-1.4	The y-intercept of the e-log( $p'$ ) curve at 1KPa
$\lambda_e$	0.01 – 0.07	The slope of CSL in e-log( $p'$ ) space defined on base e
$M_{tc}$	1.2-1.5	$q/p'$ at critical state
<b>Plasticity</b>		
$H$	50-500	Plastic hardening modulus
$\chi_{tc}$	2.5-4.5	A parameter that limits the hardening of the yield surface
$N$	0.2-0.4	The volumetric coupling parameter (used in Nova's rule)
<b>Elasticity</b>		
$I_r$	100-800	Dimensionless shear rigidity ( $=G/p'$ )
$\nu$	0.1-0.3	Poisson's ratio

## 2.6. Soil behaviour in unloading

While there have been relatively many studies addressing the overall cyclic behaviour of sand, little work has been done to study the behaviour of sand during the unloading phase in detail. It is interesting that sand also shows contractive, in addition to the expected dilative, behaviour when unloaded. The implications of this behaviour were discussed in Chapter 1. This section discusses previous work on the topic.

### 2.6.1. A Simple physical model

Jefferies (1997) explains soil contraction in unloading in terms of stored potential energy during the loading phase. Assuming the saw tooth model represents how soil dilates, when dense sand is loaded grains tend to climb over the slip surfaces (see Figure

2.30a). This is associated with increase in volume as the voids between the teeth are increased. At the end of loading the potential energy of those particles has been increased by the virtue of their new location. When unloading, it is then easy to imagine that those particles will tend to slide backwards (see Figure 2.30b). This is associated with decrease in volume as the voids between the saw teeth get smaller ( $d_2 < d_1$ ).

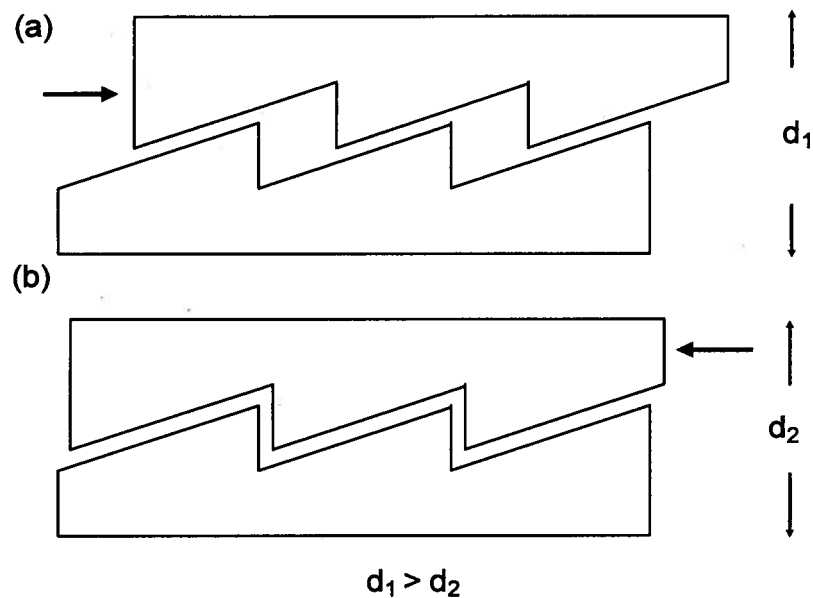


Figure 2.30. The Saw Tooth Model a) loading phase b) unloading phase.

### 2.6.2. Thermo-mechanical approach

The first law of thermodynamics states that “The increase in the internal energy of a system is equal to the amount of energy added by heating the system, minus the amount lost as a result of the work done by the system on its surroundings”. Alternatively, plastic work done on soil is either dissipated in the form of frictional energy or contributes to the increase of internal energy.

Cam-Clay assumes that all ‘plastic’ work done on soil is dissipated. This means that plastic work does not contribute to changing internal energy. Part of the total work increments is recoverable (termed ‘elastic’) and the other part is irrecoverable (termed

‘plastic’) as in Equation 2.45. Cam-Clay is rigid in ‘elastic’ shear and only recovers ‘elastic’ volumetric strain. Therefore, the Cam-Clay approach assumes that any change in internal energy is only due to an ‘elastic’ change of volumetric strain that can be calculated using the slope of the swelling line in a usual consolidation test (Schofield and Wroth, 1968). The ‘plastic’ component of work is dissipated and the dissipation rate is assumed constant and equal to the critical friction ratio,  $M$ . The term on the right hand side of Equation 2.45 represents plastic work dissipation and cannot be negative (as all work dissipation is positive). Dividing Equation 2.45 through by  $p \cdot \Delta \varepsilon_q^p$  and rearranging yields the Cam-Clay flow rule, Equation 2.46.

$$\frac{\dot{W}}{v} = \frac{\dot{E}}{v} - \frac{\dot{U}}{v} = q \dot{\varepsilon}_q^p + p \dot{\varepsilon}_v^p = Mp \left| \dot{\varepsilon}_q^p \right| \quad (2.45)$$

Where,

$\frac{\dot{W}}{v}$  is the ‘plastic’ work (unrecoverable according to Cam-Clay) done per unit volume

$\frac{\dot{E}}{v}$  is the total work done per unit volume

$\frac{\dot{U}}{v}$  is the ‘elastic’ work (or recoverable) per unit volume

$$D^p = M - \eta \quad (2.46)$$

However, the Cam-Clay flow rule does not fit sand data as well as Nova’s rule in Equation 2.47. Nova (1982) derived his flow rule based on experimental observations.

$$D^p = \frac{M - \eta}{1 - N} \quad (2.47)$$

Upon substituting for  $D^p$  and  $\eta$  and rearranging,

$$q\dot{\epsilon}_q^p + p\dot{\epsilon}_v^p = Mp|\dot{\epsilon}_q^p| + Np\dot{\epsilon}_v^p \quad (2.48)$$

If soils were not to violate the first law of thermodynamics, then work done on the soil sample is either dissipated or contributes to a change in the internal energy of the sample. The two terms on the right hand side of Equation 2.48 represent plastic work done. The first term on the right hand side represents the dissipation mechanism as discussed earlier in this section. It is then reasonable to assume that the second term on the right hand side contributes to a change in internal energy. In other words it represents a stored energy. Jefferies (1997) calls it 'plastic' stored energy. It is not elastic as it is not reasonable to assume that plastic work done on the sample is transferred into stored elastic energy. It is stored energy, i.e. not dissipated, because the term can take negative sign.

Cam-Clay assumes that all plastic work dissipation is represented by the first term on the right hand side. Based on this assumption, any other term on the right hand side represents something other than dissipation of plastic work. Therefore, according to thermodynamics, it represents changed internal energy or stored 'plastic' energy.

The idea of a change in internal energy due to change in plastic strains was first proposed by Palmer (1967). Palmer's approach is illustrated in Figure 2.31.

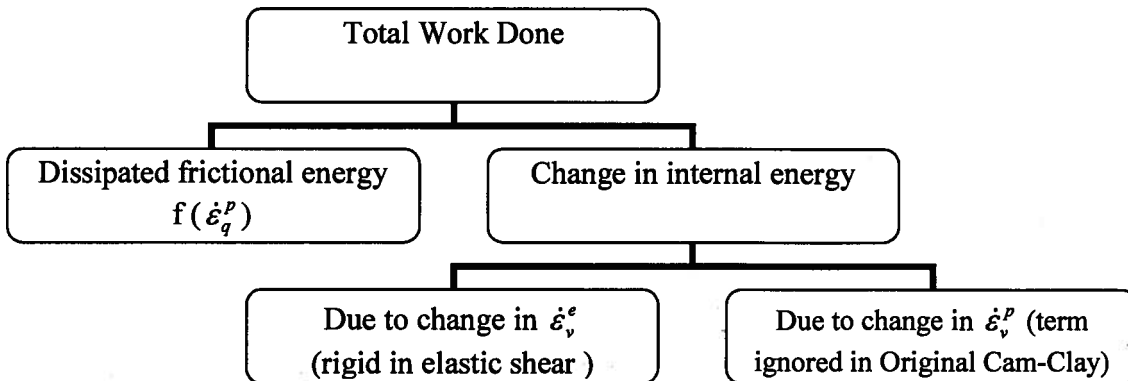


Figure 2.31. Energy balance as introduced by palmer (1967).

To justify this, Palmer (1967) considers a hypothetical experiment where the state of soil moves along the critical state line in the  $e-p'$  space. While moving along the CSL shear deformations -in this case all deformations are plastic as Palmer's model as well as Original Cam-Clay are rigid in elastic shear- resisted by friction are not expected to contribute to any change in volumetric strain and the Original Cam-Clay energy balance equation reduces to:

$$q \dot{\epsilon}_q^p = Mp |\dot{\epsilon}_q^p| \quad (2.49)$$

But because we are hypothetically moving on the CSL, and different pressures are associated with different critical void ratios, then there must be a change in volumetric strain. Most of this change is 'plastic' because the CSL is usually much steeper than the swelling lines. However, Equation 2.49 fails to predict this change. Therefore, another term should be added to represent changes in internal energy due to change in plastic volumetric strain. This term turns out to be the ' $N$ ' term on the right hand side of Equation 2.48.

Jefferies (1997) assumes that all the stored 'plastic' energy is recovered upon unloading. Solving Equation 2.48 for the case of unloading while changing the sign of the ' $N$ ' term, as it is energy recovered in unloading, gives the following:

$$q \dot{\epsilon}_q^p + p \dot{\epsilon}_v^p = -Mp \dot{\epsilon}_q^p - Np \dot{\epsilon}_v^p \quad (2.50)$$

Upon rearranging and substituting,

$$D^p = \frac{-M - \eta}{1 + N} \quad (2.51)$$

Equations 2.46, 2.47 and 2.51 are plotted in Figure 2.32. It will be shown later that triaxial laboratory data shows a different trend for stress-dilatancy in unloading from that represented by Equation 2.51.

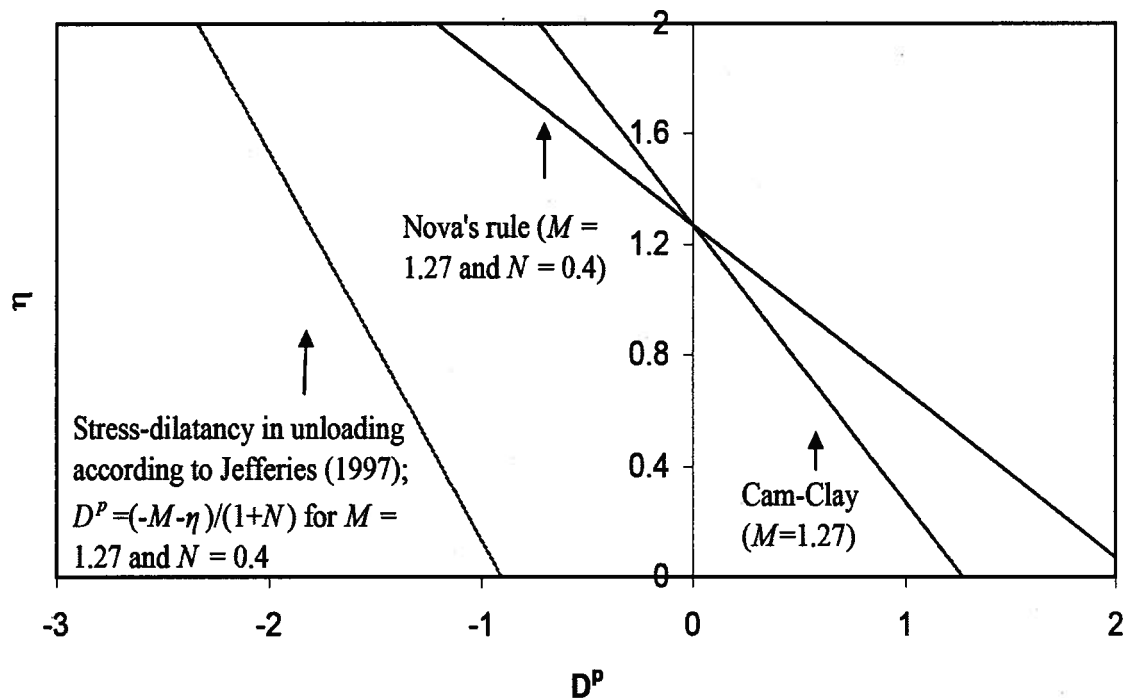


Figure 2.32. Stress-dilatancy for Cam-Clay loading, Nova loading, and Jefferies (1997) unloading.

Collins (2005) discusses a different conceptual model for yield in unloading from a thermo-mechanical viewpoint, taking into consideration differences between the micro scale where the particles interact, and the continuum scale where most soil constitutive models are defined. The model is summarized in Figure 2.33. The difference between Collins (2005) approach and that of Palmer (1967) and Jefferies (1997) is that the former assumes that stored elastic energy is the cause for yield in unloading while this is not the case for the latter. Collins model is illustrated in the following paragraph.

Pure hydrostatic loading on the continuum scale is assumed and following the usual convention the applied work may be separated into an elastic and plastic component. During loading part of the applied work is dissipated while the remainder is stored in terms of elastic compression of soil particles. In subsequent unloading, part of the stored elastic work is released causing dilation while the other part can only be released if

associated with particle rearrangement. Particle rearrangement is not elastic and hence plasticity occurs during unloading. Hence it is implied that all plastic strains during unloading are dilative. It is assumed that most of the total shear energy is dissipated as plastic work.

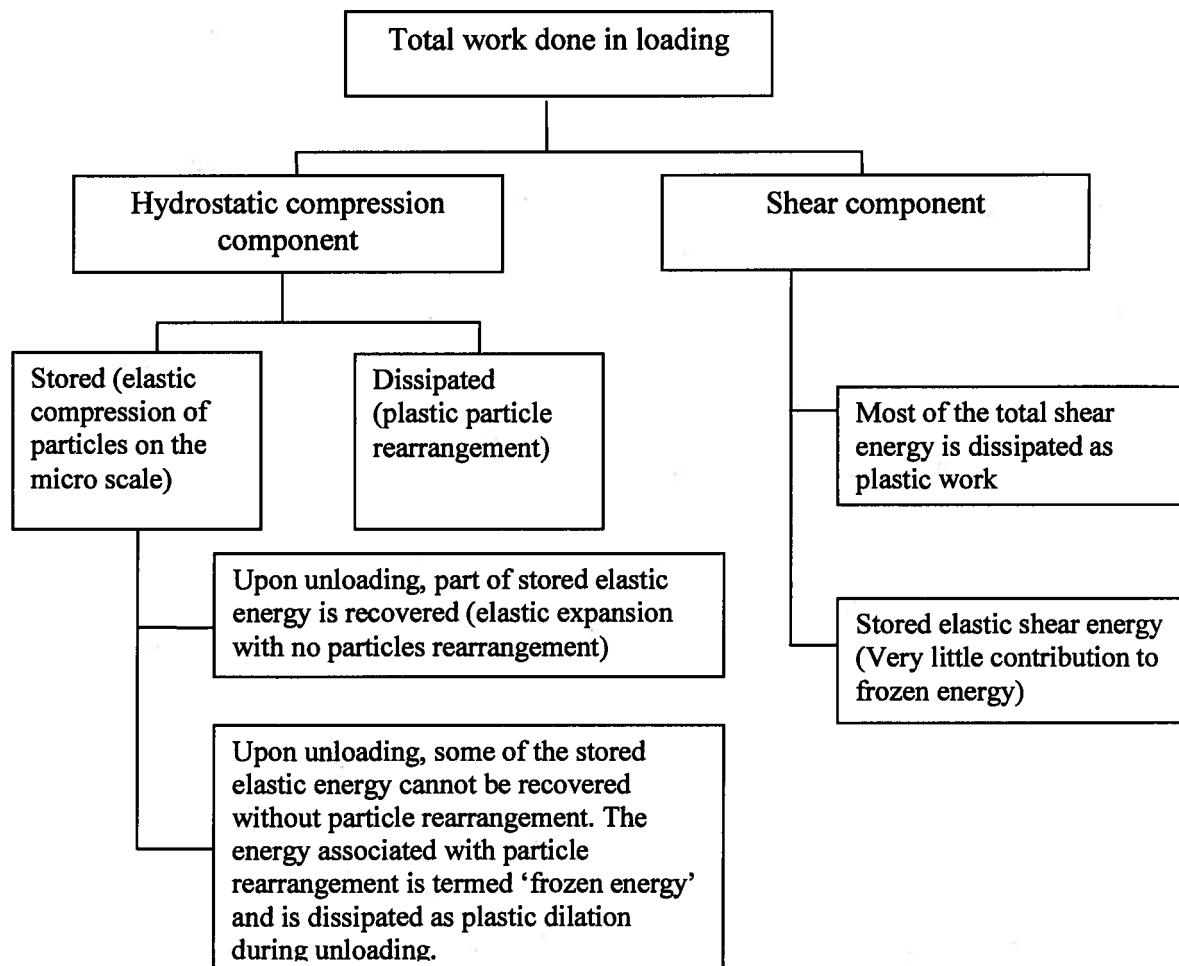


Figure 2.33. Schematic representation of work storage and dissipation according to Collins (2005).



### 2.6.3. Unloading in NorSand

Jefferies (1997) presented a framework for the NorSand model in unloading and subsequent reloading. Because this model is extended as part of the current work, a more detailed discussion of the Jefferies (1997) unloading model is provided in this section. The NorSand model was described in Section 2.5 with emphasis on monotonic loading conditions. This section discusses in more details the unload-reload version of NorSand.

In unloading, soil yields at the inner cap. The inner yield surface (or inner cap) is the vertical part of the yield surface shown in Figure 2.28. Its location at the outer yield surface is chosen to fit within the framework of the NorSand model in loading and is a vertical straight line for simplicity. This internal cap scales with the outer yield surface and is located at:

$$p_{cap} = \frac{P_i}{e^{(-D_{min}/M_i)}} \quad (2.52)$$

The NorSand flow rule in unloading was derived earlier in Section 2.6.2 as Equation 2.51. Jefferies (1997) introduced a rule to govern the movement of the inner cap, i.e. a hardening rule, as:

$$\dot{\epsilon}_v^p = -\frac{1}{H_u} \frac{\dot{p}'}{p'} \ln\left(\frac{p'_{fy}}{p'}\right) \quad (2.53)$$

Where,

$H_u$  is the hardening (softening) modulus in unloading

$p'_{fy}$  is the mean effective stress at first yield in unloading (i.e. the mean stress of the cap when first intersected)

So far the model definition is completed. The rest of this section presents two examples of stress paths (Figure 2.34 and Figure 2.35) to illustrate the model behaviour. Figure 2.34 shows a stress-strain curve with a single unload-reload loop and the yield surfaces corresponding to the load-unload-reload phases. The points of interest are annotated on the stress-strain curve, i.e. the plot at the left top side, and on the yield surfaces corresponding to loading, unloading and reloading, i.e. plots on the right top, left bottom, right bottom sides respectively. The darker lines represent the surface where current yield is occurring. The thicker lines represent the stress path. The yield surface hardens with loading until the internal cap is reached as in Figure 2.34, i.e. path 1-2. Point 2 in the figure represents peak strength and is associated with the maximum size of the yield surface. With continued shearing further strain causes softening and the stress path softens to reach point 3.

Another stress path is illustrated in Figure 2.35 which has a similar arrangement as for Figure 2.34. Unloading in this case occurs from a point before reaching the internal cap that represents peak conditions. Loading causes hardening of the yield surface along path 1-2. The internal cap scales with the yield surface.

In unloading, there are three possible cases for the stress point to move on or inside the yield surface:

**Case 1:**

The stress point touches the internal cap in loading, unloading then cause plastic softening of the yield surface. This is illustrated in Figure 2.34 where yielding occurs as the stress point moves on the internal cap from point 3 to point 4. As the cap moves with the stress point, the outer yield surface also softens.

**Case 2:**

The stress point does not touch the internal cap in loading, as shown in Figure 2.35. Upon unloading, the yield surface does not move until the stress point touches the internal cap. Before this point, unloading is purely elastic (Figure

2.35). After the stress point touches the cap yielding starts on the cap and the yield surfaces soften until the stress point reaches location 3.

Case 3:

The third case occurs for unloading early in the stress path. Under these circumstances the stress point does not touch the cap during unloading and the whole unloading phase remains elastic.

Under all situations reloading is elastic as long as the stress point is inside the outer yield surface (see Figure 2.34 and Figure 2.35). Once the stress point touches the outer yield surface, plastic reloading continues as in the virgin loading phase.

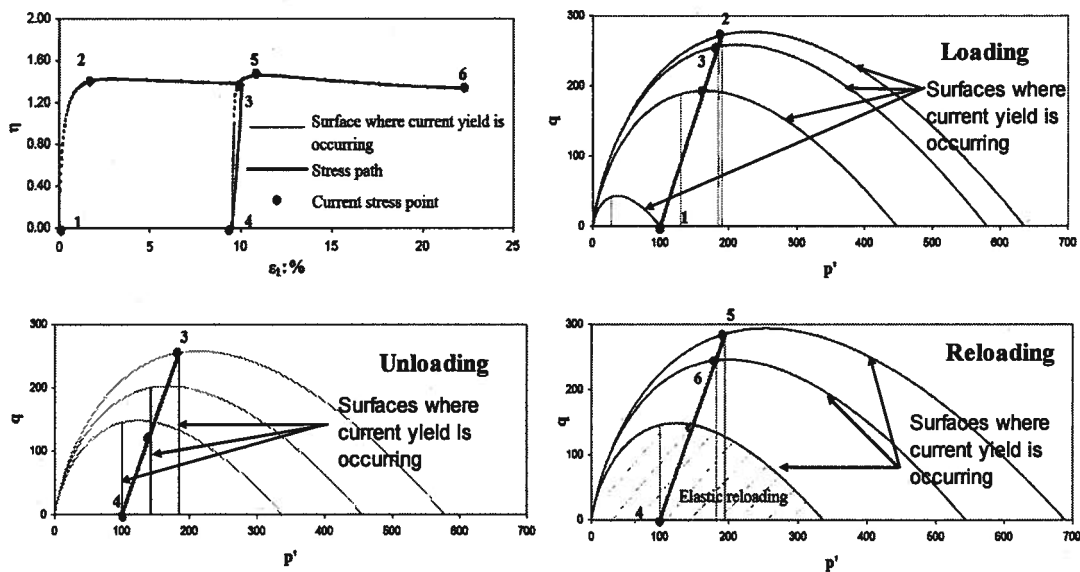


Figure 2.34. Movement of yield surface in NorSand: Case of unloading from a point on the internal cap.

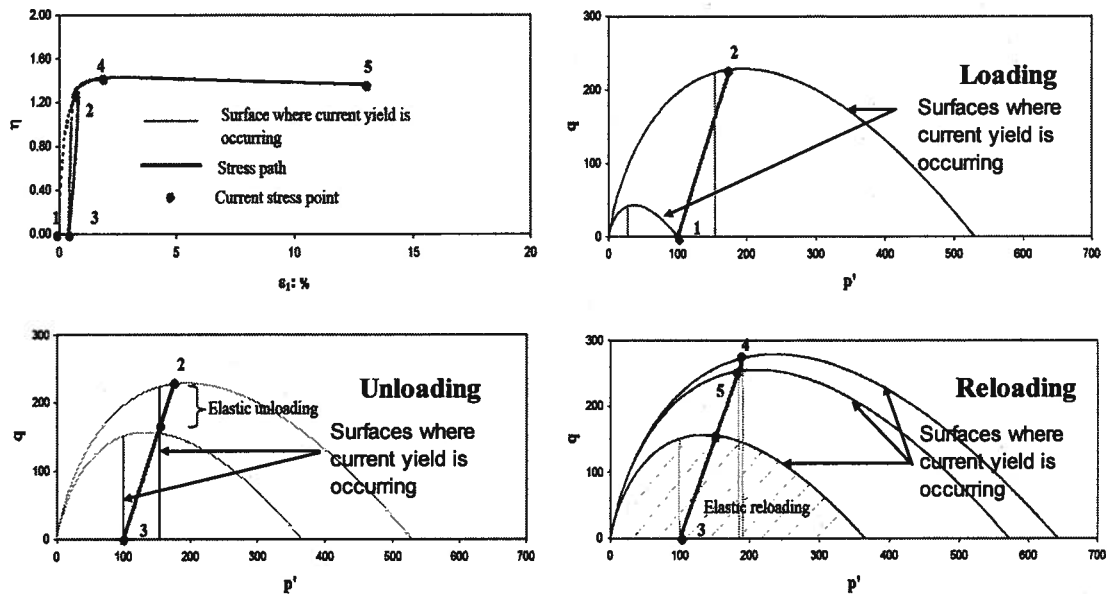


Figure 2.35 Movement of yield surface in NorSand: Case of unloading from a point before reaching the internal cap.

## 2.6.4. Summary

It can be seen from this selective review of soil behaviour in unloading that soil behaviour in unloading is still not well understood. There is no agreement on the cause of yield in unloading, for example the Jefferies model implies that it is mainly caused by plastic shear deformation in loading while Collins attributes yield in unloading to rearrangement caused by elastic dilation of particles associated with reduction in mean effective stress. Clearly, this topic needs more investigation as it is important for earthquake engineering. A practical model that accounts for yield in unloading is required. Understanding stress-dilatancy in unloading is one of the requirements of such a model and is discussed in the following chapter.

### **3. DILATANCY IN UNLOAD-RELOAD LOOPS: A THEORETICAL INVESTIGATION**

Dilatancy in loading has been investigated by many researchers as discussed in Section 2.4. Most elasto-plastic constitutive models have yield surfaces that were developed for stress paths involving increasing shear; a reduction of shear stress (i.e. unloading) within that surface is considered elastic. But contraction has been observed during unloading for the standard triaxial stress path. Standard elasticity would predict expansion during unloading. Hence, these observations suggest that the soil is yielding during unloading. Constitutive models that incorporate yield in unloading are rare. The topic is not well covered and is controversial as shown in Section 2.6. The objective of this chapter is to develop theoretical understanding of dilatancy in unloading as well as in subsequent reloading phases. The investigation is done at the micro-mechanical level.

#### **3.1. Micro-Mechanical perspective for dilatancy in unloading**

The standard elasto-plastic approach assumes that soil is a continuum. However, in reality, soil is composed of discrete particles and plasticity is an abstraction used to explain what really happens between the grains. It is of interest to develop an understanding of why soil contracts in unloading from a microscopic point of view.

Rowe (1962) derived an expression for dilatancy in loading based on frictional forces between rigid cylindrical rods (see Section 2.4). Rowe assumed identical rods that are rigid and have a circular cross-section. The forces at the contacts are assumed purely frictional and the initial packing does not change during shearing. Packing represents the pattern at which particles are arranged relative to each other. For example, Figure 3.1 shows one possible packing for the rods but three different particle assemblies. The three

different particle assemblies in the middle of Figures 3.1 a,b, and c have the same packing. The relative arrangement of particles in the three assemblies does not change, i.e. if particle 'x' happens to be to the right of particle 'y' in the first assembly, then it stays to the right of particle 'y' in the other two assemblies.

A change in the volume of the packing can be explained by taking four particles aside. In loading, as illustrated using the four particles on the left hand side of Figure 3.1, if the upper grain is pushed vertically downward the two side grains will move outwards. This will be associated with an increase in volume if the angle between the tangent to grains interface and the vertical direction,  $\beta > 45^\circ$  (see Figure 3.1a). However, for  $\beta < 45^\circ$  when the upper particle is pushed down the assembly decreases in volume (see Figure 3.1c).

By computing the work done by the major principal stress on the assembly to the work done by the assembly on the minor principal stress for rigid rods, Rowe derived the following equation (the complete derivation is given in Section 2.4):

$$\frac{\sigma'_1 \dot{\epsilon}_1}{\sigma'_2 \dot{\epsilon}_2} = \frac{\sigma'_1}{\sigma'_2 (1 + \dot{\epsilon}_v / \dot{\epsilon}_1)} = \frac{\tan(\phi_\mu + \beta)}{\tan \beta} \quad (3.1)$$

Where,

$\sigma'_1$  is the major principal effective stress

$\sigma'_2$  is the minor principal effective stress

$\dot{\epsilon}_1$  is the rate of change in major principal strain

$\dot{\epsilon}_2$  is the rate of change in minor principal strain

$\dot{\epsilon}_v$  is the rate of unit volume change

$\phi_\mu$  is grain to grain friction angle

$\beta$  is the angle between the tangent to grains interface and the vertical direction

And for the packing in Figure 3.1,

$$\frac{\sigma_1}{\sigma_2} = \tan(\beta) \tan(\phi_\mu + \beta) \quad (3.2)$$

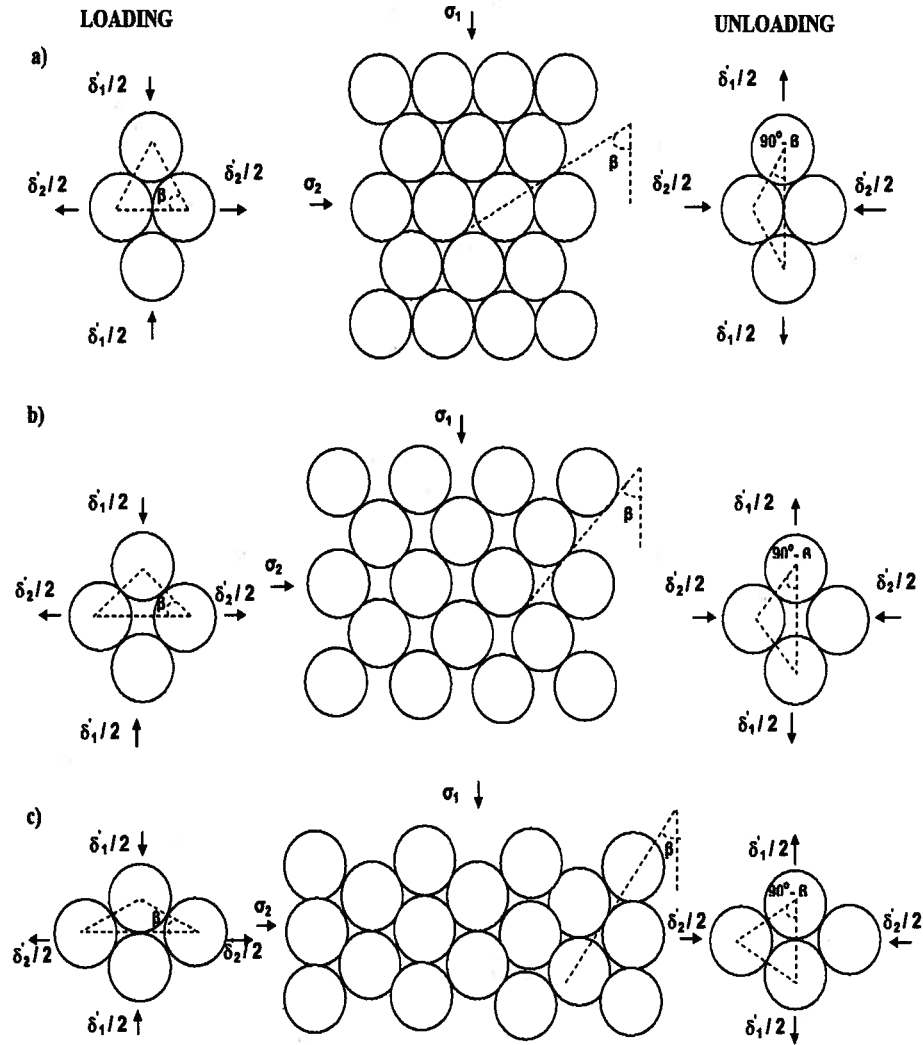


Figure 3.1 Micro-mechanical representation of dilatancy for a uniform packing of rigid rods during both loading and unloading a) Minimum void ratio for  $\beta = 60^\circ$  b) Maximum void ratio for  $\beta = 45^\circ$  c) Minimum void ratio for  $\beta = 30^\circ$

Equation 3.1 is valid for different packings of rigid rods but the stress ratio in Equation 3.2 depends on the packing type (i.e. the pattern at which particles are arranged relative to each other). For the packing in Figure 3.1, Rowe showed that stresses and strains in

direction 1 over those in direction 2 can be expressed as in Equations 3.2 and 3.3, respectively.

$$\frac{\dot{\varepsilon}_1}{\dot{\varepsilon}_2} = \frac{1}{\tan^2 \beta} \quad (3.3)$$

Multiplying Equation 3.2 by 3.3 yields equation 3.1. Note that Equations 3.2 and 3.3 are identical to Equations 2.20 and 2.21 for  $\alpha = \beta$ , which is the case for this packing.

For the packing on the right hand side of Figure 3.2 Li and Dafalias (2000) showed, following a similar derivation as for Equations 2.20 and 2.21 in Section 2.4, that Equations 3.4 and 3.5 below should be used instead of equations 3.2 and 3.3, respectively. The reason for having different equations is that the volume of the basic unit defined by the dashed rectangle in Figure 3.2 for each of the packings is different. The complete derivation is given in Li and Dafalias (2000).

$$\frac{\sigma_1'}{\sigma_2'} = \tan(\phi_\mu + \beta) \frac{2 \sin \beta}{1 + 2 \cos \beta} \quad (3.4)$$

$$\frac{\dot{\varepsilon}_1}{\dot{\varepsilon}_2} = \frac{(1 + 2 \cos \beta) \cos \beta}{2 \sin^2 \beta} \quad (3.5)$$

Note that multiplying Equation 3.4 by 3.5 also yields Equation 3.1. Therefore, Equation 3.1 is valid for different packings, while the ratio between stress in direction 1 to that in direction 2 is packing specific. Therefore, if the term  $\dot{\varepsilon}_v / \dot{\varepsilon}_1$  in Equation 3.1 is assumed to represent dilatancy, then there are different stress-dilatancy relations for different packings.



Unloading can be explained in the physical sense by reference to the illustrations on the right hand side of Figure 3.1. If the side grains are pushed inwards, the upper and lower grains will move outwards. This is associated with decrease of volume if  $\beta > 45^\circ$ .

As discussed above, Equation 3.1 is derived for loading based on an energy balance between the ratio of work done by a strain increment in direction 1 on the assembly to that done by the assembly in direction 2. Part of work done in the form of a strain increment on direction 1 is dissipated in the assembly by friction while the remaining work is transferred to direction 2.

Assuming that soil is an isotropic material and the packing does not change during the loading and unloading phases, work balance in unloading can be thought of as the ratio between the work done by a strain increment in direction 2 on the assembly to that done by the assembly on direction 1. In other words, the proposed expression for dilatancy in unloading based on grain to grain friction is the same as the usual one of Rowe (1962) but with the assembly rotated by  $90^\circ$ , i.e.:

$$\frac{\sigma_1' \dot{\varepsilon}_1}{\sigma_2' \dot{\varepsilon}_2} = \frac{\sigma_1'}{\sigma_2' (1 + \dot{\varepsilon}_v / \dot{\varepsilon}_1)} = \frac{\tan(\phi_\mu + 90 - \beta)}{\tan(90 - \beta)} \quad (3.6)$$

$$\frac{\sigma_1'}{\sigma_2'} = \tan(90 - \beta) \tan(\phi_\mu + 90 - \beta) \quad (3.7)$$

Figure 3.3a plots the proposed relation for dilatancy for unloading, i.e. Equations 3.6 and 3.7, as compared to that for loading.  $\beta$  for unloading is equal to  $90^\circ - \beta$  of that for loading, as a consequence of rotating the assembly (Figure 3.3b). Note that Equation 3.7 is only valid for the packing in Figure 3.1.

Erksak 330/0.7 sand is a quartz sand with an average grain size of  $330\mu\text{m}$ . The grain to grain friction angle,  $\phi_\mu$ , can be estimated for quartz as  $25^\circ$  (Rowe, 1962). Figure 3.3a

shows a comparison between the dilatancies for the loading phase and first unloading for a drained triaxial test on Erksak sand ( $p' = 100$  kPa and  $e_o = 0.653$ ) to the theoretical expressions based on grain to grain friction for  $\phi_\mu = 25^\circ$ . The fit is a very good one for both loading and unloading considering the previously stated assumptions involved in deriving the theoretical expression. However, it is not as good for the reloading phase and the second unloading loop (not shown in the figure). This is to be expected as soil fabric changes with continued shearing, while the theoretical expression is only valid for the packing in Figure 3.1.

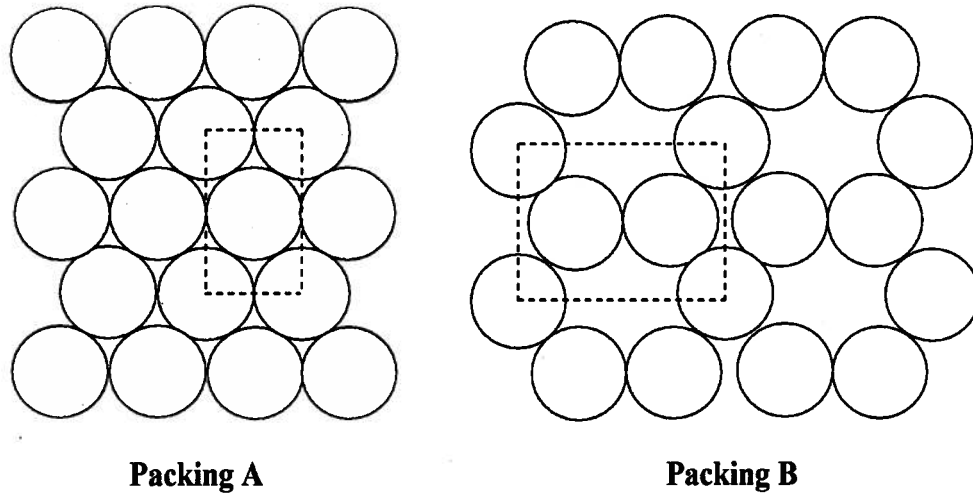


Figure 3.2. Two different uniform assemblies of rigid rods; the dashed rectangle represents the basic unit volume (reproduced after Li and Dafalias, 2000).

### 3.2. Micro-Mechanical perspective for dilatancy in reloading

The stress-dilatancy relation is expected to change for different reloading phases. The reason is due to particle arrangement (i.e. fabric) changes during shearing. Let us assume that we have two different uniform packings of rigid cylindrical rods similar to those in Figure 3.2. Packing B has a higher void ratio than packing A. For the sake of the argument, it is assumed that during an unload-reload phase the arrangement of the rods changes from a packing similar to B to another one similar to A. This change can be

thought of as being equivalent to change in fabric in real soils. As discussed in Section 3.1, the stress-dilatancy relation is different for the two packings. Equation 3.1 is valid for the two packings. However, the stress ratio (i.e.  $\sigma'_1 / \sigma'_2$ ) is different for packing A and B as in Equations 3.2 and 3.4, respectively. The stress ratio in unloading for packing A is as in Equation 3.7. Similarly, the equation for stress ratio in unloading for packing B is:

$$\frac{\sigma'_1}{\sigma'_2} = \tan(\phi_\mu + 90 - \beta) \frac{2 \sin(90 - \beta)}{1 + 2 \sin(90 - \beta)} \quad (3.8)$$

Equations 3.1, 3.2, and 3.4 were used to plot the loading curves in Figure 3.4. Equations 3.6, 3.7 and 3.8 were used to plot the unloading curves. The predicted stress ratio for a given dilatancy is lower for the denser packing as expected. The trend from triaxial laboratory data agrees with the trends in Figure 3.4 as will be shown in the next chapter.

Rowe (1962) recognized that particle relocation occurs with shearing, and as a result the value of  $\beta$  changes in a non-uniform manner because real soil particles are not of the same size and shape. He assumed that this relocation would happen in a way such that changes in the values of  $\beta$  would keep the rate of internal work done to a minimum. This assumption changes Equation 3.1 to Equation 3.9 which is independent of  $\beta$  and therefore independent of packing and density (the complete version of Rowe's derivation is given in Section 2.4). The assumption of minimum internal work predicts a single stress-dilatancy relation to be valid for all packings. Li and Dafalias (2000) disagree with Rowe's use of the assumption of minimum internal work and therefore they predict that the stress-dilatancy relation is different for different packings. Rowe's stress-dilatancy, Equation 3.9, is an idealization that is applicable for a random mass of irregular soil particles. It contradicts the exact solution, i.e. Equations 3.1-3.8, that clearly shows that stress-dilatancy is dependent on packing.

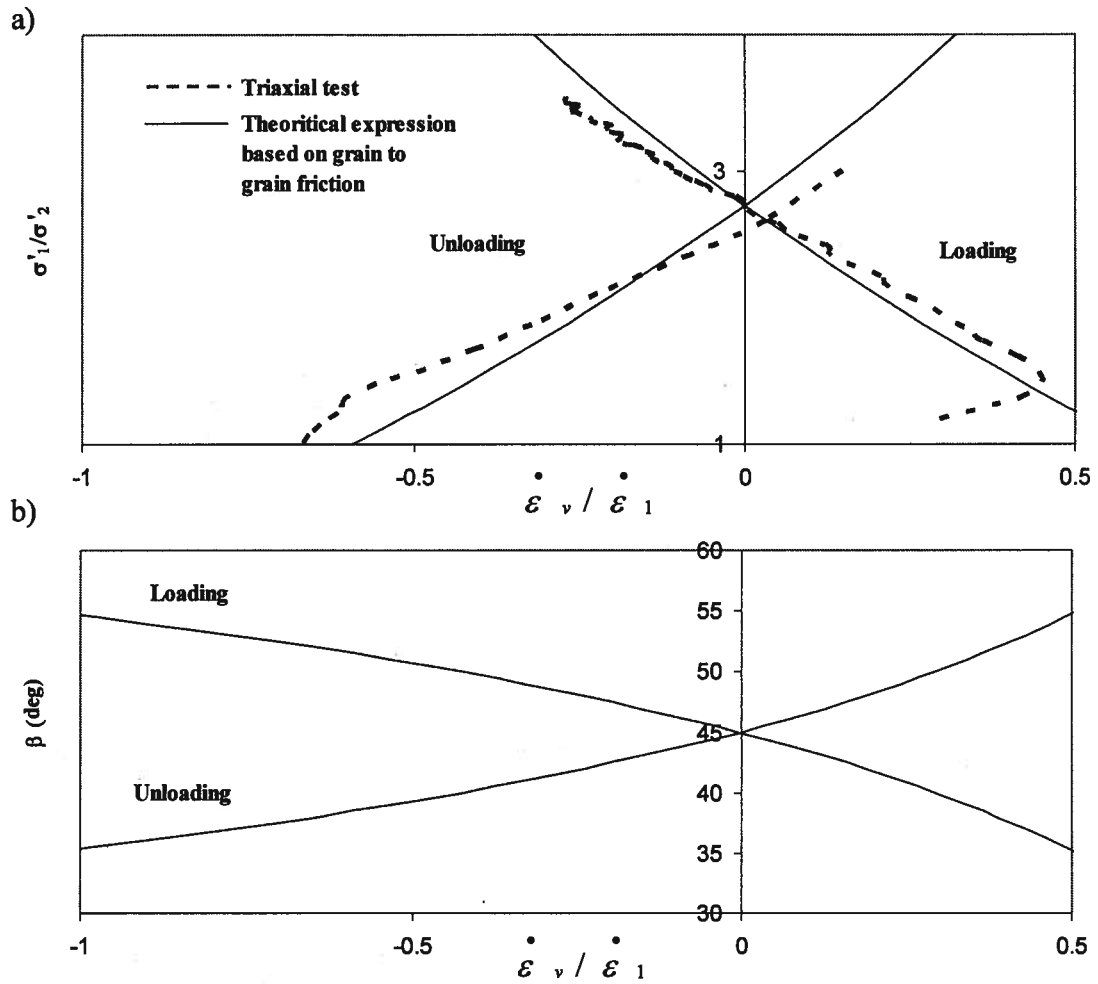


Figure 3.3 Theoretical expression based on grain to grain friction ( $\phi_\mu=25^\circ$ ) for the uniform packing in Figure 3.1 a) compared with a drained triaxial test on Erksak 330/0.7 ( $p'=100$  kPa and  $e_o=0.653$ ) in stress ratio vs. dilatancy space, b) Angle between the vertical direction and the tangent at the interface between grains.

$$\frac{\sigma'_1}{\sigma'_2(1+d\dot{V}/V\dot{\epsilon}_1)} = \tan^2(45 + 0.5\phi_\mu) \quad (3.9)$$

Overall, this section showed that the stress-dilatancy relation is dependent on packing. For example, packings A and B in Figure 3.2 have different stress-dilatancy relations as

shown in Figure 3.4. As the packing is expected to change in a reloading phase compared to that for first loading, a change in stress-dilatancy is expected in reloading.

### 3.3. Summary

The study of two packings of rigid rods showed that yield in unloading occurs. In this chapter, a stress-dilatancy relation in unloading was derived based on a micro-mechanical approach. The derived relation turns out to be identical to Rowe's stress-dilatancy in loading while rotating the packing of rods by  $90^\circ$ . The study of deformation characteristics in reloading using a micromechanical approach showed that stress-dilatancy changes in reloading compared to first loading. Reloading is associated with a more dilative response than first loading.

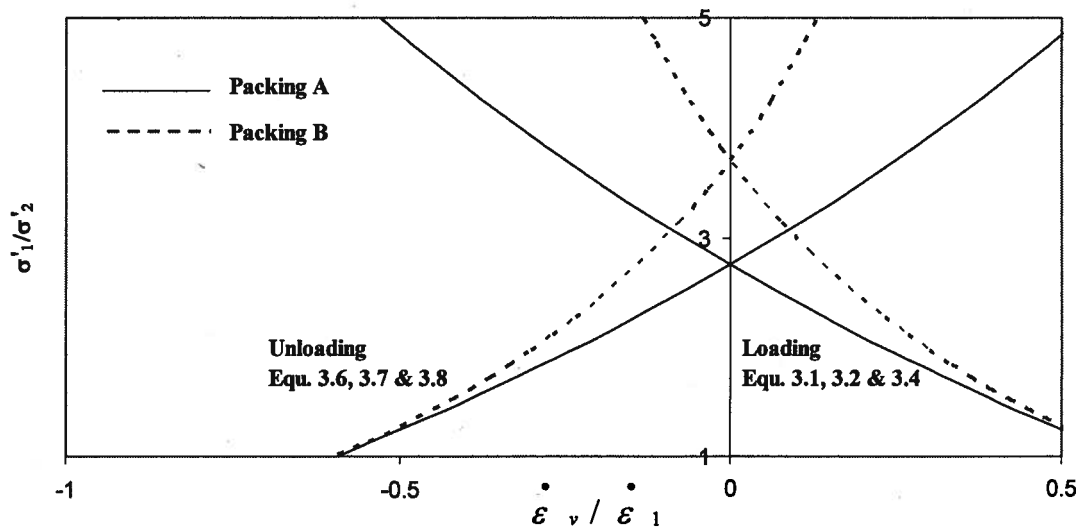


Figure 3.4. Rowe's stress-dilatancy relation based on grain to grain friction for the two packings in Figure 3.2

## **4. DILATANCY IN UNLOAD-RELOAD LOOPS: AN EXPERIMENTAL INVESTIGATION**

The previous chapter addressed dilatancy in unloading and reloading from a micro-mechanical point of view. In order to compare the trends predicted from the micro-mechanical approach to the trends observed in real soils, and to apply these observed trends to a general continuum model for future application to liquefaction modelling, this chapter investigates observed stress-dilatancy for two sands in drained triaxial tests that include unloading and reloading cycles.

### **4.1. Sands Tested**

Erksak sand (ES) and Fraser River sand (FRS) were used in this study. ES was chosen because drained triaxial tests with load-unload-reload cycles were available (Golder Associates, 1987; [www.golder.com/liq](http://www.golder.com/liq)). Note that the focus of this chapter is to investigate stress-dilatancy and therefore drained tests were used. FRS was chosen because of the availability of new monotonic triaxial tests and drained load-unload-reload triaxial tests undertaken by Golder Associates.

#### **4.1.1. Erksak Sand**

Erksak sand, a sand that was used in the construction of the Molikpak core in the Canadian Arctic, is a uniformly graded medium-grain sub-rounded sand, mainly composed of Quartz and Feldspar. The gradation of Erksak sand used, Erksak 330/0.7, had an average particles size of 330  $\mu\text{m}$  and fines content of 0.7%. The Index properties are presented in Table 4.1. Its specific gravity is 2.66. The index density measures,  $e_{\min}$

and  $e_{max}$ , according to ASTM test methods D4253-00 and D4254-00 are 0.525 and 0.775, respectively (ASTM 2006a; ASTM 2006b; after Sasitharan, 1989).

#### 4.1.2. Fraser River Sand

Fraser River sand originates from the alluvial deposits of Fraser River located in British Columbia, Canada. It is a uniformly graded medium-grain sand with angular to sub-rounded particles. It is mainly composed of Quartz, Feldspar and unaltered rock fragments with an average particles size of 260  $\mu m$  (see Table 4.1). Its specific gravity,  $e_{min}$ , and  $e_{max}$  are 2.75, 0.62, and 0.94, respectively.

Table 4.1: Index properties of Fraser River and Erksak sands

Sand/Source Property	Fraser River sand, Sriskandakumar (2004) and Chillariage et. al. (1997)	Erksak sand, Been et al. (1991) and Sasitharan (1989)
Mineralogy	40% Quartz, 11% feldspar, 45% unaltered rock fragments and 4% of other minerals	73% Quartz, 22% Feldspar, and 5% other minerals
Median grain size $D_{50}$ : $\mu m$	260	330
Effective grain size $D_{10}$ : $\mu m$	170	190
Uniformity coefficient	1.6	1.8
Percentage passing no. 200 sieve	0	0.7
Specific gravity of particle	2.75	2.66
Grain description	Angular to sub-rounded	Sub-rounded
Maximum voids ratio $e_{max}$	0.94	0.775
Minimum voids ratio $e_{min}$	0.62	0.527

## **4.2. Testing program**

All tests reported in this section are conventional triaxial compression tests (i.e. confining stress is kept constant during the shearing phase). The testing procedure and sample preparation methods are described in Appendix E.

The full Erksak testing program included 29 drained and 39 undrained triaxial tests. As this investigation focuses on volumetric changes drained tests were of primary interest, although five of the undrained tests on ES were used to better define the location of the critical state line (see Chapter 6). Of the available drained triaxial tests, the ten drained tests that followed a conventional triaxial stress path, and also contained load-unload-reload cycles, were used for this work. The data for all of the Erksak tests are available for download from the web site: [www.golder.com/liq](http://www.golder.com/liq).

The FRS testing program included 6 drained and 2 undrained triaxial tests. Six monotonic tests on FRS, 4 drained and 2 undrained, are used for the monotonic calibration of NorSand to FRS (see Chapter 6). The two drained unload-reload tests on FRS are used to validate the predictions of the calibrated unload-reload model in Chapter 7.

### **4.2.1. Erksak Sand Testing Program**

The ES load-unload-reload tests are summarized in Table 4.2. The ten tests cover a wide range of mean effective stresses (100-800 kPa). The range of void ratios is 0.603-0.723. All of the samples were water pluviated except for ES\_CID\_868 that was moist tamped. These ten tests were performed under drained conditions to enable review of the volumetric change characteristics of sand. The number of unload-reload loops in the tests varies between one and three. In some tests the unload-reload loops occur before reaching peak strength, while other unload-reload loops are post-peak. This allows the



investigation of stress-dilatancy during unloading and reloading at different strain and stress levels.

The ES undrained monotonic triaxial testing used to determine the critical state line is summarized in Table 4.3. All of the moist tamped tests are on loose samples with void ratios close to  $e_{\max}$ . Undrained conditions and loose samples were chosen so that the samples can reach critical state within the limitation of the apparatus.

Table 4.2: Drained triaxial compression tests on Erksak Sand with load-unload-reload cycles (data from [www.golder.com/liq](http://www.golder.com/liq))

Test No.	P' (kPa)	$e_o$	Preparation method <sup>1</sup>	Number of U-R loops <sup>2</sup>
ES CID 860	100	0.672	WP	1
ES CID 861	100	0.645	WP	2
ES CID 862	100	0.645	WP	3
ES CID 866	400	0.698	WP	2
ES CID 867	400	0.680	WP	3
ES CID 868	400	0.723	MT	2
ES CID 870	800	0.653	WP	1
ES CID 871	800	0.637	WP	2
ES CID 872	800	0.652	WP	3
ES CID 873	100	0.603	WP	3

<sup>1</sup> WP stands for water pluviated and MT stands for moist tamped.

<sup>2</sup> U-R stands for unload-reload

Table 4.3: Undrained monotonic triaxial compression tests on Erksak sand (data from Been et. al., 1991)

Test No.	p' (kPa)	$e_o$	Preparation method <sup>1</sup>
ES L 601	499	0.754	MT
ES L 604	699	0.768	MT
ES L 605	500	0.766	MT
ES L 606	701	0.759	MT
ES L 607	701	0.748	MT

<sup>1</sup> MT stands for moist tamped.

#### 4.2.2. Fraser River Sand

Table 4.4 presents the test conditions of two load-unload-reload tests undertaken recently by Golder Associates on FRS. Both samples were moist tamped. The confining pressure for each test is similar at 190 kPa and 198 kPa, but the corresponding void ratios differ, being 0.89 and 0.72 respectively. Both tests had more unload-reload loops than the ES tests (four and five loops, while the maximum number of loops for ES was three).

Four drained and two undrained monotonic triaxial compression tests on moist tamped samples were carried out (see Table 4.5 for a summary of the test details). The undrained tests were used to obtain critical state parameters, while the drained tests were used for the FRS monotonic calibration to the NorSand model. The consolidation stresses ranged from 50 kPa to 515 kPa and  $e_o$  ranged from 0.63 to 0.91. .

Table 4.4: Drained triaxial compression tests with load-unload-reload cycles on Fraser River sand (data provided by Golder Associates)

Test No.	$p'$ (kPa)	$e_o$	Preparation method <sup>1</sup>	Number of U/R loops
FR_CID_01	190	0.89	MT	5
FR_CID_02	198	0.72	MT	4

<sup>1</sup> MT stands for moist tamped.

<sup>2</sup> U-R stands for unload-reload.

Table 4.5. Monotonic triaxial compression tests on Fraser River sand (data provided by Golder Associates)

Test No.	P' (kPa)	$e_o$	Test type	Preparation method <sup>1</sup>
FR CID 03	114	0.67	Drained	MT
FR CID 04	410	0.63	Drained	MT
FR CID 05	515	0.69	Drained	MT
FR CID 06	50	0.75	Drained	MT
FR CU 01	388	0.91	Undrained	MT
FR CU 02	196	0.82	Undrained	MT

<sup>1</sup> MT stands for moist tamped.

### 4.3. Experimental observations

The main focus of the review of experimental results was stress-dilatancy in unloading and subsequent reloading. To the knowledge of the author, an experimental review to specifically investigate stress-dilatancy trends in unloading has not been done before. The issue of concern is what factors determine whether soil is likely to contract or dilate in unloading and the amount of those volumetric changes. The effect of the loops on peak strength and volumetric changes in reloading is also investigated.

In the following discussion “U” refers to an unloading loop and “L” refers to a loading or reloading loop. The number following the symbol denotes the order of a particular loop from the beginning of the test.

A typical test on Erksak Sand is plotted in Figure 4.1. The strength of the sand, shown in Figure 4.1a, does not seem to be highly affected by the unload-reload loops. The data shows that loop U1 does not introduce a local peak in the stress-strain curve. However, loops U2 and U3 show small peaks slightly affecting the stress-strain curve. Loop U1 occurs before the image state which marks the boundary between contractive and dilative behaviour as annotated in Figure 4.1b. Loop U1 is not followed by a small peak and the stress strain curve seems to continue as if the unload-reload loop did not exist. However, loops U2 and U3, post-image loops, are followed by small peaks. The peaks on reloading

appear larger in Figure 4.2 which plots shear stress vs. axial strain (rather than the stress ratio vs. axial strain plotted in Figure 4.1a). The other tests on Erksak sand (see Appendix B) and Fraser River sand (Figure 4.3) demonstrate similar behaviour.

Conversely, volumetric strains are dramatically influenced by the unload-reload loops. Both the absolute values and the rates of change are affected (Figure 4.1b). Unloading occurs starting from pre-image conditions for U1. Note that volumetric changes associated with unloading are very small and are initially contractive followed by a small dilative phase (see Figure 4.4 for a zoom on loop 1). However, for U2 and U3, volumetric changes associated with unloading are significant. They are dominantly contractive (see Figure 4.4 for a zoom on loop 2). Note that unloading for those two loops starts from post-image conditions.

Table 4.6 summarizes the direction of volumetric changes in unloading for the load-unload-reload tests on ES. The information provided includes the stress ratio and axial strain at image stage. For each unload-reload (U-R) loop the stress ratio at which unloading starts is given, together with the axial strain, whether the loop starts pre or post image, and whether the volumetric strains are dilative or contractive. It can be observed that whenever unloading happens from post-image conditions, volumetric strains are either totally contractive or dominated by contraction. Conversely, if unloading occurs from pre-image conditions, volumetric strains are either totally dilative or dominated by dilation.

Table 4.6. Direction of volumetric changes in unloading for the load-unload-reload tests on ES

Test	U-R loop <sup>1</sup>	Stress ratio	Axial Strain (%)	Pre/Post image	Dilative/Contractive during unloading
ES_CID_860	Image	1.114	0.402	At	-
	1	1.419	10.073	Post	Con.
ES_CID_861	Image	1.098	0.544	At	-
	1	1.362	1.778	Post	Mostly con.
	2	1.484	10.014	Post	Con.

Test	U-R loop <sup>1</sup>	Stress ratio	Axial Strain (%)	Pre/Post image	Dilative/Contractive during unloading
ES_CID_862	Image	1.163	0.667	At	-
	1	0.353	0.9	Pre	Dil.
	2	1.377	1.768	Post	Mostly con.
	3	1.481	10.122	Post	Con.
ES_CID_866	Image	1.169	2.644	At	-
	1	1.265	4.501	Post	Mostly con.
	2	1.359	10.064	Post	Mostly con.
ES_CID_867	Image	1.107	1.082	At	-
	1	1.102	1.033	Pre	Mostly dil.
	2	1.338	4.051	Post	Mostly con.
	3	1.393	10.101	Post	Con.
ES_CID_868	Image	1.209	3.68	At	-
	1	1.212	4.047	Post	Mostly con.
	2	1.269	10.146	Post	Con.
ES_CID_870	Image	1.177	1.807	At	-
	1	1.352	10.056	Post	Mostly con.
ES_CID_871	Image	1.16	1.84	At	-
	1	1.308	4.035	Post	Mostly con.
	2	1.366	10.108	Post	Mostly con.
ES_CID_872	Image	1.209	1.814	At	-
	1	1	1.022	Pre	Dil.
	2	1.348	4.018	Post	Mostly con.
	3	1.405	10.107	Post	Con.
ES_CID_873	Image	1.194	0.319	At	-
	1	1.079	0.234	Pre	Dil.
	2	1.513	1.531	Post	Mostly con.
	3	1.5	10.073	Post	Con.

<sup>1</sup> Image indicates the stress ratio at image (image marks the boundary between contractive and dilative behaviour in loading)

Figure 4.1c presents the data from the same example ES test used previously, test ES\_CID\_867, in stress-dilatancy space. The following equation was used for calculating dilatancy from laboratory data:

$$D_n = \frac{\varepsilon_{v(n+1)} - \varepsilon_{v(n-1)}}{\varepsilon_{q(n+1)} - \varepsilon_{q(n-1)}} \quad (4.1)$$

where  $n$  denotes the current step.

In the case of unloading, positive dilatancy means volume increase while negative dilatancy indicates volume decrease. For unload phases U2 and U3 in Figure 4.1c, the sample contracts in unloading except for one point in U2. Unloading for those two phases starts from post-image stress ratios. Conversely, for U1 where the sample is unloaded from a pre-image stress ratio, the sample increases in volume at the beginning of the unloading phase. Then the sample contracts towards the end of the unloading phase. This behaviour shows that soil does not unload in an elastic manner for U2 and U3. That the behaviour of U2 and U3 is not elastic is known for two reasons: 1) for constant Poisson's ratio elastic dilatancy should be constant 2) dilatancy has a negative sign which is not possible under the elastic framework for conventional triaxial stress path unloading. For U1, where the sample is unloaded from a pre-image stress ratio, there is a small elastic part represented by the first three points in the dilatancy plot (see Figure 4.5). However, there is some uncertainty in the interpretation of this part of the test because of the small number of data points. The elastic part is followed by plastic yielding. .

Similar behaviour is observed for test ES\_CID\_868 with the moist tamped sample (Figure 4.6). The previously described behaviour of sand seems to be independent of the sample preparation method.

Tests ES\_CID\_870 and ES\_CID\_872 have similar  $e_o$  and initial  $p'$ . The only significant difference between the tests is that the former has one U-R loop while the latter has three loops. The difference in the number of loops does not cause a significant effect on the stress ratio vs. axial strain curve (Figure 4.7a). The first loop in ES\_CID\_872 causes only small change in volumetric strains while the second loop causes significant contraction when compared to the results of ES\_CID\_870 (Figure 4.7b). Note that the first loop in ES\_CID\_872 is pre-image while the second is post-image. In the third loop, both tests start from approximately similar points and demonstrate similar behaviour. It can be observed that the volumetric strain curve for ES\_CID\_872 after the second loop is steeper than that for ES\_CID\_870. This implies that the unloading loop influences volumetric changes patterns in subsequent reloading. This point will be discussed in detail later in this section.

Another two tests with very similar initial conditions, and very similar stress-strain and volumetric strain curves, are tests ES\_CID\_861 and ES\_CID\_862 which have identical  $e_o$  and initial  $p'$ . The first test has two U-R loops while the second has three U-R loops. The additional loop in ES\_CID\_862 is pre-image and therefore does not cause any significant difference between the results of the two tests.

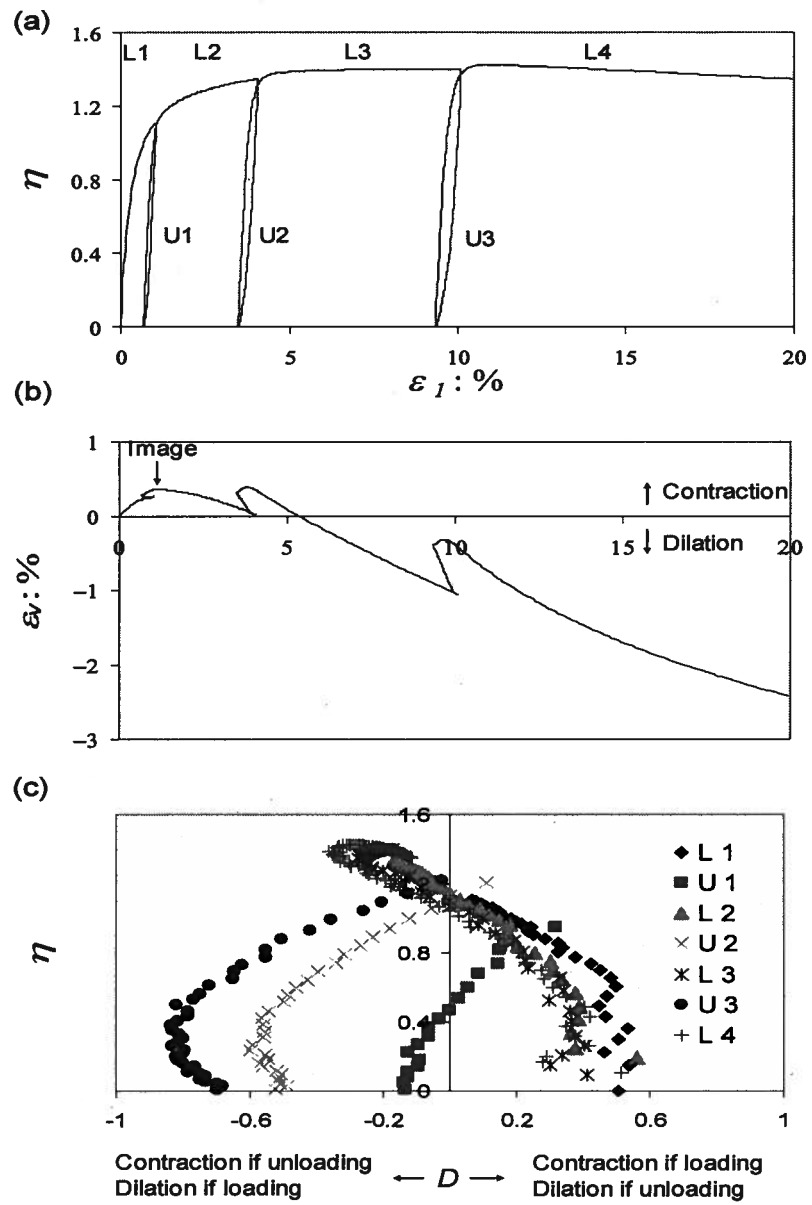


Figure 4.1. Data from ES\_CID\_867 (a) stress ratio vs. axial strain (b) volumetric vs. axial strain (c) stress ratio vs. dilatancy



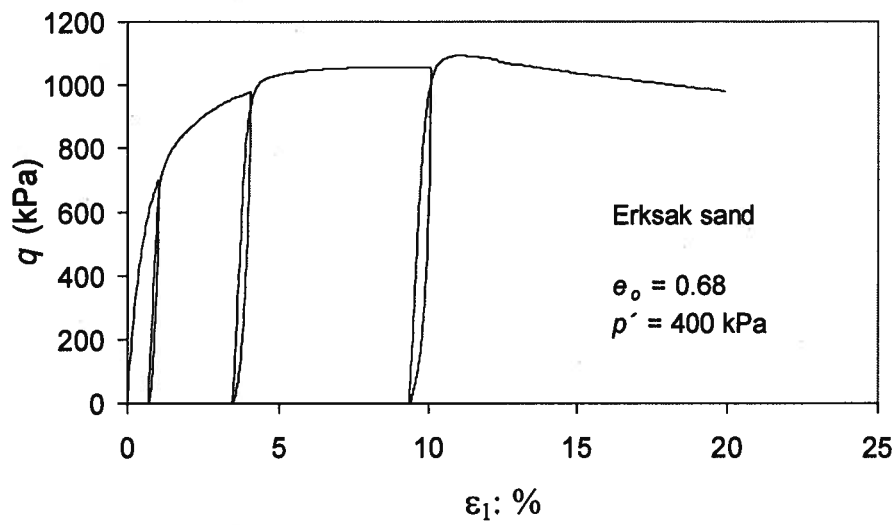


Figure 4.2. Data from ES\_CID\_867 in shear stress vs. axial strain

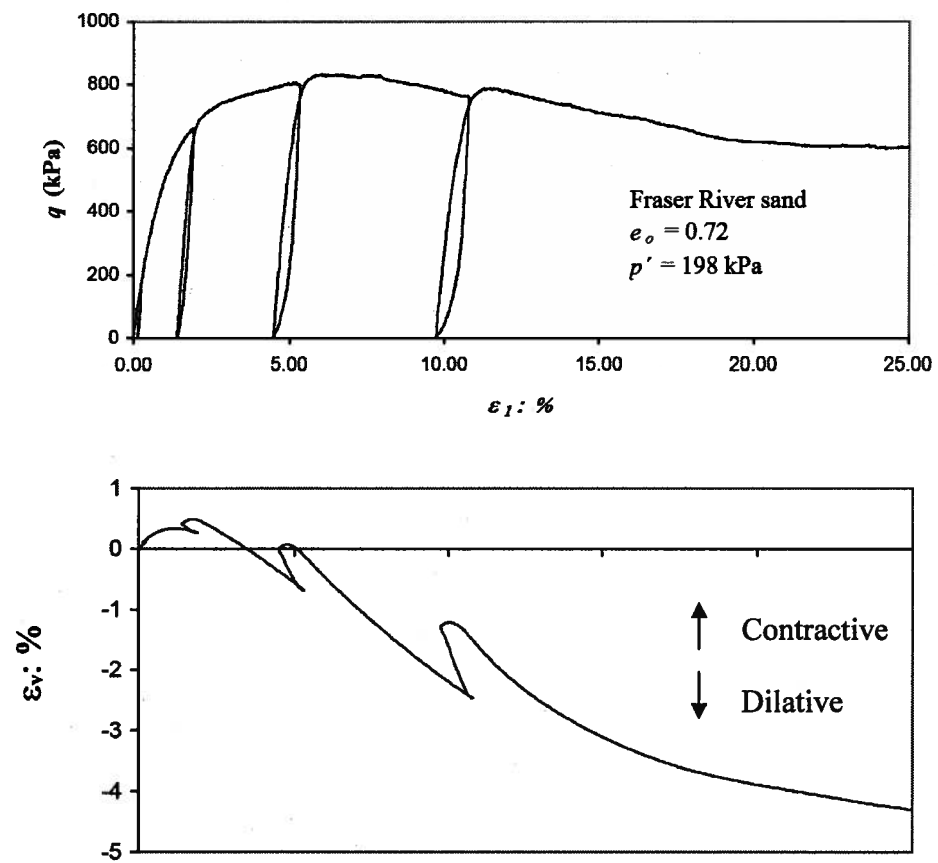


Figure 4.3. Results of FR\_CID\_02 in shear stress vs. axial strain

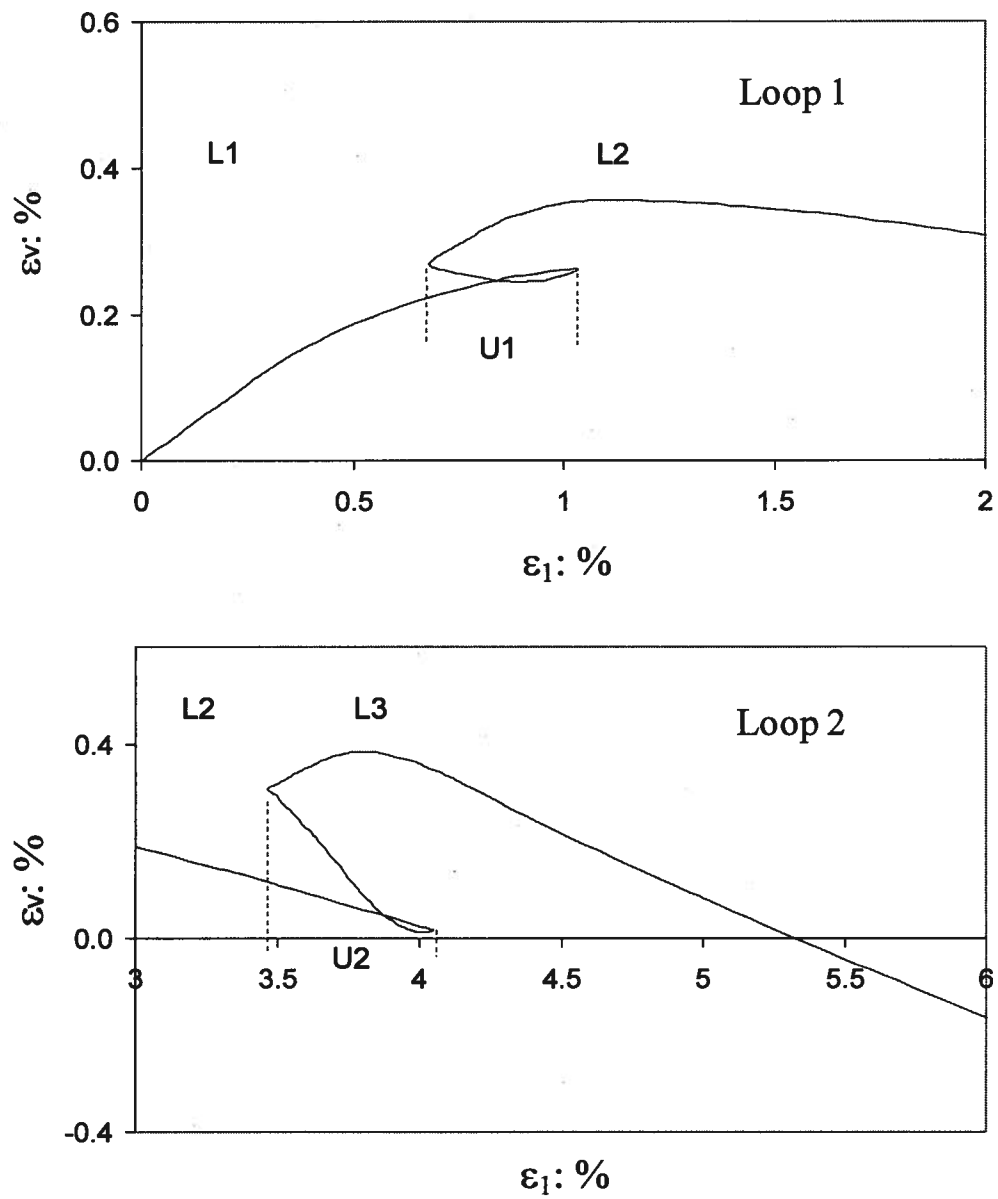


Figure 4.4. Zoom on loops 1 and 2 for test ES\_CID\_867.

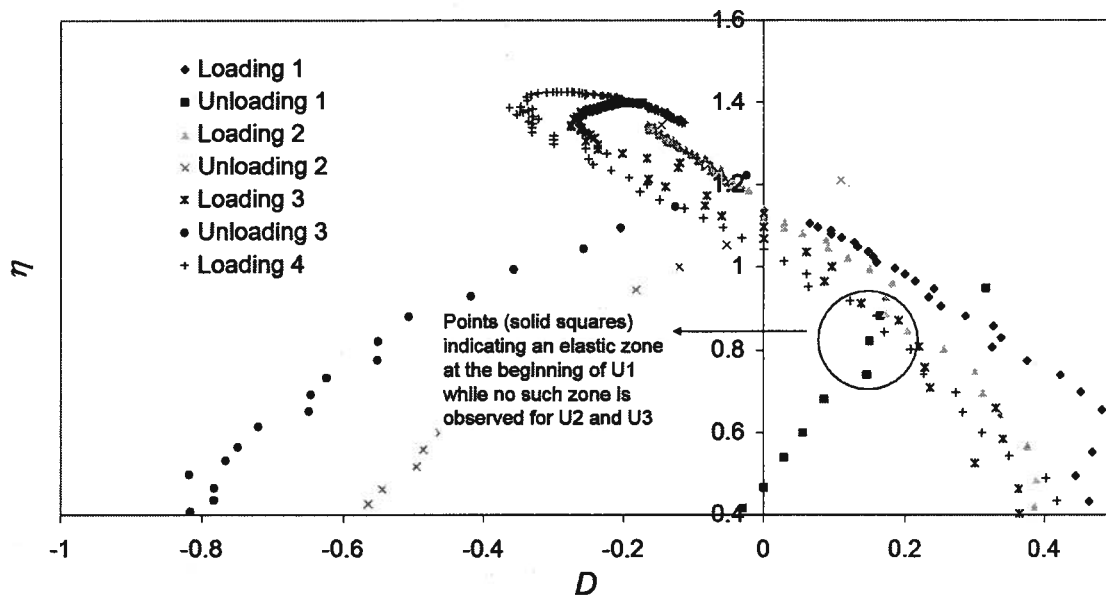


Figure 4.5. Zoom on the elastic zone in Figure 4.1c.

Volumetric strains in reloading phases are observed to be influenced by the unload-reload loops. This is investigated by plotting the data in stress-dilatancy space. A change in stress-dilatancy relation implies a change in the slope of the volumetric strain curve. Figure 4.9 shows that the stress-dilatancy relation is almost the same for phases L1-L3. Once peak stress ratio is exceeded in L3, stress-dilatancy relation changes for L4. Soil becomes more dilatant and another peak dilatancy value (termed as second peak) is reached. The increase in peak dilatancy between the two peaks exceeds 50% in some cases (Figure 4.10).

Peak dilatancy values for the available drained triaxial tests with unload-reload loops on Erksak Sand are plotted against the state parameter at peak dilatancy (Figure 4.11). The state parameter is equal to the difference between the current void ratio and that at the critical state (see Section 2.1.3). Two different trends can be seen from laboratory data for different reload loops. It is noteworthy that the slopes and intercepts of a trend line through the data points of the first peak dilatancy are different from those for the dilatancy of the second peaks.

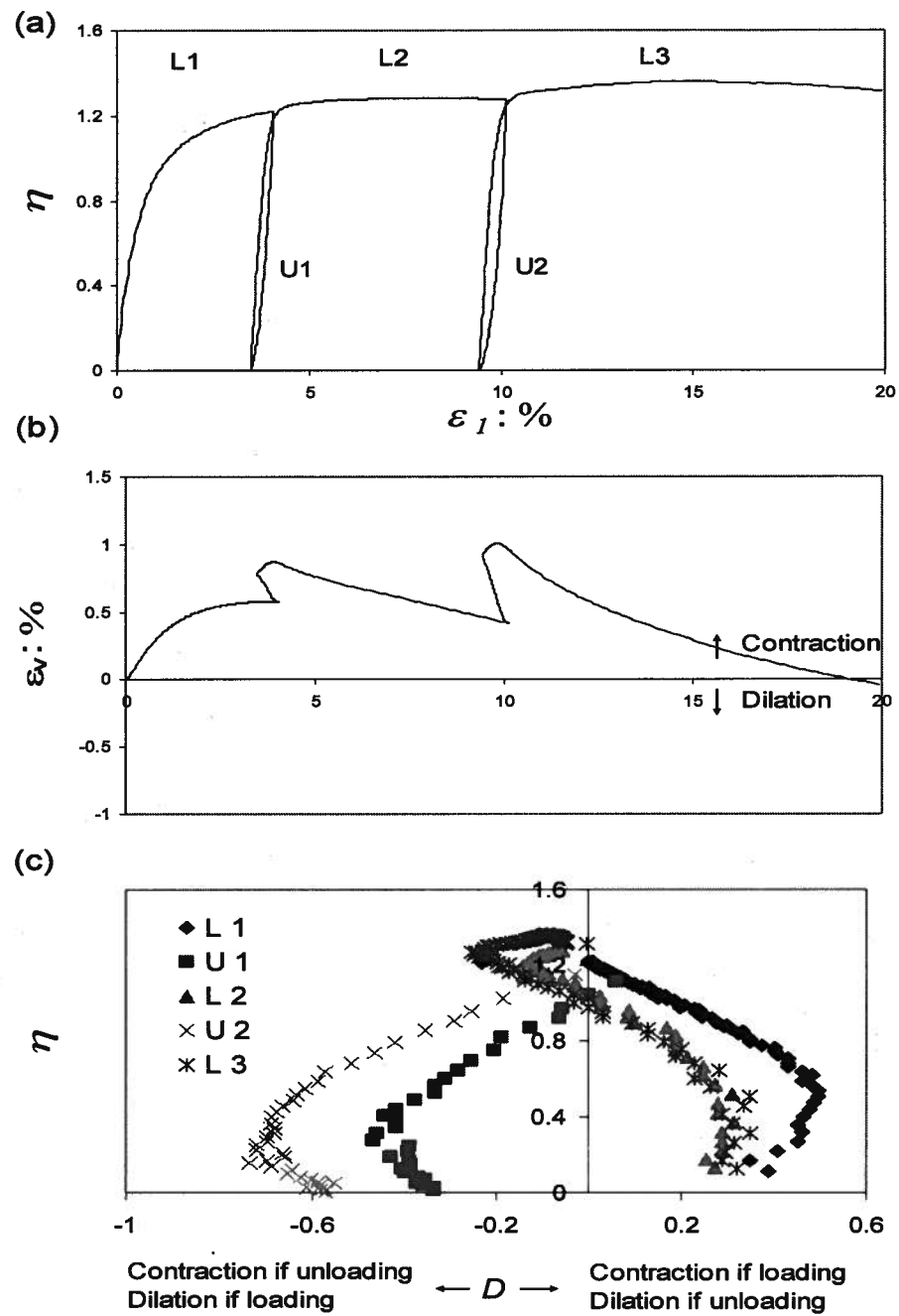


Figure 4.6. Data from ES\_CID\_868 (a) stress ratio vs. axial strain (b) volumetric vs. axial strain (c) stress ratio vs. dilatancy.

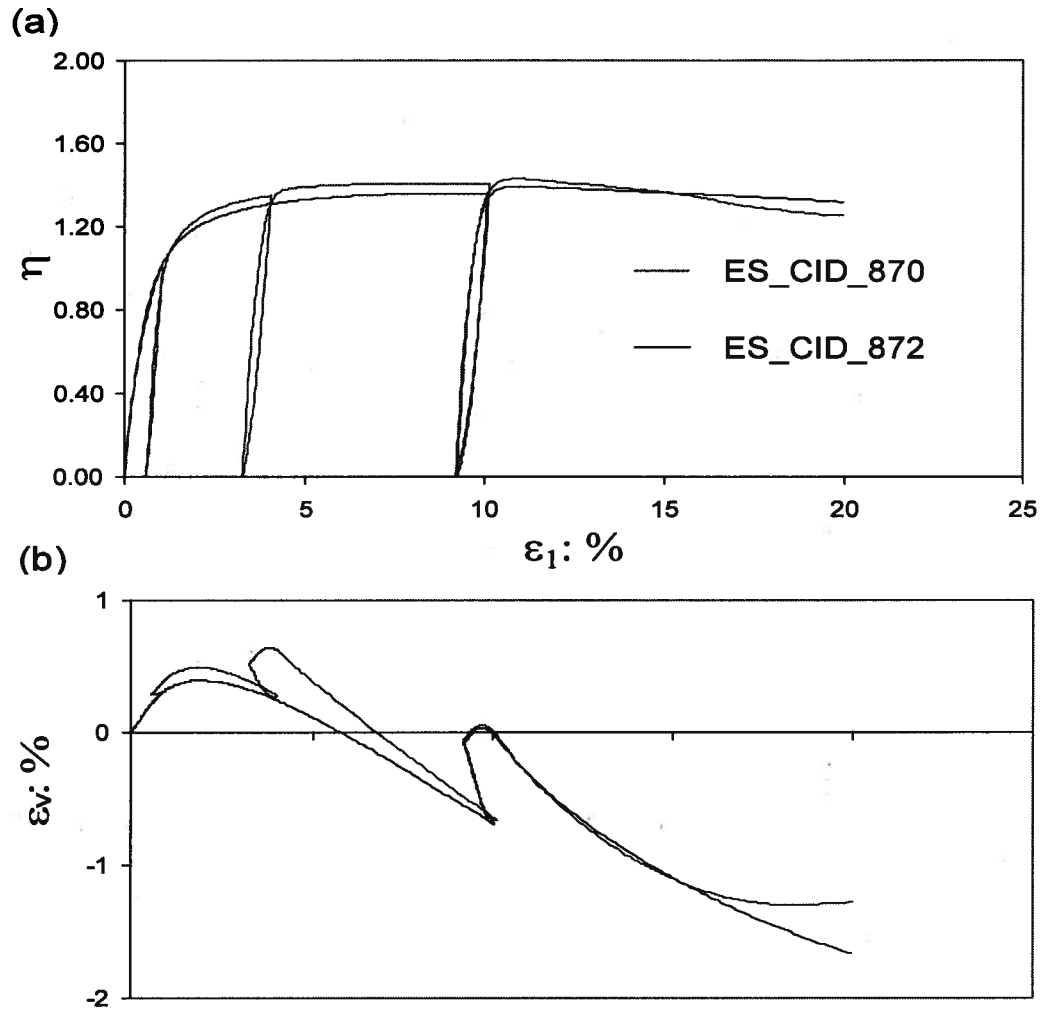


Figure 4.7. Comparison of ES\_CID\_870 and ES\_CID\_872 with similar  $e_o$  and initial  $p'$  but different number of U-R loops (a) axial strain vs. stress ratio (b) axial strain vs. volumetric strain.

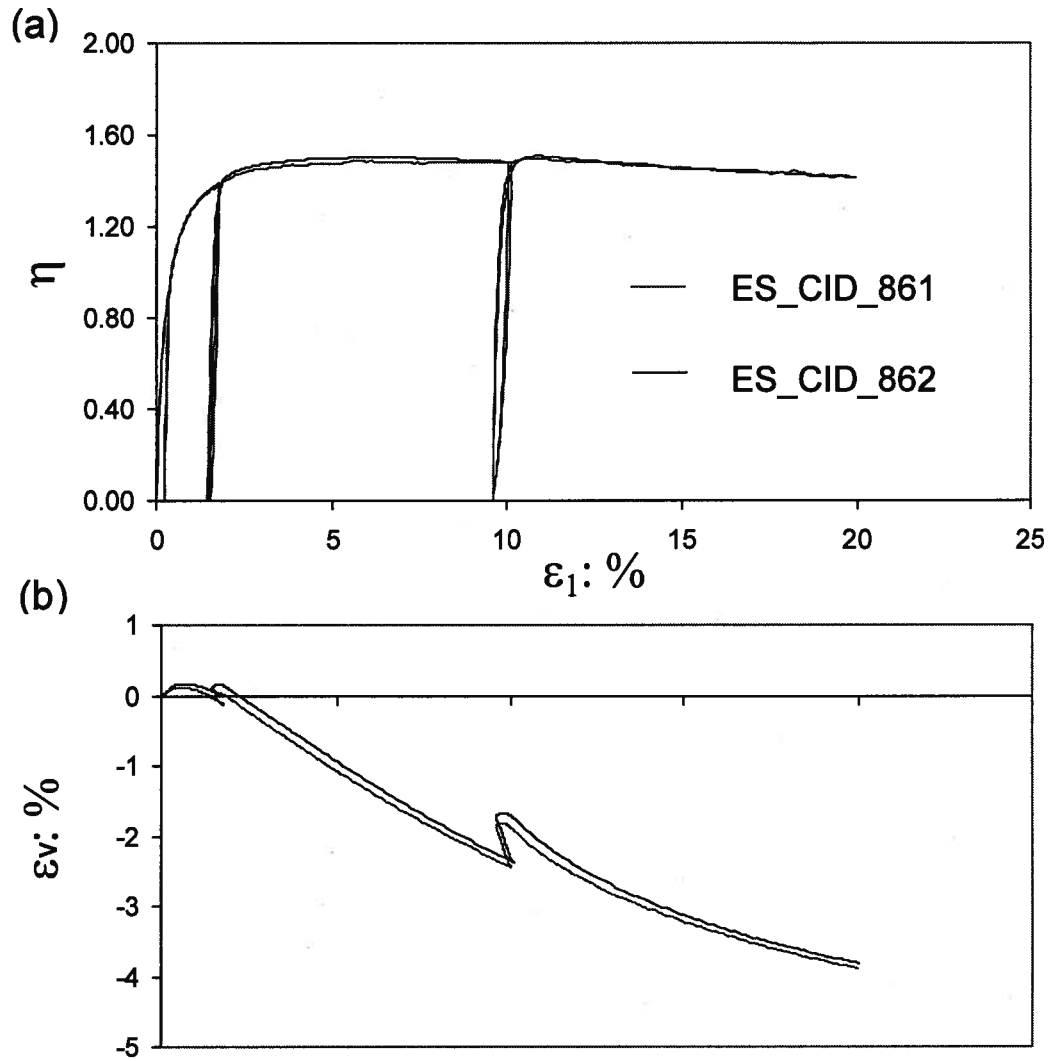


Figure 4.8. Comparison of ES\_CID\_861 and ES\_CID\_862 with similar  $e_o$  and initial  $p'$  but different number of U-R loops (a) axial strain vs. stress ratio (b) axial strain vs. volumetric strain.

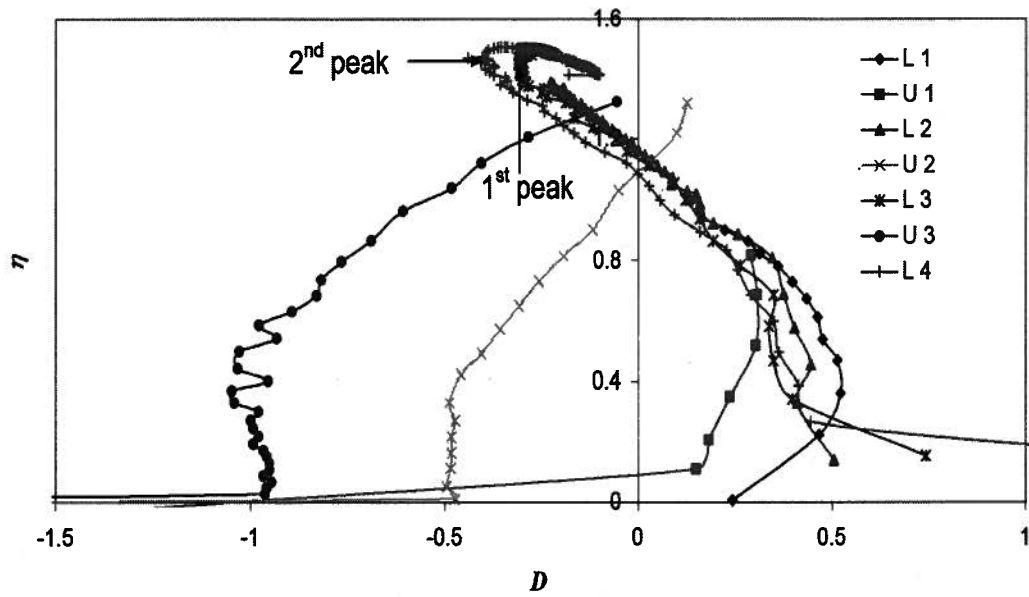


Figure 4.9. Stress ratio vs. dilatancy for pre-peak and post-peak reloading loops (ES\_CID\_862).

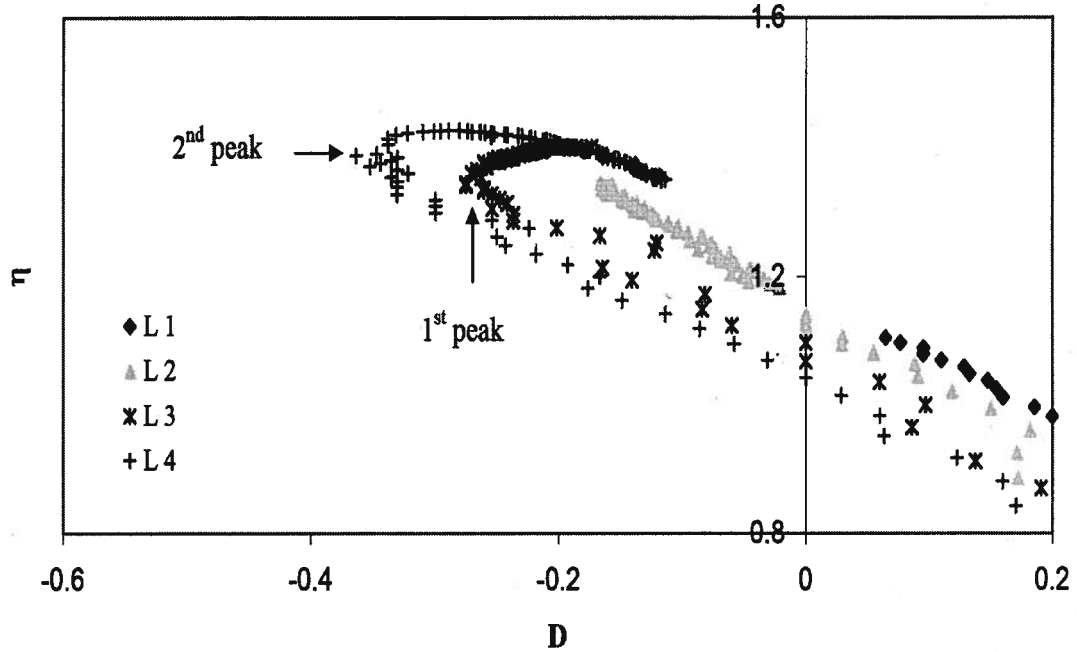


Figure 4.10. Stress ratio vs. dilatancy for different reload loops (ES\_CID\_867).

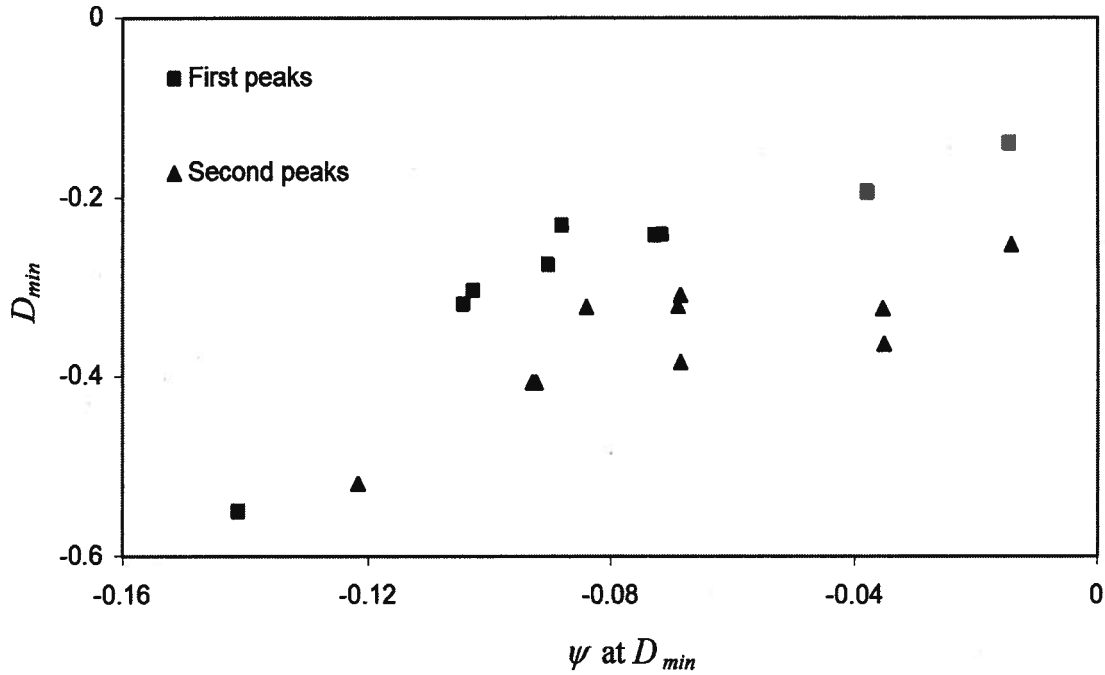


Figure 4.11.  $D_{min}$  vs.  $\psi$  at  $D_{min}$  for first and second loading of Erksak sand

#### 4.4. Implications of experimental observations

Deformation characteristics in unloading are seen to be highly dependent on the stress ratio at the start of unloading (or the end of previous loading). If this stress ratio is less than that at image, unloading is dominated by a small amount of dilation. This behaviour might be explained by elasticity. An elastic material expands in response to a decrease in mean effective stress (associated with unloading in conventional triaxial tests). However, once the image stress ratio is exceeded, unloading is associated with significant amount of contraction. This indicates non-elastic behaviour or yield in unloading. Therefore, the image condition defines the first possible location where yield in unloading can occur. Yield in unloading must occur at a post-image location as dilation in loading is a prerequisite for significant contraction in unloading. This contradicts many soil models such as those presented in Section 2.3 where unloading happens inside the yield surface and it is elastic.



Contraction due to post-image unloading can be explained based on a simple physical model as previously discussed in Section 2.6.1. When stress ratio exceeds that for image, the sample starts to dilate. It stores potential energy that can be recovered in the form of contraction in unloading (Jefferies, 1997). If dilation can be thought of as soil particles sliding on top of each other, then a situation similar to that in Figure 4.12a develops in loading. Upon unloading which can be thought of as pushing the upper part to the left, the particles would want to slide back to their original location prior to loading (Figure 4.12b). This is associated with contraction. Therefore, plastic dilation in loading is responsible for the observed contraction in subsequent unloading. The model also suggests that the amount of contraction in unloading is related to the amount of dilations in a previous loading. The more soil is allowed to dilate in loading, the more contraction is expected in subsequent unloading. This will be shown in Chapter 5.

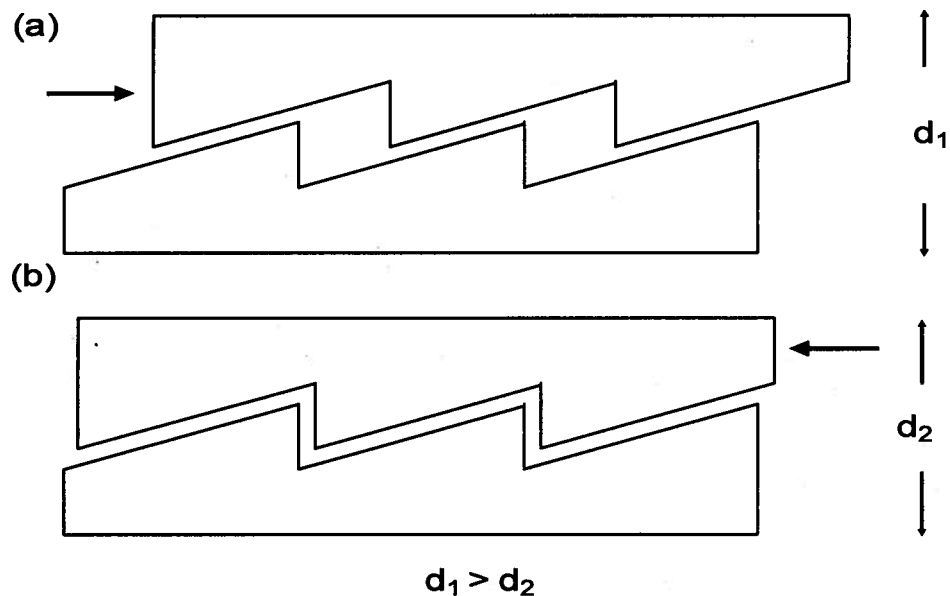


Figure 4.12. The saw tooth model (a) loading (b) unloading (Same as Figure 2.35).

It seems that this simple model can explain the observed behaviour in unloading. The saw-tooth model (Figure 4.12) is a friction based model. It can be thought of as a

simplified version, or an abstraction, of Rowe's micro-mechanical model. In Chapter 3, Rowe's model was extended to unloading. The trends observed in Section 4.3 are similar to those predicted by the model.

It was observed that post-image U-R loops demonstrate a new peak in stress-strain curves (Figure 4.3). This is consistent with the behaviour that post-image unloading is associated with contraction and a denser soil is expected to have higher peak strength.

Triaxial tests on Erksak sand show that dilatancy in reloading is significantly changed only if the previous loading phase exceeds peak stress ratio (refer to Section 4.3). Been and Jefferies (1985) showed that there is a relation between peak dilatancy and state parameter at peak dilatancy as previously discussed in Section 2.5. However, this relation is expected to change if fabric changes. Changes in fabric are induced due to shearing in unloading and reloading phases. The data suggests that once the peak stress ratio is exceeded, soil goes through permanent changes in fabric.

## 5. A MODEL TO ACCOMMODATE UNLOAD-RELOAD LOOPS USING NORSAND

NorSand is a strain hardening/softening plasticity model based on critical state theory. The most widely used version of the code that only yields in loading is described in some detail in the literature review (see section 2.5). Jefferies (1997) also presented a framework for the behaviour of a NorSand material in unloading and reloading (see section 2.6.3). This chapter expands on this framework to incorporate the observed soil behaviour in unload-reload loops discussed in Chapter 4, supported by the theoretical investigation in Chapter 3. NorSand is chosen in this study because of its simplicity, small number of parameters and accurate representation of the major aspects of soil behaviour. NorSand can be easily implemented in any programming language. The steps followed in coding the monotonic triaxial compression version of NorSand are summarized in Table 5.1. The equations were derived and the parameters were defined in Section 2.5.

Table 5.1. Equations used in the triaxial compression version of NorSand and their step by step implementation in an Euler integration code.

	Step description	Equation
1	Apply plastic shear strain increment ( $\dot{\varepsilon}_q^p$ )	
2	Obtain the value of stress ratio at image ( $M_i$ )	$M_i = M - N\chi \psi $
3	Calculate the current plastic dilatation rate	$D^p = M_i - \eta$

4	Get plastic volumetric strain increment ( $\dot{\varepsilon}_v^p$ )	$\dot{\varepsilon}_v^p = D^p \dot{\varepsilon}_q^p$
5	Get the current dilation limit	$D_{\min} = \chi \psi$ where, $\psi = e - e_c$ , $e_c = \Gamma - \lambda_e \ln(p')$ and $p'_i = \frac{p'}{e^{(1-\eta/M_i)}}$
6	Apply the hardening rule to change the size of the yield surface due to the applied plastic shear strain increment	$\frac{\dot{p}_i}{p_i} = H \left( \frac{p'}{p_i} \right)^2 \left[ e^{(-\chi \psi / M)} - \frac{p'_i}{p'} \right] \dot{\varepsilon}_q^p$
7	Apply consistency condition so that the stress state stays on the yield surface	$\dot{\eta} = \left( \eta \frac{\dot{M}_i}{M_i} + M_i \frac{\dot{p}_i}{p_i} \right) / \left( 1 + \frac{M_i}{(L - \eta)} \right)$ Where, $L = \frac{\dot{q}}{\dot{p}}$ (From Jefferies and Been, 2006)
8	Update stresses, strains and state parameter and add elastic strains	

The objective of this chapter is to extend NorSand to include the new understanding of yielding during unloading and subsequent reloading, introduced in this study. The proposed model has been implemented in the Microsoft Excel Visual Basic Application (VBA) environment. Appendix D shows the main steps followed in coding the load-unload-reload model.

The four components of any elasto-plastic model, including NorSand, are elasticity, a yield surface, a plastic potential (i.e. a flow rule) and a hardening rule.

## 5.1. Yield surface and internal cap

NorSand's outer yield surface and the inner yield surface (or internal cap) was discussed in some detail in Sections 2.5 (see Figure 5.1). Equation 2.52 (reproduced here as Equation 5.1) specifies the location of the internal cap. This is the same location used by Jefferies (1997). The current location of the cap fits the framework of the NorSand model in loading.

$$p_{cap} = \frac{p_i}{e^{(-D_{min} / M_i)}} \quad (5.1)$$

The cap is taken as a vertical line for simplicity. It is assumed to intersect the outer yield surface at peak (i.e. minimum dilatancy if the sign is taken in consideration) which occurs at peak strength. Hence the location of the cap that defines yield in unloading is coupled to the outer yield surface that was determined by the previous loading phase. It will be shown in the following sections that soil behaviour in unloading is related to previous loading phases. It is therefore reasonable to have the location of the cap defined during a previous loading phase. The adopted location of the internal cap is identical to that for Jefferies (1997). This is to avoid inconsistencies with the NorSand model in loading. Consider a case where unloading starts from peak. For convenience assume that an internal cap at the image state was chosen. Unloading would then start from a point to the left of the internal cap and the consistency condition would not be satisfied as the stress point would not be on the internal cap.

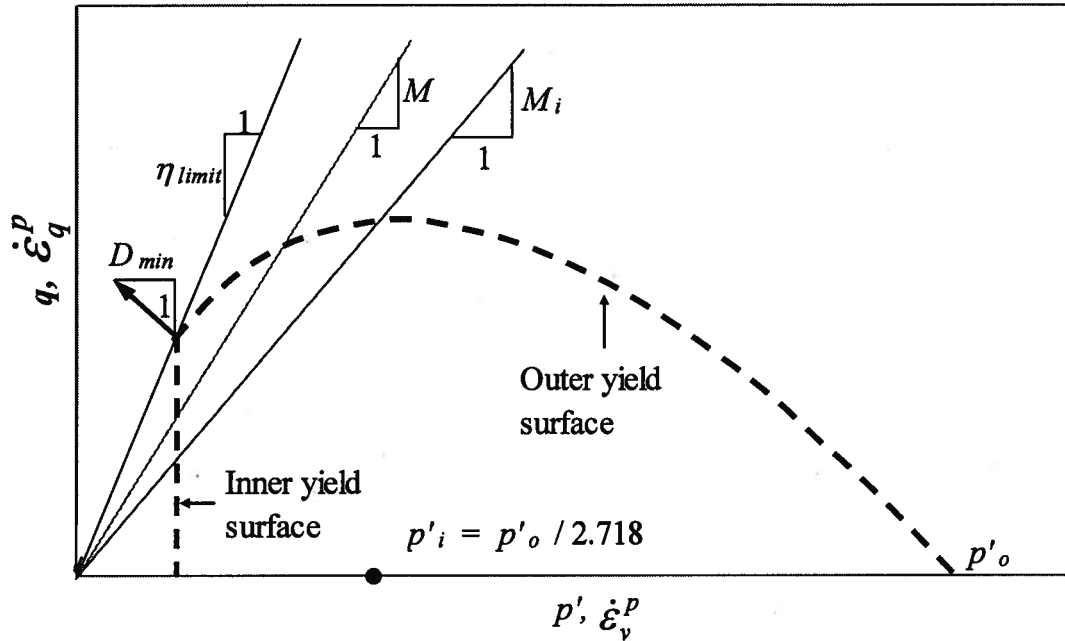


Figure 5.1. Yield surface and internal cap in NorSand, same as Figure 2.28 (modified after Jefferies and Shuttle 2005).

The proposed location of the internal cap matches the observation from the data presented in Chapter 4. It was shown that yield in unloading must occur to the left of the image. This is consistent with the saw-tooth model where significant contraction in unloading (i.e. yield in unloading) occurs only for the case where soil was allowed to dilate in a previous loading. By definition, dilation is only possible if stress ratio exceeds that of image. Therefore, having the internal cap at peak is consistent with the NorSand model and matches observations from laboratory data.

Soil unloaded after reaching peak stress yielded in unloading directly without going through an elastic phase (Figure 5.2). It is not certain whether peak was reached for L2. However, it is clear that the stress ratio is very close to reaching peak. Samples unloaded from lower stress ratios showed a purely elastic phase before yielding. This behaviour can be captured by placing the cap at the point representing peak stress in loading.

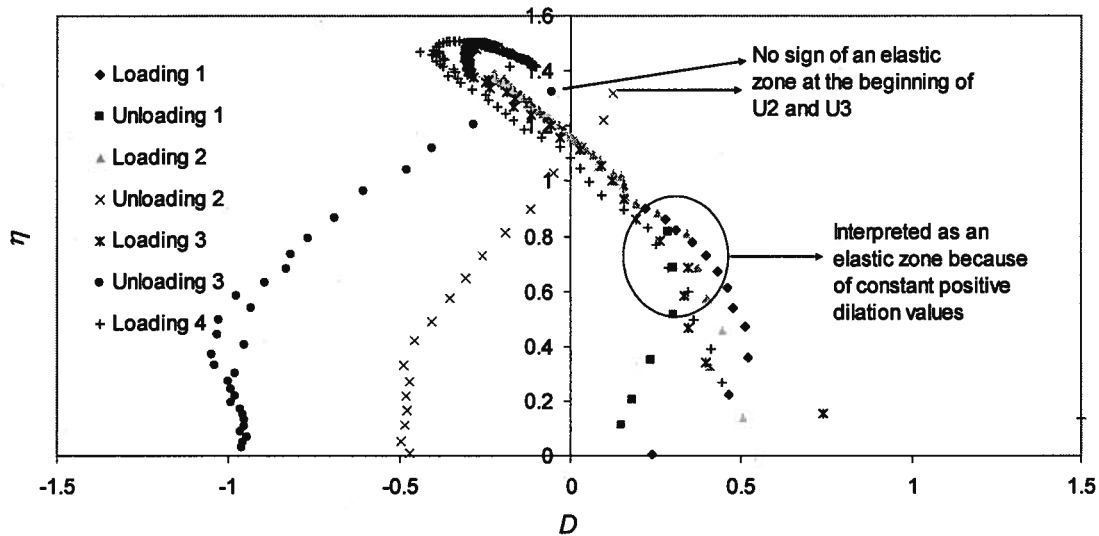


Figure 5.2. Demonstration of interpreted elastic and elasto-plastic zones on the results of ES\_CID\_682 in stress ratio vs. dilatancy plot.

## 5.2. Flow rule

### 5.2.1. Flow rule in unloading

Data indicate that dilatancy in unloading depends on the previous loading phase. Figure 5.3 shows the stress-dilatancy plots for the triaxial tests on Erksak sand discussed in Chapter 4. Three observations may be made from the data in Figure 5.3. First, it can be seen that almost all the plots for dilatancy in unloading are perpendicular to those in loading. Second, the position of stress-dilatancy curves in unloading is seen to depend on the stress ratio at which previous loading stopped (see Figure 5.4 ). In the following the stress ratio at  $D^p_u = 0$  is defined as  $M_u$  (the subscript “u” denotes unloading). The higher the stress ratio at which loading stops, the larger the value of  $M_u$  for a following unloading phase. Lastly, the measured dilatancy in unloading stops changing at a value of  $\eta = 0.4-0.5$ , and plots vertically in the stress-dilatancy plot. Note that the value of  $\eta = 0.4-0.5$  corresponds to different dilatancy values for different tests and different

unloading loops within each test. Therefore, the location of the vertical part of the plot is different for different tests and different loops within each test.

It is assumed here that the Cam-Clay flow rule ( $D^P = M - \eta$ ) represents stress-dilatancy in loading (see Section 2.3 for more details). Because stress-dilatancy curves in unloading are almost perpendicular to those for loading, the proposed expression for stress-dilatancy in unloading is negative of that for Cam-Clay, and while replacing  $M$  by  $M_u$ . It takes the form:

$$D_u^P = \eta - M_u \quad (5.2)$$

The problem is how to get a representative value for  $M_u$ , as Figure 5.3 clearly shows that for Equation 5.2 to be valid  $M_u$  needs to vary for different loops in the same test. As previously discussed, the saw-tooth model implies that the amount of contraction in unloading is related to the amount of dilation in the previous loading phase. The value of  $M_u$  for each unloading phase is then expected to depend on the previous loading phase. The last value of  $\eta$  for L3 in Figure 5.4 is higher than that for L2. Note that value of  $M_u$  for U3 (U3 follows L3) is higher than that for U2. It seems that the higher the last value of  $\eta$  (denoted as  $\eta_L$ ) in a loading phase, the higher the value of  $M_u$  in subsequent unloading. To prove this point, values of  $\eta_L$  for different loading or reloading loops for all tests on ES are plotted against values of  $M_u$  for the corresponding subsequent unloading phases (see Figure 5.5). It can be seen that  $\eta_L$  and  $M_u$  are directly related. A linear trend line representing a best fit to the data points has the following equation:

$$M_u = 2\eta_L - 1.5 \quad (5.3)$$

It is observed that there is a limit on the maximum dilatancy that can be reached in unloading at a value of  $\eta = 0.4-0.5$ , as previously discussed. At this limiting value dilatancy becomes constant for a particular unloading loop. Equation 5.4 is found to give a reasonable approximation for this maximum dilatancy in unloading (or minimum dilatancy if the sign is taken in consideration).



$$D_u^p = 0.5 - M_u \quad (5.4)$$

Figure 5.6 shows an example comparison between the stress-dilatancy predicted by the proposed equations (Equations 5.2 to 5.4) and data from test ES\_CID\_866. The predictive ability of Equations 5.2 to 5.4 is shown for all ten Erksak tests in Appendix A.

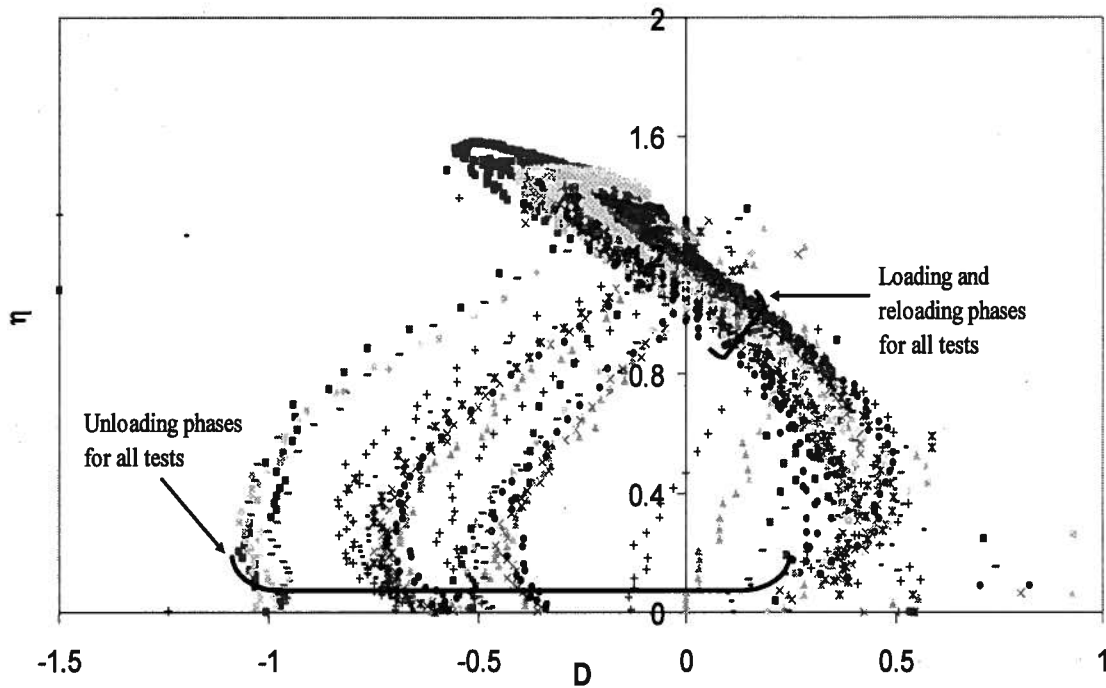


Figure 5.3. Drained triaxial tests on Erksak sand with unload-reload loops plotted in the dilatancy vs.  $\eta$  space.

### 5.2.2. Flow rule in reloading

The usual NorSand flow rule for monotonic loading is  $D^p = M_i - \eta$ . Triaxial data on Erksak sand plotted in Figure 5.3 show that stress-dilatancy is altered if the soil is unloaded and reloaded. It changes for different reloading loops (see Section 4.3). It is observed that in most tests, the stress-dilatancy relation in reloading changes if the previous loading phase reached peak dilatancy (see Figures 4.9, 4.10, and 4.11). It was shown that peak dilatancy values increase for post-peak reloading phases.

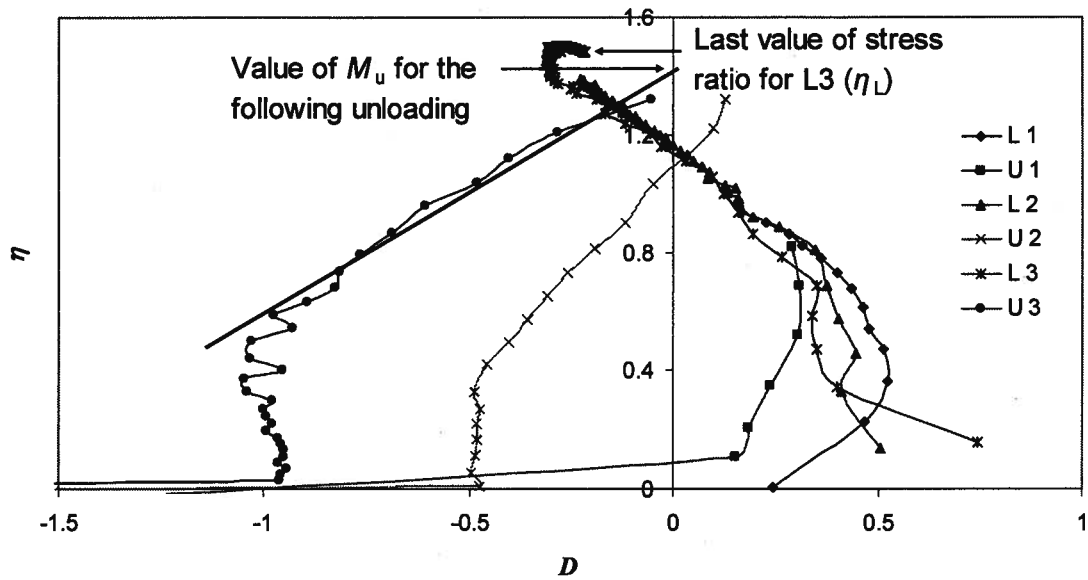


Figure 5.4.  $\eta_L$  and  $M_u$  for L3 and U3, respectively, for ES\_CID\_862.

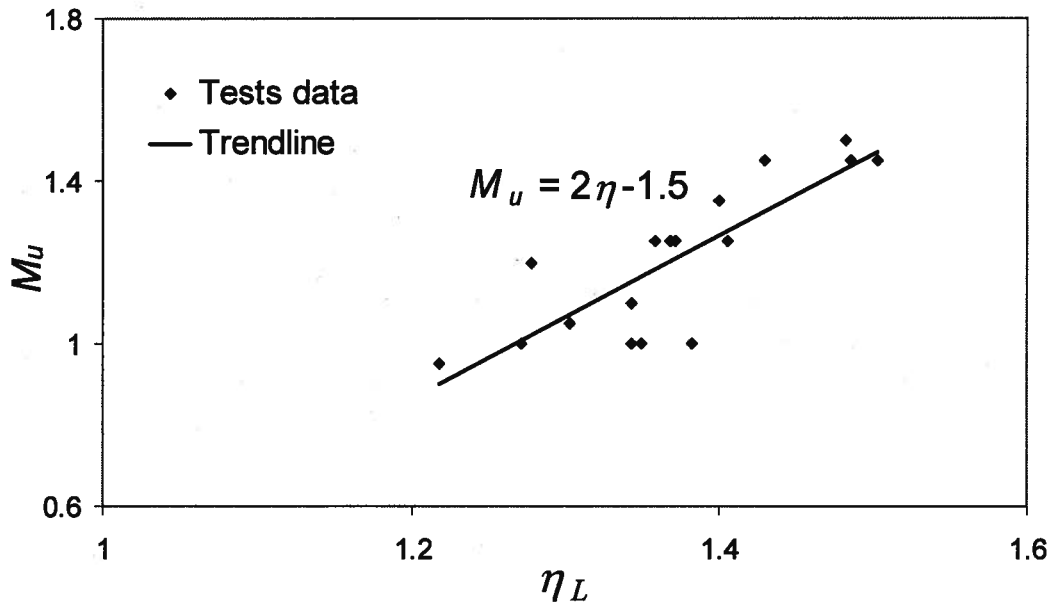


Figure 5.5. Correlation between  $M_u$  and  $\eta_L$  from previous loading (drained triaxial tests on Erksak sand).

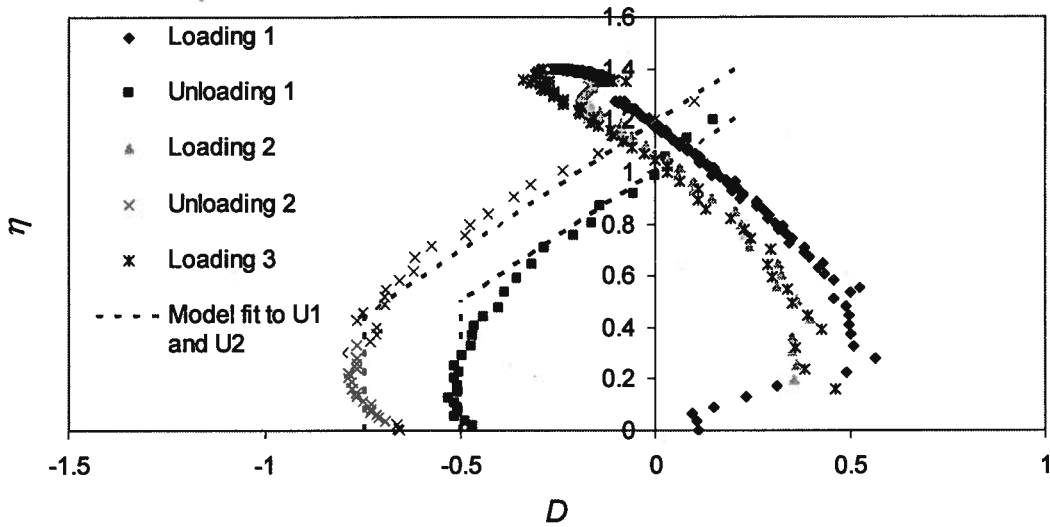


Figure 5.6. Predicted and measured stress-dilatancy for ES\_CID\_866.

In NorSand the peak stress is coincident with peak dilatancy, which is also the location of the internal cap (the location and shape of the assumed internal cap in NorSand was discussed in Section 5.1). Following the observed behaviour of change in peak dilatancy in post-peak reloading, it seems reasonable to introduce some changes to how soil dilates in the code if the stress state reaches the cap in a previous loading/reloading. The triaxial data for all tests on Erksak sand was plotted in Figure 4.11 in  $\psi$  vs.  $D_{min}$  space. It is clear that there are two different trends for the different peaks within each test and for all tests. The points for second peaks are lower on the plot compared to the points of first peaks. Change in particle arrangement due to the cyclic load is responsible for this change as previously discussed in Section 4.4 supported by the results of the theoretical investigation in Section 3.2. It is noteworthy that if a trend line (based on a best fit to the data points) is drawn through the points of the second peaks, it would have an intercept that is far from zero. This is not in accordance with the critical state theory on which NorSand is based.

A major feature of NorSand is that it limits dilatancy based on a relation between  $\psi$  and  $D_{min}$ . The slope of a linear trend line with a zero intercept in the  $\psi$  and  $D_{min}$  plot is termed

$\chi$  (used as a parameter in NorSand). A zero intercept of the trend line is consistent with Critical State Soil Mechanics (CSSM). This is because if peak dilatancy happens at the critical state (i.e. for a test on loose sand) then  $D_{min}=0$  and  $e = e_c$  (by definition  $\psi$  must equal zero as  $\psi = e - e_c$ ). Therefore, the trend line through the data points of the second peaks should also be drawn with an intercept of zero, as well as the trend for the first peaks.

It could be argued that soil reaches other peaks for subsequent unload-reload loops (i.e. a third peak may exist). The limited number of tests in the currently available data with three or more loops does not provide sufficient information to determine whether other peaks exist or not. However, the stress-dilatancy relation is not expected to change indefinitely. A change in stress-dilatancy relation is caused by changes in fabric. As the reported tests do not reach critical state (where major fabric changes occur), no further changes in the stress-dilatancy relation are expected to occur.

The proposed model assumes that only two peaks exist. Once the first peak is exceeded in a loading/reloading phase, all subsequent reloading phases follow a different stress-dilatancy relation with a different peak (i.e. second peak) associated with more dilation. Those two peaks can be represented in NorSand by the slopes of two trend lines through the points of the first and second peaks. The slopes of the two lines are denoted as  $\chi_1$  and  $\chi_2$ . The parameter  $\chi_1$  is identical to  $\chi$  in standard NorSand. The code uses the second peaks value,  $\chi_2$ , only if the stress state in the previous loading or reloading phase hits the internal cap which represents peak conditions. This is consistent with observations in triaxial tests. The second peaks are attained only if peak stress was reached in a previous loading/reloading (see Section 4.3).

The implication of a changing  $\chi$  on the NorSand model is twofold. Firstly, a change in  $\chi$  results in a change in the location of the internal cap for a certain yield surface. As  $\chi$  increases from an initial value of  $\chi_1$  to a larger value of  $\chi_2$ , the location of the internal cap (Figure 5.1) is shifted to the left. This allows for higher dilatancy values. Secondly, the computed values of  $M_i$  change (see Equation 5.5). A higher  $\chi$  value yields a smaller  $M_i$ .

This is consistent with the observed behaviour. Figure 5.7 shows that  $M_i$  for a second peak reloading (i.e. higher  $\chi$  value) is higher than  $M_i$  for the first peak reloading with the smaller  $\chi$ .

$$M_i = M - \chi N |\psi| \quad (5.5)$$

Where,

$\chi = \chi_1$  for the case of first loading or previous loading/reloading does not touch the internal cap.

$\chi = \chi_2$  for the case where previous loading/reloading touches the internal cap.

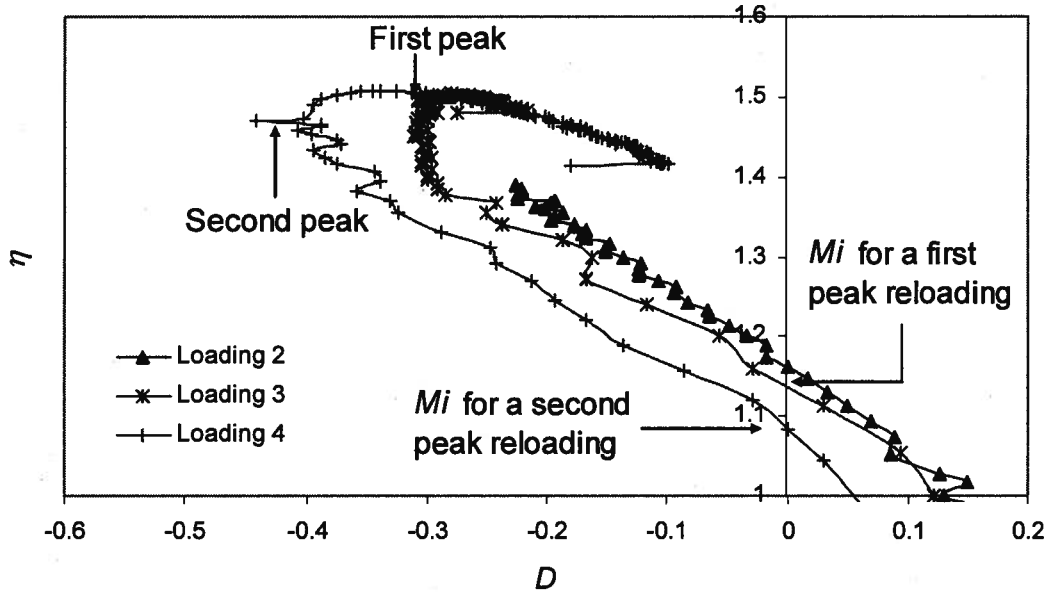


Figure 5.7. Change of  $M_i$  for different reloading loops (ES\_CID\_862).

### 5.2.3. Potential surface in unloading

NorSand uses an associated flow rule, meaning that the plastic potential surface and yield surface are the same. In unloading, yield happens on the internal cap. As

previously discussed in Section 5.1, the cap is a vertical line. Using an associated flow rule with a vertical cap yields zero dilatancy. However, a significant amount of contraction was observed in unloading. Therefore, a non-associated flow rule is used (Equation 5.2). Having a non-associated flow rule in unloading makes it necessary to have a potential surface that is different from the yield surface.

An expression for the potential surface is derived as it will be necessary to implement this model in any finite element formulation for future work. The derivation involves two assumptions: normality (i.e. plastic strain increments ratio is normal to the surface) and the stress-dilatancy relation (Equation 5.2). Starting with the definition of stress ratio  $\eta$ :

$$q = \eta p' \quad (5.6)$$

Taking the differential of 5.6 gives:

$$\dot{q} = p' \dot{\eta} + \eta \dot{p}' \quad (5.7)$$

And to satisfy normality,

$$\frac{\dot{q}}{\dot{p}'} = -\frac{\dot{\epsilon}_v}{\dot{\epsilon}_q} = -D^p \quad (5.8)$$

From 5.7 and 5.8,

$$\frac{\dot{p}'}{\dot{p}'} + \frac{\dot{\eta}}{D^p + \eta} = 0 \quad (5.9)$$

From Equations 5.2 and 5.9,

$$\frac{\dot{p}'}{\dot{p}'} + \frac{\dot{\eta}}{2\eta - M_u} = 0 \quad (5.10)$$

Integrating Equation 5.10 gives:

$$\int \left( \frac{\dot{p}}{p} + \frac{\dot{\eta}}{2\eta - M_u} \right) = C \quad (5.11)$$

The solution of the integral is:

$$\ln|p| + \frac{1}{2} \ln|2\eta - M_u| = C \quad (5.12)$$

When  $\eta = M_u$ , the stress state would be at the image and  $p = p_{iu}$ , hence:

$$C = \ln p_{iu} + \frac{1}{2} \ln M_u \quad (5.13)$$

And the equation of the potential surface in unloading is:

$$\ln \left( \frac{p}{p_{iu}} \right) + \frac{1}{2} \ln \left| \frac{2\eta}{M_u} - 1 \right| = 0 \quad (5.14)$$

Rearranging gives:

$$p_{iu} = \frac{p}{e^{-\frac{1}{2} \ln \left| \frac{2\eta}{M_u} - 1 \right|}} \quad (5.15)$$

Equations 5.14 and 5.15 were used to plot the potential surface in Figure 5.8 for  $M_u = 1.2$ . The potential surface has two parts that eventually meet at a high  $p$  value. The upper part is applicable for the case where  $(2\eta/M_u - 1) > 0$  while the lower part is for  $(2\eta/M_u - 1) < 0$ .

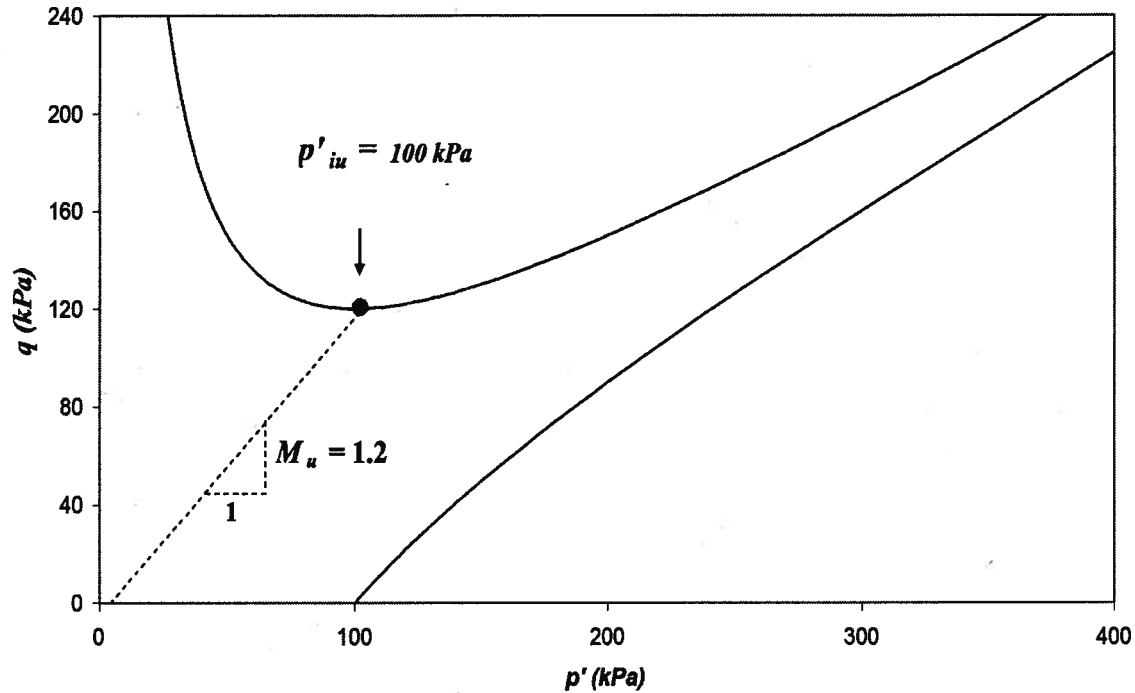


Figure 5.8. The shape of the potential surface in unloading

### 5.3. Hardening in loading, unloading and reloading

Hardening of the NorSand yield surface in loading, unloading and reloading is described in Section 2.6.3. A similar framework is adopted here because it matches the way Erksak sand behaves. If unloading occurs from a low stress level, the behaviour is elastic until yield occurs when the stress path hit the internal cap. Figure 5.2 shows that U1 is dominated by elastic behaviour at the beginning of the unloading phase and yield occurs only later on. Note that unloading in U1 starts from a low stress ratio. However, for the other loops, unloading is dominated by plasticity. NorSand would yield in unloading for those loops without passing through an elastic phase.

The outer yield surface softening during unloading is important for accurate predictions. If the outer yield surface would not soften in unloading, reloading would be elastic until the stress level prior to unloading is exceeded. Figure 5.9 shows that



reloading is not entirely elastic: stiffness decreases before the stress level is as high as the stress level at the start of previous unloading.

In unloading, the internal cap contracts. And because the internal cap intersects the outer yield surface, it softens as well. Jefferies (1997) introduced a rule for the contraction of the internal cap, reproduced as Equation 5.16. The term  $\ln(p_y'/p)$  was thought by Jefferies to introduce an effect similar to overconsolidation. The further the stress point is from first yield in unloading, the larger are the generated strains. This is consistent with observations from laboratory data. Figure 5.9 shows an expanded view of U2 for ES\_CID\_868. More axial strains are generated in U2 at lower stress ratios. The lower the stress ratio, the further the stress point is from first yield in unloading.

$$\dot{\varepsilon}_v^p = -\frac{1}{H_u} \frac{\dot{p}'}{p'} \ln\left(\frac{p_y'}{p'}\right) \quad (5.16)$$

Where,

$H_u$  is the hardening (softening) modulus in unloading

$p_y'$  is the mean effective stress at first yield in unloading (i.e. the mean stress of the cap when first intersected)

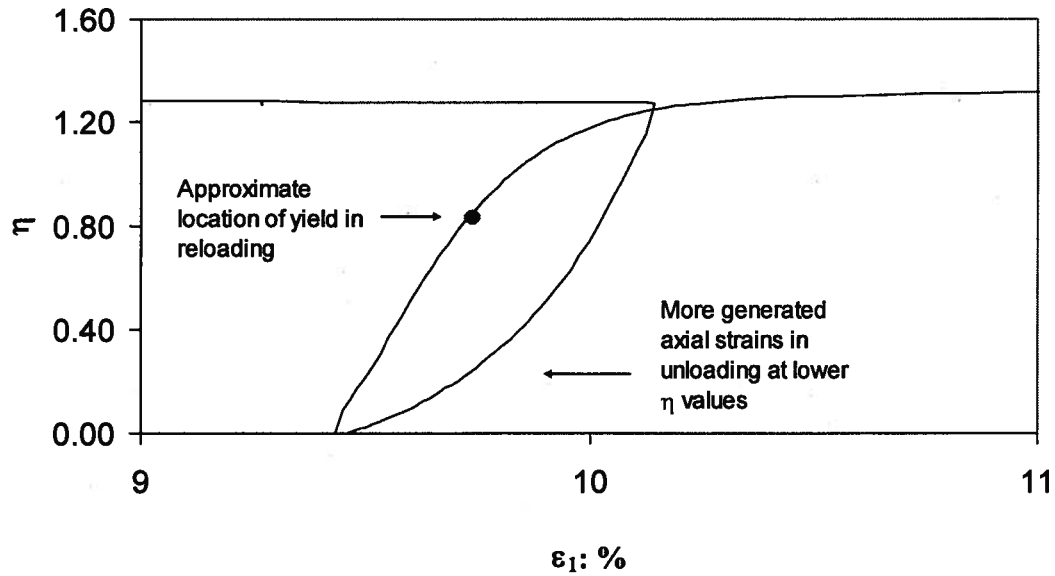


Figure 5.9. Expanded scale view of U2/L3 for ES\_CID\_868 in Figure 4.6a.

The use of Equation 5.16 in the code can result in infinite plastic shear strain increments. Consider the case of  $\eta = M_u$ . According to Equation 5.2  $D_u^p$  becomes zero. And for the sake of the argument, assume that volumetric strain increments are computed according to Equation 5.16. This results in a division over zero as  $\dot{\varepsilon}_q^p = \dot{\varepsilon}_v^p / D_u^p$ . To get around this problem, Equation 5.17 is used instead of Equation 5.16. Plastic shear strain increments are first calculated according to Equation 5.17 then plastic volumetric strain increments are recovered through stress-dilatancy (i.e.  $\dot{\varepsilon}_v^p = \dot{\varepsilon}_p^p D_u^p$ ). For the case of zero  $D_u^p$ , plastic volumetric strain increments become zero and the problem of having to divide over zero is solved. The sign of Equation 5.16 is changed as unloading is associated with negative mean effective stress increments and negative plastic shear strain increments.

$$\dot{\varepsilon}_q^p = \frac{1}{H_u} \frac{\dot{p}}{p} \ln \left( \frac{p_{fy}}{p} \right) \quad (5.17)$$

As yield in unloading causes softening of the outer yield surface, it is important to derive an equation to quantitatively describe the amount of that softening. The size of the outer yield surface depends on  $p_i$ . As previously discussed in Section 2.6.3,  $p_{cap}$  is related to  $p_i$  as follow:

$$p_{cap} = \frac{p_i}{e^{(-D_{min}/M_i)}} \quad (5.18)$$

From 5.18,

$$\dot{p}_{cap} = \frac{\dot{p}_i}{e^{(-D_{min}/M_i)}} \quad (5.19)$$

Since the stress point remains on the internal cap in unloading, mean effective stress in Equation 5.17 is equal to  $p_{cap}$  and,

$$\dot{p} / p = \dot{p}_{cap} / p_{cap} \quad (5.20)$$

From Equations 5.17 to 5.20,

$$\frac{\dot{p}_i}{p_i} = \dot{\varepsilon}_q^p H_u / \ln \left( \frac{p_{fy}}{p} \right) \quad (5.21)$$

Equation 5.21 describes the softening of the outer yield surface due to yield in unloading.

As the size of NorSand yield surface is controlled by  $p'_i$ , the term  $\dot{p}'_i / p'_i$  describes the change in the size of the outer yield surface due to an applied plastic shear strain increment relative to its original size before applying that increment. Figure 5.10 shows different outer yield surfaces corresponding to different points on the unloading stress path. The inner cap moves to the left with the stress path dragging the outer yield surface with it.

As previously discussed in Section 5.2.3, the potential surface in unloading is different from the yield surface (i.e. the internal cap). It can be noted from Figure 5.10 that plastic strain ratios (i.e.  $\dot{\varepsilon}_q^p / \dot{\varepsilon}_v^p$ ) represented by the arrows are not normal to the internal caps. However, the arrows are normal to the potential surfaces in Figure 5.11 (see Section 5.2.3 for the derivation of the potential surface).

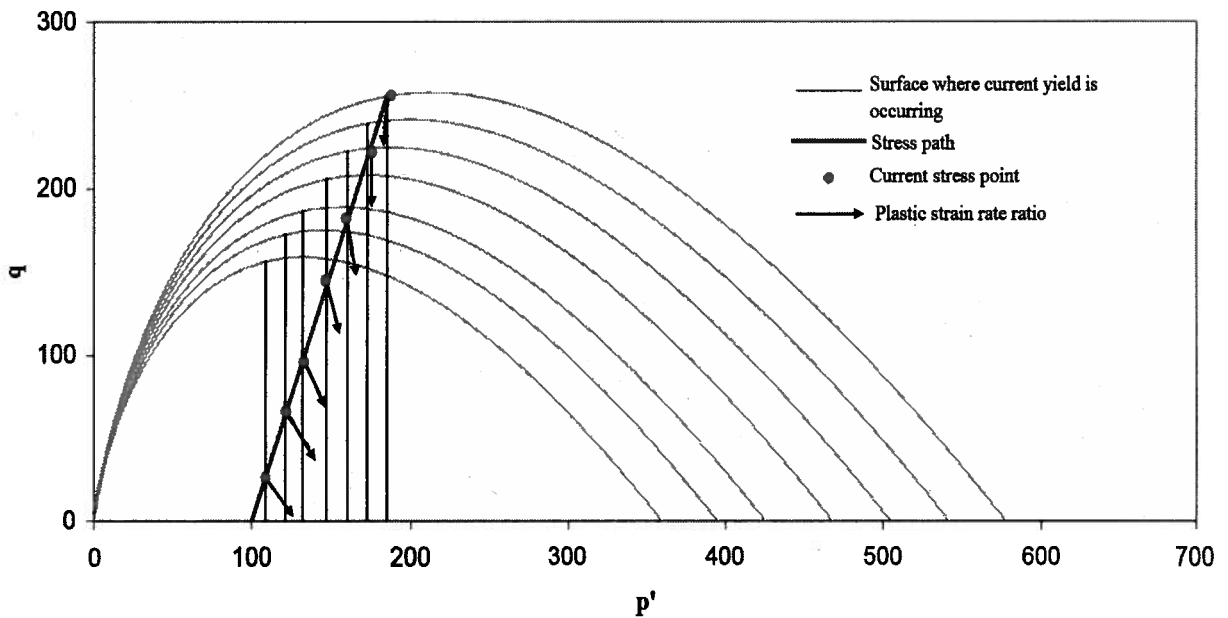


Figure 5.10. The direction of plastic strain increment ratios in unloading with the corresponding yield surfaces and internal caps.

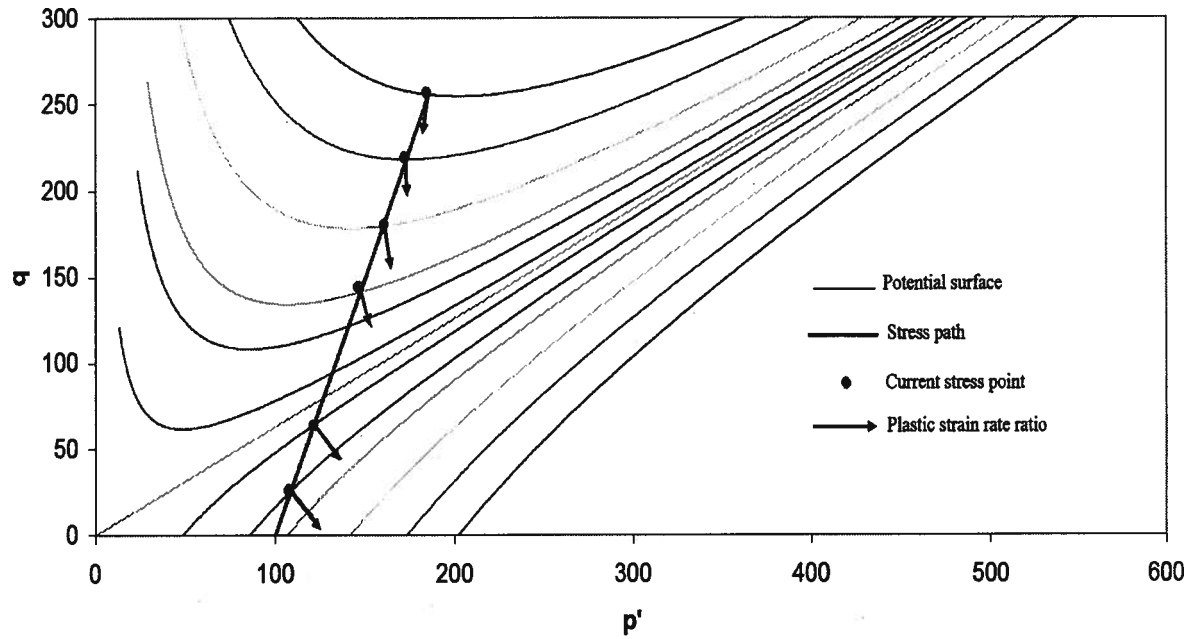


Figure 5.11. The direction of plastic strain increments ratios in unloading normal to the potential surfaces.

## 5.4. Comparison with other models

This chapter presented an unload-reload model for sands that is based on the NorSand soil model. One of the main features of the proposed model is that it yields in unloading. The model uses a non-associated flow rule in unloading. A summary of the unloading part of the model and the main assumptions are presented in Table 5.2. It was shown in this chapter that those assumptions match the observations from laboratory results presented in Chapter 4.

It was observed that soil becomes more dilatant in post-peak reloading loops. The behaviour was simulated in the model by a changing  $\chi$ . The value of  $\chi$  increases to a higher value of  $\chi_2$  once first peak is exceeded.

Table 5.2. Summary of the unloading part of the model.

Model components	Equation	Assumptions
Yield surface	$p'_{cap} = \frac{p'_i}{e^{(-D_{min}/M_i)}}$	<ul style="list-style-type: none"> <li>Yield in unloading happens on a vertical cap.</li> <li>The inner cap intersects the outer yield surface at a point that corresponds to <math>D_{min}</math> in loading.</li> </ul>
Flow rule	$D_u^p = \eta - M_u$ <p>Where,</p> $M_u = 2\eta_L - 1.5$ <p>And the minimum dilatancy in unloading is:</p> $D_u^p = 0.5 - M_u$	<ul style="list-style-type: none"> <li>Stress-dilatancy plots in unloading are perpendicular to those in loading.</li> <li>There is a direct relation between <math>M_u</math> and <math>\eta_L</math> of the previous loading.</li> <li>There is a minimum value for dilatancy in unloading.</li> </ul>
Hardening rule	<p>Movement of the internal cap:</p> $\dot{\epsilon}_q^p = \frac{1}{H_u} \frac{\dot{p}'}{p'} \ln \left( \frac{p'_{fy}}{p'} \right)$ <p>Softening of the outer yield surface in unloading:</p> $\frac{\dot{p}_i}{p_i} = \dot{\epsilon}_q^p H_u / \ln \left( \frac{p'_{fy}}{p'} \right)$	<ul style="list-style-type: none"> <li>The further the stress point from first yield in unloading, the slower the rate of movement of the internal cap.</li> <li>The outer yield surface softens due to yield in unloading.</li> </ul>

Jefferies (1997) derived an equation for stress-dilatancy in unloading based on the assumption that soil stores 'plastic' energy in loading that is recovered upon unloading. The model was described in Section 2.6.3. Starting from Nova's flow rule (Equation 5.22), and substituting for  $D^p$  and  $\eta$  (i.e.  $\dot{\epsilon}_v^p / \dot{\epsilon}_q^p$  and  $q/p'$ , respectively) and expanding yields Equation 5.23.

$$D^p = \frac{(M - \eta)}{(1 - N)} \quad (5.22)$$

$$q\dot{\epsilon}_q^p + p\dot{\epsilon}_v^p = Mp|\dot{\epsilon}_q^p| + Np\dot{\epsilon}_v^p \quad (5.23)$$

The terms on the left hand side of Equation 5.23 represent plastic work done. The right hand side represents what soil does with that work. The first term on the right hand side represents energy dissipation (Schofield and Wroth, 1968). The second term on the right hand side represents ‘plastic’ energy stored in loading and recovered in unloading (Jefferies, 1997). The saw tooth model gives a simple physical explanation of ‘plastic’ energy storage. Accordingly, the potential energy of individual soil particles is increased in loading as the particles assume new locations. This energy is released upon unloading as the particles tend to recover their original locations before loading. This is associated with contractive response in unloading. For the unloading phase,  $\dot{\epsilon}_q^p < 0$  and the  $N$  term in Equation 5.23 takes a negative sign as it represents ‘plastic’ energy recovered. Substituting and rearranging gives Equation 5.24 for stress-dilatancy in unloading. Equation 5.24 is plotted in Figure 5.12.

$$D^p = \frac{-M - \eta}{1 + N} \quad (5.24)$$

Equation 5.24 predicts different trends, more contraction in unloading, compared to laboratory data and the predictions of Equations 5.2 to 5.4 (Figure 5.12). The expression assumes that all ‘plastic’ energy stored in a loading phase must be released in the subsequent unloading phase which does not seem to be the case (i.e. only part of this energy is released in the subsequent unloading phase).

The proposed model in this chapter, similar to measured laboratory data, shows that contraction in unloading depends on shear deformation in previous loading. This is consistent with the saw tooth model where shear deformation is a major source of plastic work stored in loading and recovered in unloading. Jefferies (1997) was the first to adopt the saw tooth model to explain soil behaviour in unloading. Therefore, the proposed model and that for Jefferies (1997) are very similar conceptually.

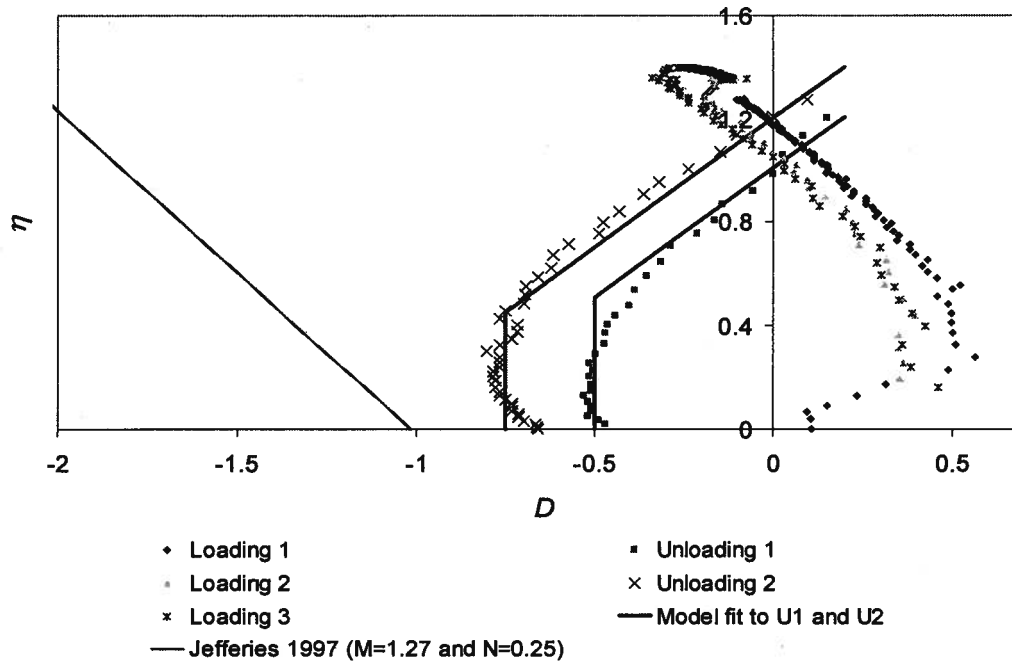


Figure 5.12. Predicted and measured stress-dilatancy for ES\_CID\_866.

The proposed model and that for Jefferies (1997) are different from Collins (2005) conceptual model that assumes plastic shear is not a significant source of plastic work storage while isotropic compression is the major source. Collins model was described in Section 2.6.2. Pure isotropic loading on the continuum scale is assumed and following the usual convention the applied work may be separated into an elastic and plastic component -  $\delta W = \delta W^e + \delta W^p$ . During loading, part of the applied work is dissipated ( $\delta W^p$ ) while the remainder is stored in terms of elastic compression of soil particles ( $\delta W^e$ ). In subsequent unloading, part of the stored elastic work is released causing dilation while the other part can only be released if associated with particles rearrangement (causes dilation as well). Particle rearrangement is not elastic and hence plasticity occurs during unloading. It is noteworthy that if soil particles were rigid, Collins model predicts no volumetric strains in unloading. However, it was shown in Chapter 3 based on Rowe's theoretical model that an assembly of rigid particles changes



in volume in unloading. Unloading according to Collins model is associated with dilation while laboratory data shows that significant contraction occurs in unloading.

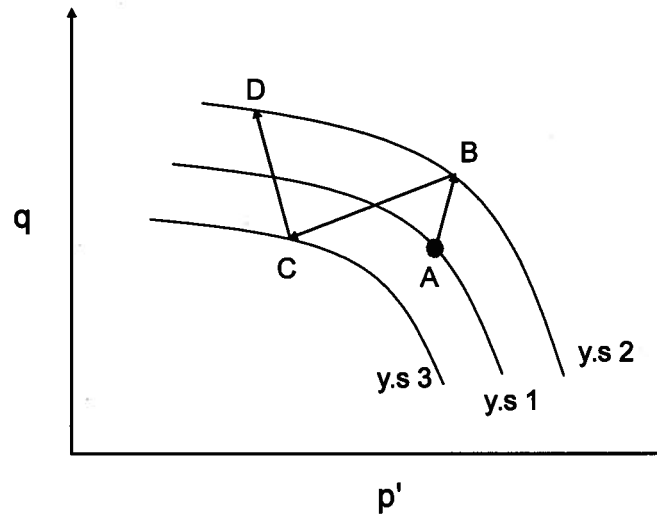


Figure 5.13. Drucker and Seereeram model (reproduced from Drucker and Seereeram, 1987).

Drucker and Seereeram (1987) proposed a hypothetical model for yield in unloading (Figure 5.13). It is assumed that point A, located on yield surface (y.s.) number 1, is the starting point. The yield surface moves to y.s. 2 during the loading path of A-B. Upon unloading (i.e. path B-C), the yield surface moves with the stress path reaching y.s. 3. During subsequent reloading (i.e. path C-D), the yield surface returns to y.s. 2. Accordingly, the yield surface always moves with the stress path. The model assumes that B-C is purely elastic while A-B and C-D are elasto-plastic.

Hardening in the proposed model which is identical to hardening proposed by Jefferies (1997) was discussed in Section 2.6.3 (Figure 5.14). Loading for normally consolidated conditions is elasto-plastic (Figure 5.14b). Unloading is purely elastic only for the phase before the stress path hits the internal cap (Figure 5.14c). In this phase, the outer yield surface does not move. Otherwise, unloading is elasto-plastic and causes softening of the outer yield surface. Reloading is elastic until the stress path hits the outer yield surface

(Figure 5.14d). Clearly, this is different from Drucker and Seereeram model described in the previous paragraph. The differences are summarized in Table 5.3.

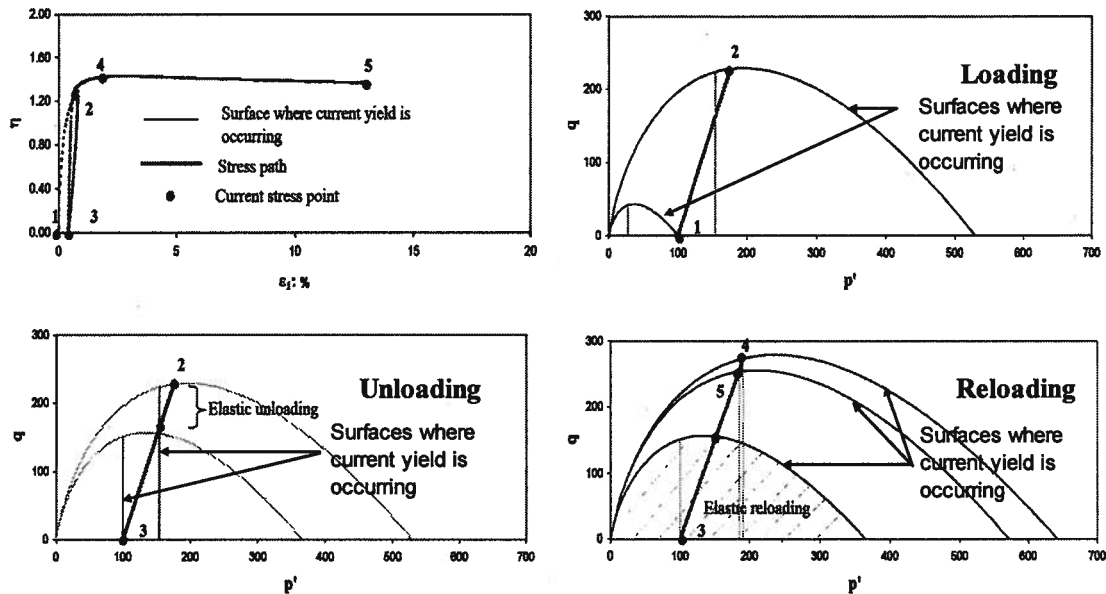


Figure 5.14. Hardening according to Jefferies (1997) (same as Figure 2.35).

Table 5.3. Comparison between hardening in the proposed model and Drucker and Seereeram (1987).

Phase/model	Proposed hardening (identical to Jefferies, 1997)	Drucker and Seereeram (1987)
Unloading	<ul style="list-style-type: none"> <li>• Either elastic or elasto-plastic</li> <li>• Yield surface moves only if stress path hits the cap</li> </ul>	<ul style="list-style-type: none"> <li>• Purely elastic</li> <li>• Yield surface always moves with the stress path</li> </ul>
Reloading	<ul style="list-style-type: none"> <li>• Either elastic or elasto-plastic</li> <li>• Yield surface moves if the stress path hits the outer yield surface</li> </ul>	<ul style="list-style-type: none"> <li>• Elasto-plastic</li> <li>• Yield surface always moves with the stress path</li> </ul>

## 5.5. Summary

This chapter presented a practical continuum model for unload-reload cycles on sands that takes the NorSand soil model as its starting point (Jefferies, 1993; Jefferies, 1997, Jefferies and Shuttle, 2005). One of the main features of the model is that it yields in unloading, a behaviour that is consistent with observations from lab data presented in Chapter 4 and the conclusions of the theoretical investigation of stress-dilatancy presented in Chapter 3. Like Jefferies model, yield in unloading is assumed to occur on a vertical cap in the  $p'-q$  space. Unlike Jefferies model, stress-dilatancy in unload and reload phases in the proposed model is consistent with the observations from lab data. Unloading is linked to previous loading such that the amount of dilation in unloading is directly proportional to the stress ratio at end of previous loading. The model accounts for the observed increase in dilation for post-peak reloading.

## 6. MODEL CALIBRATION

This chapter presents a load-unload-reload calibration of the model presented in Chapter 5 to ten triaxial tests on Erksak sand (see Table 4.2). The calibrated model is then used to predict two drained triaxial tests with unload-reload loops on Fraser River sand later in Chapter 7. As the unload-reload model uses NorSand as its starting point, a monotonic calibration of NorSand for both sands is performed first.

The monotonic calibration to Erksak sand is presented in Section 6.1. Section 6.2 is a monotonic calibration to Fraser River sand. Section 6.3 presents the unload-reload calibration to Erksak sand.

### 6.1. Monotonic calibration for Erksak sand

A calibration of NorSand for Erksak sand under monotonic loading in a triaxial test is presented in this section. The calibration uses the tests described earlier in Chapter 4 (Tables 4.2 & 4.3). The required parameters were previously described in Section 2.1.2 and Section 2.5. Table 2.2, reproduced here for convenience as Table 6.1, is a summary of the required parameters and their typical ranges. The critical state parameters  $\Gamma$  and  $\lambda$  are the slope and the y-intercept of the critical state line in  $e$ - $\log(p')$  plot, respectively. The critical stress ratio for triaxial compression,  $M_{cs}$ , is  $q/p'$  at critical state. The plastic hardening parameter ' $H$ ' specifies the rate of the hardening of the yield surface. The slope of a trend line with zero intercept through the data points in the  $D_{min}$ - $\psi$  is designated as  $\chi$  (e.g. Figure 2.29). It is used to control the maximum allowable absolute value of the dilation rate. The volumetric coupling parameter ' $N$ ' was introduced by Nova (1982). It is based on fits to stress-dilatancy from the results of laboratory tests.

Finally, the elasticity parameters are the dimensionless shear rigidity parameter ( $G/p'$ ) and Poisson's ratio.

Table 6.1. Typical ranges for monotonic parameters (same as Table 2.2, modified after Jefferies and Shuttle, 2005).

Parameter	Typical range	Description
<b>Critical state</b>		
$\Gamma$	0.9-1.4	The y-intercept of the e-log( $p'$ ) curve at 1KPa
$\lambda_e$	0.01 – 0.07	The slope of CSL in e-log( $p'$ ) space defined on base e
$M_{tc}$	1.2-1.5	$q/p'$ at critical state
<b>Plasticity</b>		
$H$	50-500	Plastic hardening modulus
$\chi_{tc}$	2.5-4.5	A parameter that limits the hardening of the yield surface
$N$	0.2-0.4	The volumetric coupling parameter (used in Nova's rule)
<b>Elasticity</b>		
$I_r$	100-800	Dimensionless shear rigidity ( $=G/p'$ )
$\nu$	0.1-0.3	Poisson's ratio

### 6.1.1. Critical state parameters

There is more than one way to obtain  $M_{tc}$  from triaxial data. Ghafghazi & Shuttle (2006) reviewed four methods reported in the literature to obtain the critical state stress ratio from drained triaxial tests: the terminal value of stress ratio method, maximum contraction method, Bishop method, and Stress-dilatancy method.

1. Plotting the curves for each test in the stress ratio vs. strain space and simply picking up the terminal value for the stress ratio. The problem with this method is that the dense tests, and even most of the loose tests, do not go far enough to reach the critical state.

2. The stress ratio at maximum contraction is taken as  $M_{tc}$ . This method assumes that the stress ratio at maximum contraction is equivalent to that at the critical state. The point of maximum contraction is not the same as the critical state and hence the method would only be appropriate if the true stress dilatancy behaviour of soil was a unique locus (i.e. only one stress ratio corresponded to one dilatancy). Although this assumption has been used in flow rules such as CamClay, modified CamClay, and Nova, real soils do not show this behaviour. The real measured soil response shows a different stress ratio at maximum contraction and at the critical state, consistent with Rowe's idea of an evolving  $M$  with increasing strain. More recent soil models such as NorSand and Li and Dafalias's (2000) model also incorporate this evolving  $M$ . Therefore this method of determining  $M_{tc}$  provides poor predictions.
  
3. Bishop (1971) suggests plotting the data for all the available tests in  $D_{min} - \eta_{max}$  space. The method is based on the idea that a very loose soil should reach the critical state at peak stress ratio, i.e.  $D_{min}$  and  $\eta$  at peak should be zero and  $M_{tc}$  respectively. Hence, assuming the trend in the data is linear (which is consistent with experimental measurements), the y-intercept of a trend line through the data points will correspond to  $M_{tc}$ . The unload-reload Erksak tests have different peaks associated with different reloading phases as was previously discussed in Section 4.3. A peak is termed a 'first peak' if peak strength was never exceeded in previous loading or reloading loops for a certain test. All other peaks are termed 'second peaks'. Two linear trend lines are plotted for first and second peaks data points in Figure 6.1 resulting in two  $M_{tc}$  values. According to critical state, a single sand must have a single  $M_{tc}$  value. Therefore, the two  $M_{tc}$  values must be identical. However,  $D_{min}$  is affected by changes in fabric due to shearing in different reloading loops and therefore  $M_{tc}$  based on extrapolating data in  $D_{min} - \eta_{max}$  is expected to change for different reloading loops. The trend line for the first peaks gives  $M_{tc} = 1.15$  ( $\phi_{cv} = 28.85^\circ$ ) while that for the second peaks gives a very similar value of  $M_{tc} = 1.1$  ( $\phi_{cv} = 27.7^\circ$ ). Therefore, Bishops method gives  $M_{tc}$

in the range of 1.1-1.15. It can be noticed that the two best fit lines are parallel. It seems that slope of the lines is very similar for different reloading phases. However, the y-intercept is slightly different.

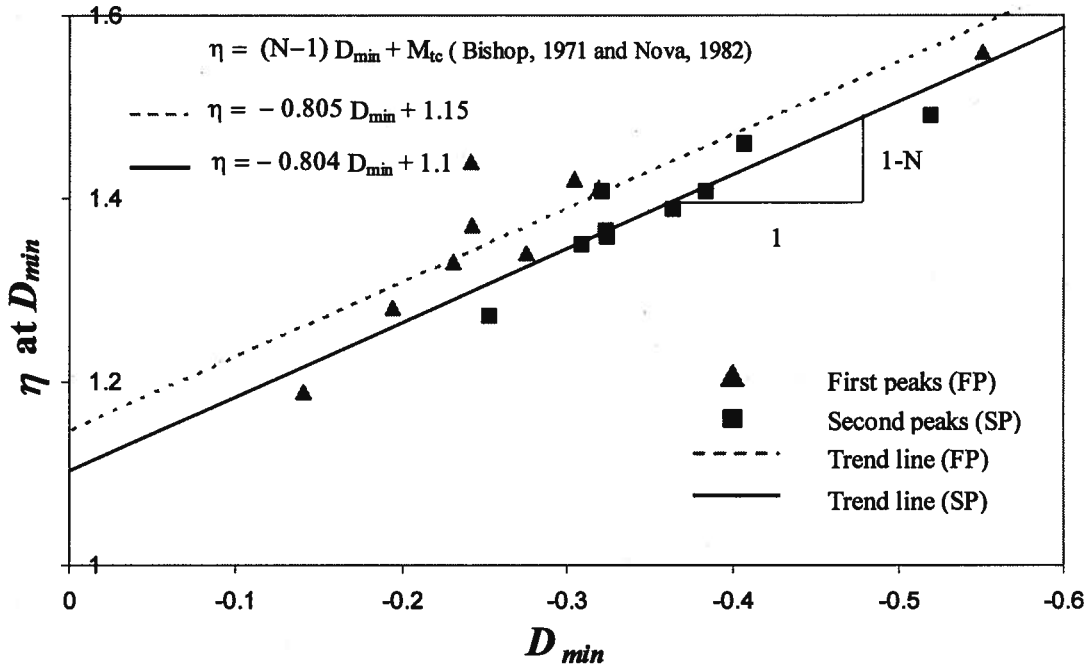


Figure 6.1.  $M_{tc}$  using Bishop's method for Erksak sand.

4. The stress-dilatancy method for obtaining  $M_{tc}$  suggests linearly extrapolating the returning curves in the dilatant part of the stress-dilatancy plots to  $D = 0$  (see Figure 6.2). The extrapolated value of  $\eta$  at  $D = 0$  is  $M_{tc}$ . Table 6.2 shows  $M_{tc}$  using the stress-dilatancy method for all tests but for ES\_CID\_868 (post peak behaviour for this test is questionable). Stress-dilatancy method gives  $M_{tc}$  values of 1.24-1.35 as shown in Figure 6.3 with an average of 1.286 ( $\phi_{cv} = 31.97^\circ$ ).

Ghafghazi & Shuttle (2006) recommended the use of the Bishop method or Stress-Dilatancy approach. The Bishop method gave a lower  $M_{tc}$  than the stress-dilatancy method. Ghafghazi & Shuttle (2006) showed that “with only a small number of tests available, the Bishop method is sensitive to any outlying data points”. Table 6.3 shows that the range of  $M_{tc}$  obtained in this work using 9 tests with the Bishop method is lower

than the  $M_{tc}$  obtained by Ghafghazi & Shuttle (2006) for 34 tests using the same method. However, despite using many fewer tests than Ghafghazi and Shuttle, the  $M_{tc}$  values of both sets of authors using the Stress-Dilatancy method are very similar. Therefore, the stress-dilatancy method seems to provide a repeatable value of  $M_{tc}$  even for a small number of tests. Therefore, a value of  $M_{tc} = 1.286$  ( $\phi_{cv} = 31.97^\circ$ ) was adopted for Erksak sand.

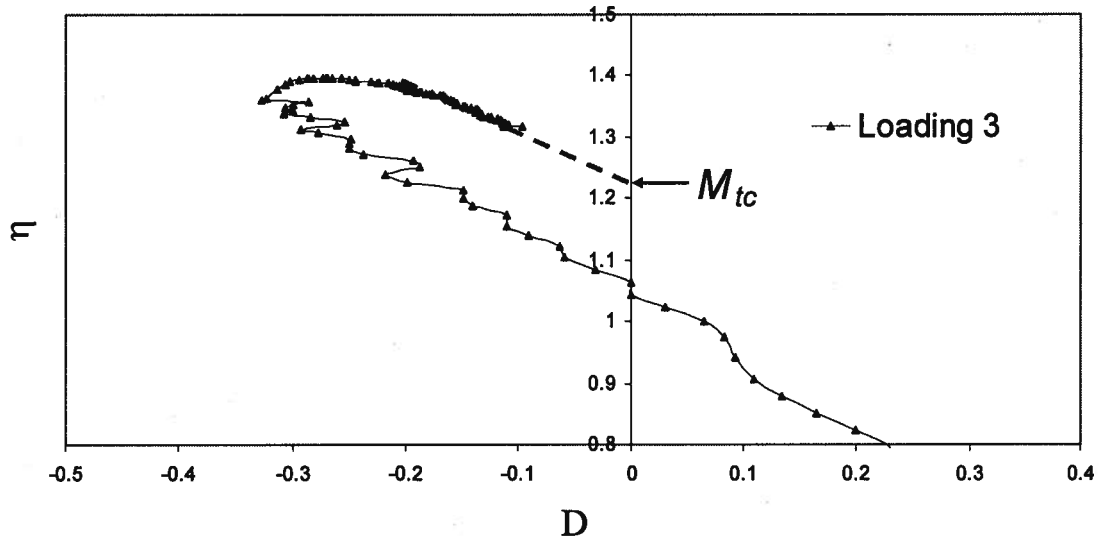


Figure 6.2.  $M_{tc}$  using stress-dilatancy method (ES\_CID\_871).



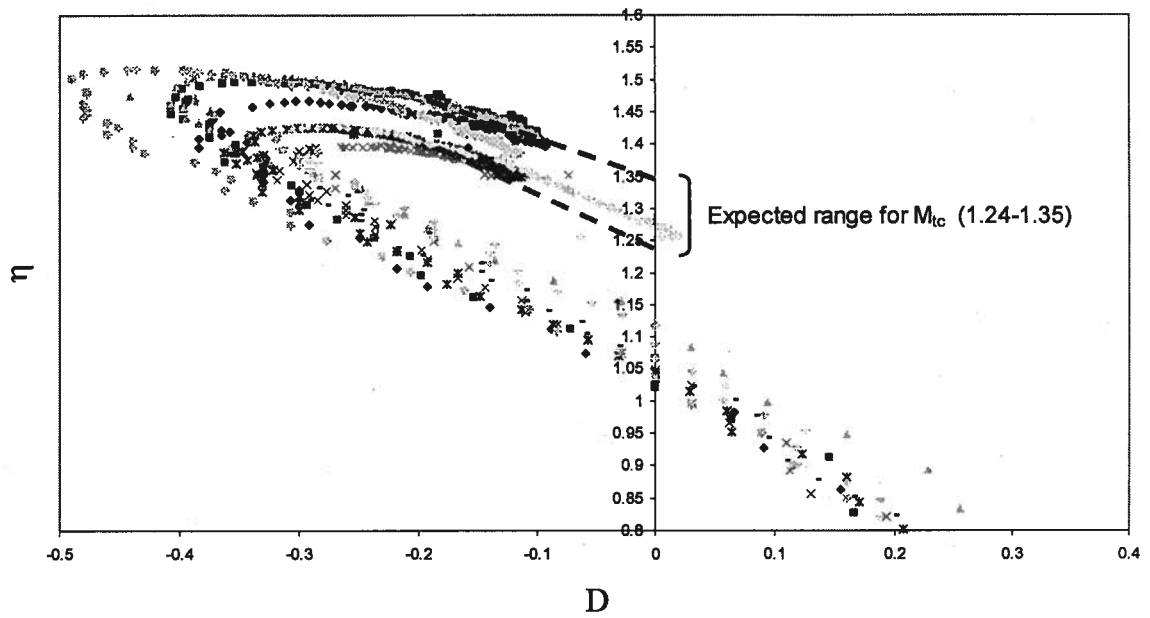


Figure 6.3. Range of  $M_{tc}$  using the stress-dilatancy method from the last reloading loops for the 9 tests in Table 4.2.

Table 6.2.  $M_{tc}$  using stress-dilatancy method for the unload-reload tests on Erksak sand.

Test name	$M_{tc}$ (extrapolated) <sup>1</sup>
CID-G860	1.33
CID-G861	1.35
CID-G862	1.33
CID-G866	1.27
CID-G867	1.25
CID-G868	Ignored <sup>2</sup>
CID-G870	1.24
CID-G871	1.24
CID-G872	1.27
CID-G873	1.3
<b>Average</b>	<b>1.286</b>

<sup>1</sup> All values are extrapolated but for CID-872 that reached critical state.

<sup>2</sup> Post-peak behaviour for this test is judged to be unrepresentative.

Table 6.3. Summary of  $M_{tc}$  values for Erksak sand

Method/source	Current work (9 tests)	Ghafghazi & Shuttle, 2006 (34 tests)
Bishop method	1.1 (1 <sup>st</sup> peak) 1.15 (2 <sup>nd</sup> peak)	1.26
Stress-Dilatancy method	1.286	1.28

The critical state parameters in  $e$ - $\log p'$  space were determined using undrained triaxial tests from Jefferies and Been, 2006 (see Figure 6.4). The tests were described in Section 4.2 and summarized in Table 4.3. The derived critical state parameters are  $\Gamma = 0.82$  and  $\lambda_{10} = 0.031$  (equivalent to  $\lambda_e = 0.0135$ ) which are very similar to  $\Gamma = 0.816$  and  $\lambda_{10} = 0.031$  in Jefferies and Been (2006). These derived parameters are accurate for  $p' < 800$  kPa. Been et al. (1991) showed that at higher mean effective stresses the line becomes steeper, attributed to grain crushing, and therefore a single linear CSL would not be applicable. Hence the fits for tests ES\_CID\_870, ES\_CID\_871, and ES\_CID\_872 with high mean effective stress of 800 kPa are not expected to be accurate.

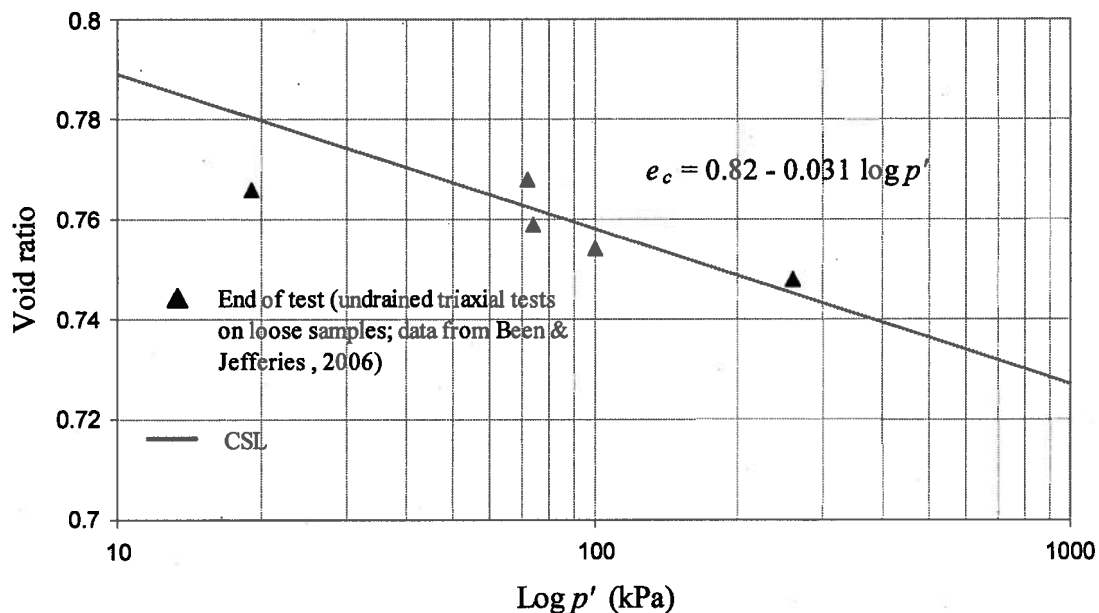


Figure 6.4. CSL determination for Erksak sand from loose undrained tests.

### 6.1.2. Elasticity parameters

Ideally, elastic shear modulus is measured using bender elements. However, tests with bender elements on Erksak sand were not available. In the absence of bender tests, elastic properties may be estimated from the elastic portion of unload-reload loops. Jefferies and Been (2000) presented hydrostatic compression triaxial tests with unload-reload cycles. Equation 6.1 gives the elastic bulk modulus from best fit to their experimental data:

$$K = \frac{C}{(e - e_s)} \left( \frac{p'}{p_{ref}} \right)^{0.5} p_{ref} \quad (6.1)$$

where  $C$  is a material 'compressibility' constant equal to 260,  $p_{ref}$  is 100 kPa and  $e_s$ , the void ratio at which the volumetric compressibility becomes zero is equal to 0.355. The parameter  $e_s$  represents the void ratio where soil behaviour changes from predominantly particulate to that of a solid, and is significantly less than the typically defined  $e_{min}$  (e.g. ASTM D-4254-00). Assuming a Poisson's ratio of 0.2, the dimensionless shear modulus is given by:

$$I_r = \frac{G}{p} = \frac{3}{4} \frac{K}{p} \quad (6.2)$$

However, there is scatter of as much as  $\pm 50\%$  in Jefferies and Been data. The elastic bulk modulus can be directly obtained from the unload-reload tests on Erksak sand presented in Chapter 4. Figure 6.5 is an enlarged view of the elastic part at the beginning of L3 for ES\_CID\_866. It can be seen that the plot in that zone is nearly linear and it is assumed that all deformations are elastic. The elastic bulk modulus was calculated directly from the data points for that elastic zone using a linear difference approximation as in the following equation:

$$K_{j+1/2} = \frac{p_{j+1} - p_j}{e_j - e_{j+1}} \left( 1 + \frac{e_{j+1} + e_j}{2} \right) \quad (6.3)$$

Where  $j+1/2$  is the midpoint between consecutive measurements at which  $K$  is computed,  $j$  is the previous measurement, and  $j+1$  is the next measurement. Figure 6.6 plots the results of Equations 6.1 and 6.3 for the elastic part of L3. It is clear that Equation 6.1 underestimates the values of the bulk modulus compared to those directly computed from laboratory data (i.e. Equation 6.3). A higher value of  $C = 750$  in Equation 6.1 would give a better estimate of  $K$ . A better fit to the laboratory data was obtained using equation 6.1 using  $C = 750$ , and  $e_s$  equal to 0.355 (i.e. the same  $e_s$  as in Jefferies and Been, 2000 but different  $C$ ) as shown in Figure 6.6.

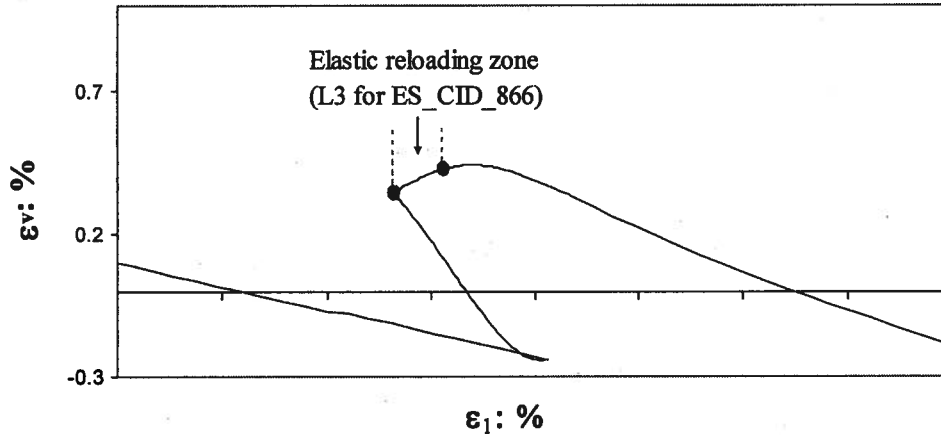


Figure 6.5. Enlarged view of the elastic part in L3 for ES\_CID\_866.

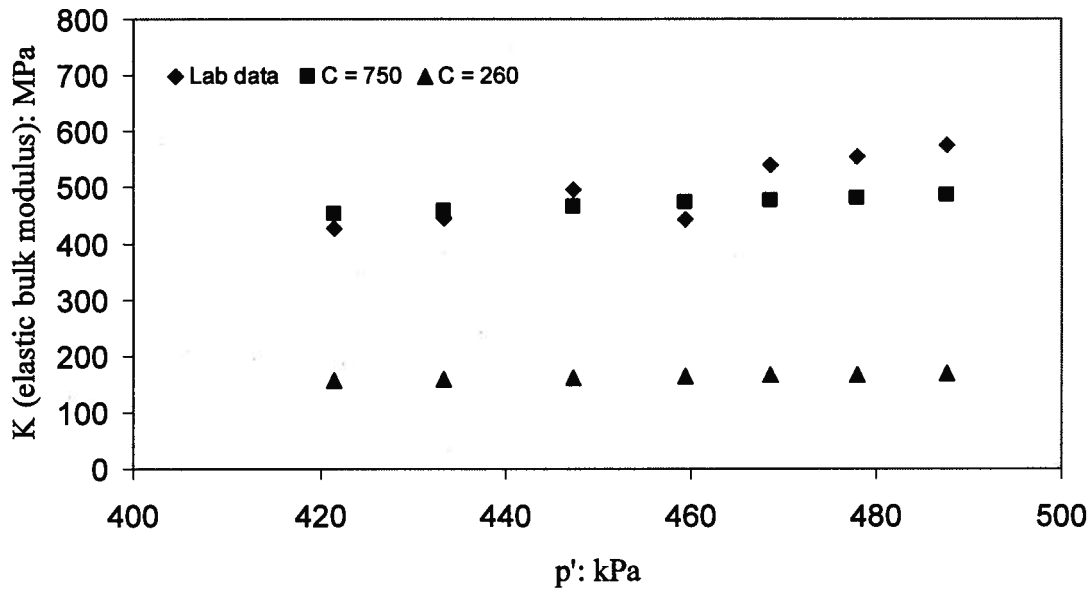


Figure 6.6. The elastic bulk modulus from Equations 6.1 and 6.3 against  $p'$  for the elastic zone in L3 for ES\_CID\_866.

### 6.1.3. Plasticity parameters

The monotonic loading version of NorSand requires three plasticity parameter;  $N$ ,  $\chi$  and  $H$ .

The  $N$  parameter in NorSand is defined in the same way as the  $N$  used by Nova (1982). It is derived from experimental stress-dilatancy data. The slope of the trend line through  $\eta_{max} - D_{min}$  plot is  $(N-1)$  as shown in Figure 6.1. The two trend lines through both the first and second peak points have very similar slopes of around 0.8. Therefore, the value of  $N$  is 0.2.

Figure 6.7 plots the dilatancy at peak versus the corresponding state parameter at peak. The figure clearly shows that the slope of the trend for the dilatancy at first peak is smaller than that for second loading (i.e. after one unload-reload loop). The NorSand

plasticity parameter  $\chi$  is defined as the slope of a line through the points in Figure 6.7, and correspondingly there are two values for  $\chi$  as discussed in Chapters 4 and 5. Note that the best fit straight line through the second peaks does not have a Y-intercept of zero. However, the trend line for the second peaks is required to pass through the point (0,0) as if peak stress ratio (equivalent to minimum dilatancy) occurs at the critical state then, by definition,  $D_{min}$  must have a value of zero.

The hardening modulus,  $H$ , was determined by iterative forward modelling of each drained pluviated triaxial test. The value of  $H$  was observed to be correlated to the initial value of state parameter (Figure 6.8). Appendix B shows the fits for all of the drained tests on Erksak sand in  $\eta - \varepsilon_1$  and  $\varepsilon_v - \varepsilon_1$  plots; an example fit for test ES\_CID\_867 is given in Figure 6.9. The general trend line for “ $H$ ” (i.e.  $H = -1727.3 \psi_o + 75.9$ ) was used to obtain the monotonic parts of the fits (i.e. before unload-reload cycles).

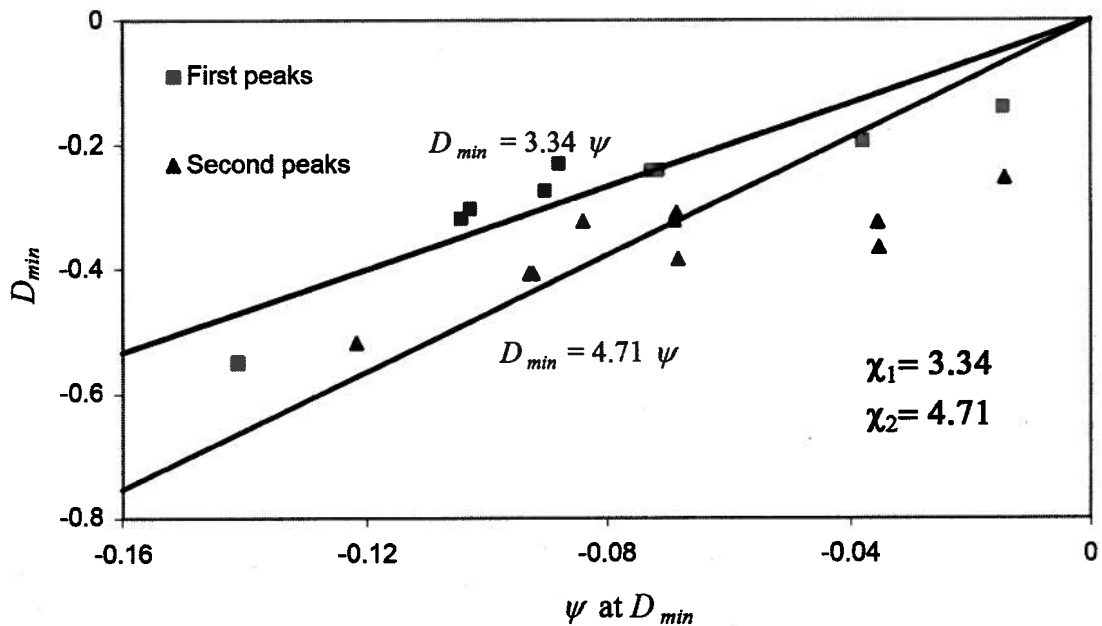


Figure 6.7. Trend lines through  $D_{min}$  vs.  $\psi$  at  $D_{min}$  for first and second peaks for Erksak sand

Although the hardening modulus is expected to also depend on initial fabric, for Erksak sand the moist tamped sample, ES\_CID\_868, also fitted well in the overall trend for the pluviated samples. Tests ES\_CID\_870, ES-CID\_871, and ES-CID\_872 showed a different trend for  $H$  values. This is likely due to the curved critical state line observed by Been et al. (1991), often associated with grain crushing at high mean effective stress values. If a steeper critical state line was used at higher mean effective stress, the value of initial state,  $\psi_o$ , for tests ES-CID\_870, ES-CID\_871, and ES-CID\_872 would be less negative and closer to the typical trend line. Hence these three tests were ignored in the calibration.

#### 6.1.4. Summary of Erksak monotonic calibration

A summary of the Erksak monotonic calibration is presented in Table 6.4. Figure 6.10 summarised the procedure followed for the monotonic calibration of NorSand.

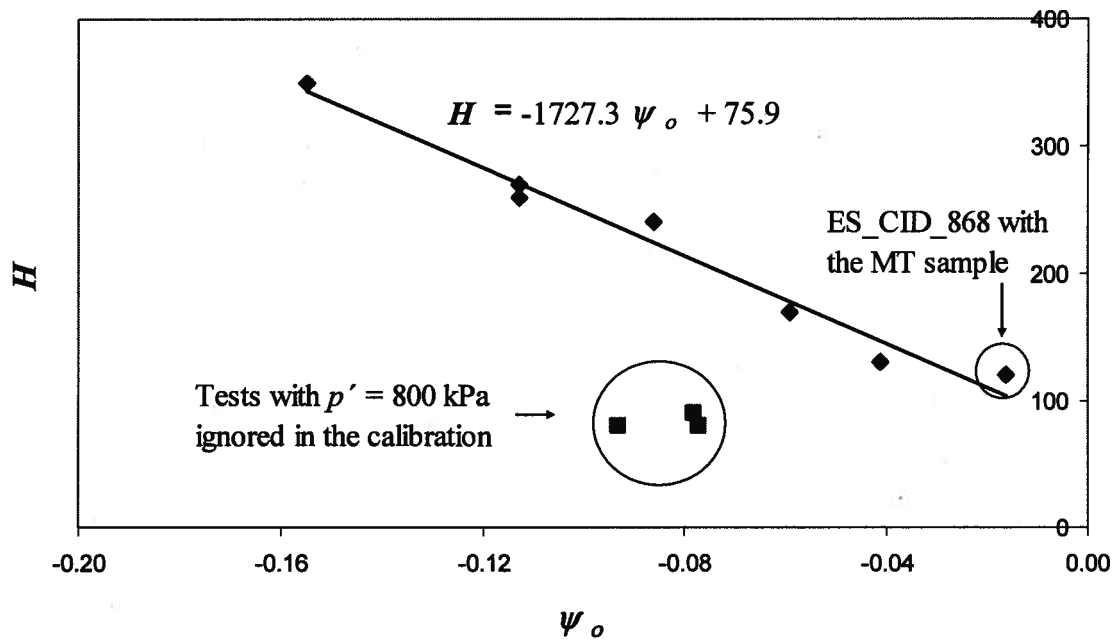


Figure 6.8. Best fit to  $H$  vs.  $\psi_o$  for Erksak sand.

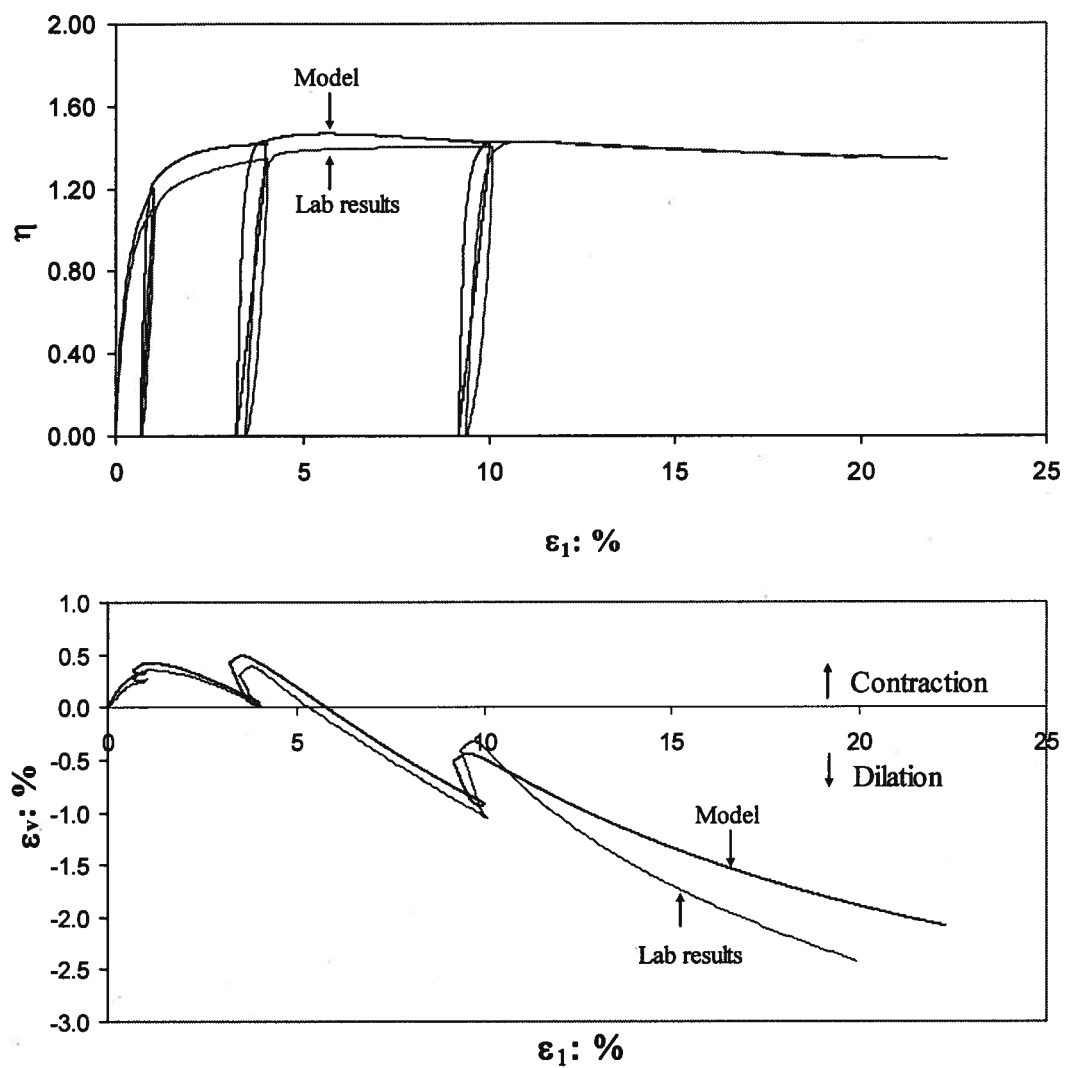


Figure 6.9. Example fit to test ES\_CID\_867.



Table 6.4. Summary of monotonic calibration for Erksak sand

Parameter	Erksak sand	Remark
<b>CSL</b>		
$\Gamma$	0.82	Altitude of CSL at 1 KPa
$\lambda$	0.0135	Slope of CSL, defined on base e
$M_{tc}$	1.286	Triaxial critical friction ratio
<b>Plasticity</b>		
$H$	$-1727.3 \psi_o + 75.9$	Monotonic plastic hardening parameter
$\chi_{tc}$	3.34	Slope of the line relating $D_{min}$ to $\psi$ at $D_{min}$ defined for triaxial conditions
$N$	0.2	The volumetric coupling parameter (used in Nova's rule)
<b>Elasticity</b>		
$I_r$	$\frac{3}{4} \frac{C}{(e - e_s)} \left( \frac{p'}{p_{ref}} \right)^{-0.5}$	Rigidity $I_r = \frac{G}{p}$ , $C = 750$ , $p_{ref} = 100$ kPa, and $e_s = 0.355$
$\nu$	0.2	Poisson's ratio (assumed)

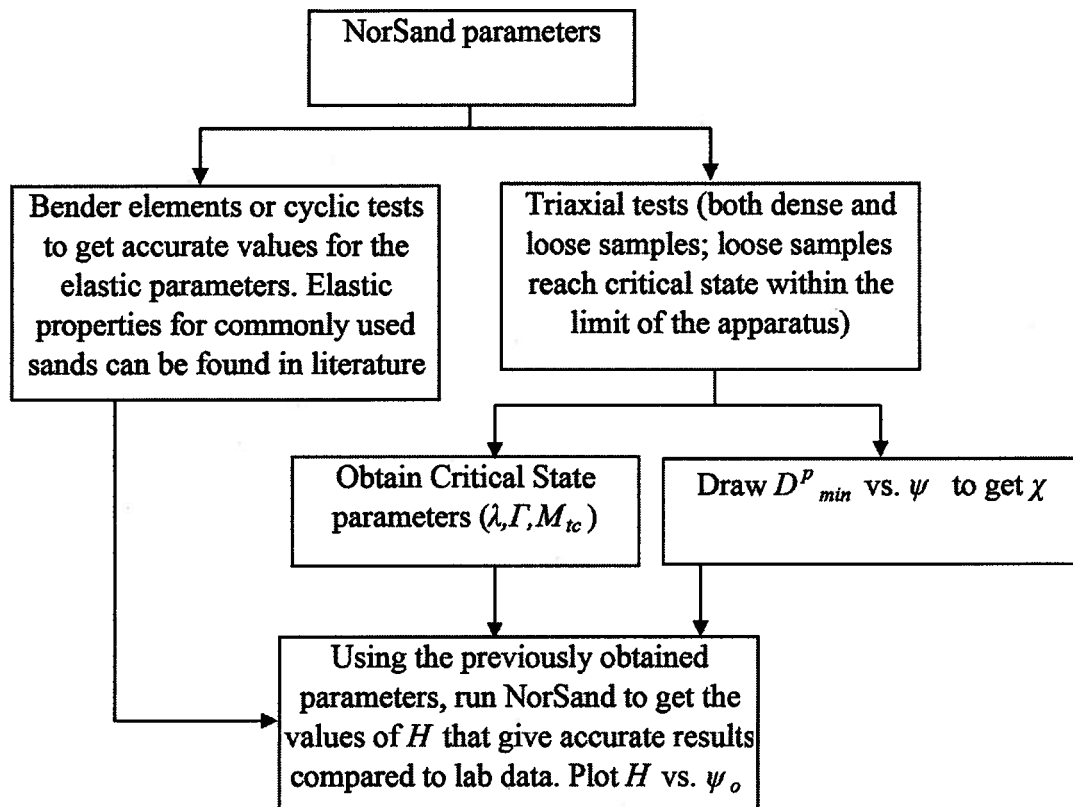


Figure 6.10. Recommended procedure for obtaining NorSand parameters.

## 6.2. Monotonic calibration for Fraser River sand

The same general procedure was used for the monotonic calibration of Fraser River sand as for Erksak sand in Section 6.1. Therefore, the calibration to Fraser River sand is only briefly described in this section. The tests used in the calibration were described in Section 4.2 (see Table 4.5).

### 6.2.1. Critical State parameters

It was shown in the previous section that the Bishop method can provide unrealistic parameter values, especially for small number of tests (four tests in this case). This also appeared to be the case for Fraser River Sand where the Bishop method gave a higher

value of  $M_{tc}$  of 1.55 ( $\phi_{cv} = 38.02^\circ$ ), see Figure 6.11, which is greater than  $M_{tc}$  from the stress-dilatancy approach. Therefore, the stress-dilatancy method was adopted. The post-peak behaviour for two of the tests (FR\_CID\_03 & FR\_CID\_06) was questionable. Figure 6.12 shows that the post-peak data points (i.e. the returning curves) for ES\_CID\_03 in stress-dilatancy plot are scattered and do not follow a consistent trend. However, post-peak behaviour for tests FR\_CID\_04 & FR\_CID\_05 seems to be more reliable. Both tests gave  $M_{tc}$  of 1.42 ( $\phi_{cv} = 35.04^\circ$ ) using the stress-dilatancy method (see Figure 6.13 for FR\_CID\_04). Therefore,  $M_{tc}$  of 1.42 was adopted for Fraser River sand. This is similar to  $M_{tc}$  of 1.4 ( $\phi_{cv} = 34.58^\circ$ ) obtained by Chillarige et al. (1997).

The critical state parameters in the  $e$ -log  $p'$  space are deduced from the data for the six tests as in Figure 6.14. Chillarige et al. (1997) also performed triaxial tests on Fraser River sand and got the critical state parameters. The line in Figure 6.14 has a larger y-intercept value than that of Chillarige et al. (1997), but it is steeper. Most of the Chillarige et al. data match the line in Figure 6.14 except for two outliers. It is noteworthy that those two tests are drained and therefore might not have reached critical state. Drained tests that reach the critical state at large strains are often associated with localization.

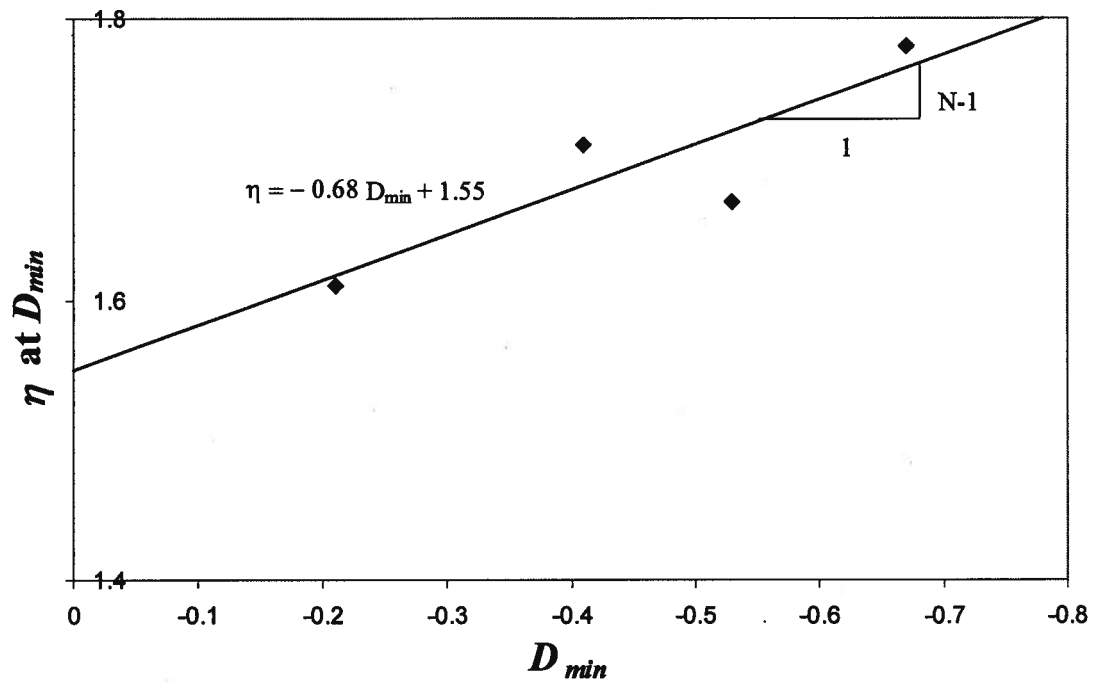


Figure 6.11.  $M_{tc}$  using Bishop method for Fraser River sand.

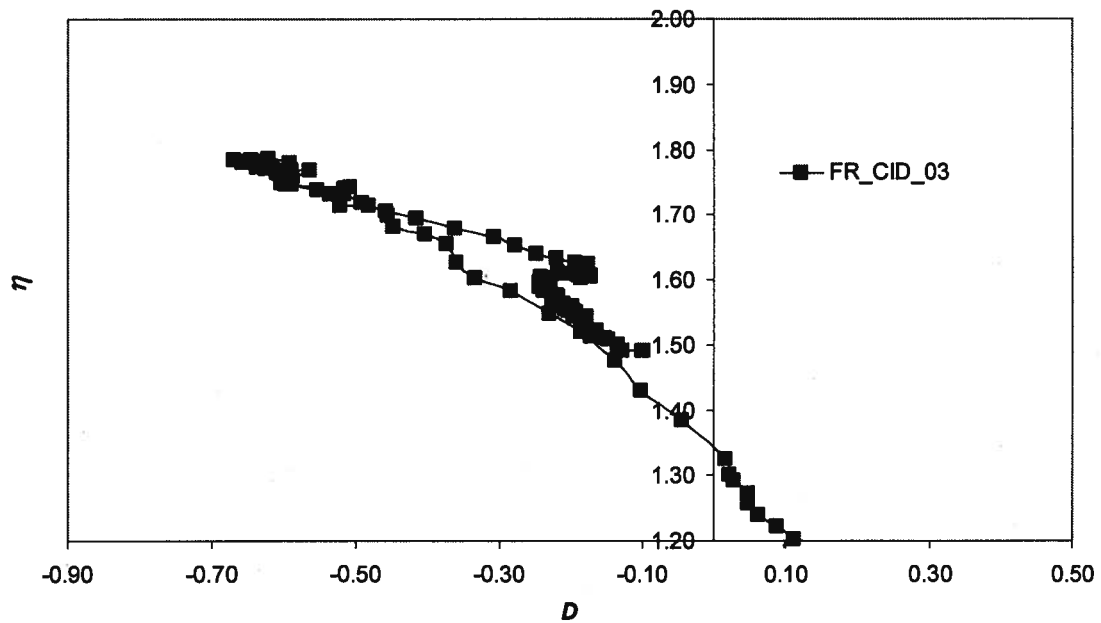


Figure 6.12. Enlarged view of the dilatant zone for FR\_CID\_03.

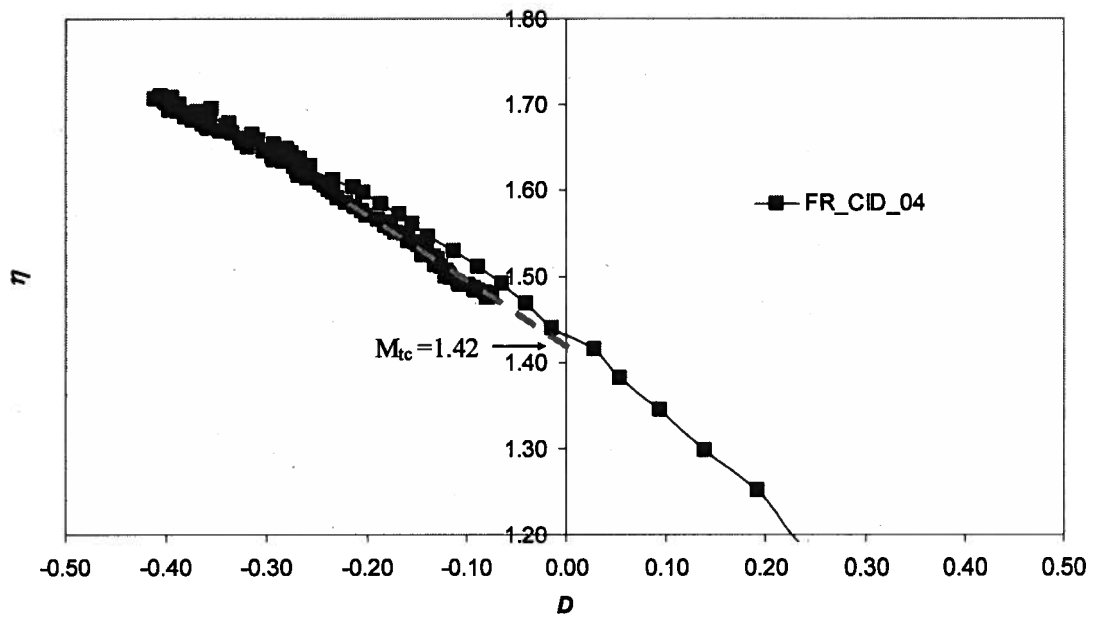


Figure 6.13.  $M_{tc}$  using stress-dilatancy method for FR\_CID\_04.

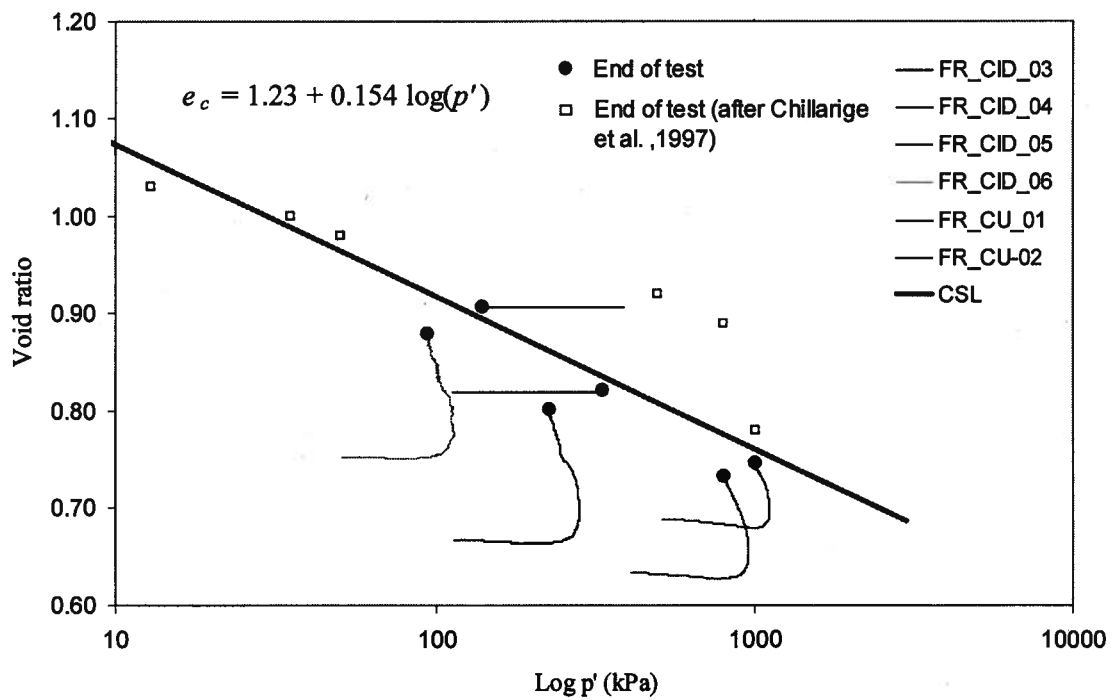


Figure 6.14. CSL for Fraser River sand.

### 6.2.2. Elasticity parameters

Chillarige et al. (1997) performed tests with bender elements on Fraser River sand. They introduced the expression in Equation 6.4. It was adopted in the code to define elastic conditions.

$$G_o = \rho \left[ (295 - 143e) \left( \frac{p}{p_a} \right)^{0.26} \right]^2 \quad (6.4)$$

### 6.2.3. Plasticity parameters

The value of the  $\chi$  parameter was determined as 4.34 from the best fit to the data points in peak dilatancy vs. state parameter at peak (Figure 6.15). The slope of the Bishop line in Figure 6.11 is equal to  $N-1$ . Therefore the value of  $N$  is 0.32. Finally, the plastic hardening modulus,  $H$ , which gives a good fit to stress strain and volumetric strain curves is correlated to initial state parameter (see Figure 6.16). The calibrated model results as compared to laboratory tests results are included in Appendix C, and an example fit to test FR\_CID\_03 is provided in Figure 6.17.

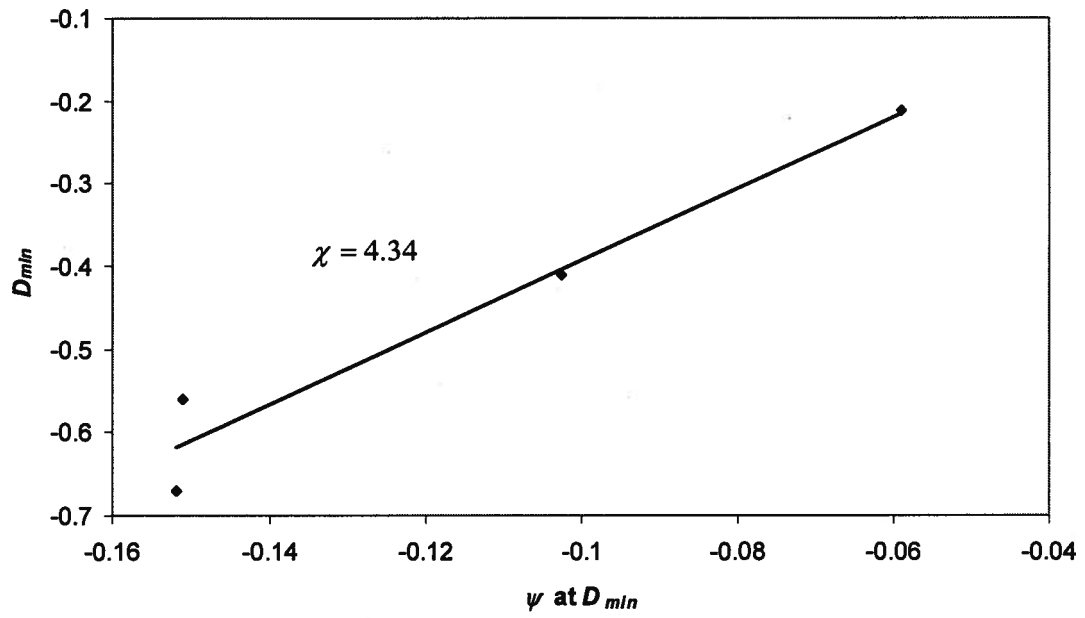


Figure 6.15. Peak dilatancy vs.  $\psi$  at peak for Fraser River sand.

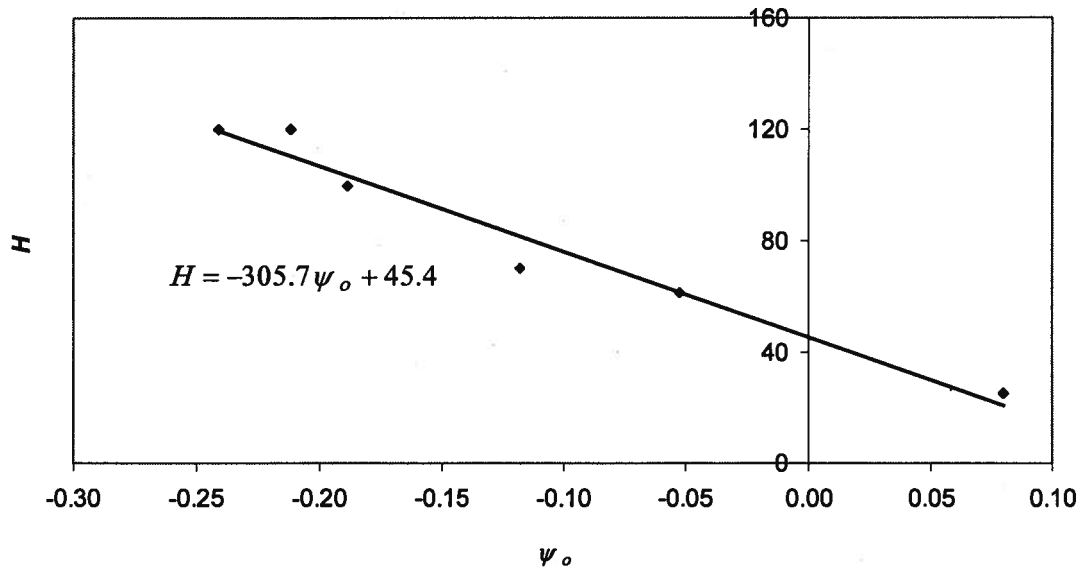


Figure 6.16. Best fit for  $H$  for monotonic triaxial tests on Fraser River sand.

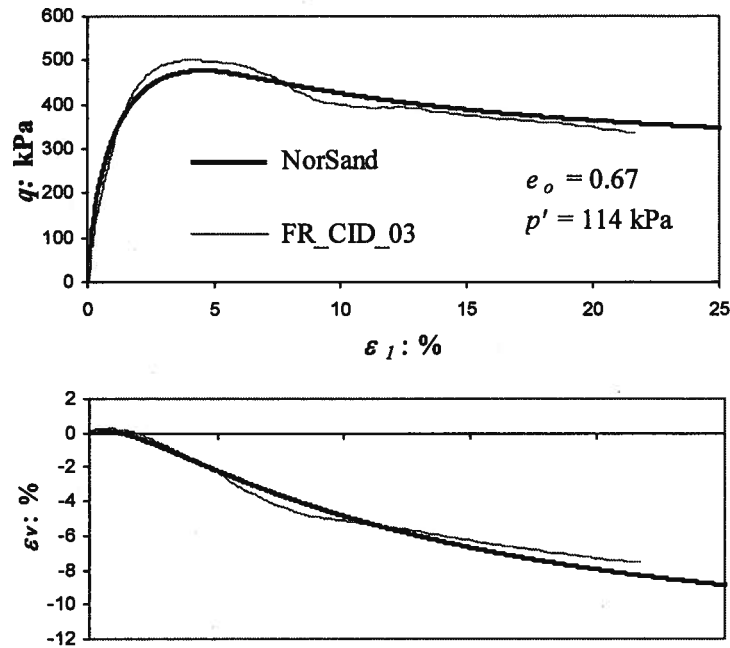


Figure 6.17. Example fit to test FR\_CID\_03.

Table 6.5. Summary of NorSand monotonic calibration to Fraser River sand.

Parameter	Fraser River Sand	Remark
<b>CSL</b>		
$\Gamma$	1.23	Altitude of CSL at 1 KPa
$\lambda$	0.067	Slope of CSL, defined on base e
$M_{tc}$	1.42	Triaxial critical friction ratio
<b>Plasticity</b>		
$H$	$-305.7 \psi_o + 45.4$	Monotonic plastic hardening parameter
$\chi_{tc}$	4.34	Slope of the line relating $D_{min}$ to $\psi$ at $D_{min}$ defined for triaxial conditions
$N$	0.32	The volumetric coupling parameter (used in Nova's rule)
<b>Elasticity</b>		
$I_r$	$G = \rho \left[ (295 - 143e) \left( \frac{p'}{p_{ref}} \right)^{0.26} \right]^2$ After Chillarige et al. (1997)	$I_r = \frac{G}{p'}$ , $p_{ref} = 100$ kPa and $\rho$ is soil density in ton/m <sup>3</sup>
$\nu$	0.2	Poisson's ratio (assumed)



#### 6.2.4. Summary of Fraser River Sand monotonic calibration

Table 6.5 presents a summary of NorSand monotonic calibration to Fraser River sand.

### 6.3. Unload-reload calibration to Erksak sand

The unload-reload model requires three additional parameters: “ $H_u$ ” and “ $H_r$ ”, the plastic hardening modulus in unloading and reloading respectively and “ $\chi_2$ ”, the slope of a trend line through the second peaks.  $\chi_2$  is used to capture the effect of induced fabric changes when stress conditions exceed peak.

Ideally it would be preferable to relate the three additional unload-reload parameters to parameters derived from a monotonic calibration. However, this is the first calibration of the unload-reload model and therefore it is being used to provide guidance on whether  $H_u$ ,  $H_r$  and  $\chi_2$  show any relation to the monotonic calibration.

The plastic hardening modulus in unloading “ $H_u$ ” specifies the rate of movement of the internal cap (i.e. inner yield surface) as previously discussed in Section 5.3. It is used in the model as in Equation 5.17. Laboratory data on Erksak sand suggests that  $H_u$  is shear strain level (at the start of unloading) dependent and that the response of soil in unloading is softer for higher strain levels. Figure 6.18a shows the model fits for  $H_u = 30$  and 40 to unload-reload loop U2 for test ES\_CID\_867 . An  $H_u$  of 40 is a better fit. The fits for unload-reload loop U3 are presented in Figure 6.18b. An  $H_u$  of 20 is a better fit in this case. It is noteworthy that U3 is at a higher axial strain level than U2. Therefore, higher strain levels appear to be associated with softer unloading. This trend of reducing  $H_u$  with increasing strain level was applicable for all the unload-reload tests. A constant value of  $H_u = 30$  was adopted for simplicity. This value fits the unload plots on average (see Appendix B for the fits of Erksak sand tests).

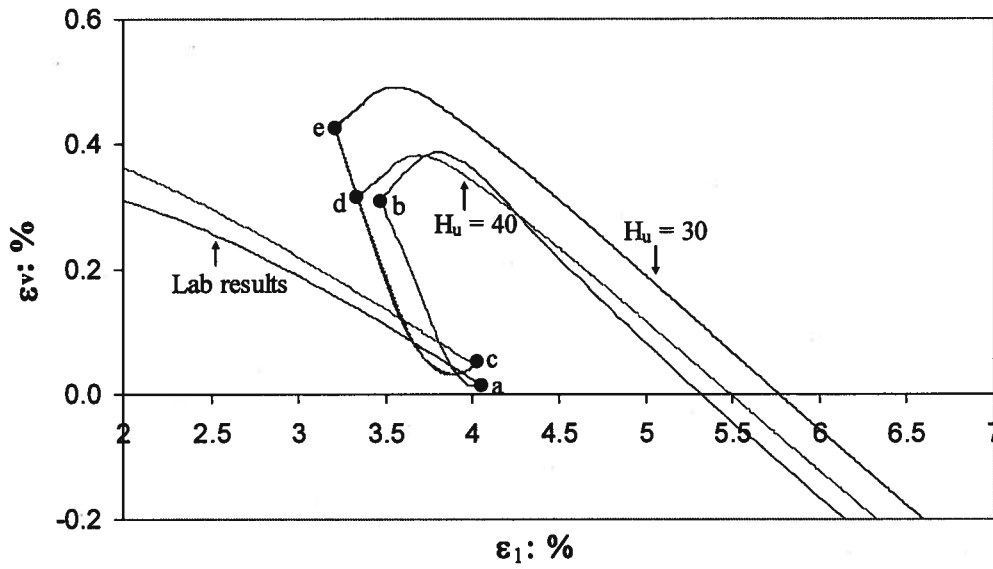
The plastic hardening modulus in reloading " $H_r$ " specifies the rate of movement of the outer yield surface in reloading. Figure 6.19 shows that  $H_r = 4H$  fits laboratory data. It is also clear that the results are not sensitive to  $H_r$  as it has a very high value (i.e. there is a small difference in the model predictions for  $H_r = 4H$  and  $H_r = 8H$ ). The first portion of L4 is elastic and therefore the model gives similar results regardless of the value of  $H_r$ .

The reload loops in stress strain curves are very steep until a point where the yield surface prior to unload-reload is exceeded. Jefferies (1997) suggested that soil 'remembers' its past yield surface before unload-reload. Current observations are in agreement with this observation. The plastic hardening modulus in reloading " $H_r$ " calibrated well with a very high value of  $4H$  until the yield surface prior to unload-reload is exceeded. At this point  $H_r = H$ . Figure 6.20 shows model simulations for a test with a constant  $H_r = 4H$  and one with a changing  $H_r$ . The solid dots are on the yield surface before the unload-reload loop. A constant  $H_r$  results in sharp peaks for the cases of L2 and L3 that were not observed in laboratory results. A changing  $H_r$  is adopted as it is consistent with laboratory data.  $H_r$  changes from a value of  $4H$  to a value of  $H$  once the yield surface before unload-reload is exceeded.

The slope of a trend line through the second peaks,  $\chi_2$ , is used to capture the effect of induced changes in particle arrangement on stress-dilatancy when stress conditions exceed peak. A value of  $\chi_2 = 4.71$  was obtained in Section 6.1.3 (see Figure 6.7) (the original value of  $\chi$  for first loading was 3.34). The first loading  $\chi_1$  is used for pre-peak load or reload loops while  $\chi_2$  is used for post-peak reload loops. A higher  $\chi$  value results in a more dilative behaviour. Figure 6.21 shows that a changing  $\chi$  gives a better fit than a constant  $\chi$ . It is noteworthy that the two simulations (i.e. constant and changing  $\chi$ ) are identical for the first reloading loop, a pre-peak loop. However, they are different for the other two reloading loops as they are post-peak loops.

Table 6.6 is a summary of the unload-reload calibration for Erksak sand presented in this section.

(a)



(b)

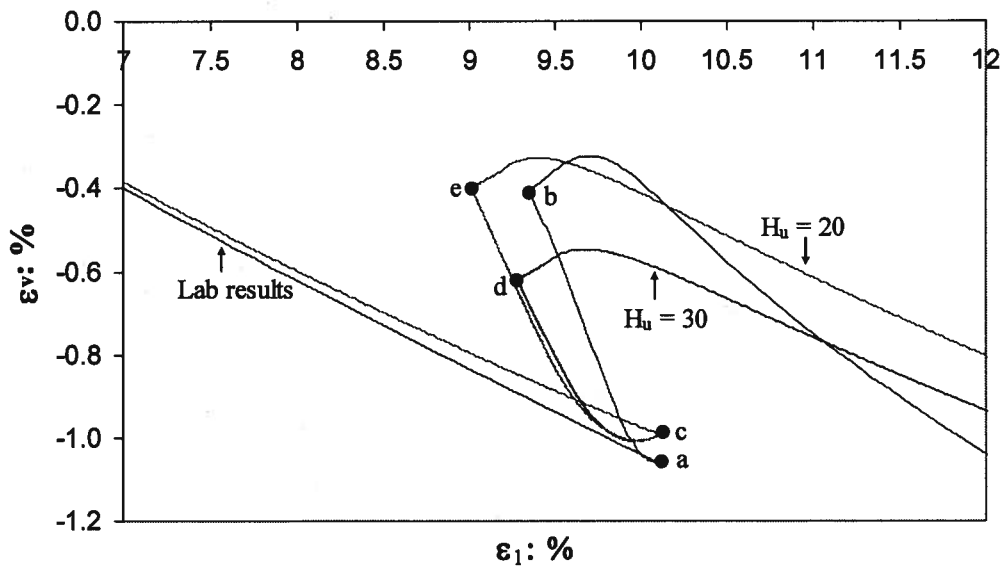


Figure 6.18. Model fits using different  $H_u$  values compared to laboratory data (a) U2 for ES\_CID\_867 (b) U3 for ES\_CID\_867.

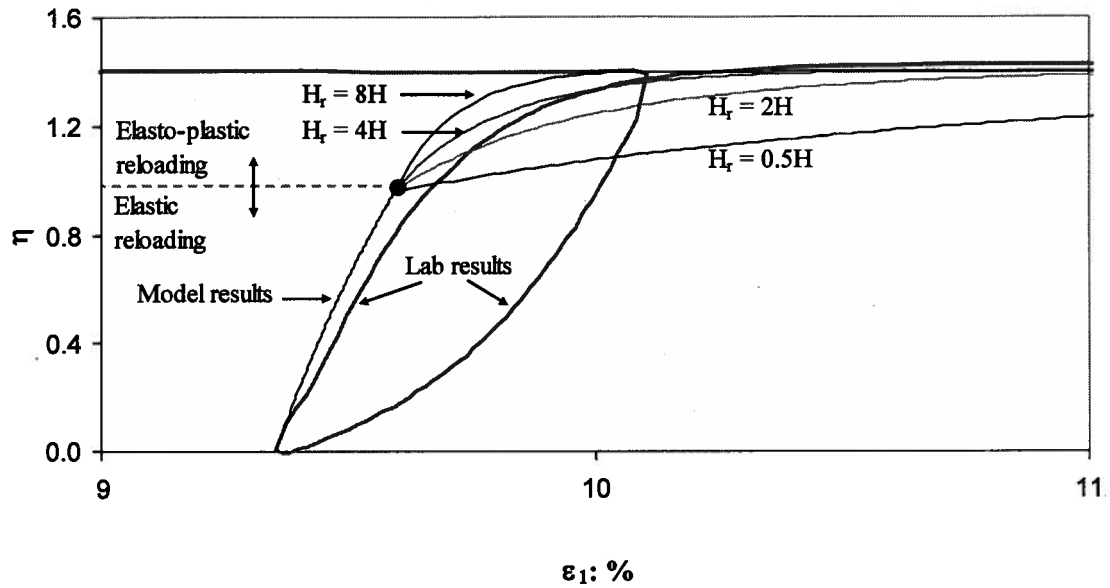


Figure 6.19. Model fits for different  $H_r$  values compared to L4 for ES\_CID\_867.

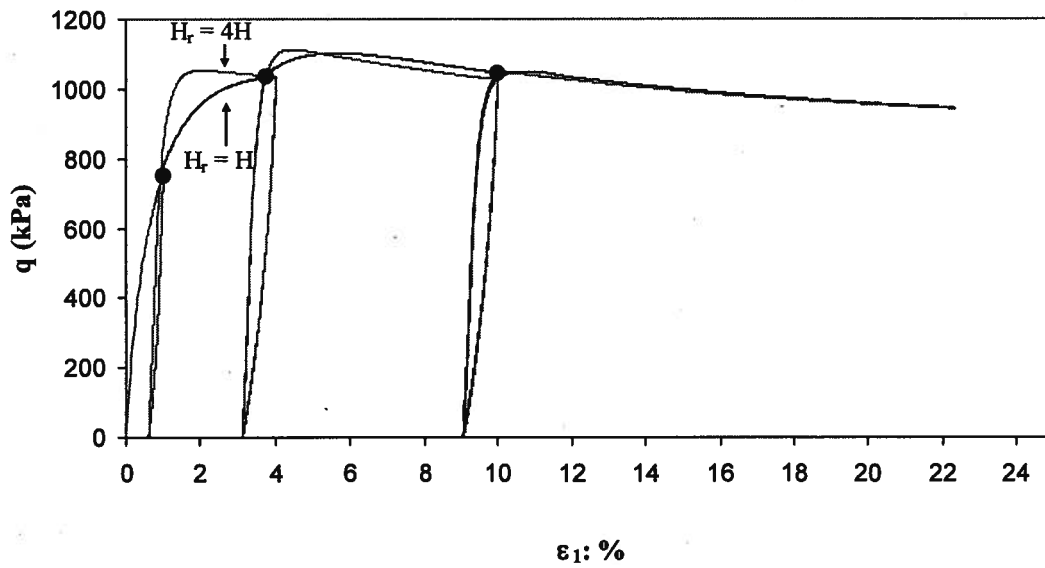


Figure 6.20. Model simulation for a changing and constant  $H_r$  values.

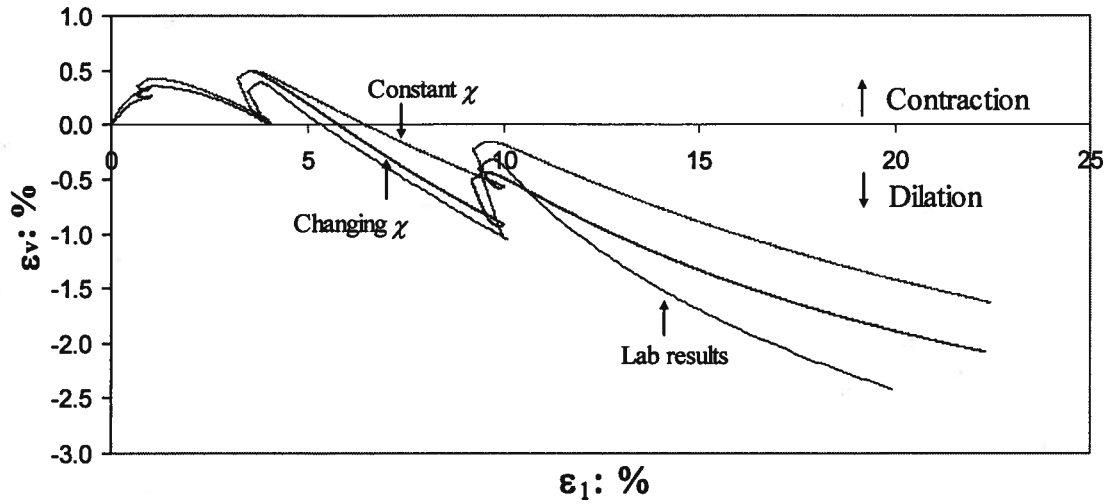


Figure 6.21. Model fits for constant and changing  $\chi$  values compared to ES\_CID\_867.

Table 6.6. Summary of the unload-reload calibration for Erksak sand.

Parameter	Erksak sand	Remark
$H_u$	30	Plastic hardening parameter in unloading
$H_r$	$4H$	Plastic hardening parameter in reloading
$\chi_2$	4.71	Slope of the line relating $D_{min}$ to $\psi$ at $D_{min}$ defined for the second peaks

### 6.3.1. Overview of Erksak Unload-Reload Calibration

The proposed model captures the main features of soil behaviour including the volume changes observed during unloading and reloading accurately. Appendix B presents the calibrations for the Erksak sand triaxial tests. Figure 6.22 shows a comparison between the  $\eta - \varepsilon_1$  and  $\varepsilon_v - \varepsilon_1$  plots of the calibrated NorSand model and ES\_CID\_867. Unloading for Loop 2, shown at larger scale in Figure 6.23, does not go through an elastic phase. The response in unloading, phase a-b, is elasto-plastic. Unloading in the NorSand model calibration is elasto-plastic as the stress point touched the cap in the

previous loading phase. A small amount of dilation is seen at the beginning of segment a-b which is contrary to what is expected according to plasticity. The reason for that is at the beginning of the unloading phase, the ratio of elastic strains that are dilative to total strains is large. This ratio decreases dramatically later in the unloading phase with plastic strains taking over. Figure 6.24 shows the same simulation as in Figure 6.23 but with plastic unloading instead of elasto-plastic unloading. It is noteworthy that the small dilative part in segment a-b disappeared. This proves that this dilative part is due to the large influence of elasticity at the beginning of the unloading phase. Similar behaviour is observed in the simulations for all other tests. It was shown in Section 6.1.2 that the values of the elastic bulk modulus used in the model are lower than those directly calculated from the unload-reload tests data (see Figure 6.6). This could be one of the reasons for the bigger loops at the beginning of a-b compared to those for laboratory data. Although plastic unloading fits the current data set better than elasto-plastic unloading, the latter was adopted in the model. Particles are expected to expand elastically with the decreasing  $p'$  and this well known behaviour cannot be ignored. The elastic properties used for Erksak sand are not accurate in the absence of bender element testing (see Section 6.1.2). Therefore, other data sets with bender elements tests are needed to verify this point. Reloading for loop 2 is elastic (part b-c) until yield occurs once the stress point hits the outer yield surface.

Unloading for the first loop, shown at large scale in Figure 6.25, starts with a linear elastic phase where soil expands in unloading (part a-b), followed by an elasto-plastic phase (part b-c). Note that the stress point does not touch the internal cap in the previous loading for this loop. Reloading is elastic (part c-d) until the stress point touches the outer yield surface.

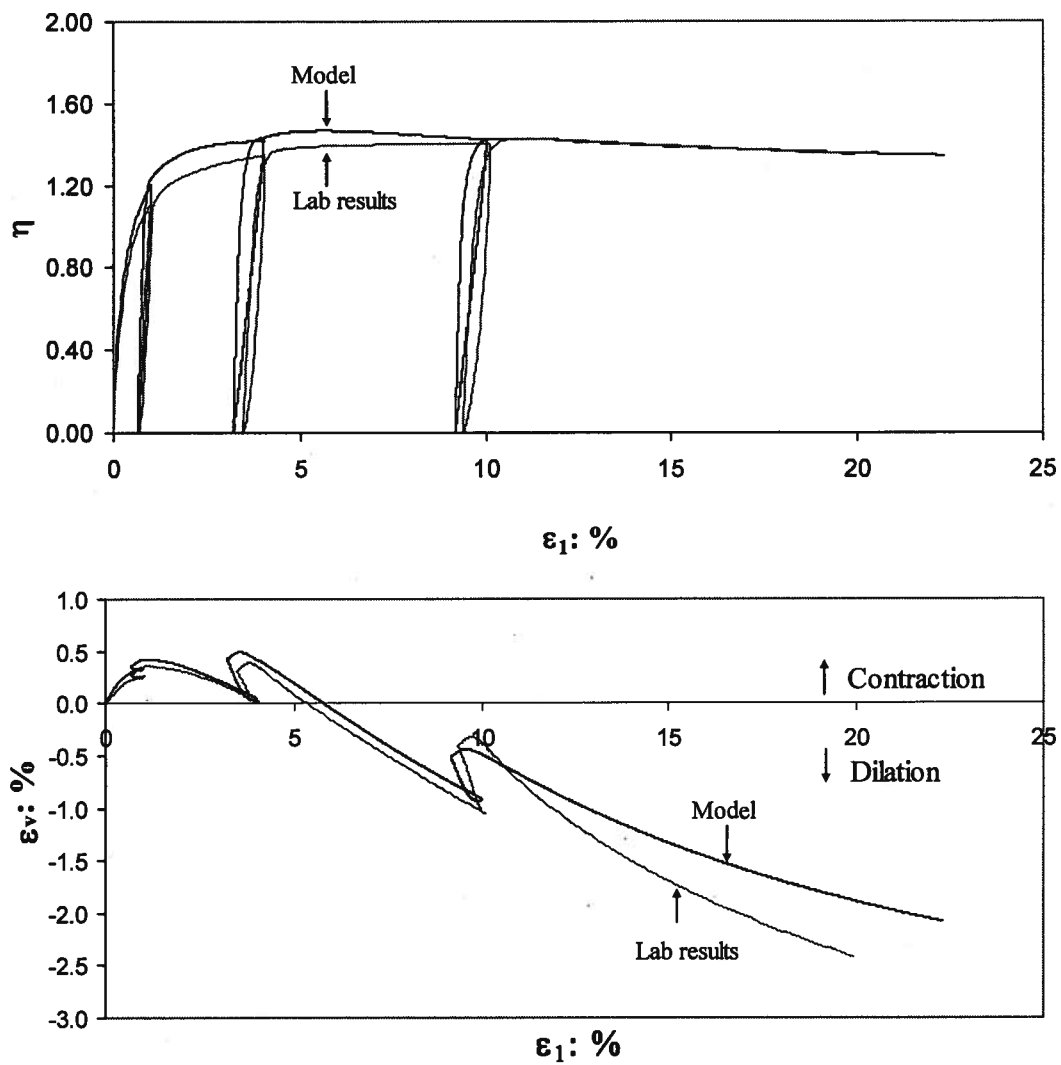


Figure 6.22. Comparison between calibrated NorSand model and ES\_CID\_867.

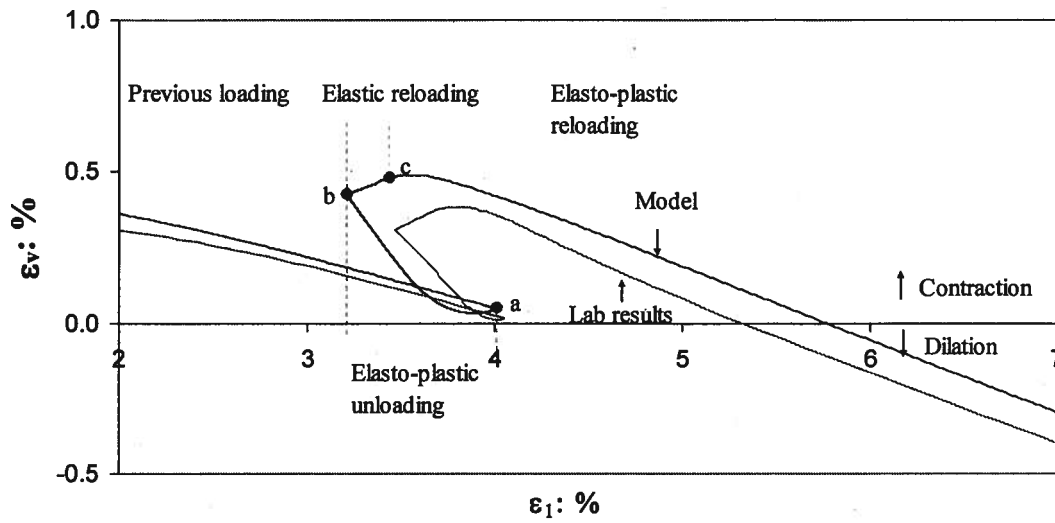


Figure 6.23. Zoom on the second loop of comparison between calibrated NorSand model with elasto-plastic unloading and ES\_CID\_867.

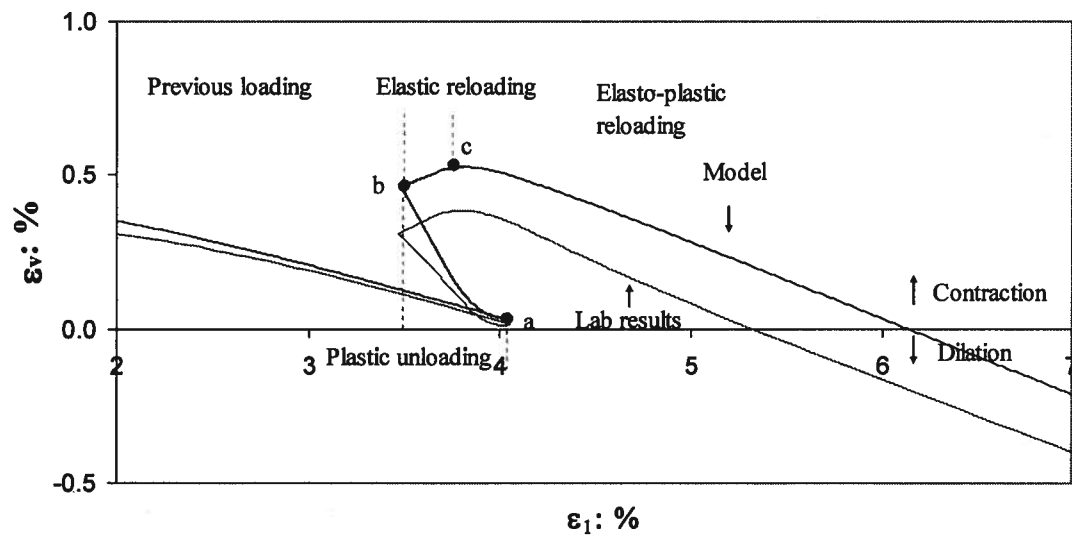


Figure 6.24. Zoom on the second loop of comparison between calibrated NorSand model and ES\_CID\_867 with plastic unloading.



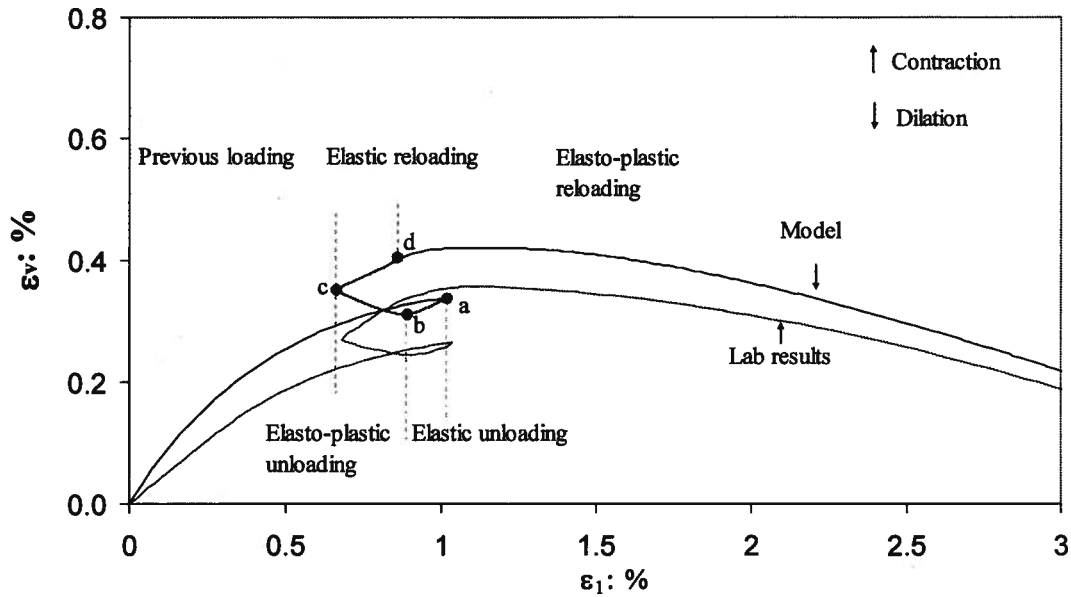


Figure 6.25. Zoom on the first loop for ES\_CID\_867.

## 6.4. Summary

This chapter presented a triaxial monotonic calibration of the NorSand model to Erksak sand and Fraser River sand. NorSand requires 8 parameters: 3 critical state parameters, 3 plasticity parameters, and 2 elasticity parameters. The unload-reload model presented in Chapter 5 requires 3 additional parameters:  $H_u$ ,  $H_r$ , and  $\chi_2$ . An unload-reload calibration was performed on Erksak sand using cyclic triaxial tests. It was found that  $H_r$  and  $\chi_2$  are related to the monotonic parameters  $H$  and  $\chi_1$ , respectively, such that  $H_r = 4H$  and  $\chi_2 = 1.41\chi_1$ .  $H_r$  changes from a value of  $4H$  to a value of  $H$  once the yield surface before unload-reload is exceeded. A constant  $H_u$  of 30 fits the unload plots on average.

## 7. PREDICTIONS OF FRASER RIVER SAND UNLOAD-RELOAD BEHAVIOUR

The parameters/relations from the monotonic calibration for Fraser River sand supplemented by the parameters/relations derived from the unload-reload calibration for Erksak sand were used to predict the two load-unload-reload triaxial tests on Fraser River sand using the modified NorSand model developed earlier in Chapter 5. The two triaxial tests modelled, FR\_CID\_01 and FR\_CID\_02 were described in Table 4.4. Test FR\_CID\_01 is on a loose sample ( $p'=190$  kPa &  $\psi_o = 0.012$ ) while test FR\_CID\_02 is on a dense sample ( $p'=198$  kPa &  $\psi_o = -0.156$ ). Both samples were moist tamped.

### 7.1. Model parameters

As discussed previously in Chapter 6, three additional material parameters are needed for the proposed unload-reload calibration: “ $H_u$ ” and “ $H_r$ ”, the plastic hardening modulus in unloading and reloading respectively and “ $\chi_2$ ”, the slope of a trend line through the second peaks of the  $D_{min}$  versus  $\psi$  at  $D_{min}$  data. The same value for  $H_u$  as used for Erksak sand was assumed (i.e.  $H_u = 30$ ). The relation  $H_r = 4H$ , derived for the Erksak Sand calibration, was also used for the reloading portion of the stress path.  $H_r$  is used during loading until the yield surface in existence prior to the current unload-reload is exceeded. At this point  $H_r$  returns to the monotonic loading value of  $H$ . The value of  $\chi_2$  for Fraser River sand was obtained by assuming the same ratio between  $\chi_1$  and  $\chi_2$  for Fraser River sand as obtained from the Erksak calibration. Table 7.1 is a summary of the unload-reload parameters used for the predictions. The monotonic parameters were presented previously in Table 6.5.

Table 7.1. Parameters used for Fraser River sand unload-reload predictions.

Parameter	Erksak sand	Remark
$H_u$	30	Plastic hardening parameter in unloading
$H_r$	$4H$	Plastic hardening parameter in reloading
$\chi_2$	6.12	Slope of the line relating $D_{min}$ to $\psi$ at $D_{min}$ defined for the second peaks

## 7.2. Model predictions

The updated NorSand model was run using the Fraser River monotonic calibration and the unload-reload properties/relations derived from the Erksak unload-reload calibration. No iteration to the input parameters to improve the fits was attempted. The true measured and NorSand computed stress and strain responses are given in Figure 7.1 and Figure 7.2 for the loose (FR\_CID\_01) and dense (FR\_CID\_02) tests respectively.

The prediction for FR\_CID\_01 in both  $q-\varepsilon_I$  and  $\eta-\varepsilon_I$  shows slightly lower curves than laboratory data in the range of  $\varepsilon_I$  values greater than 2% (Figures 7.1a-b). The difference between the predictions and the laboratory data starts decreasing at higher axial strains, i.e. > 15%. Although the predictions and laboratory data for the monotonic parts of the curves are slightly different, they are very similar in the unload-reload parts. The slopes of the predicted unload-reload loops are almost identical to those for the laboratory data. It can be noticed that the area inside the loops is larger at higher axial strains. The predictions simulate this behaviour.

The model generally predicts more contractive behaviour for FR\_CID\_01 compared to laboratory data (Figures 7.1c). Both laboratory data and the predictions are very similar up to  $\varepsilon_I$  of around 5%. At higher axial strains, the difference between  $\varepsilon_I$  from laboratory

data and predictions increases with a maximum difference of more than 1% at very high axial strains.

Similar to FR\_CID\_01, the monotonic parts of  $q - \varepsilon_I$  and  $\eta - \varepsilon_I$  for the predictions for FR\_CID\_02 are slightly lower compared to laboratory data (Figure 7.2a-b). The difference between the two plots, i.e. laboratory data and predictions, decreases at higher axial strains close to critical state. The slopes of the unload-reload loops are almost identical for both the predictions and laboratory data.

The predictions are quite accurate in  $\varepsilon_v - \varepsilon_I$  for FR\_CID\_02. The maximum difference between  $\eta$  values for the predictions and laboratory data in  $\varepsilon_v - \varepsilon_I$  for FR\_CID\_02 is around 0.5% at  $\varepsilon_I = 25\%$  (Figure 7.2c). However, this difference is much smaller at lower  $\varepsilon_I$  values and the predictions are very accurate. The unload response for the loop at  $\varepsilon_I = 5\%$  is stiffer than the predictions while it is softer for the unload loop at  $\varepsilon_I = 10\%$ . This is similar to observations for Erksak sand described in Section 6.3.

The area inside the unload-reload loops is larger for FR\_CID\_02 than that for FR\_CID\_01. The model captures this behaviour accurately. FR\_CID\_02 has a higher  $H$  value, and therefore a higher  $H_r$ . This yields a stiffer reloading response for FR\_CID\_02 and the area inside the unload-reload loops is increased.

The predictions for FR\_CID\_02 in the  $\varepsilon_v - \varepsilon_I$  plot better match laboratory data than those for FR\_CID\_01 (Figures 7.1c & 7.2c). This is because most of the tests used in the monotonic calibration for Fraser River sand were done on dense samples (see Section 6.2). Therefore, the derived parameters are expected to better fit dense samples. The predictions are still accurate even for test FR\_CID\_01 up to strain levels of around 5%.

In summary, it seems that the unload-reload parameters obtained from the calibration of Erksak sand provide a reasonably good calibration for Fraser River sand. In  $q - \varepsilon_I$  and  $\eta - \varepsilon_I$ , the monotonic parts of the plots for the predictions for both tests are slightly lower than those for laboratory data. However, the slopes of the unload-reload parts are very

similar. In  $\varepsilon_v - \varepsilon_I$ , test FR\_CID\_02 with the dense sample had better fits than test FR\_CID\_01 with the loose sample. This is expected as the calibration in Chapter 6 was done using dense samples. Using a constant  $H_u$  value fits the unloading parts on average. A constant  $H_u$  results in a simpler calibration although it is evident that unloading is softer at higher strains.

For future work, other sets of unload-reload tests are needed to better understand the factors that  $H_u$  depends on. The predictions could be further improved by including more unload-reload tests on loose samples in the calibration and tests with more unload-reload loops.

### 7.3. Discussion of model predictions

To understand the unload-reload behaviour of sands, special laboratory testing programs that are not commonly performed in industry are required. However, monotonic laboratory testing is part of the routine in industry. Hence, a model that can simulate the unload-reload behaviour using unload-reload parameters that can be correlated to monotonic parameters is of practical significance.

A challenge for any constitutive model is obtaining good quality laboratory information to calibrate the model. Typically, the simpler the model calibration, the greater the utility of the model for real engineering problems. This section has investigated whether the standard monotonic calibration for NorSand, supplemented by relations observed between the monotonic and three unload-reload parameters for Erksak sand, can be used to accurately predict the behaviour of a different sand: in this instance Fraser River sand.

Three additional material parameters are needed for the unload-reload calibration: " $H_u$ ", and " $H_r$ ", the plastic hardening modulus in unloading and reloading respectively and " $\chi_2$ ", the slope of a trend line through the second peaks of the  $D_{min}$  versus  $\psi$  at  $D_{min}$  data. From the unload-reload calibration to Erksak sand presented in Chapter 6, it was shown that  $H_r$

and  $\chi_2$  are correlated to the monotonic  $H$  and  $\chi_1$ , respectively ( $H_r = 4H$  &  $\chi_2 = 1.41\chi_1$ ). A constant value of  $H_u$  equal to 30 was shown to fit the unloading curves on average.

The predictions for Fraser River sand presented in this chapter suggest that using correlations from the Erksak calibration gives quite good fits. The slopes of the predicted unload-reload loops in  $q - \varepsilon_1$  and  $\eta - \varepsilon_1$  were very similar to those for laboratory data. The dense sample gave reasonably accurate fits in  $\varepsilon_v - \varepsilon_1$  plot. The predictions for the dense sample were better than those for the loose sample. However, the fits for the loose sample are still quite good up to axial strain of around 5%.

Similar to observation from Erksak data, Fraser River sand simulations show that the code is not sensitive to changes in  $H_r$  because it has a high value of  $4H$  (see Figure 6.19). As in the Erksak calibration,  $H_u$  of 30 fits the data on average. Changing  $\chi$  gives better predictions. Figure 7.3 shows a model simulation for FR\_CID\_02 with constant  $\chi$  equal to  $\chi_1$ . The predictions with changing  $\chi$  shown in Figure 7.2b better fit the laboratory data. It can be seen both simulations (i.e. changing and constant  $\chi$ ) are identical up to  $\varepsilon_1$  of around 5%. This is because the reloading loops in that range are pre-peak (i.e. start from pre-peak conditions) and therefore both simulations are based on  $\chi = 4.34$ . The later reloading loops start from post-peak conditions and therefore  $\chi$  changes to 6.12 for the simulation in Figure 7.2c. It is noteworthy that changing  $\chi$  gives identical predictions as constant  $\chi$  for FR\_CID\_01 as it is a loose test that never reaches peak.

Overall, the results of the prediction are promising. The current correlation between monotonic and unload-reload parameters was undertaken based on the triaxial tests for a single sand, Erksak. It is likely that these correlations will be improved as the database of triaxial tests with high resolution measurements of the unload reload behaviour expands. However, where possible it is best to calibrate the unload-reload response directly. A few triaxial tests with unload-reload loops should be done for more accurate results.

## **7.4. Summary**

The standard monotonic calibration for NorSand, supplemented by relations observed between the monotonic and the three unload-reload parameters for Erksak sand, was successfully used to predict the cyclic behaviour of another sand: in this instance Fraser River sand. The main finding of this chapter is that the unload-reload behaviour can be simulated using unload-reload parameters that can be correlated to monotonic parameters. It is likely that these correlations will be improved as the database of unload-reload tests expands.

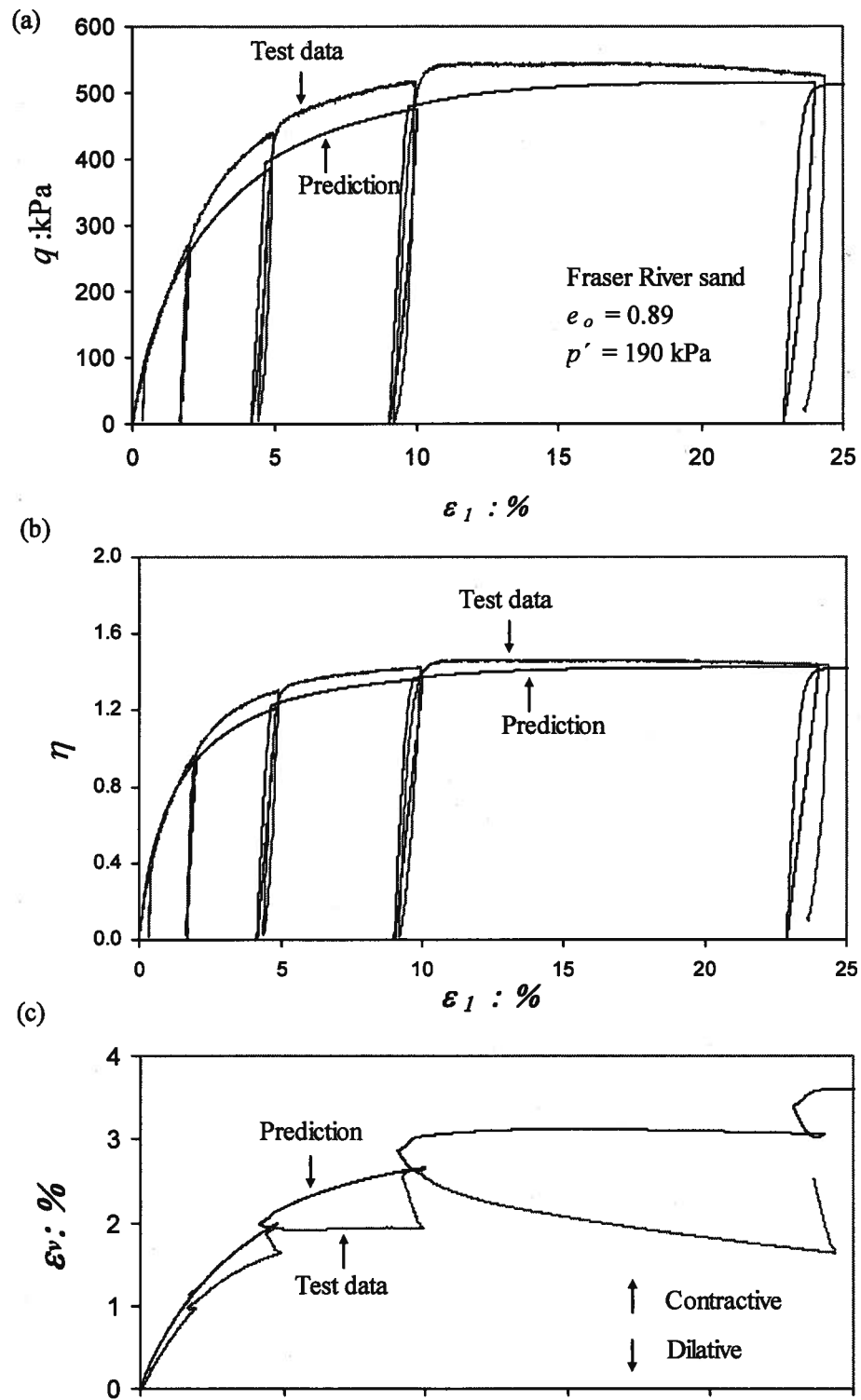


Figure 7.1. Predictions for Test FR\_CID\_01 (a)  $q-\varepsilon_1$  (b)  $\eta-\varepsilon_1$  (c)  $\varepsilon_v-\varepsilon_1$ .



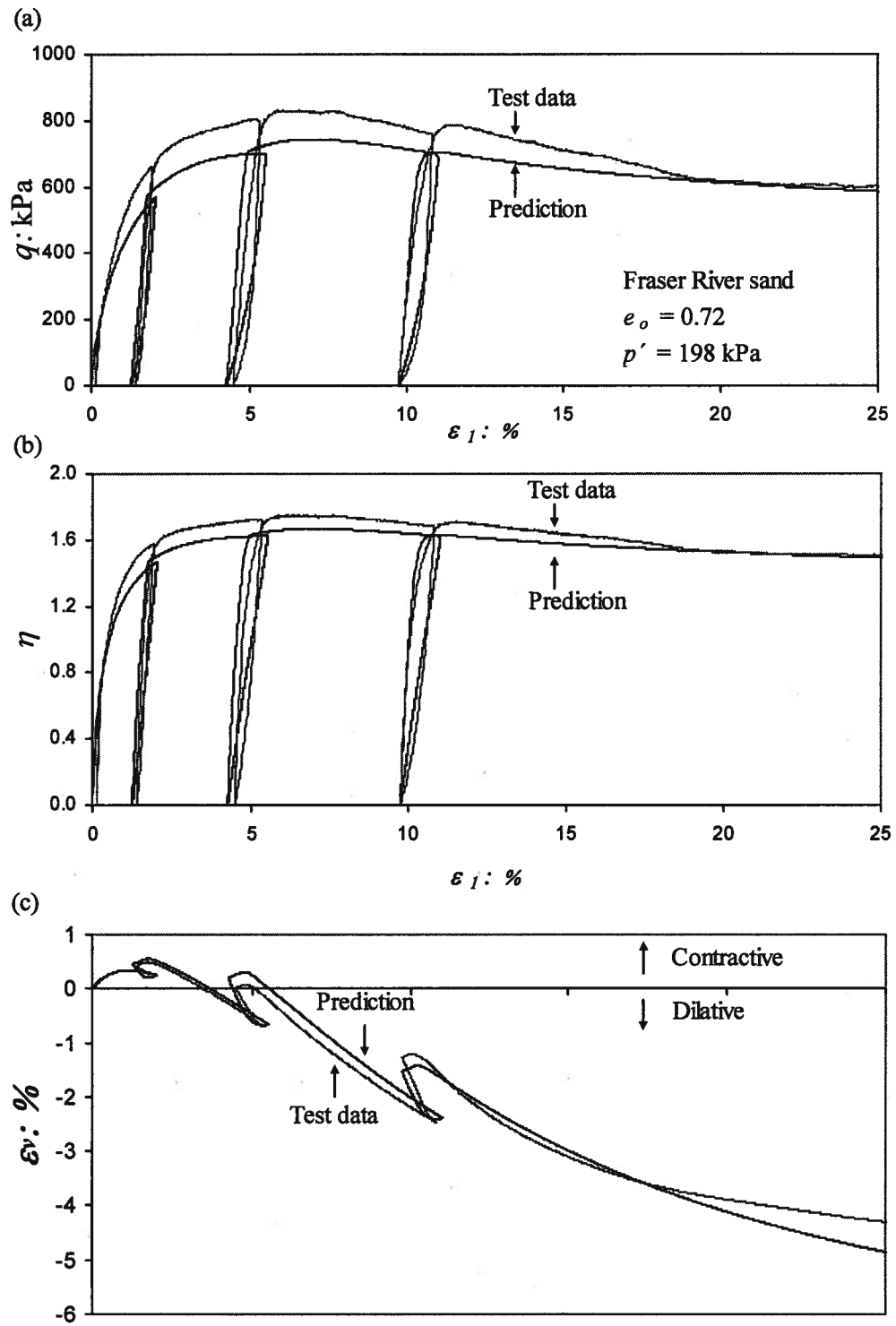


Figure 7.2. Predictions for Test FR\_CID\_02 (a)  $q-\epsilon_1$  (b)  $\eta-\epsilon_1$  (c)  $\epsilon_v-\epsilon_1$ .

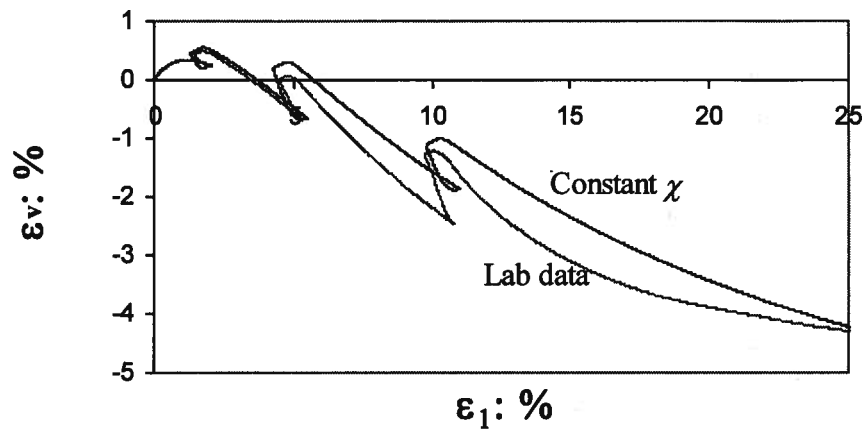


Figure 7.3. Model simulation for Test FR\_CID\_02 in  $\epsilon_v$ - $\epsilon_l$  with constant  $\chi$  of 4.34.

## **8. SUMMARY AND CONCLUSIONS**

### **8.1. Context of Research**

The behaviour of sands during loading has been studied in great detail. However, little work has been devoted to understanding the response of sands in unloading. This is surprising as the behaviour of sands in unloading is of great practical importance for earthquake engineering.

An elastic material is expected to expand upon unloading in a conventional triaxial test. Drained triaxial tests indicate that, contrary to the expected elastic behaviour, sand may exhibit contractive behaviour when unloaded. Drained cyclic simple shear tests show similar behaviour in unloading (Sriskandakumar, 2004). Therefore, it is clear that soil behaviour in unloading is not wholly elastic. The drained behaviour of sands in unloading was investigated in this work as well as strength and deformation characteristics in reloading. A practical continuum model that accounts for inelastic unloading (i.e. yields in unloading) was introduced.

The tendency to contract upon unloading during an earthquake could result in liquefaction. Undrained cyclic simple shear tests show that the increase in pore water pressure generated during the unloading cycle often exceeds that generated during loading. A model that yields in unloading is needed to predict this behaviour.

## **8.2. Research Objectives**

The main objectives of this research were:

1. Develop a theoretical understanding of stress-dilatancy in unloading. This investigation includes the interaction between soil fabric and stress-dilatancy.
2. Utilize the theoretical understanding to guide development of unload-reload behaviour, including yielding during unloading, into a constitutive model.

## **8.3. Methodology**

The theoretical approach followed is based on Rowe's stress-dilatancy (Rowe, 1962). The introduced unload-reload model adopted the NorSand soil model (Jefferies, 1993; Jefferies and Shuttle, 2005) as its starting point. The flow rule used in the model was based on observations from a series of triaxial tests with unload-reload loops on Erksak sand. Calibration of the model for monotonic and unload-reload stress path were performed for Erksak sand. To determine whether the monotonic to unload-reload relations observed from the Erksak unload-reload calibrations could be applied generally, a prediction for unload-reload on Fraser River Sand was undertaken. First a monotonic calibration of NorSand to Fraser River sand was done. Then the monotonic calibration on Fraser River sand and the unload-reload parameters for Erksak sand were used to predict the results of triaxial tests with load-unload-reload cycles on Fraser River sand.

## **8.4. Conclusions**

The theoretical study of deformation characteristic of an assembly of rigid rods shows that the observed soil contraction in unloading is to be expected. The relation between stress and dilatancy during unloading depends on particle arrangement. As the

arrangement of particles is expected to change with cyclic loading, the stress-dilatancy relation in reloading differs from that for first loading.

The study of ten drained conventional triaxial tests on Erksak sand, including between one and three unload-reload loops, indicates that significant amounts of contraction can occur during unloading. This is contrary to the dilatant elastic unloading response often assumed in constitutive models of soil. This observed behaviour is consistent with the results of the theoretical study.

Experimental observations indicate that unloading loops starting from pre-image stress ratio are dominated by small amounts of dilation, while those starting from post-image stress ratio are dominated by significant amounts of contraction. The effect of the unload-reload loops on peak strength is small. This observed contraction in unloading can be explained based on the saw-tooth model. The sawtooth model suggests that the more soil dilates in loading, the more potential energy the soil stores. This energy is available to be released as contraction in subsequent unloading, as observed experimentally.

The results of the series of tests on Erksak sand show that soil becomes more dilatant in post-peak reloading phases (i.e. reloading loops occurring post-peak). However, the stress-dilatancy relation remains as in first loading for pre-peak reloading loops.

The NorSand constitutive model was extended to represent the experimentally observed yielding during unloading. The introduced model uses non-associated flow in unloading. Dilatancy in unloading is a function of stress ratio,  $\eta$ , and the stress ratio ( $q/p'$ ) at zero dilatancy in unloading,  $M_u$ . Soil is assumed to yield in unloading on a vertical cap at  $D_{min}$ . This assumption fits the framework of monotonic NorSand and is consistent with observations from laboratory data. The cap contracts in unloading dragging the outer yield surface with it. As a result the outer yield surface softens due to yield in unloading.

The resulting model requires the standard 8 NorSand monotonic parameters ( $\Gamma$ ,  $\lambda$ ,  $M_{tc}$ ,  $H$ ,  $\chi_{tc}$ ,  $N$ ,  $I_r$ , and  $\nu$ ). It also requires three additional unload-reload parameters introduced in this work: “ $H_u$ ” and “ $H_r$ ”, the plastic hardening modulus in unloading and reloading respectively and “ $\chi_2$ ”, the slope of a trend line through the second peaks (i.e. for post-peak reloading phases) in  $D_{min} - \psi$  plot.  $\chi_2$  is used to capture the effect of induced changes in particles arrangement on stress-dilatancy when stress conditions exceed peak.

The results of the calibration show that the model captures the details of the behaviour of sand under load-unload-reload cycles.  $H_u$  was significantly smaller than the monotonic loading hardening,  $H$ , and the constant value of 30 provided good fits to the experimental unload-reload data on average. The code is not sensitive to changes in  $H_r$  because it has a high value of around  $4H$ .  $\chi_2$  was always observed to be higher than  $\chi_1$  and for Erksak sand  $\chi_2$  exceeded  $\chi_1$  by 40%. The calibrated model predicted the results of triaxial tests with load-unload-reload cycles on Fraser River sand with good precision.

Overall, this thesis introduced stress-dilatancy relations for unloading and reloading based on experimental observation, supported by the findings of an investigation done at the micro-mechanical level. An elasto-plastic continuum model that yields in unloading was proposed. It was shown that the unload-reload behaviour can be simulated using unload-reload parameters that can be correlated to monotonic parameters.

## 8.5. Suggestions for Future Work

In summary, this research presents a practical model for load-unload-reload cycles on sand that incorporate inelastic unloading. It accounts for induced changes in particle arrangement. The model gives accurate predictions for triaxial laboratory data. This research is limited to a triaxial compression framework. For future research, the proposed model can be implemented in a finite elements code and therefore it needs to be

validated for general stress path conditions. An example of this would be a stress path with decreasing mean effective stress at constant shear stress.

## REFERENCES

- ASTM 2006a, "Standard test methods for maximum index density of soils using a vibratory table (D4253-00-2006), In 2006 Annual Book of ASTM Standards, sect. 4, Vol. 4.08, ASTM, Philadelphia.
- ASTM 2006b, "Standard test methods for minimum index density of soils and calculation of relative density (D4254-00-2006), In 2006 Annual Book of ASTM Standards, sect. 4, Vol. 4.08. ASTM, Philadelphia.
- Been, K., and Jefferies, M., 1985, "State parameter for sands", *Géotechnique*, Vol. 35, No. 2, pp. 99-112.
- Been, K., Jefferies, M., and Hachey, J., 1991, "Critical state of sands", *Géotechnique*, Vol. 41, No. 3, pp. 365-381.
- Bishop, A. W., 1971, "Shear strength parameters for undisturbed and remoulded soil specimens", *Proc. Roscoe Memorial Symp.*, Cambridge, 3-58.
- Bolton, M. D., 1986, "Strength and dilatancy of sands", *Géotechnique*, Vol. 36, No. 1, pp. 65-78.
- Byrne, P., Cheung, H., Yan, L., 1987, "Soil parameters for deformation analysis of sand masses", *Canadian Geotechnical Journal*, Vol.24, pp. 366-376.
- Casagrande, A., 1936, "Characteristics of cohesionless soils affecting the stability of earth fill", *Journal of Boston Society of Civil Engineers*, Vol. 23, pp. 257-276.



- Chillarige, AnnajiRao, V., Robertson, P., Morgenstern, N., and Christian, H., 1997, "Evaluation of the in situ state of Fraser River sand", Canadian Geotechnical Journal, Vol. 34, No. 4, pp. 510-519.
- Collins, I. F., 2005, "The concept of stored plastic work or frozen elastic energy in soil mechnics", Géotechnique, Vol. 55, No. 5, pp. 373-382.
- Drucker, D. C., 1951, "A more fundamental approach to stress-strain relations", Proc. First US National Congress of Applied Mechanics, ASME, pp. 487-491.
- Drucker, D. C., and Seereeram, D., 1987, "Remaining at yield during unloading and other unconventional elasto-plastic response", Journal of Applied Mechanics, Vol. 54, No. 1, pp. 22-26.
- Duncan, J. M., and Chang, C., 1970, "Nonlinear analysis of stress and strain in soils", Journal of the Soil Mechanics and Foundations Division, Vol. 96, No. 5, pp. 1629-1653.
- Golder Associates, 1987, "Report on unload testing to assess initial fabric of Erksak sand", Golder Associates, Calgary, Alberta
- Golder Associates. Erksak 330/0.7 triaxial tests, available at [www.golder.com/liq](http://www.golder.com/liq).
- Ghafghazi, M., and Shuttle, D., 2006, "Accurate determination of the critical state friction angle from triaxial tests", Proc. 59<sup>th</sup> Canadian Geotechnical Conference, Vancouver, BC., Canada.
- Ishihara, K., Okada, S., 1978, "Yielding of overconsolidated sand and liquefaction model under cyclic stresses", Soils and Foundations, Vol. 18, No. 1, pp. 57-72.
- Jefferies, M., 1993, "NorSand; a simple critical state model for sand" Géotechnique, Vol. 43, No. 1, pp. 91-103.

- Jefferies, M., 1997, "Plastic work and isotropic softening in unloading" *Géotechnique*, Vol. 47, No. 5, pp. 1037-1042.
- Jefferies, M., and Been, K., 2000, "Implications for critical state theory from isotropic compression of sand" *Géotechnique*, Vol. 50, No. 4, pp. 419-429.
- Jefferies, M., and Been, K., 2006, "Soil liquefaction: A critical state approach", Taylor & Francis, London and New York.
- Jefferies, M., and Shuttle, D., 2002, "Dilatancy in general Cambridge-type models" *Géotechnique*, Vol. 52, No. 9, pp. 625-638.
- Jefferies, M., and Shuttle, D., 2005, "NorSand: Features, calibration and use", Geotechnical special publication No. 128, American Society of Civil Engineers, United States, pp. 204-236.
- Li, X., and Dafalias, Y., 2000, "Dilatancy for cohesionless soils" *Géotechnique*, Vol. 50, No. 4, pp. 449-460.
- Mitchell, J., and Soga, K., 2005, "Fundamentals of soil behavior", 3<sup>rd</sup> edition, John Wiley & sons, New Jersey, USA.
- Nova, R., 1982, "A constitutive model for soil under monotonic and cyclic loading", in *Soil Mechanics Transient and Cyclic Loads*, Wiley, pp. 343-373.
- Oda, M., 1972, "Initial fabrics and their relation to mechanical properties of granular material", *Soils and Foundations*, Vol. 12, No. 1, pp. 17-37.
- Palmer, A. C., 1967, "Stress-strain relations for clays: Energy theory", *Géotechnique*, Vol. 17, No. 4, pp. 348-358.
- Reynolds, O., 1885, "On the dilatancy of media composed of rigid particles in contact, with experimental illustrations", *Philosophical Magazine*, Vol. 20, pp. 469-481.

- Roscoe, K., Schofield, A., and Wroth, C., 1958, "On yielding of soils", *Géotechnique*, Vol. 8, No. 1, pp. 22-53.
- Roscoe, K., and Burland, J., 1968, "On the generalised stress-strain behaviour of wet clay", *Engineering Plasticity*, Cambridge University Press, Cambridge, pp. 535-609.
- Rowe, P. W., 1962, "The stress-dilatancy relation for static equilibrium of an assembly of particles in contact", *Proc. of the Royal Society*, A269, 500-527.
- Rowe, P. W., 1969, "The relation between the shear strength of sands in triaxial compression, plane strain and direct shear", *Géotechnique*, Vol. 19, No. 1, pp. 75-86.
- Schofield, A. N., and Wroth, C. P., 1968, "Critical state soil mechanics", McGraw-Hill, London.
- Sasitharan, S., 1989, "Stress path dependency of dilatancy and stress-strain response of sand", M.A.Sc Thesis, University of British Columbia, Vancouver, BC, Canada.
- Skandakumar, S., 2004, "Cyclic loading response of Fraser River sand for validation of numerical models simulating centrifuge tests", M.A.Sc Thesis, University of British Columbia, Vancouver, BC, Canada.
- Tatsuoka, F., and Ishihara, K., 1974, "Yielding of sand in triaxial compression", *Soils and Foundations*, Vol. 14, pp. 63-76.
- Terzaghi, K., Peck, R., and Mesri, G., 1996, "Soil Mechanics in Engineering Practice", 3<sup>rd</sup> edition, John Wiley & sons, New York, USA.
- Vaid, Y., and Sasitharan, S., 1992, "The strength and dilatancy of sand", *Canadian Geotechnical Journal*, Vol. 29, No. 3, pp. 522-526.
- Vesic, A. S., and Clough, G. W., 1968, "Behavior of granular materials under high stresses", *Journal of the Soil Mechanics and Foundations Division*, Vol. 94, pp. 661-688.

- Wijewickreme, D., Sriskandakumar, S., and Byrne, P., 2005, "Cyclic loading response of loose air-pluviated Fraser River sand for validation of numerical models simulating centrifuge tests", *Canadian Geotechnical Journal*, Vol. 42, No. 2, pp. 550-561.
- Wood, D. M., 1990, "Soil behaviour and critical state soil mechanics", Cambridge University Press, Cambridge, UK.
- Yasufuku, N., Murata, H., and Hyodo, M., 1991, "Yield characteristics of anisotropically consolidated sand under low and high stresses", *Soils and Foundations*, Vol. 31, No. 1, pp. 95-109.

## APPENDIX A: PREDICTION OF STRESS DILATANCY IN UNLOADING

It is assumed that stress-dilatancy in unloading can be represented by Equation A.1. This appendix presents a quantitative justification using the available data on Erksak sand (Table 4.2). Figures A.1 to A.10 show a comparison between Equations A.1 to A.3 and laboratory data.

$$D_u^p = \eta - M_u \quad (\text{A.1})$$

Where,

$$M_u = 2\eta_L - 1.5 \quad (\text{A.2})$$

Where  $\eta_L$  is the last value of stress ratio from the previous loading phase. Plastic dilatancy in unloading becomes constant at:

$$D_u^p = 0.5 - M_u \quad (\text{A.3})$$

Note that the fits for the unload/reload loops at low stress levels are not presented in the following figures. Those loops are highly influenced by elasticity. Using plastic dilatancy relation to fit those loops would give inaccurate results. It is assumed that the effect of elasticity is negligible for the unload/reload loops at higher stress levels.

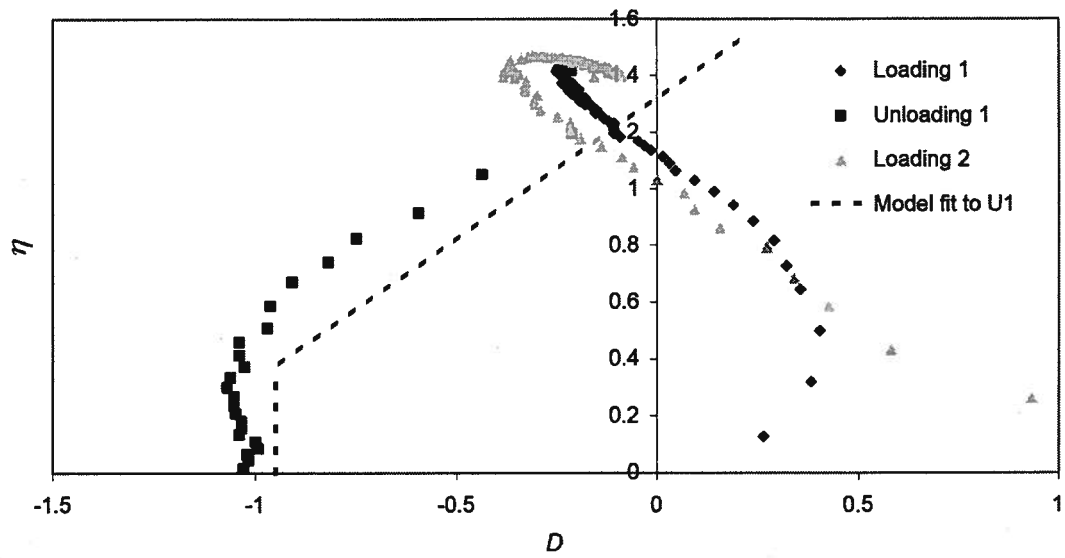


Figure A.1. Predicted and measured stress-dilatancy for ES\_CID\_860.

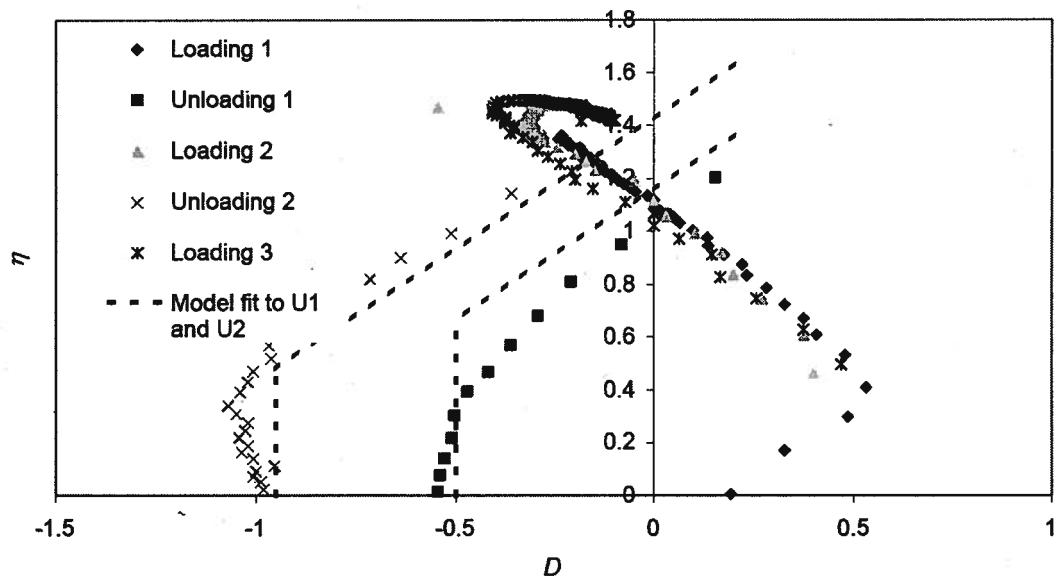


Figure A.2. Predicted and measured stress-dilatancy for ES\_CID\_861.

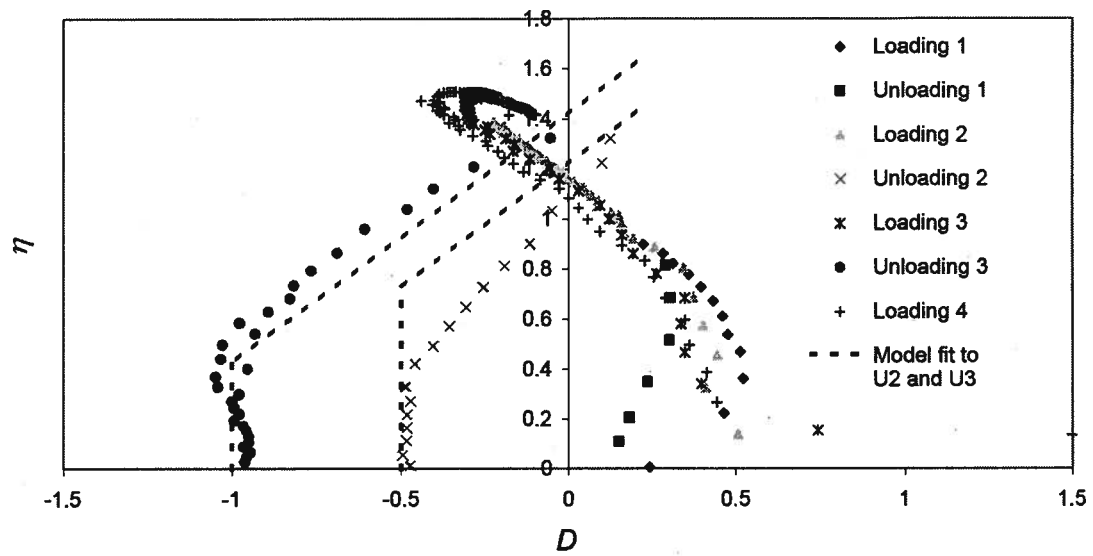


Figure A.3. Predicted and measured stress-dilatancy for ES\_CID\_862.

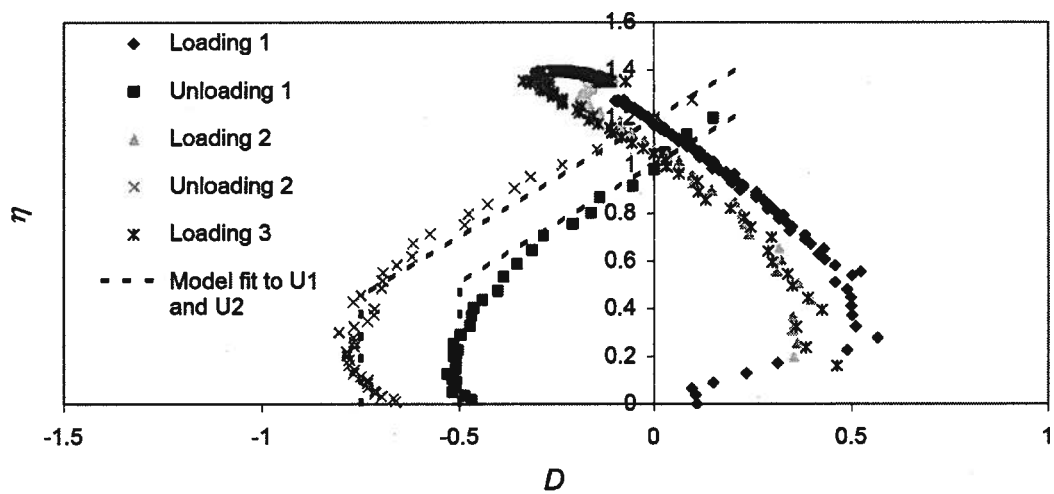


Figure A.4. Predicted and measured stress-dilatancy for ES\_CID\_866.

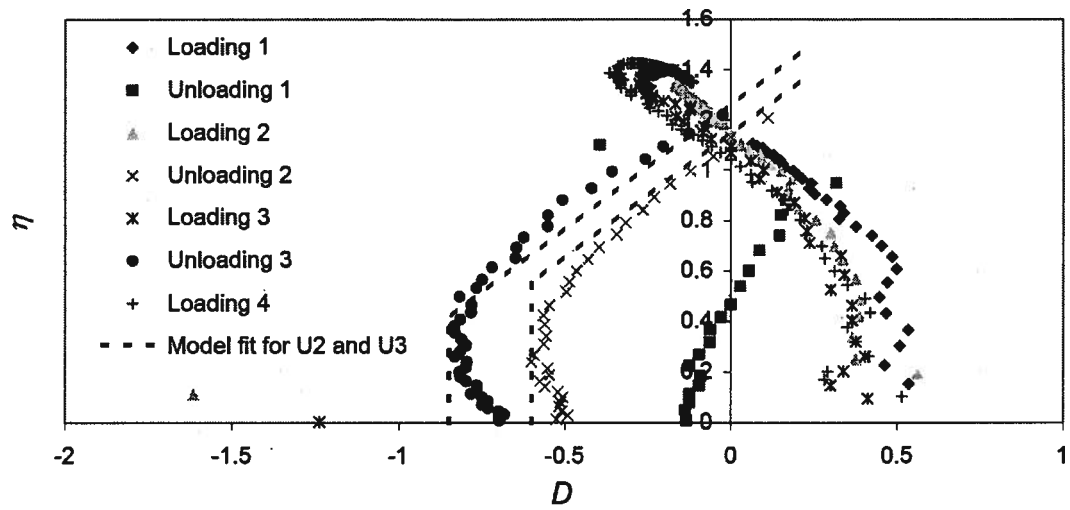


Figure A.5. Predicted and measured stress-dilatancy for ES\_CID\_867.

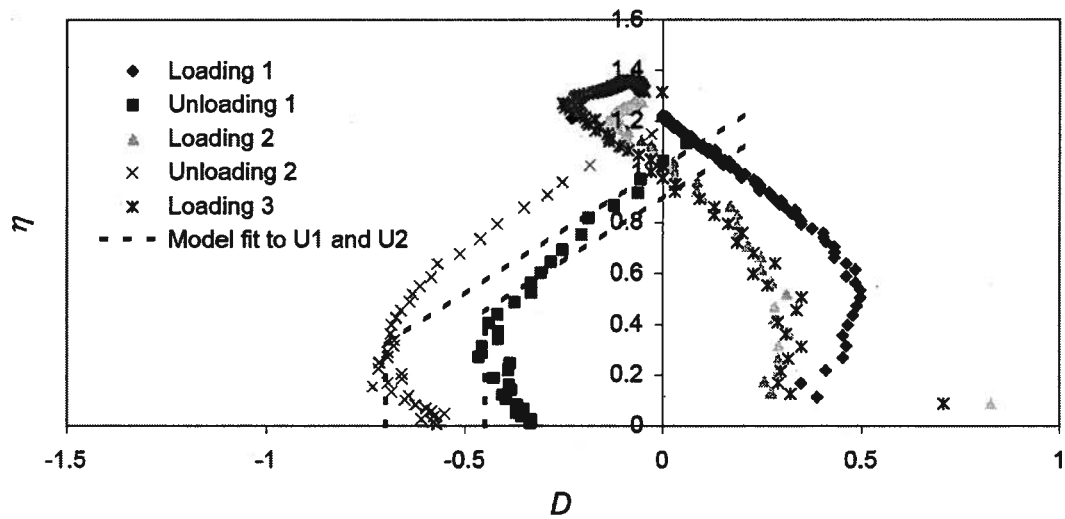


Figure A.6. Predicted and measured stress-dilatancy for ES\_CID\_868.



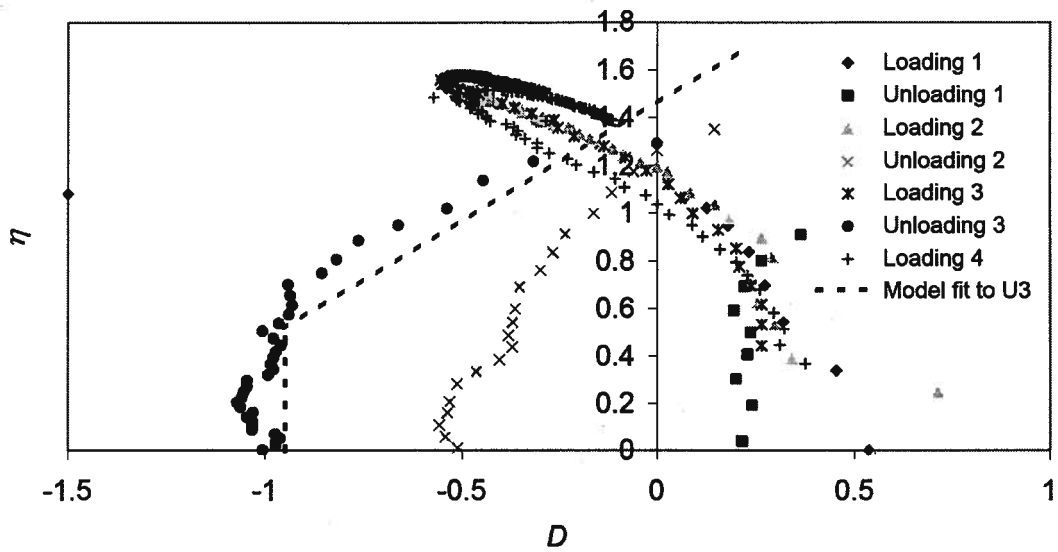


Figure A.7. Predicted and measured stress-dilatancy for ES\_CID\_870.

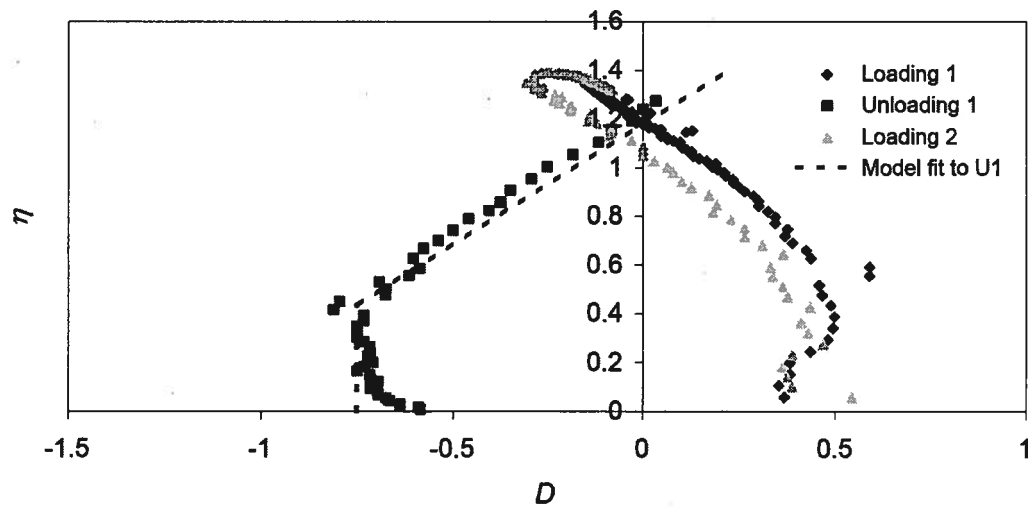


Figure A.8. Predicted and measured stress-dilatancy for ES\_CID\_871.

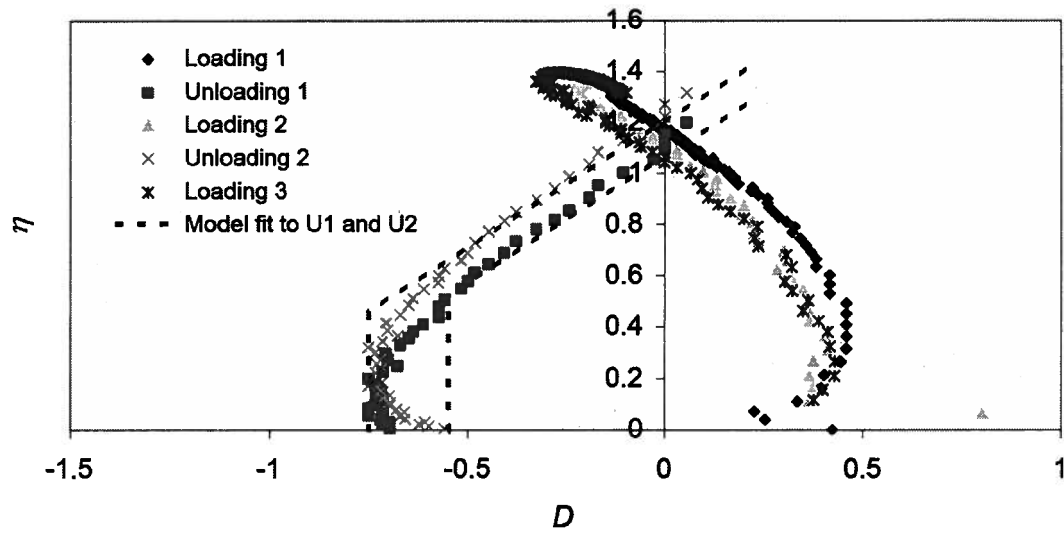


Figure A.9. Predicted and measured stress-dilatancy for ES\_CID\_872.

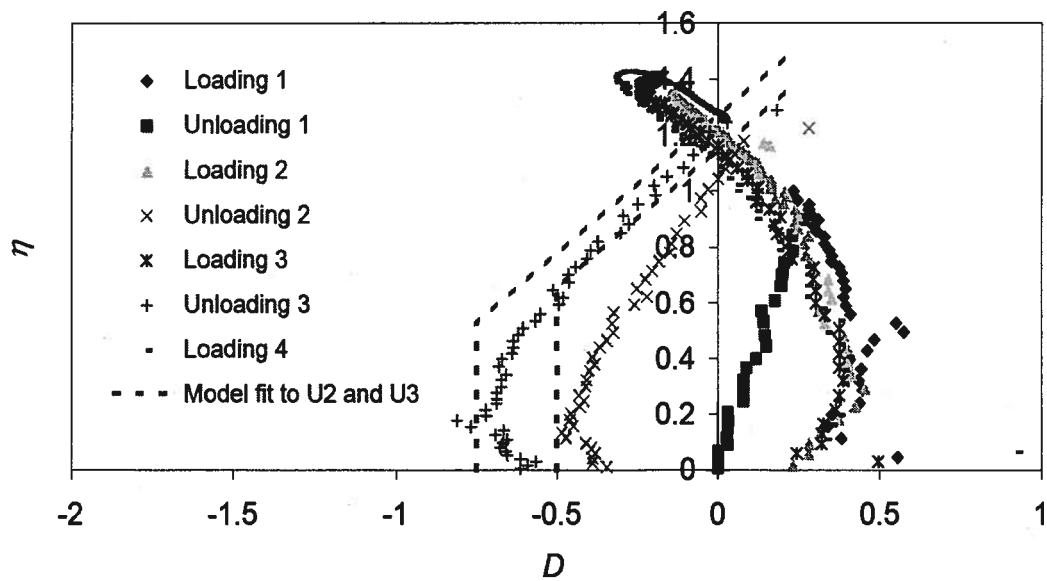


Figure A.10. Predicted and measured stress-dilatancy for ES\_CID\_873.

## APPENDIX B: RESULTS OF THE UNLOAD-RELOAD CALIBRATION FOR ERKSAK SAND

This appendix presents a comparison between the calibrated model results for Erksak sand as compared to triaxial data. The load-unload-reload calibration used to produce Figures B.1 to B.7 was introduced in Section 6.1.

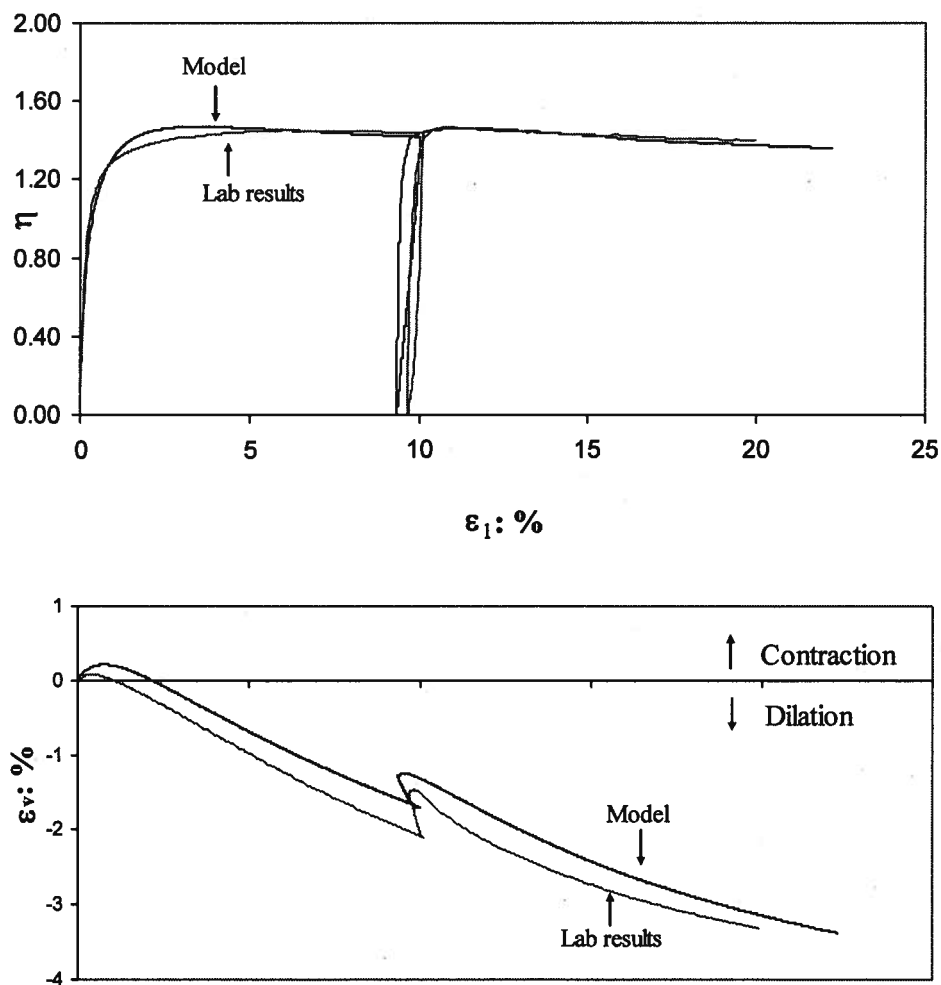


Figure B.1. Load-unload-reload calibration results compared to laboratory data for ES\_CID\_860.

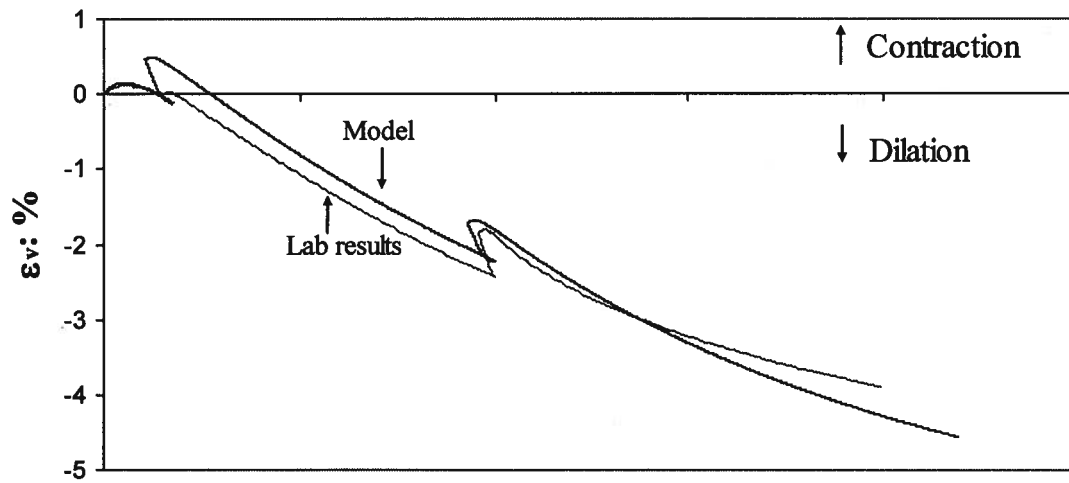
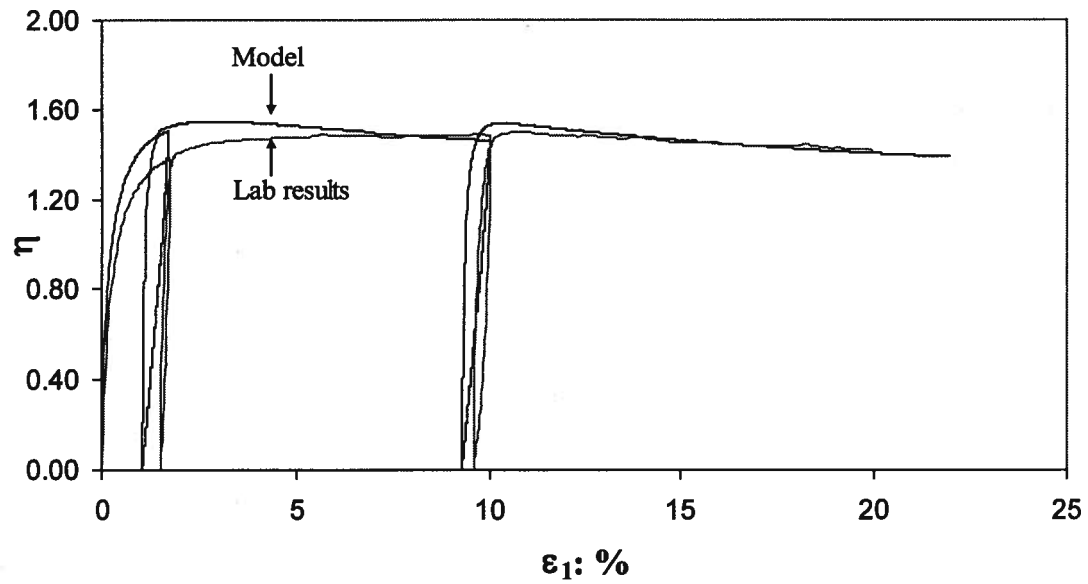


Figure B.2. Load-unload-reload calibration results compared to laboratory data for ES\_CID\_861.

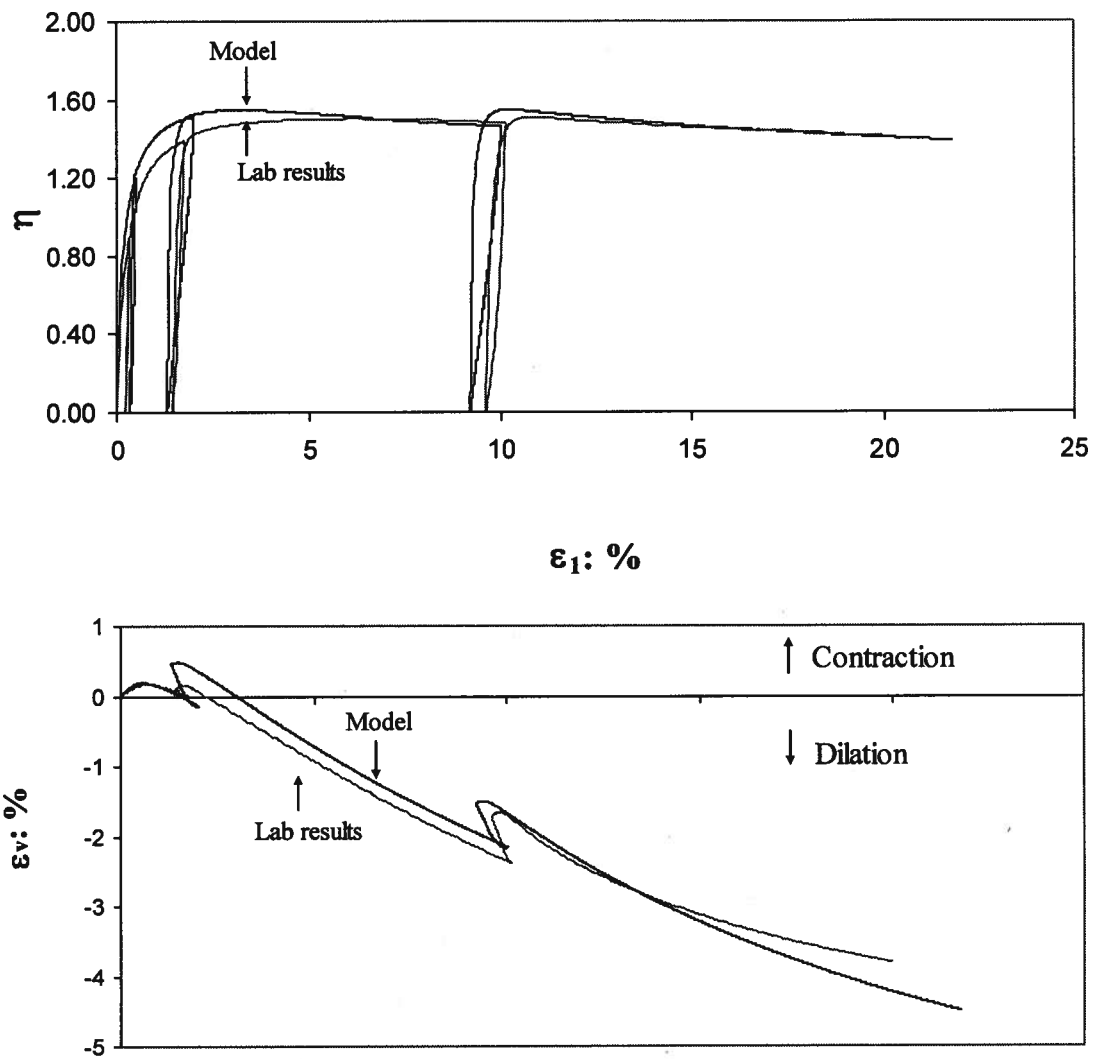


Figure B.3. Load-unload-reload calibration results compared to laboratory data for ES\_CID\_862.

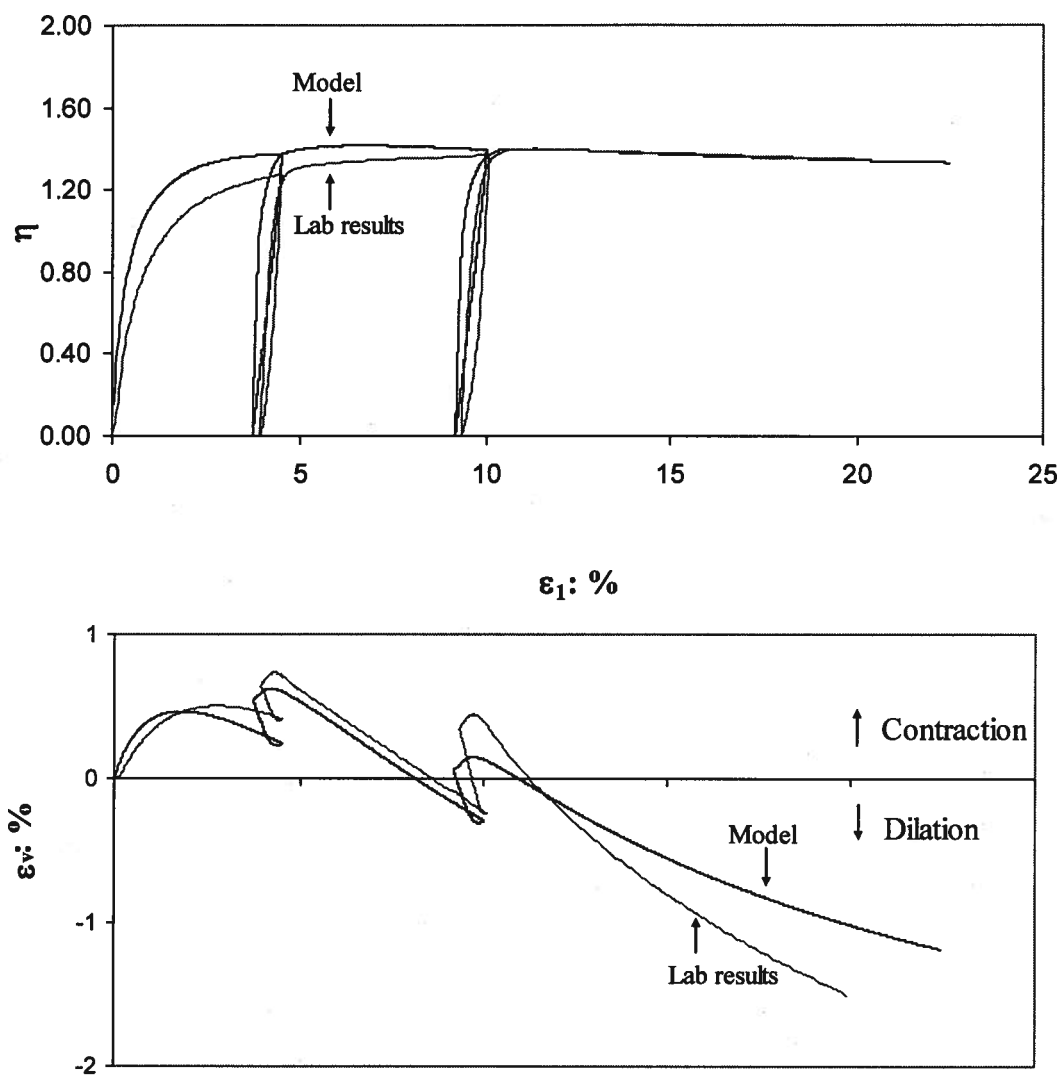


Figure B.4. Load-unload-reload calibration results compared to laboratory data for ES\_CID\_866.

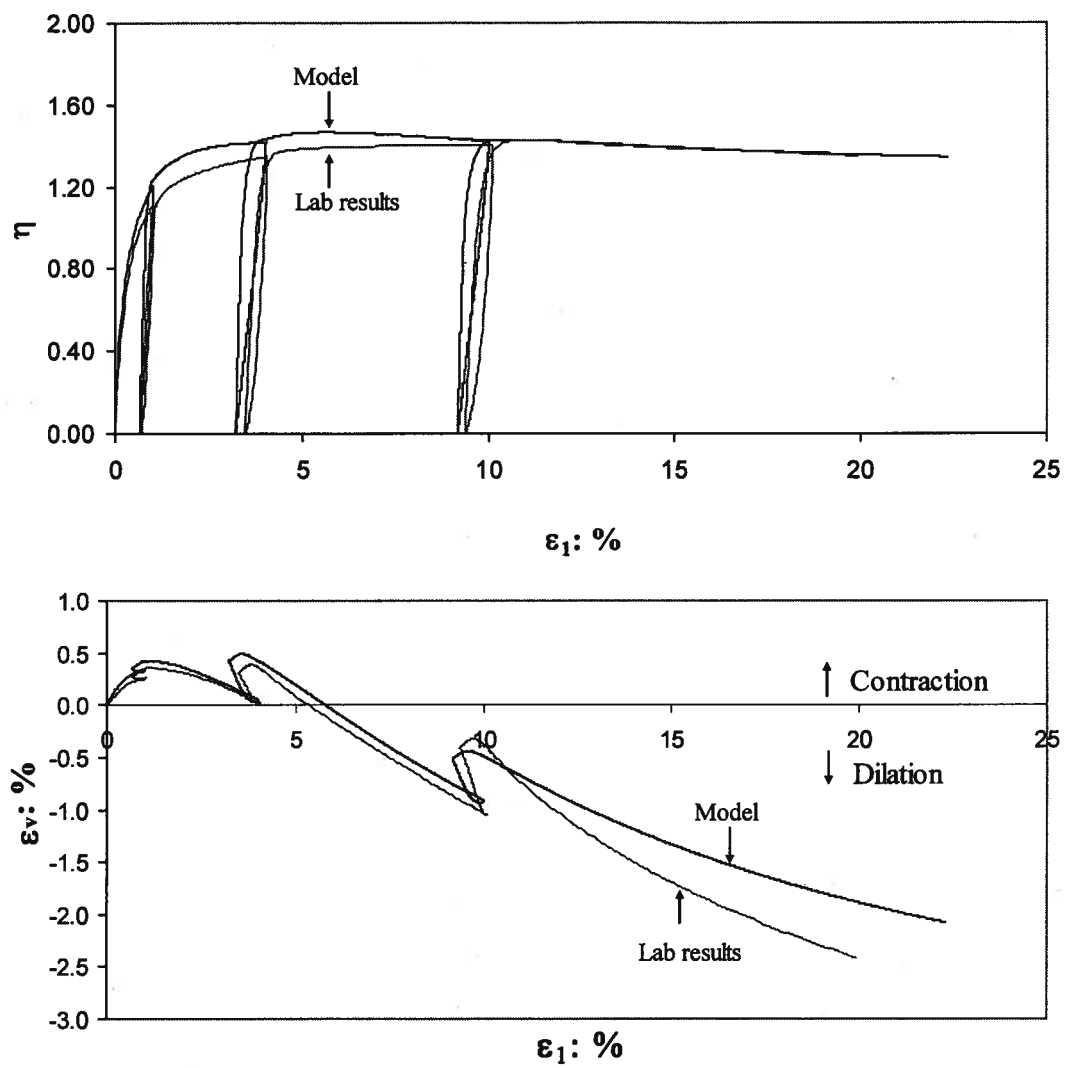


Figure B.5. Load-unload-reload calibration results compared to laboratory data for ES\_CID\_867.

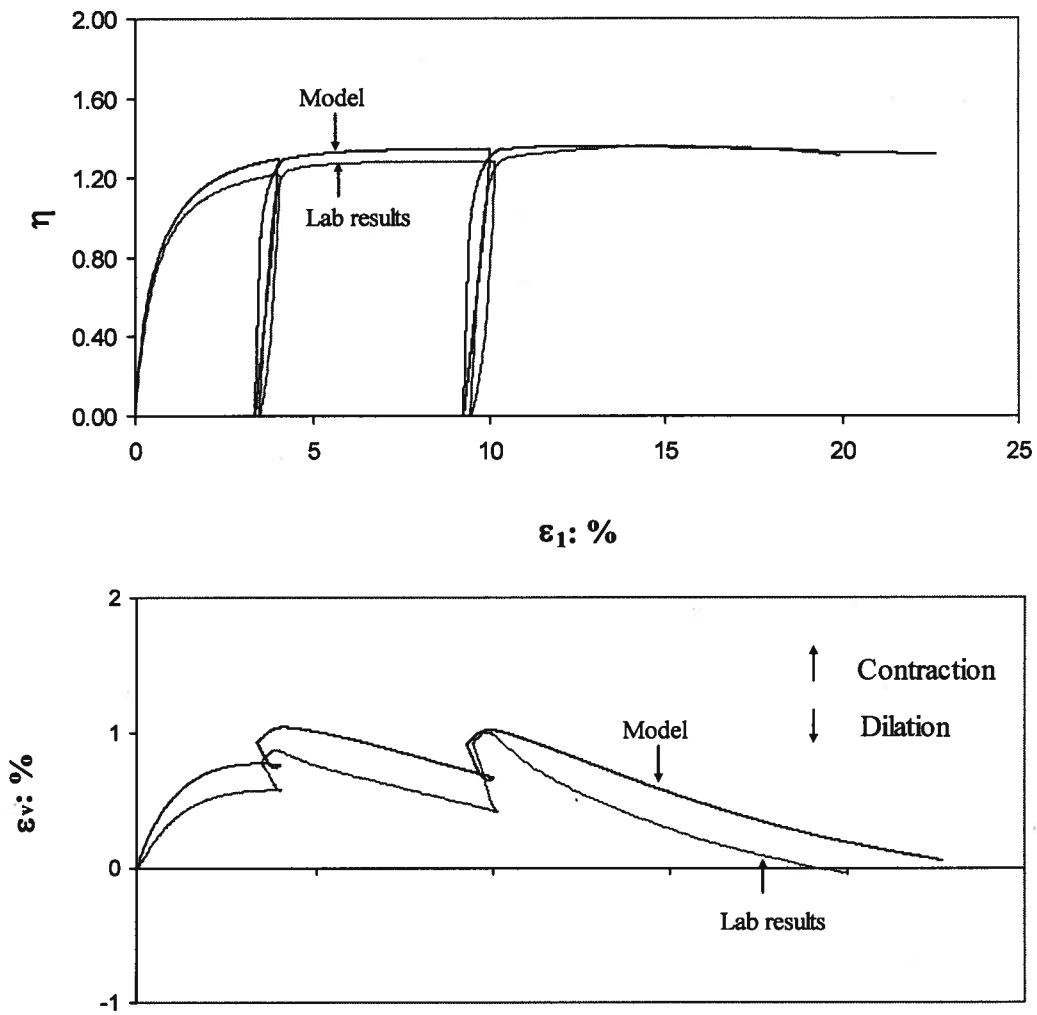


Figure B.6. Load-unload-reload calibration results compared to laboratory data for ES\_CID\_868.



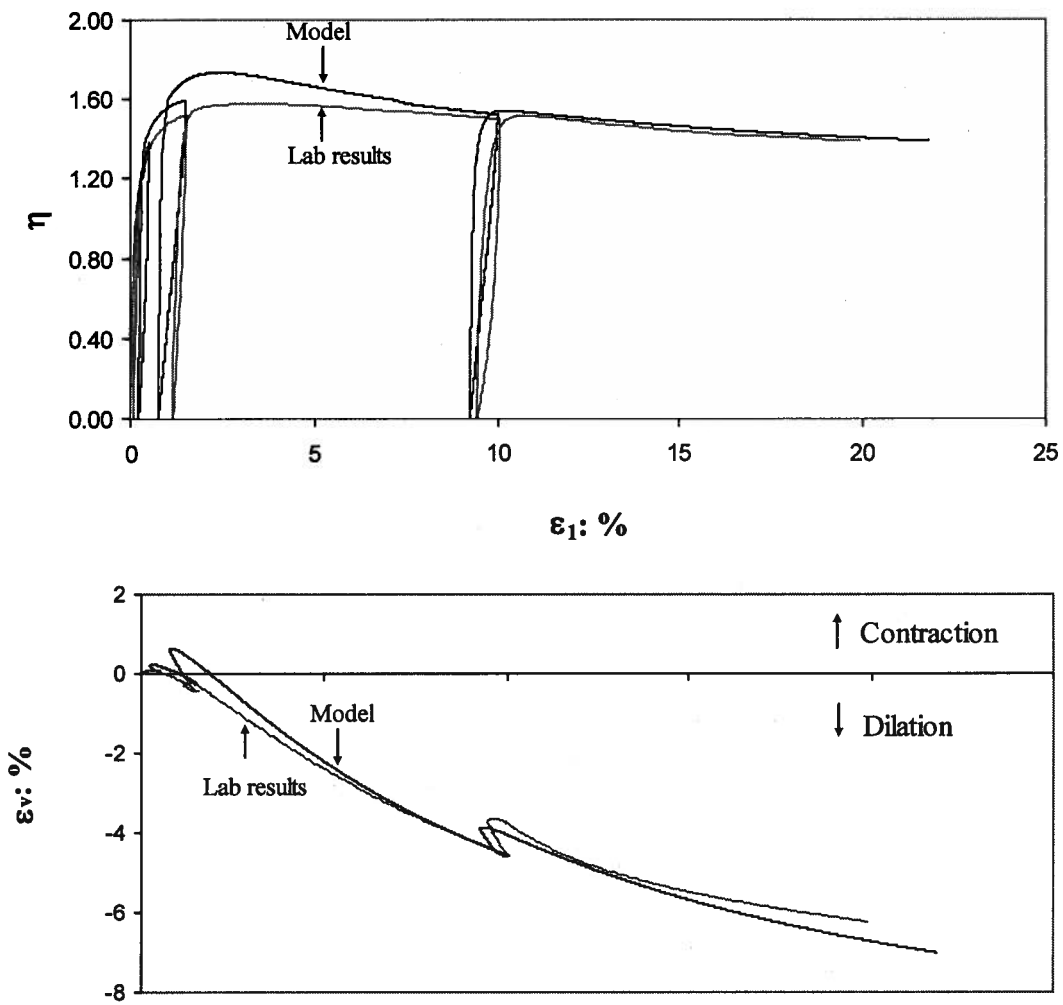


Figure B.7. Load-unload-reload calibration results compared to laboratory data for ES\_CID\_873.

## APPENDIX C: FRASER RIVER SAND MONOTONIC CALIBRATION RESULTS

A monotonic calibration of NorSand for Fraser River sand was introduced in Section 6.2. The tests used in the calibration are presented in Table 4.5. Figures C.1 to C.6 show a comparison between the calibrated model results and laboratory data.

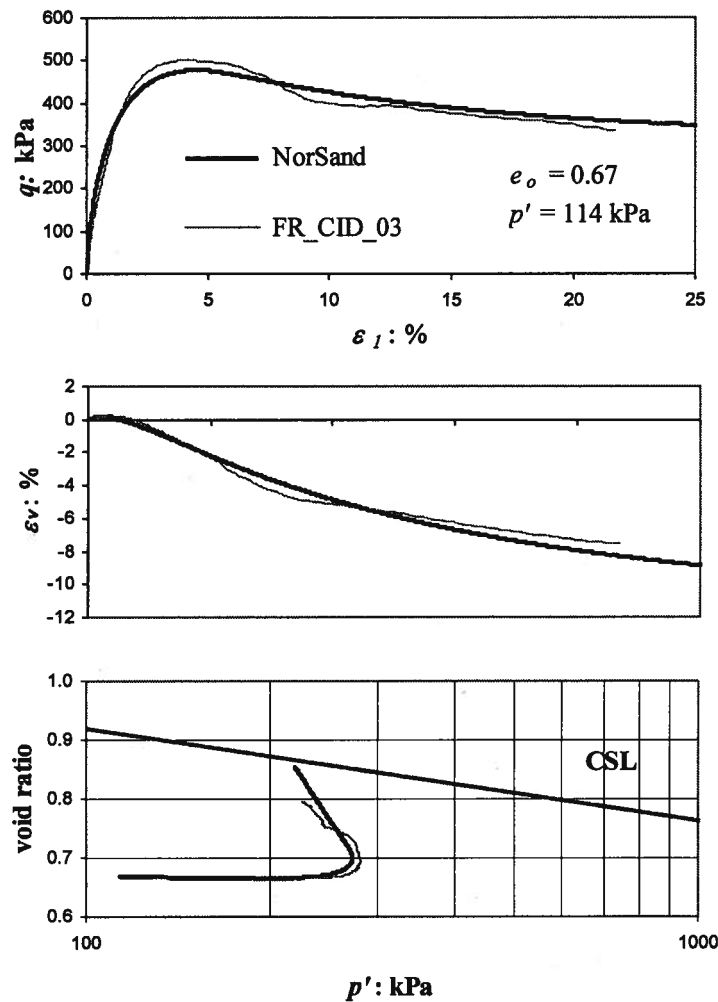


Figure C.1. Monotonic calibration results compared to tests data for FR\_CID\_03

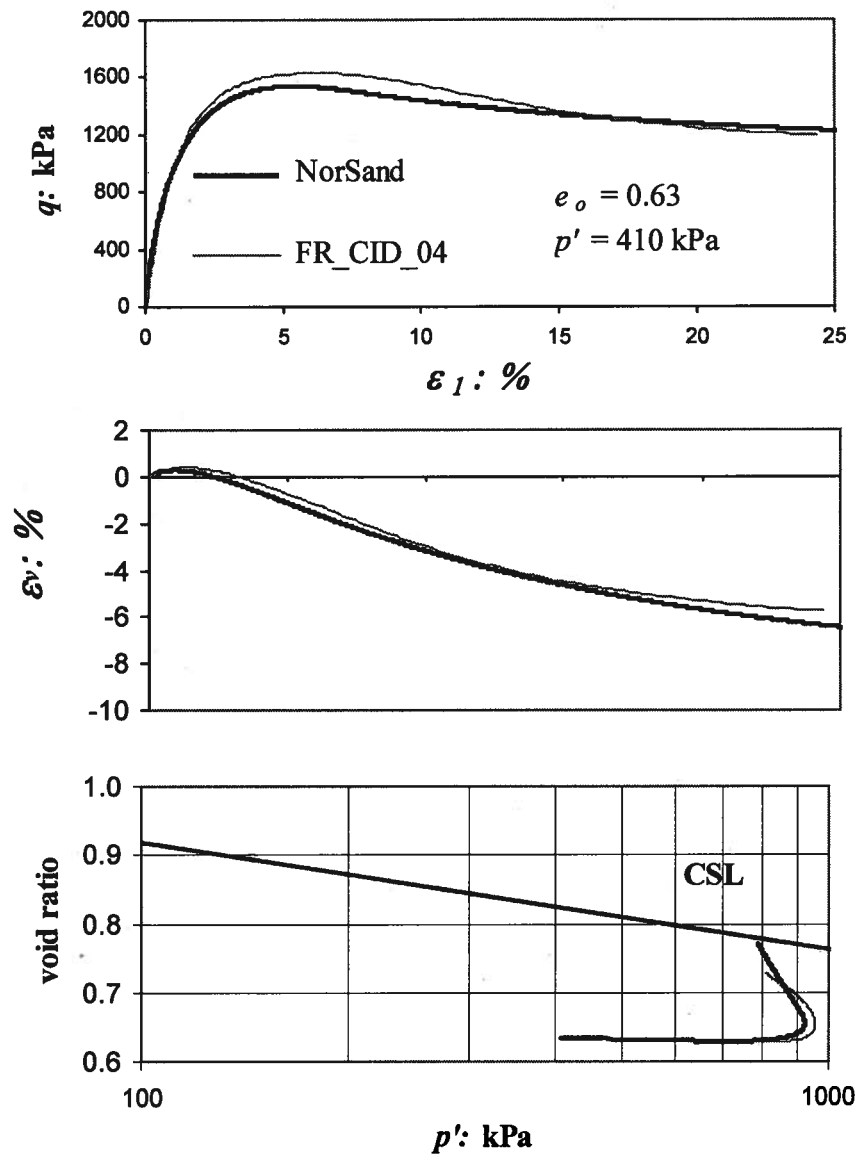


Figure C.2. Monotonic calibration results compared to tests data for FR\_CID\_04.

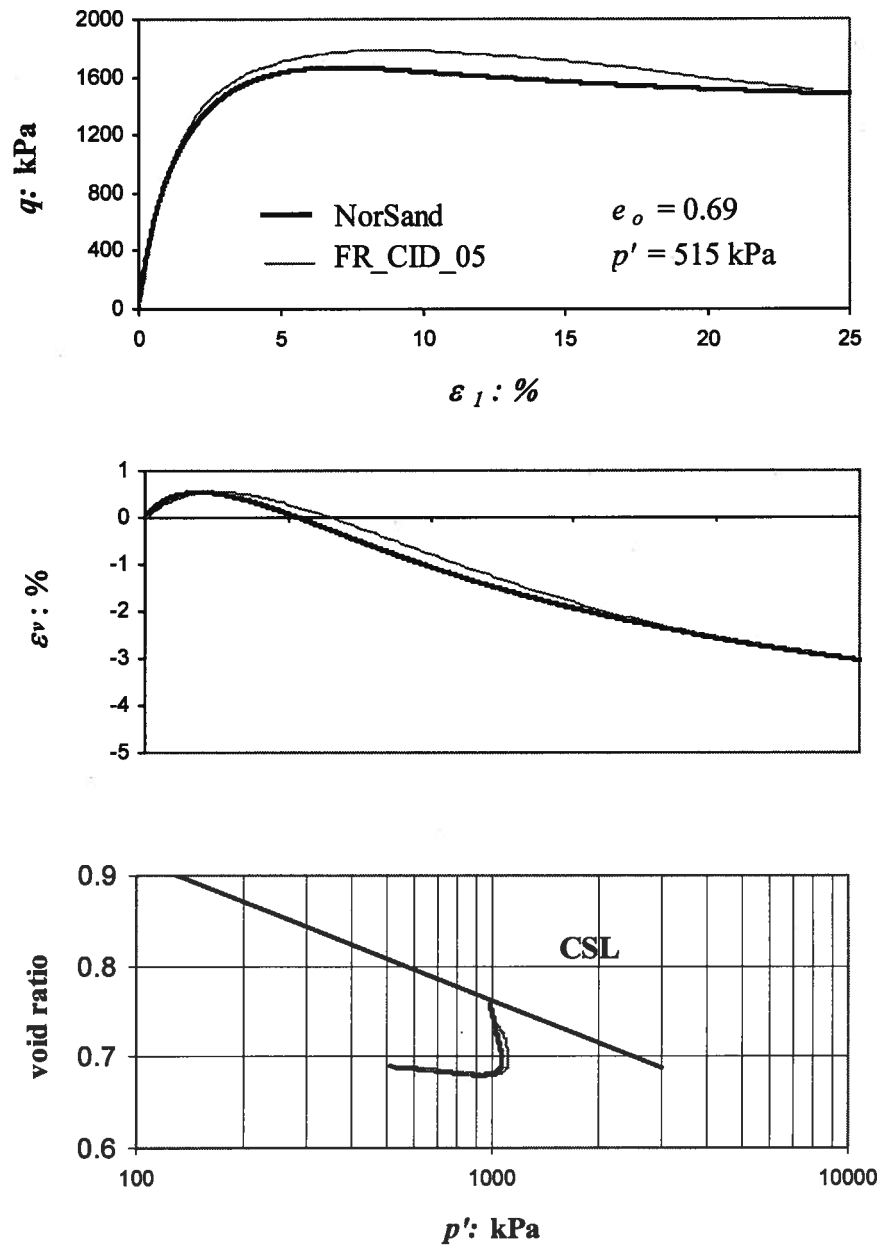


Figure C.3. Monotonic calibration results compared to tests data for FR\_CID\_05.

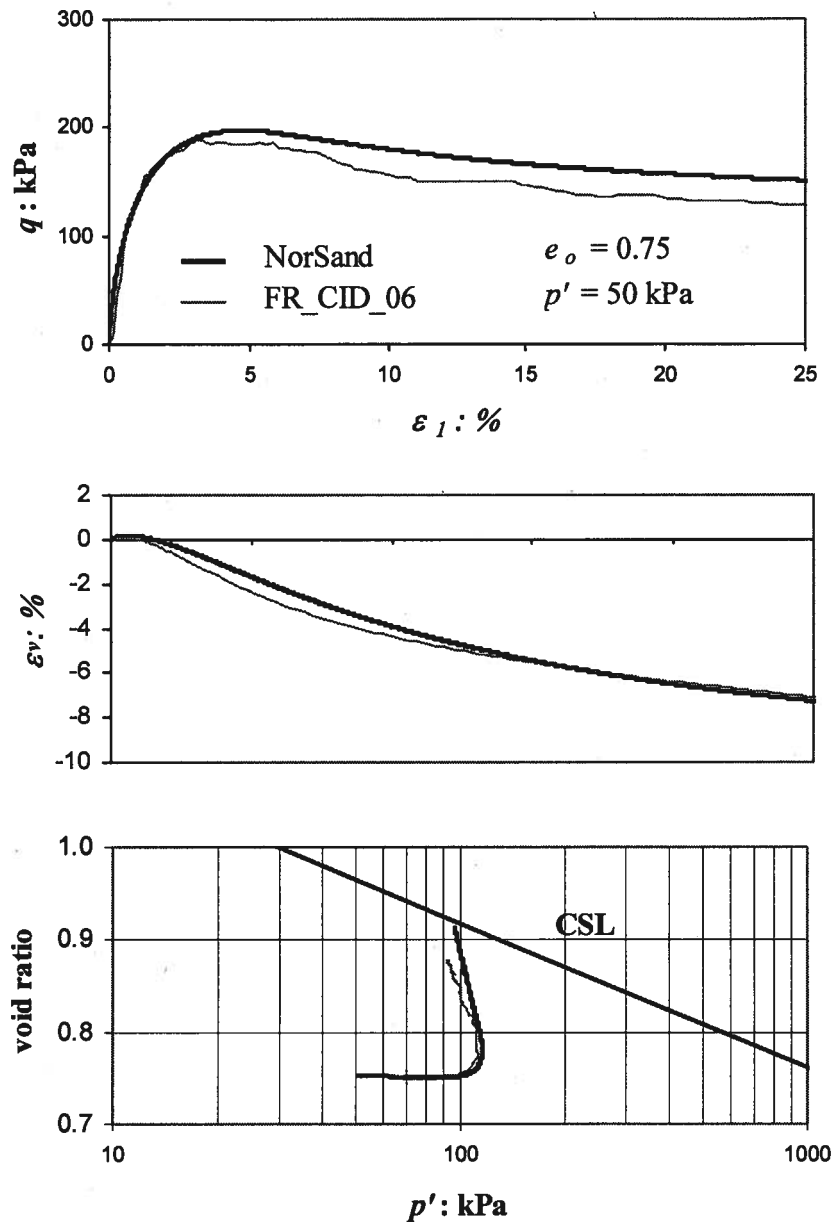


Figure C.4. Monotonic calibration results compared to tests data for FR\_CID\_06.

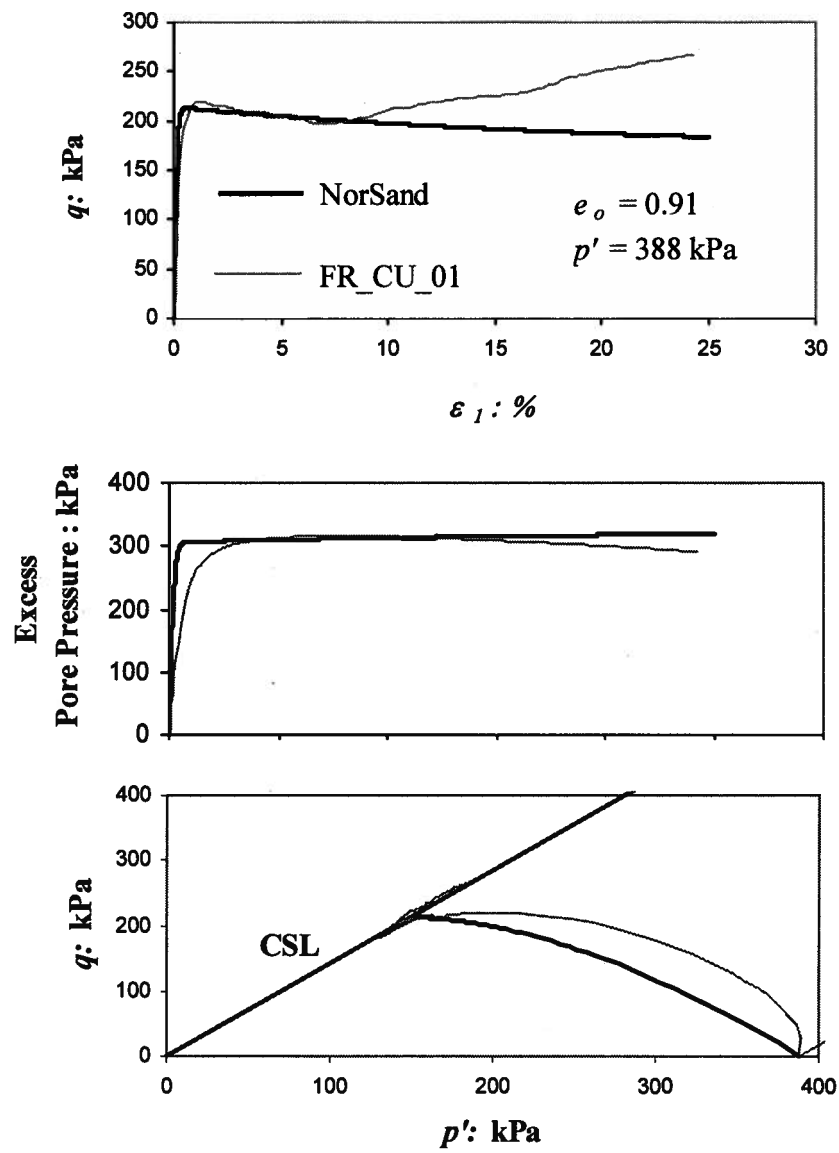


Figure C.5. Monotonic calibration results compared to tests data for FR\_CU\_01.

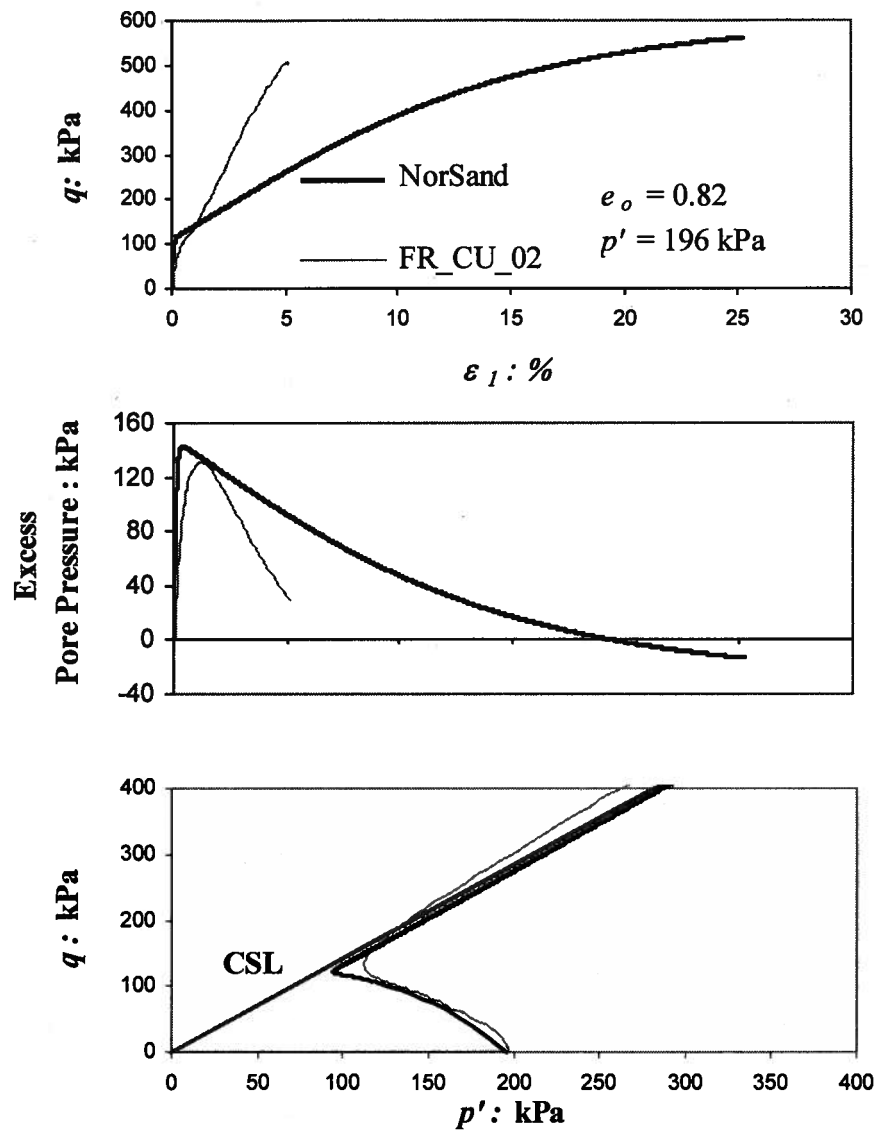


Figure C.6. Monotonic calibration results compared to tests data for FR\_CU\_02

## APPENDIX D: STEPS TO IMPLEMENT THE LOAD-UNLOAD-RELOAD MODEL IN A CODE

Figures D.1 to D.3 show the steps that can be followed in coding the load-unload-reload model.

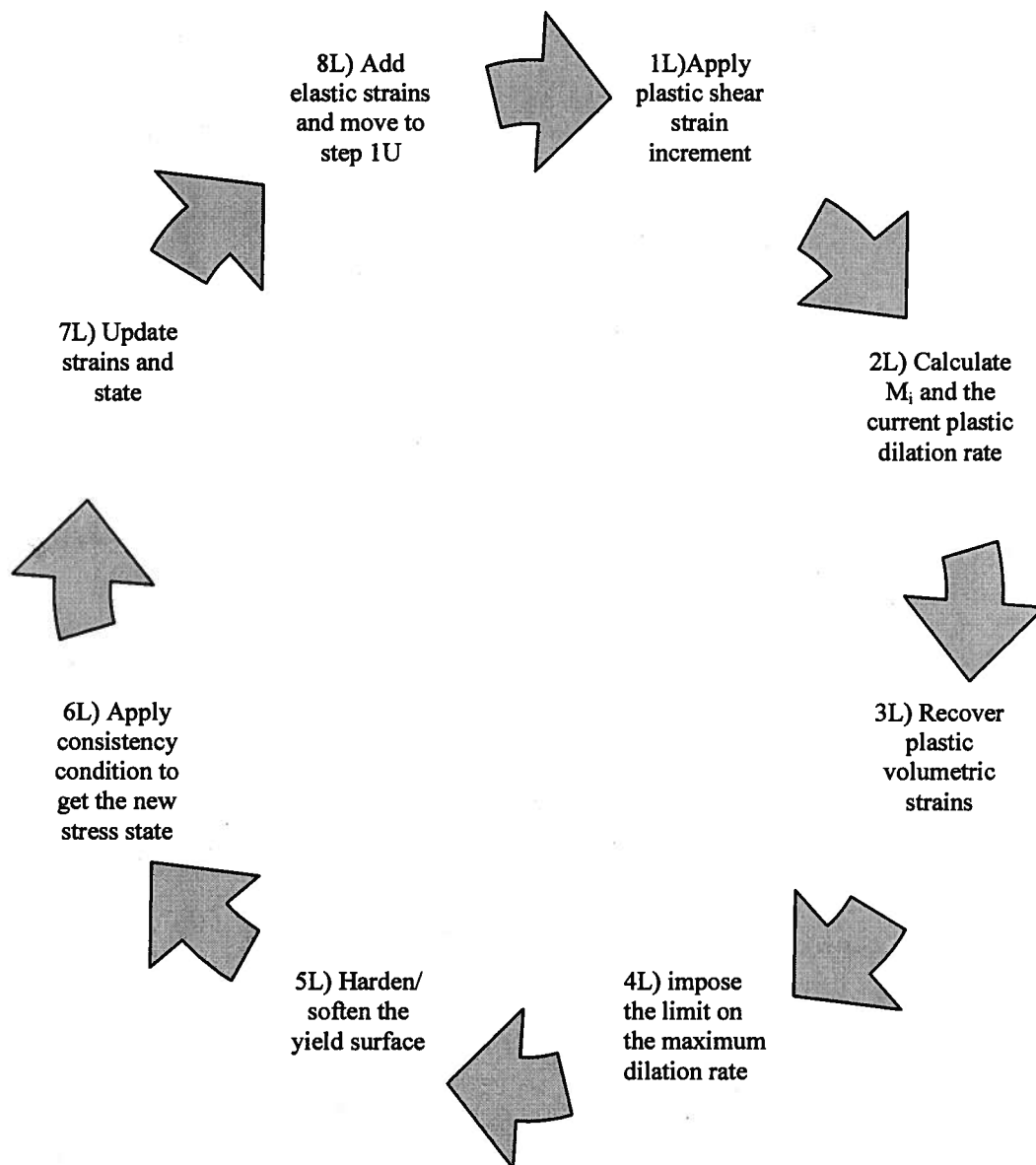


Figure D.1. A diagram illustrating loading in NorSand.



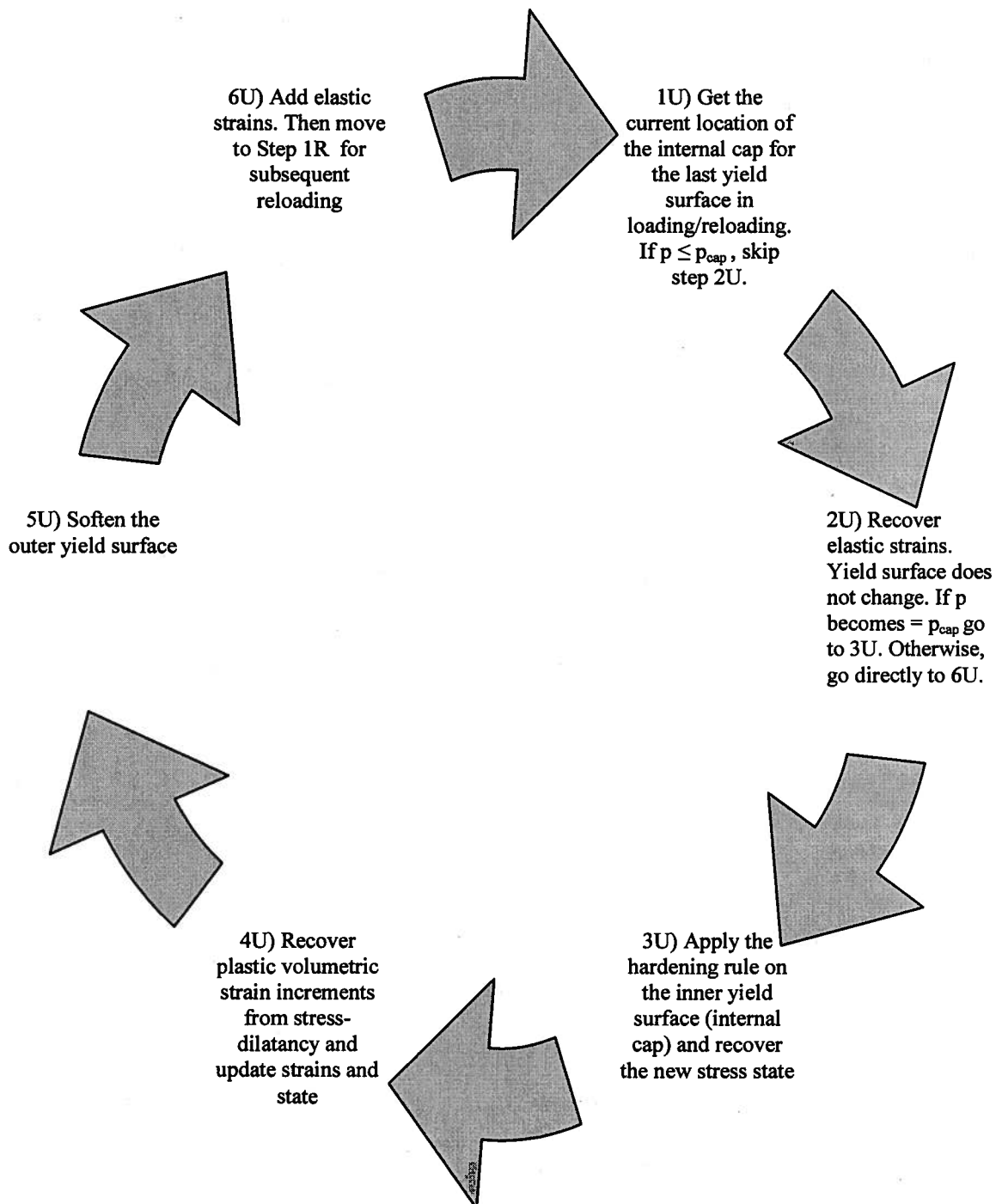


Figure D.2. Description of unloading in the model.

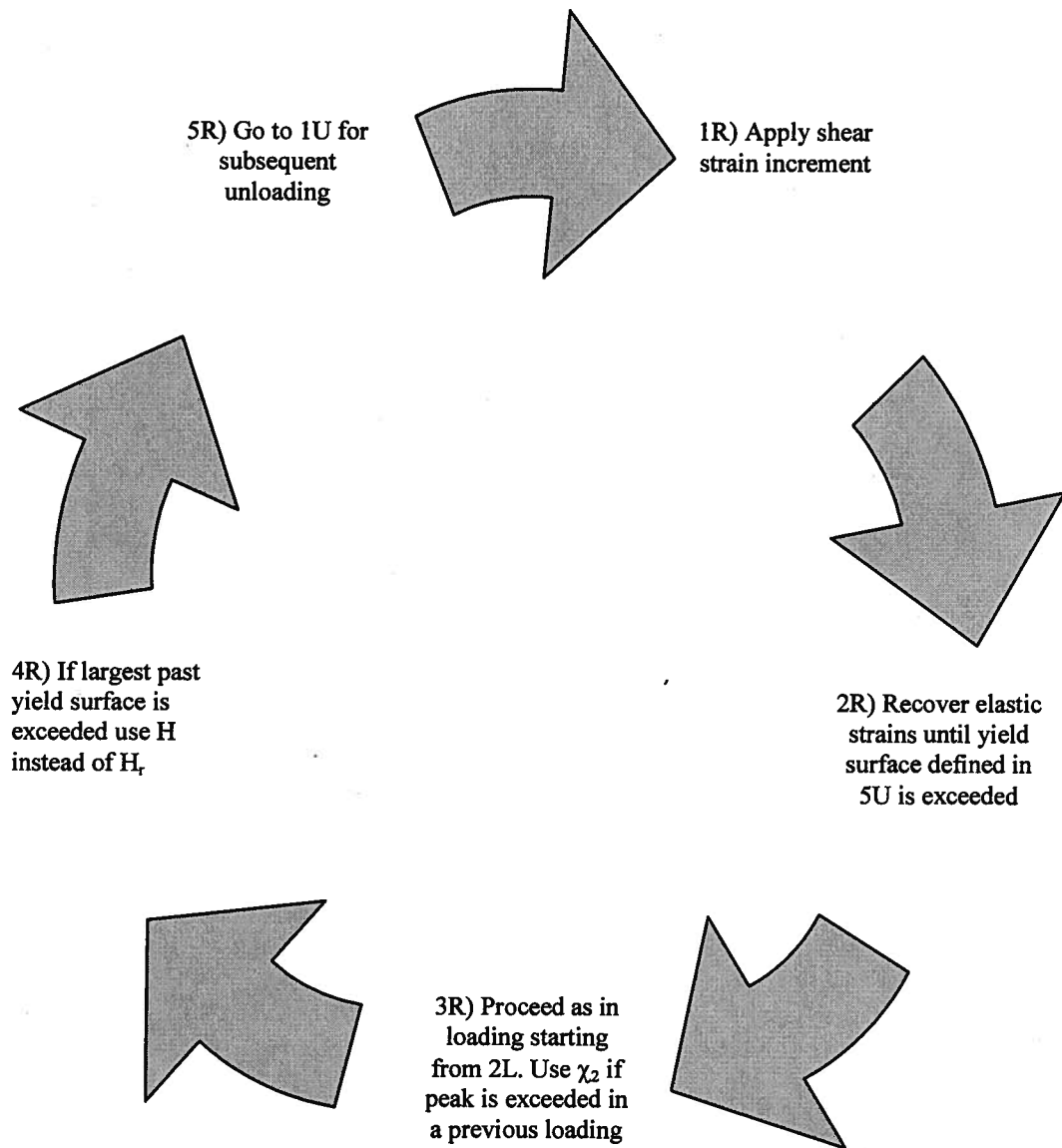


Figure D.3. Description of reloading in the model.

## **APPENDIX E: TRIAXIAL TESTING PROCEDURE**

### **1. Introduction**

This appendix briefly presents the triaxial testing procedure and sample preparation methods followed to produce the results of the triaxial tests presented in Chapter 4. A more comprehensive description of the testing procedure can be found in Golder, 1987.

The triaxial apparatus used was described in Section 2.2 (Figure 2.13). All tests reported in Chapter 4 were displacement controlled. Load was applied by a 19mm diameter stainless steel piston. The load was measured by a load cell. Cell pressure was measured using a pressure transducer. Volume change was measured using a cylindrical piston with a linear displacement transducer that was calibrated to measure volume change.

### **2. Sample preparation**

- **Wet pluviation:** A sample of air-dried sand is placed in a long neck flask. The flask is then filled with de-aired water and placed under vacuum. The membrane mould is filled with de-aired water and the flask is inverted with its neck 25mm above the bottom of the mould. Sand then flows out of the flask. The side of the mould is tapped to reach the desired void ratio.
- **Most tamping:** The sample is tamped in 6 layers. Distilled water is added to air-dried sand to yield water content of 5-6%. 6 equal weights, prepared to give the desired void ratio, are tamped inside the mould using a tamper with adjustable stops.

### **3. Testing procedure**

- The lower platen is installed and the membrane (0.3mm thick) is attached using the O-rings. The split mould is mounted and vacuum is applied to keep the membrane stretched.
- The sample is prepared using one of the previously described methods.
- The top platen is placed and the membrane is rolled around the platen and attached with O-rings. Vacuum is released and a negative pore pressure of 10-20kPa is applied. The mould is then removed.
- The sample diameter is measured at 5 locations and height is determined.
- The cell is filled with water. The loading piston is set in contact with the top platen and then locked. The LVDT is zeroed.
- A cell pressure of 20kPa is applied while the negative pore pressure is being released. The change in volume is recorded.
- For moist tamped samples, carbon dioxide is bubbled through the sample for 3 hours. The sample is then flooded with de-aired water from bottom.
- The cell pressure and back pressure are increased gradually by 100 kPa and the “B” value is measured. The piston is unlocked and the change in height due to saturation is recorded. The change in volume is also recorded.
- The sample is consolidated hydrostatically by increasing the cell pressure in increments. The change in height and volume are recorded.
- All transducers are zeroed and the sample is sheared under either drained or undrained conditions.
- The drainage line is shut and the sample is frozen. The water content and void ratio are determined using the frozen sample.